Universiteit Gent
Faculteit Wetenschappen
Vakgroep Vastestofwetenschappen

Dual magnetron sputter deposition of yttria-stabilized zirconia thin films

Jérika Suely Lamas

DRAFT

Thesis submitted to obtain the academic degree of
Doctor in Sciences: Physics
Supervisor: Prof. Dr. Diederik Depla
2013-2014

Universiteit Gent
Faculteit Wetenschappen
Vakgroep Vastestofwetenschappen

Supervisor: Prof. Dr. Diederik Depla

Universiteit Gent
Faculteit Wetenschappen

Vakgroep Vastestofwetenschappen
Krijgslaan 281, B-9000 Gent, België

Tel.: +32-9-264.43.68
Fax.: +32-9-264.49.96

Jury members:

Prof. Dr. F. Callens (UGent, chairman)
Prof. Dr. D. Depla (UGent, supervisor)

Members of the reading committee:
Prof. Dr. K. Sarakinos (Linköping University, Sweden)
Prof. Dr. N. Martin (Institut FEMTO-ST, Besançon, France)
FRS-FNRS S. Konstantinidis (Université de Mons, Belgium)

Members of the exam committee:
Prof. Dr. C. Detavernier (UGent)
Prof. Dr. I. Van Driessche (UGent)
Prof. Dr. K. Verbeken (UGent)
Prof. Dr. A. Hubin (VUB, Brussels)

DRAFT

Thesis submitted to obtain the academic degree of
Doctor in Sciences: Physics

Acknowledgements

This doctoral work is the result of 4 years of research. Several people contributed to my work in many different ways. Therefore, I wish to express my appreciation to them.

First of all, I would like to express my gratitude to my supervisor Prof. Diederik Depla who gave me the opportunity to develop this work. I was certainly motivated by his inquisitiveness in science, letting his experience and knowledge, guiding me during these years of Ph.D.

I am particularly grateful for the assistance of Dr. Wouter Leroy. His insightful comments and suggestions certainly improved the quality of this research.

I was greatly benefited from the practical help of Olivier Janssens and Nico de Roo. Furthermore, I am also grateful to the S1 staff that somehow helped me during these years.

I also appreciate the collaboration of EMAT group (Antwerpen) for the STEM measurements, LaBoMaP (Cluny) for the ballistic simulations and TUWien (Vienna) for the EIS measurements.

To my dear DRAFT colleagues I would like to say thank you. I can assure that I had a very nice time working together with you.

Not a lot of people have the opportunity and experience to work abroad. It consists of many pleasant and unpleasant challenges in a very short period of time. I was lucky to get great support from my family and friends from Belgium. Special thanks to my family in law who always welcomed me. Also to my international friends who shared experiences, joys and frustrations. I owe my deepest gratitude to Anne Dekkers who weekly listened to all my dilemmas.

Agradeço a ajuda e o carinho de minha família no Brasil. Sem vocês e nossas conversas semanais eu não teria terminado este doutorado. Obrigada por escutarem minhas lamentações e por me apoiarem da melhor forma possível. Nossos encontros sempre me deram forças para continuar o meu trabalho. Agradeço também o carinho de meus amigos que sempre me receberam de braços abertos.

And finally I appreciate all the support received from my husband, Henk, who had the patience to listen to me in the good and bad days. Your affection means the world to me. Thank you for the constructive comments, the scientific insight and warm encouragement. And especially to give me Sammeke who takes care of the happy environment at home! :)

Jérika Lamas

"Science never solves a problem without creating ten more."
George Bernard Shaw

Table of Contents

List of Figures

List of Tables

Nederlandse samenvatting –Summary in Dutch–

Yttrium gestabiliseerd zirconium (YSZ) heeft vele interessante eigenschappen en is daarom een vaak gebruikt materiaal in talrijke toepassingen: als bufferlaag, in zuurstofsensoren, in nucleaire toepassingen en warmte-isolerende coatings. Een ander typisch voorbeeld is het gebruik van YSZ als elektrolyt in vastestofbrandstofcellen. Dit elektrolyt heeft een hoge ionengeleidbaarheid bij hoge temperatuur. Momenteel wordt er onderzoek gedaan om de werkingstemperatuur te verlagen door het elektrolyt te verdunnen. Door de laagdikte te minderen, kunnen de eigenschappen van YSZ echter veranderen ten opzichte van de bulkeigenschappen van deze materialen. Dit is te wijten aan het optreden van nano-effecten. Het doel van dit werk is om een beter inzicht te verwerven in de YSZ microstructuur en kristalliniteit. Een beter begrip van het materiaal laat toe om de YSZ eigenschappen te manipuleren.

De YSZ dunne lagen werden afgezet door middel van DC dual reactief magnetron sputteren (een fysische dampafzettingstechniek). In deze techniek wordt een negatieve spannning aangelegd tussen de target en de kamer. Hierdoor worden positieve ionen versneld naar de target en botsen ze met de atomen van het bronmateriaal. Deze atomen verlaten het bronmateriaal als gesputterde atomen, en worden finaal afgezet op de kamerwanden en het substraat. Door lokaal op het substraatoppervlak een reactief gas te blazen, wordt een oxidelaag gevormd. Bovendien laat deze lokale gasstroming een afzetting bij hoge depositiesnelheid toe. Op deze manier kunnen dunne lagen met diktes van enkele nanometers tot enkele micrometers afgezet worden. Door twee onafhankelijke bronnen te gebruiken (yttrium en zirconium), kan de samenstelling van de dunne lagen gevarieerd worden. Een variatie van de afzettingsparameters laat ook toe om de morfologie en textuur van de dunne lagen te beïnvloeden. In dit werk worden YSZ lagen afgezet op glas, silicium en saffier. De substraatkeuze wordt bepaald door de toegepaste karakteriseringmethode.

De dunne lagen hebben een typische kolomstructuur. Uit de microstructuur kan afgeleid worden dat onze lagen in zone T van het uitgebreid structuurzonemodel groeien. Het uitgebreide structuurzonemodel toont aan dat de eigenschappen van lagen in zone T sterk beïnvloed worden door de depositieparameters. Daarom wordt de invloed van de depositieparameters op vier karakteristieke laageigenschappen bestudeerd. De onderzochte laageigenschappen zijn de

samenstelling, de laagdikte, de kristalgrootte en de roosterparameter. De depositieparameters worden telkens veranderd om een gewenste laag te bekomen. Op deze manier wordt er een databibliotheek aangemaakt van het YSZ systeem als functie van de depositieparameters target-substraatafstand, ontladingsstroom, gasdruk en depositietijd. De chemische samenstellingen werden ook vergeleken met simulatieresultaten. Hierbij werd de hoekdistributie in de simulaties aangepast tot er een goede overeenkomst werd gevonden tussen de experimentele data en de simulatieresultaten.

De onderzochte lagen vertonen een biaxiale alignering. Dit betekent dat de samenstellende korrels niet enkel een uit-het-vlak oriëntatie hebben, maar eveneens een in-het-vlak alignering. Een biaxiale alignering wordt bekomen door magnetron sputterdepositie op een gekanteld substraat ten opzichte van de magnetron. De biaxiale alignering werd bepaald door de poolfiguren van de (111) en (100) netvlakken op te meten. De [200] richting is de uit-het-vlak preferentiële oriëntatie. Hoewel de dunne lagen groeien onder verschillende depositiecondities werd er geen zonetransitie in het uitgebreid structuurzonemodel vastgesteld. Er werd wel een kanteling van de [200] richting waargenomen bij een toenemende hoeveelheid Y. Er worden twee technieken voorgesteld om deze kanteling te bepalen. De eerste techniek is gebaseerd op de azimutale hoek van poolfiguren en de tweede techniek maakt gebruik van de resultante van de hoogste intensiteiten van de X-straaldiffractie (XRD) bij een $\theta/2\theta$ meting. Beiden kunnen voorgesteld worden in een polaire plot. De XRD/polaire plot kan echter op twee manieren geïnterpreteerd worden. In ons geval is het resultaat van het overhellen van de korrels. Deze interpretatie geeft snellere en nauwkeurige resultaten.

Een goed begrip van de factoren die de kantelhoek van de kolommen bepalen is ook belangrijk voor dunne laagtoepassingen, omdat de kolomoriëntatie één van de hoofdassen bepaalt voor alle anisotrope laageigenschappen. De kolomgroei vertoont een andere helling in functie van de Y hoeveelheid. De kantelhoek van het rooster en de kolomhelling werden gecorreleerd. Tot een zekere samenstelling werd er een goede overeenkomst tussen beiden vastgesteld. Voor hogere waarden echter werd er een afwijking gevonden. Deze afwijking is te wijten aan de 3D groei van de kolommen. Deze kan immers niet gevisualiseerd worden door een dwarssectie van de dunne laag waargenomen door middel van rasterelektronenmicroscopie (SEM).

Er werd een model opgesteld die toelaat de kolomhelling te voorspellen. Dit model is gebaseerd op de samenstellingsgradiënt. De macroscopische samenstellingsgradiënt werd bepaald via een een rasterelektronenmicroscopie /energie dispersieve X-straal analyse (SEM/EDX) op de volledige YSZ laag. De samenstellingsgradiënt op nanoschaal daarentegen werd bepaald via een scanning transmissie elektronen microscopie /energie dispersieve X-straal analyse (STEM/EDX). Deze laatste beschouwt de variatie in samenstelling langs een aantal kolommen van de laag. Uit de vergelijking volgt dat de samenstellingsgradiënt op macroschaal gelijk is aan deze op nanoschaal.

Bijgevolg is het voldoende om een macroscopische schaal te gebruiken om het beoogde model op te stellen. Het ontwikkelde model werd toegepast op beide analysemethoden om de gelijkheid te bevestigen. Het ontwikkelde model komt goed overeen met de experimentele resultaten.

Een goed begrip van en volledige controle over het YSZ systeem laten toe om de groei van de nanostructuur lagen te manipuleren. Door de microstructuur van de lagen te veranderen, kunnen er lagen gemaakt worden met anderen kolomvormen. Een voorbeeld is de zig-zag vorm. Een verandering van de microstructuur kan eveneens de laageigenschappen beïnvloeden. De microstructuur heeft een effect op de optische eigenschappen. Ook andere factoren die een invloed hebben op de optische eigenschappen moeten in rekening gebracht worden (bv. dikte, Y hoeveelheid, gasdruk en porositeit). De microstructuur kan eveneens de ionengeleidbaarheid van dunne lagen beïnvloeden. De meting van de impedantie is echter niet zo voor de hand liggend omdat talrijke externe factoren in rekening moeten gebracht worden. Daarom kon een uitgebreide studie naar het verband tussen de ionengeleidbaarheid en de laagmicrostructuur niet uitgevoerd worden. Eerste testresultaten zijn echter veelbelovend: de ionengeleidbaarheid van onze monsters blijkt vergelijkbare te zijn aan de geleidbaarheid van de bulk YSZ. Verder onderzoek is nodig om de invloed van de microstructuur en textuur op de ionengeleidbaarheid van YSZ dunne lagen beter te begrijpen.

English summary

Due to its many interesting properties, yttria-stabilized zirconia (YSZ) is a popular material used in several applications: buffer layers, oxygen sensors, nuclear applications and thermal barriers coatings. Another typical example is the use of YSZ as an electrolyte in solid oxide fuel cells. This electrolyte has a high ionic conductivity, but only at higher temperatures. Current studies aim to lower the process temperature by reducing the thickness of the electrolyte. However, a reduction in thickness might change the YSZ properties in comparison to the bulk properties of these materials. The fundamental aspects involved change due to the occurrence of nano-effects. The objective of this work is to gain a better understanding of the YSZ microstructure and crystallinity, which opens the possibility to manipulate the YSZ properties.

In this study, the YSZ thin films were produced using DC dual reactive magnetron sputtering (a physical vapor deposition technique). In this technique a negative bias is applied between the target and the vacuum chamber. Positive ions are then accelerated and collide with the target atoms This results in the ejection of the target atoms which are then deposited on the chamber surfaces (e.g. the substrate). The addition of a reactive gas on the substrate surface allows the growth of an oxide film. In this work, a localized gas flow directed to the substrate is used to permit the growth of an oxide film at high deposition rate. This technique allows to deposit thin films with thicknesses ranging between a few nanometers up to micrometers. By using two independent sources (yttrium and zirconium) the elemental composition of the thin films can be varied in a flexible way. Additionally, varying the deposition conditions enables us to modify the thin film morphology and texture. In this work YSZ thin films are deposited on glass, silicon or sapphire substrate. Each of these substrates was selected based on the applied characterization method.

The thin films have a columnar structure which indicates that the films grow in the so-called zone T of the extended structure zone model. In addition, it is known that zone T is strongly affected by the deposition conditions. Therefore, four film characteristics (i.e. composition, thickness, grain size and lattice parameter) are studied as function of the deposition conditions. Full control of the deposition conditions is achieved to obtain a desired film. In this way, the results provide a full library of the YSZ system under the specific conditions of target-substrate distance, current, pressure and deposition time. Additionally, the compositional data are compared to simulation results. The angular distribution in the simulation data

was tuned until a good fit (approximately 9%) was found between experimental data and simulations.

Interestingly, the studied films present a biaxial alignment which means that the constituent grains not only have an out-of-plane orientation but also an in-plane alignment. The biaxial alignment is easily achieved using magnetron sputter deposition by inclining the targets with respect to the substrate. The biaxial alignment could be concluded from pole figures of the (111) and (100) lattice planes. The [200] direction is identified as the out-of-plane preferentially oriented. Although the deposited films were grown under different deposition conditions, no transition in the structure zone model was noticed. Instead, a tilt of the [200] direction is noticed as soon as the content of Y increases. In order to identify the grain tilt on the YSZ system two techniques were proposed. The first technique is based on the azimuthal angle of pole figures while the second technique uses the resultant vector from the highest intensities of the X-ray ($\theta/2\theta$) diffraction (XRD). Both are depicted in a polar plot. The XRD/ polar plot, however, can be interpreted in two ways. In our case is the result of the tilting of the crystals. Using this interpretation leads to faster and accurate results.

An understanding of the factors that determine the columnar growth angle is also important for thin film applications, because the column orientation defines one of the principal axes for all anisotropic film properties. The columnar growth shows a different tilt as a function of the content of Y. The grain and columnar tilt were correlated. An agreement between both occurs until approximately 20 at.%Y. Above this value, a difference is noticed. This difference is related to the 3D growth of the columns which cannot be identified by a scanning electron microscopy (SEM) cross section view.

A stress model to determine the grain tilt was developed. The tilt is predicted based on the characteristics of YSZ. The characteristics were investigated taking into consideration the macroscopic as well as the nano scale compositional gradient. The macroscopic compositional gradient is obtained via scanning electron microscopy/energy dispersive X-ray spectroscopy (SEM/EDX) analysis on the full YSZ layer while the compositional gradient at nano scale was obtained via scanning transmission electron microscopy/energy dispersive X-ray spectroscopy STEM/EDX. The latter considers the compositional variation along few columns of the film. The comparison showed that the compositional gradients on macro and nano scale are equivalent. Hence, the use of a macroscopic scale is sufficient to develop the model. However, the model was applied to both analysis methods to confirm their equivalence. It was found that the proposed model agrees well with the experimental results.

The control and understanding of the YSZ system allow manipulating the growth of nanostructured films. Playing with the microstructure of the films, it is possible to create films with different columnar shapes, as for example in a zig-zag shape. The change of the microstructure can affect the optical properties of the films. Films with refractive index of 2.2 (at wavelength of 550 nm) and a band gap

of 5.63 eV were deposited. However, it is necessary to take into consideration other factors that also contribute to the variation of the optical properties, for example, thickness, Y content, pressure and porosity. The film microstructure can also affect the ionic properties of thin films. Unfortunately, an extensive study on the relations between ionic conductivity and film microstructure could not be performed. The main reason is that the measurement of the impedance is not trivial because several external factors need to be taken into account. However, a first trial of our samples returned a positive feedback, indicating that the samples possess a meaningful ionic conductivity (1.37×10^{-6} S/cm) in comparison to the conductivity of a bulk YSZ (1.67×10^{-5} S/cm). Therefore, we incentive the investigation of the influence of the microstructure and texture on the ionic conduction of YSZ thin films.

Introduction

Driven by the global quest for alternative materials, several initiatives have been started to develop better materials to be applicable not only in research but also in industry. There are two possible ways to obtain these materials. The first comprises the discovery of a new material, while the second involves the understanding of the behavior of an existing material in order to control its characteristics. Due to the strong driving force towards creation of new technologies, up to now more effort has been done in the development of new materials, leaving the understanding to a side.

This research focuses on Yttria-stabilized Zirconia (YSZ), which is commonly known as solid electrolytes. These types of electrolytes are electrically conductive materials due to the presence of mobile ions acting as charge carrier. The charge carrier can be a cation (such as H^+, Li^+, Ag^+) or an anion (such as F^- and O^{2-}). A vast amount of literature data on these materials is mostly related to bulk materials and thick films. However, there is at present a limited amount of information on the fundamental aspects related to solid state electrolytes on academic level, specially in Flanders. Nevertheless, this fundamental research is needed to support the idea of understanding the material in order to control its properties.

In order to discern the relations happening in the solid state electrolyte, it is necessary to reduce its proportions to atomic level. Downscaling the electrolytes to thin films, for example, changes their fundamental aspects due to the occurrence of small scale or nano effects. Essentially, two fundamental questions arise when reducing the film thickness.

First, one can question if the results related to the influence of the composition on the ion conductivity as measured for bulk solid state electrolytes can be transferred to thin film materials. The pronounced scatter of the activation energies for the oxygen ion migration and electrical conductivity properties of solid state electrolytes as a function of their composition makes it difficult to answer this question.

The second question is related to microstructure and crystallinity. At present, it is not clear how the microstructure of solid state electrolytes affects the properties of the thin films. However, a good understanding of this relationship would open the possibility to manipulate the YSZ properties by controlling the nanocrystalline microstructure of the thin film.

Naturally, one must realize that this subdivision based on these two questions is somewhat artificial as the thin film morphology and texture can be related to the composition. Hence, only a multi-axis approach allows a full understanding due to

the relationship between composition and microstructure (and texture). Therefore, it is necessary to investigate the morphological and textural characteristics of thin films as function of both composition and deposition conditions. In this way, the three principal axes are i) elemental composition, ii) microstructure and texture and, iii) properties.

Therefore, the development of this thesis is divided in the following structure:

Chapter 1: Presentation of the YSZ system, its properties and some applications.

Chapter 2: Description of thin film techniques. A focus is given to DC unbalanced reactive magnetron sputtering, which is the technique used in this work. In addition, some fundamentals aspects involved in this technique are explained.

Chapter 3: Growth of thin films, starting from nucleation up to a developed thin film. Fundaments of the film growth necessary to the comprehension of this work are given.

Chapter 4: Definition of the experimental setup used to deposit YSZ thin films. The deposition conditions are included as well as the characterization techniques used.

Chapter 5: Examination of the influence of deposition conditions on the film characteristics. Due to its extension, this chapter is subdivided in five parts.

Part I talks about the influence of the deposition conditions on the thickness, composition, grain size and lattice parameter.

Part II shows the use of the experimental data to validate simulation results.

Part III investigates the YSZ microstructure as a function of the deposition conditions.

Part IV focus on the YSZ texture as a function of the deposition conditions.

Part V discusses the relations between microstructure and texture.

Chapter 6: Analyses in nano scale supported by the development of a model to elucidate the effects occurring during film growth.

Chapter 7: Tuning the microstructure and texture to produce zig-zag films and the effects on the optical properties due to the changed film microstructure.

Chapter 8: Recommendations for future work based on the ionic properties of the YSZ system.

This series of chapters enable us to reach the goal of the research project, i.e. to unravel the behavior of YSZ thin films which can form the basis to improve the current properties of the YSZ system. Unfortunately, some aspects will still remain unsolved but with this research, it is expected to contribute to a large extent to the fundamental knowledge related to the YSZ system.

1

Yttria-Stabilized Zirconia, characteristics and applications

This work focuses on Yttria-Stabilized Zirconia (YSZ) thin films. In this chapter, we will first discuss the phase diagram of the considered YSZ system and its characteristics. Next, some examples of the applicability of YSZ are shown.

1.1 Crystal phases of Yttria-stabilized zirconia

Zirconium dioxide or zirconia (ZrO_2) exists in three crystal phases at different temperatures: monoclinic, tetragonal and cubic. These can be seen as variants of the cubic fluorite structure. At room temperature, zirconia is monoclinic. The structure changes to the tetragonal phase above 1180 °C. And above 2370 °C, it reaches the cubic phase [1, 2]. This cubic phase is one of the most interesting phases of zirconia due to its chemical stability, and its excellent mechanical, thermal and electrical properties. But, its applicability is limited because it can only exist at high temperatures. When cooling to room temperature, a volume change caused by the phase transformation from cubic to tetragonal and then to monoclinic induces large stresses, causing a possible rupture of the ZrO_2 lattice [1]. However by adding other oxides, the zirconia can be stabilized in the cubic phase at room temperature [2].

Investigations performed by Ruff and Ebert [3] and by Geller and Yavorsky [4] demonstrated that yttria (Y_2O_3) in the zirconia lattice stabilizes the cubic form

at room temperature. This is illustrated in Figure 1.1, where the phase diagram for the zirconia yttria system is shown. At 0 mol% of Y_2O_3 the transformations described above occur. The addition of yttria exceeding 7 mol%, for example, completely stabilizes the cubic phase at room temperature. Lange et al. [5] showed a combination of monoclinic and cubic phase from 2 to 7 mol% Y_2O_3, see also Figure 1.1. Above 7 mol% the cubic phase is present. Other authors have also studied the Y_2O_3-ZrO_2 system. According to the work of Duwez et al. [6], up to 5 mol% of yttria the phase present is monoclinic. From 5 to 7 mol% there is a combination of cubic and monoclinic phase. Between 7 and 70 mol% of yttria, the cubic phase is dominant and the lattice parameter of the cubic phase varies linearly following Vegard's law [7]. More information and results about this linearity dependence will be explained in further sections. And finally, above 70 mol% of yttria a certain amount of yttria solid solution can be found until a pure yttria structure is obtained.

Due to the addition of yttria, oxygen vacancies are introduced in the ZrO_2 lattice, resulting in an improved ionic conductivity at high temperatures. YSZ are also known due to other advantageous properties such as high thermal stability, corrosion resistance, low thermal conductivity and good optical properties [8, 9]. These make yttria-stabilized zirconia (YSZ) suitable as electrolyte in solid oxide fuel cells [10, 11], oxygen sensors [12], as well as in other applications [13–15].

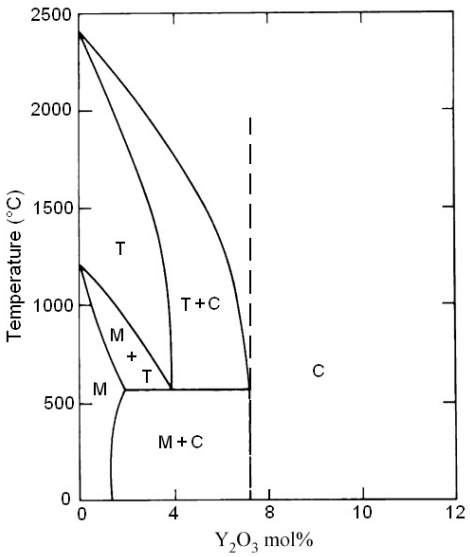

Figure 1.1: Phase diagram of the Zirconia-Yttria system, the tetragonal, cubic and monoclinic phase are indicated by the letters T, C and M, respectively [5].

The basic structure is described as face centered cubic (FCC) zirconia lattice. The cations (Zr^{4+}) occupy the tetrahedral sites while the anions (O^{2-}) fill the octahedral sites. This structure is illustrated in Figure 1.2.

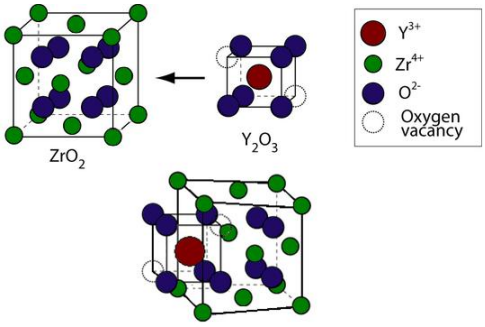

Figure 1.2: Schematic figure of yttria inserted in the zirconia lattice. (Image adapted from University of Cambridge [16].

Divalent or trivalent cations, such as: Ca^{2+}, Mg^{2+}, Sc^{3+}, Y^{3+}, etc. [17–23], can stabilize zirconia in the cubic phase at room temperature, the latter shown above. These dopant ions replace the Zr^{4+} ions, introducing oxygen vacancies in return, maintaining the charge neutrality of the system. The creation of oxygen vacancies can be expressed by the Kröger-Vink notation:

$$O_0^x \leftrightarrow V_0^{\bullet\bullet} + 2e^{'} + \frac{1}{2}O_2$$

where O_0^x is the oxygen with zero effective charge, $V_0^{\bullet\bullet}$ is charged oxygen vacancy, $e^{'}$ is the electron and O_2 is the oxygen molecule.

When doping with Y_2O_3, the Y^{3+} ions substitute the positions of Zr^{4+} while keeping the FCC lattice. The tetrahedral sites remain occupied by O^{2-} ions. Due to the difference in the ionic radius of both elements (0.90 Å for Y^{3+} and 0.72 Å for Zr^{4+}), there is a small deformation of the zirconia lattice when the Y^{3+} is inserted (see Figure 1.2).

1.2 Properties of YSZ

Due to its excellent characteristics, YSZ can be employed in several areas of interests. The characteristics are also mutually dependent, which make them suitable for different applications. Some key benefits for the use of YSZ are listed below.

- Dielectric properties: Lanagan et al. [24] studied the effect of microwave frequencies, temperature and yttria concentration on the dielectric properties of zirconia. The dielectric constant exponentially increases with temperature and frequency, as indicated in Figure 1.3a. At room temperature and an yttria content of 14 mol%, the dielectric constant is independent of the frequency, having a value of 27. However, as soon as the temperature increases, the frequency starts to play a role in the dielectric value, going from 27 to 30 at 100 kHz and from 27 to 55 at 100 Hz. In Figure 1.3b, it is shown that YSZ has a low-loss dielectric behavior, presenting an exponential behavior going from approximately 0 at low temperature to 0.1 (100 kHz) and to 1.3 (100 Hz) with a temperature range from 25 °C to 200 °C. The content of yttria varying from 0 to 9 mol% also increases the dielectric constant from 18 to 27 as well as the dielectric loss from 0.0007 to 0.0047. In the work of Samara [2] similar results were reported. A sample of 9.5 mol% Y_2O_3 presents the same exponential behavior for the dielectric constant and dielectric loss at higher temperatures and frequencies.

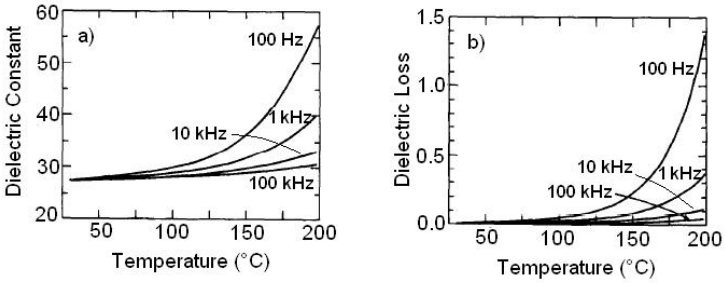

Figure 1.3: a) Dielectric constant and b) Dielectric loss as a function of temperature and frequency at 14 mol% Y_2O_3 [24].

- Ionic properties: YSZ is well known for its high ionic conductivity at high temperatures [25]. The Arrenhius plot for the total conductivity of a 8YSZ bulk [26] (grain and grain boundary contribution) is represented in Figure 1.4. Note that the conductivity increases from 1x10^{-5} S/cm at 500 °C up to 4x10^{-3} S/cm at 900 °C, illustrating the increase of conductivity at higher temperatures. Some authors [27–29] have studied nano YSZ films with thickness varying from 20 to 100 nm obtaining conductivities in the order of 1x10^{-5} S/cm at 400 °C, meaning that thinner films allows a reduction of temperature for this value of conductivity.

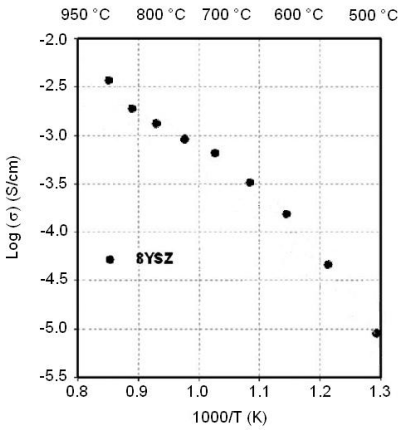

Figure 1.4: Arrhenius plot for the conductivity of a 8YSZ. Figure adapted from [26].

- Mechanical properties: Excellent mechanical properties, such as high hardness and bending strength make yttria-stabilized tetragonal zirconia polycrystal (Y-TZP) a good replacement material for biochemical components [30–32]. The cracks due to fatigue are a main drawback since Y-TZP is susceptible to fracture due to its brittleness. But, Y-TZP is stronger than alumina, as indicated in the work of Zhang et al. [33] who examined the fatigue response in repetitive stress behavior. Piconi and Maccauro [34] compared the mechanical properties of several materials, currently used for biomedical applications, including Y-TZP. These values can be found in Table 1.1. The Young's modulus of Y-TZP indicates that this material, as well as the metals and alloy can be easier handled than alumina. In addition the high bending stress suggests the use of this material under higher bending loads. However, lower hardness makes it less susceptible to impact than Al_2O_3.

Properties	**Ti6Al4V**	**316 SS**	**CoCr Alloy**	**Y-TZP**	**Al_2O_3**
Youngs modulus [GPa]	110	200	230	210	380
Bending strength [MPa]	800	650	700	900-1200	>500
Hardness [HV]	100	190	300	1200	2200

Table 1.1: Mechanical properties of some materials [34]

- Optical properties: YSZ has also good optical properties such as high refractive index, large optical band gap and transparency in a wide wavelength range. The first has been shown to decrease with the increase of Y content. However, the values of the refractive index remain high in the range of 2.11 to 2.23 (550 nm) [35, 36]. The large band gap of YSZ between 5.2 - 6 eV [36–39] allows YSZ to support stronger electrical fields and higher temperatures [40]. Finally, YSZ is transparent from the near infrared (800 - 1400 nm) to the ultraviolet (10 - 400 nm) due to its high spectral transmission [41].

- Structural and chemical properties: YSZ presents a great chemical stability in both, reducing atmospheres and oxidizing atmospheres. It is also structural stable, which means that it does not experience any disruptive phase transformation when submitted to a change of environment or temperature [42]. The texture and the crystallinity of the layers are also desirable to reduce the in- and out-of-plane misalignment between layers [43, 44].

- Thermal properties: Thermal expansion is an important factor when layers are combined in stacks [45]. Figure 1.5 shows the comparison in thermal conductivity between YSZ, nano-YSZ and 5La-YSZ as a function of temperature from the work of [46].

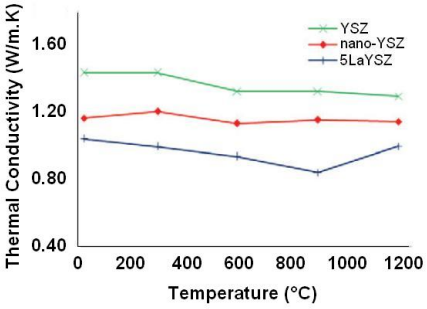

Figure 1.5: Variation in thermal conductivity as a function of temperature [46].

A large difference in thermal expansion between adjacent layers can cause cracking and/or delamination, especially when submitted to thermal cycles. The coefficient of thermal expansion of YSZ remains unchanged despite of the working temperatures and pressures. Another important thermal property is the ability to conduct heat, quantified by the thermal conductivity. In the work of Rauf et al. [46], the thermal conductivity of the lanthana-doped yttria-stabilized zirconia

reduces the thermal conductivity from 1.037 W/m.K at room temperature down to 0.839 W/m.K at 900 °C. Bulk YSZ also presents a small decrease of the thermal conductivity from 1.42 W/m.K at room temperature down to 1.35 W/m.K at 1200 °C. Reductions of the thermal conductivity are associated with the creation of additional oxygen vacancies. On the other hand, nano-YSZ shows a constant thermal conductivity of 1.18 W/m.K.

1.3 Applications of YSZ

It was already mentioned that YSZ presents excellent properties that makes it an interesting material for several applications. YSZ in different forms and shapes have been studied and manufactured. YSZ can be found as bulk [47], thick films [8,48,49], thin films [10,50–52] or nanolayers [12,14,15] and nanoparticles [53,54]. The main applications using YSZ will be briefly introduced in the next sections. This includes the use of YSZ as buffer layers, thermal barriers coatings, oxygen sensors and solid oxide fuel cells.

1.3.1 Buffer layers

Thin films of $YBa_2Cu_3O_{7-\delta}$ (YBCO) are used as superconductors due to their capacity of carrying very high current densities. These films can be produced on substrates made of $SrTiO_3$, $LaAlO_3$ or $LaGaO_3$ [55]. However, these substrates are not only expensive but also present large electrical losses. Despite of its mechanical fragility, MgO substrates have been an economic solution. Other solutions have also been investigated, e.g. using buffer layers between the YBCO layer and the substrate. These buffer layers align the individual grains of YBCO, replicating the crystallographic texture of the alloy substrate. It also avoids contaminations from the substrate metals [56]. A mismatch in texture can severely decrease the current density of the superconductor. Sapphire and YSZ are possible candidates as buffer layers. The disadvantage of sapphire is the mismatch in thermal expansion, causing microcracks in the final structure. YSZ, on the other hand, has become popular due to its good mechanical strength, low dielectric loss and its chemical stability.

1.3.2 Thermal barrier coatings (TBCs)

A TBC consist of several layers which increases the engine efficiency performance in gas turbines due to the reduction of temperature from the hot gases to the turbine blade. This drop in temperature delays failure by oxidation increasing the life time of the components. A schematic drawing of such a TBC can be seen in Figure 1.6.

The insulating thermal barrier coating consists of a substrate, an oxidation resistant bond coat, an YSZ layer with a columnar structure and a thermally

grown oxide (TGO). The YSZ layer thickness is approximately 150 μm and the temperature drop across this thickness of the coating is 170 °C [57], see Figure 1.6. The main characteristics of these YSZ layers are the low thermal conductivity necessary to maximize the thermal drop, high coefficient of thermal expansion, chemical inertness and thermal shock tolerance. Porous YSZ layers are preferred because a decrease of the thermal conductivity occurs as the pore fraction increases. The 75 to 150 μm thickness oxidation resistant bond coat [15], made of platinized β-NiAl or NiCrAlY [58], is required to protect the blade from environmental degradation. It must remain stress free, adherent and stable during long term exposure. At elevated temperatures, oxidation of the bond coat results in the formation of thermally grown oxide [59]. If this oxide layer is composed of Al_2O_3, it will grow slow, uniform and defect free. Moreover, such layer becomes a diffusion barrier retarding further bond-coat oxidation. However, the formation of other oxides can cause separation of the ceramic layer from the substrate or it can accelerate crack nucleation during thermal exposure, leading to TBC failure. A possible solution is a heat treatment which suppresses the formation of detrimental oxides [60].

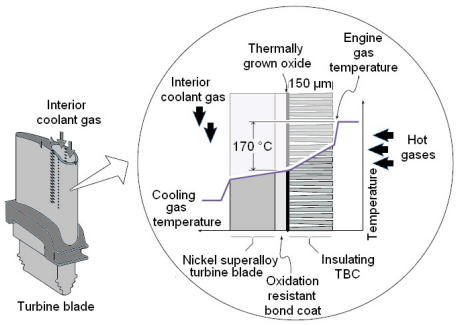

Figure 1.6: Schematic drawing of a thermal barrier coating [57].

Other possible failure reasons of the TBCs are stresses due to the thermal expansion mismatch and the continuous changing in composition, microstructure, interfacial morphologies, and properties of the TBC system. One possible approach to improve the performance and to guarantee components durability is to optimize the morphology of the YSZ layer, for example using nanostructured YSZ [14, 61]. The microstructure can be manipulated in order to grow a columnar structure. The columnar structure not only allows the increase of pore volume fraction reducing thermal conductivity but also accommodates possible strains in the system [62].

1.3.3 Oxygen sensors

Oxygen sensors are devices that convert the difference between two different partial pressures into an electrical signal. Some sensors operate by detecting the difference between partial pressures of a reference air and the unknown partial pressure of a gas. One of the most popular systems at high temperatures is the potentiometric sensor, based on ceramic ion conducting electrolytes. Figure 1.7 shows a schematic drawing of such a sensor. It consists of a diffusive layer, a YSZ electrolyte and electrodes. The diffusive layer prevents the electrode from degradation. It also enhances sensor response by improving diffusion between measured gas and electrode. The electrodes, usually made of Pt or Ir, have high electrical conductivity and should induce the dissociation of oxygen molecules [63]. Finally, the cubic YSZ electrolyte is commonly employed due to its high ionic conductivity and mechanical strength.

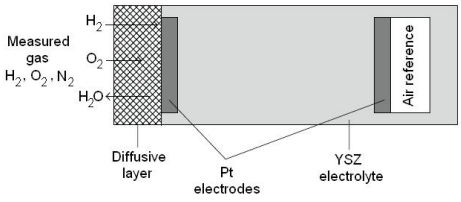

Figure 1.7: Schematic drawing of a potentiometric planar oxygen sensor [12].

The oxygen molecules are in equilibrium with the oxygen ions in the electrolyte. This equilibrium is represented by the reaction below [12]:

$$O_2 + 4e^- \leftrightarrows 2O^{2-}$$

When the oxygen concentration is different between both atmospheres, the electrochemical cell of the sensor goes to a non-equilibrium state. As a consequence, a non zero voltage is detected in the electrode-electrolyte interface due to a non uniform charge distribution along the sensor. In order to reach equilibrium the distribution of oxygen ions across the electrolyte is altered. The non zero voltage is used to quantify the concentration of the species involved. At thermodynamic equilibrium, the voltage between the reference electrode and measured electrode can be expressed by the Nernst equation given by:

$$E = E_0 + \frac{RT}{4F} \ln\left(\frac{p_{ref}}{p_{meas}}\right) \tag{1.1}$$

where E is the measured electrode potential (voltage) and E_0 is the standard

electrode potential, p_{ref} and p_{meas} are the partial pressures of the reference and the measured gas, respectively. F is the Faraday constant, R is the ideal gas constant and T the temperature. The number of transferred electrons (see reaction above) explains the use of 4 in equation 1.1.

The applicability of oxygen sensors is extended in several industrial processes where the oxygen partial pressure might affect some properties or processing steps, for example in automotive applications and in medical and food processing [64–66]. Failures and drawbacks of the use of oxygen sensors are associated to the destabilization of the cubic structures with formation of monoclinic phases [64], to the current limitation in the electrode/electrolyte contacts and to the high temperature operation to reach a high ionic conduction of the electrolyte [12]. Possible solutions can be obtained with the use of nanomaterials. This solution can improve gas selectivity, lower the electrode impedance, avoid current limitation in the electrode/electrolyte interfaces and lower the activation energies for ion conduction.

1.3.4 Solid oxide fuel cells

A fuel cell is an electrochemical device which can provide efficient and clean electrical energy from a chemical reaction [67–70]. An individual fuel cell consists of an electrolyte layer in contact with a porous anode and cathode. A typical example is the solid oxide fuel cell (SOFC) of which a basic schematic drawing is presented in Figure 1.8.

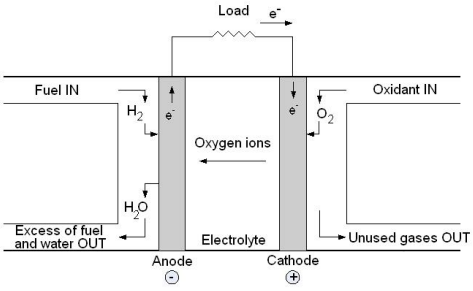

Figure 1.8: Schematic drawing of an individual fuel cell (SOFC).

In the SOFC, there is a continuous external supply of fuel (e.g. H_2) on the anode side and an oxidant on the cathode side. The electrochemical reactions take place at the electrodes and the result of the chemical reaction is the production of electrical current. The process is a cycle and occurs as follow: On the cathode side, there is the flow of oxidants (usually oxygen). The cathode reaction

generates oxygen ions. These oxygen ions are transported to the anode through the electrolyte. On the anode, the fuel passes through the surface of the anode. The anode reaction takes place and electrons are generated. The electrons move to an external electrical circuit connected to the cathode, where they will participate again in the cathode reaction. In summary, electrical energy is generated by the electrochemical oxidation of fuel, e.g. hydrogen, and the electrochemical reduction of the oxidant, oxygen. The reactions below summarize this process:

Anode Reaction: $2H_2+2O^{2-} \leftrightarrows 2H_2O+4e^-$

Cathode Reaction: $O_2+4e^- \leftrightarrows 2O^{2-}$

Overall Cell Reaction: $2H_2+O_2 \leftrightarrows 2H_2O$

Gaseous hydrogen has become the fuel of choice for most applications due to its reactivity, its ability to be produced from hydrocarbons and its high density when stored. The electrolyte can be based on YSZ [9, 10, 51, 71–75], CeO_2 [51, 76–79], Sc_2O_3 [80–82], Bi_2O_3 [83], or or pyrochlore oxides $(A^{3+})_2(B^{4+})_2O_7$ such as, $Ln_2Zr_2O_7$, $Gd_2(Zr_xTi_{1-x})_2O_7$, $Y_2(Zr_xTi_{1-x})_2O_7$ [84], being YSZ the most popular electrolyte. It is important that the electrolyte presents high chemical and thermal stability, low electrical conductivity, preventing losses from leakage current, and high ionic conductivity over a wide operating range [10].

Although SOFCs have a high efficiency, their utility is limited by the ionic conductivity of the electrolyte, which depends on the temperature. The nominal operating temperature is between 700 to 1000 °C [85]. Lowering the operational temperature is one of the main goals in current research due to their restricted application at high temperature. One possible solution is to reduce the thickness of the electrolyte layers and thus, minimize ohmic losses, decrease SOFC cost and improve its performance.

1.4 Summary

Yttria-stabilized zirconia is a suitable material for several areas of interest. The superior chemical, mechanical, electrical and structural properties of YSZ allow them to be used in different applications. The ability of controlling the structural phase, by doping the zirconia lattice, permits the manipulation of these properties. However, the high temperature required for high values of ionic conductivity remains a problem in some of the applications cited above, because the high temperature can provoke mechanical failure or even a destabilization of the structural phase by forming other phases. A possible solution is to control the microstructure by changing the thickness of the YSZ to thin films.

Downscaling the thickness of YSZ to a thin film, however, changes the

fundamental aspects of the oxygen ion conduction due to the occurrence of small-scale or nano effects. Moreover, this reduction changes the characteristics and structure of the electrolyte. At present, it is not clear how the microstructure of solid state electrolytes affects the behavior of the film and its properties. Therefore, the fundamental aspects of YSZ growth would open the possibility to manipulate the YSZ properties by controlling thin film microstructure and texture.

2

Overview of thin film deposition techniques

In the previous chapter several applications of YSZ were discussed. The YSZ films can be produced using different growth techniques. A technique is chosen as a function of the final characteristics of the desired film. In this study, YSZ thin films were deposited by dual reactive unbalanced magnetron sputtering, a so-called physical vapor deposition technique.

In this chapter we will briefly discuss some techniques to obtain YSZ thin films. Next, reactive unbalanced magnetron sputtering is described. Finally, the main characteristics and the processes involved in sputtering are discussed.

2.1 Thin film deposition

Figure 2.1 illustrates some techniques described in literature to produce YSZ thin films.

The deposition of thin films can be performed by two major routes: a chemical and a physical deposition process. In this section we present some techniques for depositing YSZ thin films found in literature. The chemical methods consist of gas phase deposition methods and solution techniques. The gas phase methods include plasma-enhanced chemical vapor deposition (CVD) and atomic layer deposition (ALD), while the solution techniques include spray pyrolysis, sol-gel methods and and ink-jet printing. Physical methods include physical vapor deposition (PVD),

such as, electron beam deposition, pulsed laser deposition and sputtering.

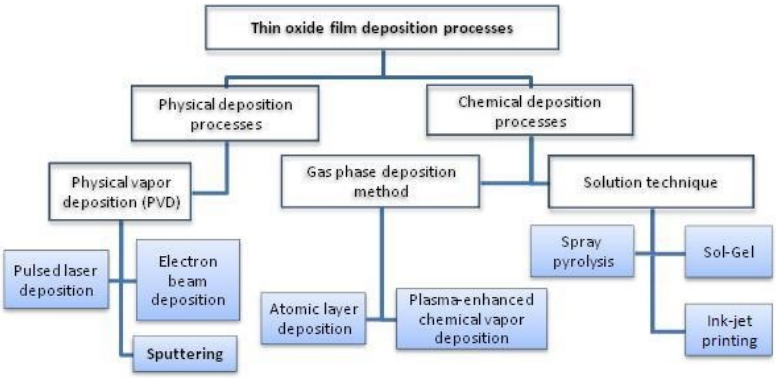

Figure 2.1: Diagram of some techniques described in literature to produce YSZ thin films [86].

2.1.1 YSZ films deposited by chemical deposition processes

Chemical vapor deposition (CVD), results in a uniform and selective distribution over large areas, avoiding eventual compositional gradients along the substrate. An advantage of the CVD process is that there is no need of breaking vacuum when changing source material. On the other hand, the evaporation of toxic, inflammable or corrosive materials is the main drawback of such technique [87]. Moreover, the number of variables involved on the CVD process makes it a difficult technique to get the right growing parameters on YSZ films. An example of a CVD technique for the deposition of YSZ thin films can be found in the work of Holzschuh and Suhr [50]. In their work, YSZ films were deposited on different substrates using plasma-enhanced CVD. Films with a (100) textured were obtained at relative low deposition temperatures (773 K) for a wide range of composition. Other authors used atomic layer deposition (ALD) to fabricate nanostructured thin films to be used as electrolyte for solid oxide fuel cells [88–91]. The reduction of the thickness enhanced the ionic conductivity performance in comparison with a bulk YSZ.

In the solution techniques group we can describe the deposition of YSZ using ultrasonic spray pyrolysis, sol-gel and ink-jet printing. Ramírez et al. [92] showed that the use of ultrasonic spray pyrolysis is suitable for depositions of YSZ. However, the main drawback in this spray technique is the presence of contaminants from the precursor, e.g. carbon, which limits the conductivity depending on the film composition. Another approach given in [27, 93] suggests the use of sol-gel for the formation of an YSZ layer. In the work of Zhang et al. [27]

dense crack-free YSZ nano layers were deposited. The electrical conductivity enhancement allows the use as an electrolyte. While in the work of Zalga et al. [93] different sol gel routes were experienced in order to change the hydrophobic properties of YSZ. Ink-jet printing was used in the work of Van Driessche [94] to deposit YSZ films to be used as electrolyte for solid oxide fuell cells as well as thermal barrier coatings, showing the flexibility of this method to deposit porous and dense films.

2.1.2 YSZ films deposited by physical deposition processes

The physical vapor deposition (PVD) consists of three steps:

- Vaporization of the material from a solid;
- Transportation of the vapor in vacuum or partial vacuum to a substrate surface;
- And condensation onto the substrate to generate thin films.

In general, the advantages of PVD process lay over the higher deposition rate, simplicity of the deposition, easy control of the deposition parameters (porosity, stoichiometry, and growth rate), use of a variety of materials as source, deposition in large scale and being more environmental friendly when compared to some CVD techniques. Some drawbacks of PVD can be attributed to the high vacuum needed and to the difficulty in coating sharp or undercut surfaces.

Many authors have studied the YSZ thin films morphology, texture and electrical properties using films produced by different PVD processes. The most common PVD techniques present in the literature for YSZ thin films are electron and ion beam deposition, pulsed laser deposition and sputtering. The latter will be discussed in more detail in the following section.

- Electron and ion beam deposition: during the electron beam deposition a source material is heated by an electron beam. Figure 2.2a shows a schematic drawing of the electron beam deposition. Some authors studied YSZ thin films to be applied as an electrolyte for SOFC by controlling the growth rate as a function of the e-beam gun power [95, 96] and the concentration of mobile charge carriers through the substrate temperature [97, 98]. In the first case, the growth rate is dependent on the e-beam gun power and the best film adherence was obtained at higher e-beam powers. Increasing the deposition temperature directly affects the final texture of the YSZ films, varying from amorphous to a well defined cubic structure. At higher e-beam gun powers, YSZ starts to evaporate in different types of clusters affecting the surface of the deposited film.

Due to the low energy involved when using electron-beam deposition, the thin film material contains micro pores which can become a serious problem to reach high refractive index materials. A way to overcome this is to add an ion source where highly energetic ions are produced and directed to the substrate surface [99]. This technique significantly improves adhesion, control of internal stress [100], morphology [56, 77, 101–103], density and composition. The addition of an ion source can be adapted to the evaporation deposition by an electron beam [100, 102] but it can also be incorporated to sputtering [104–106].

A way to increase film roughness and to sculpture the columnar film growth by geometric shadowing is changing the substrate angle (θ) with respect to the material flux. This method is known as glancing angle deposition (GLAD), represented in Figure 2.2b. Nanostructured films studied in [107–109] are an example of the use of the GLAD in combination with electron beam evaporation. The degree of control in nanostructured films allows easy modification of the shape, alignment, and orientation of the films.

The combination of ion implantation with a physical deposition technique [110–114] is often used to study the biaxial alignment of YSZ and the competition between the (100) and (110). The schematic drawing of an ion beam assisted deposition (IBAD) is presented in Figure 2.2c. The interaction between ions and the deposited atoms improves the final texture of the deposited film [115]. Therefore, it is frequently used to prepare highly textured thin films on amorphous substrates. Other benefits are: adhesion, morphology and control of internal stress [99].

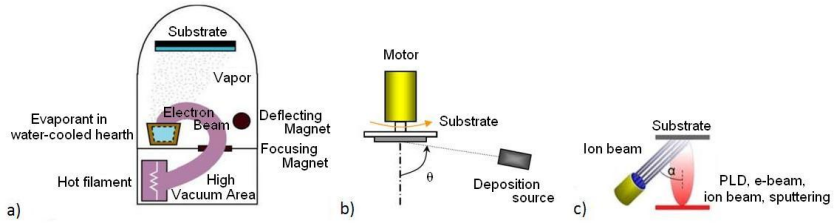

Figure 2.2: Schematic drawing of a) electron beam deposition [86]; b) glancing angle deposition [109]; c) ion beam assisted deposition [116].

- Pulsed laser deposition (PLD): this technique uses high power laser pulses to remove material from the surface of a source material to a substrate. As the laser beam is an external source, the deposition is carried out in a clean vacuum environment and the deposition can consequently occur either in inert, reactive background gases or even without the presence

of a background gas. Figure 2.3 illustrates the schematic drawing of the PLD. One of the most significant benefits is the stoichiometry transfer, including the one of complex materials, i.e. the ability to transfer the same composition from the source material to the film layer. That is why the use of PLD for the deposition of superconductors on a buffer layer or on a metallic substrate is suggested in [43, 117–119]. Some authors [120–122] have also studied the ionic conductivity of YSZ deposited via this technique. PLD has also some disadvantages making this technique less suitable at industrial level, namely, ejection of macroparticles from the target, the non-uniform thickness, small area of deposition, conceptual complexity and the plasma processes involved which are not yet fully understood [123].

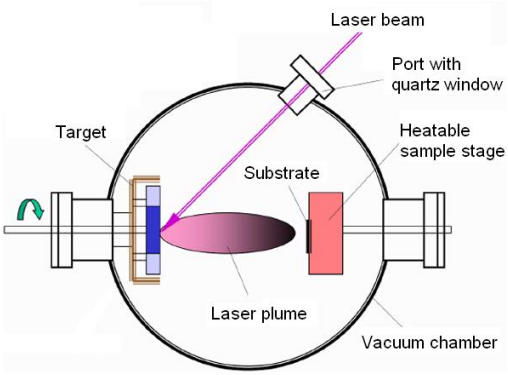

Figure 2.3: Schematic drawing of a PLD setup [124].

2.1.3 Sputtering

Sputtering is the ejection of atoms by bombarding the source material (also referred as target) with heavy energetic particles, mostly ions. Like the techniques described above, sputtering has also been used for deposition of thin films [11, 75, 85, 125–139], in the scientific community as well as in industrial applications [140–149].

The variants of the sputter deposition are: direct current (DC), radio-frequency (RF), magnetron, reactive deposition and high-power impulse magnetron sputtering (HiPIMS). Naturally, a combination of the variants can also coexist as well as the utilization of different tools to change the deposition conditions of the sputtering. Although the sputtering process involved in the different sputtering techniques is basically the same, the geometrical and operational differences are responsible to make them suitable for different types of depositions.

- DC sputtering: DC glow discharge or diode sputtering consists of two

parallel electrodes in a vacuum chamber with an external high-voltage power supply [150]. The schematic drawing is illustrated in Figure 2.4a. When power is supplied, an electrical field is formed between the electrodes. A free electron is accelerated towards the anode. This electron has sufficient energy to ionize the gas atom, which is responsible for the removal of the target material. This kind of sputtering is suitable for deposition of metals but it only works under appropriate gas conditions. If the pressure in the chamber is too low, the electron will only strike the anode without ionizing any gas atoms. On the other hand, if the pressure is too high, the electron does not have sufficient energy to ionize a gas atom [151]. Another disadvantage of the diode sputtering is that it cannot be used to deposit dielectrics because an insulating cathode will cause charge build up during bombardment. Moreover, the positive charge on the target surface rejects the ion flux and stops the sputtering process.

- RF sputtering: A possible solution for the latter is the use of a high frequency potential, a so called RF sputtering, as illustrated in Figure 2.4b. The advantage of the alternated cycles is that the positive charge, accumulated on the target during the negative portion of each cycle, is neutralized by electrons during the positive part of the cycle [152].

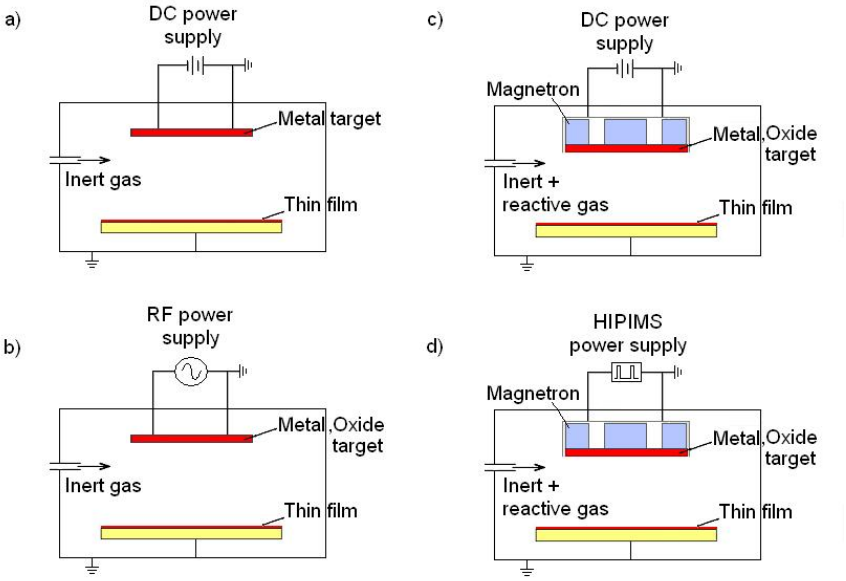

Figure 2.4: Examples of sputtering: a) DC; b) RF; c) reactive magnetron; d) HIPIMS.

- DC magnetron sputtering (DCMS): Magnets are used to increase the percentage of electrons that take part on ionization events. In this way, the probability of electrons colliding with the gas atoms increases, resulting in improved ionization efficiency. This technique combined with reactive sputtering allows the deposition of oxides from a metallic target in a reactive atmosphere, i.e. the oxidation reaction occurs on a surface, e.g. on the substrate. The drawing of this technique is seen in Figure 2.4c.

- High-power impulse magnetron sputtering (HiPIMS): The use of HiPIMS, Figure 2.4d, can provide substantial ionization of the sputtered material. In a HiPIMS process, the current of the magnetron is pulsed, which allows very high instantaneous powers in a very short period of time [153, 154]. The major disadvantage of this technique is the lower deposition rate for the same power when compared to magnetron sputtering [155]. However, similar deposition rates have been achieved in reactive processes [153, 154].

  The four sputtering techniques listed above have been used to deposit YSZ films for different applications. Optical properties, for example, were evaluated in [11, 128] for YSZ films with different concentrations of yttria using RF sputtering. The same technique was used in [127] to produce YSZ thin films to be used as buffer layer for superconductors. For the use as electrolyte for SOFC the most popular technique is reactive DC magnetron sputtering [125, 130, 135, 156, 157], which allows the deposition of oxides with a high deposition rate. As this technique was chosen to deposit YSZ thin films in this work, it is discussed in detail below.

2.2 Fundamental processes of sputtering

Before more details about reactive DC magnetron sputtering are given, it is necessary to get familiar with some processes that occur at the target and during the transport from the material source to the substrate.

Collision Cascade: collision cascades are the series of collisions that occur when Ar^+ ions penetrate the target. There are three regimes of collision cascades, as indicated in Figure 2.5: the single knock-on, the linear cascade and the spike regime [158]. In the first regime, Figure 2.5a, the bombarding particle collides with an atom of the target, transferring energy and momentum. These atoms receive sufficient energy to be sputtered from the target, but not enough to generate further recoil cascades. In the linear cascade, Figure 2.5b, the recoiled target atoms have enough energy to eject atoms from the target and to generate a low density of recoil atoms. The cascade is generated but dominated by knock-on events, meaning that each generation of recoil atoms has on average less energy than the previous one. When the density of recoil atoms is high, the collisions go to the spike regime,

Figure 2.5c, where the majority of atoms are in motion [159].

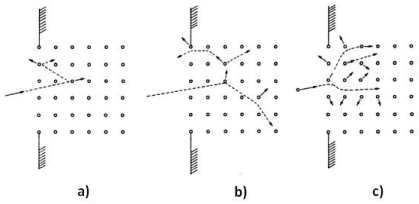

Figure 2.5: Collision cascades: a) Single knock-on regime; b) the linear cascade; c) the spike regime [159].

Secondary Electron Emission: not only atoms but also electrons are emitted from the target by the ion bombardment. Those electrons are known as secondary electrons. The number of emitted electrons per incoming ion is known as the secondary electron emission yield and depends on the condition of the target material and on the energy and the type of bombarding particle. The secondary electrons are necessary to ionize the Ar atoms in order to self-sustain the plasma.

Sputter Yield: the basic parameter for a quantitative description of the sputtering efficiency is the sputter yield (γ) and it is defined as the ratio of the number of sputtered atoms to the number of incident ions. In the work of Sigmund [158], an analytical relation was derived using a linear cascade model based on binary collisions. He simplified the expression for the sputter yield of a particle with energy E and angle $\theta = 0^\circ$ for low energetic ion bombardment (E $<$ 1 keV) to:

$$\gamma(E) = \frac{3}{4\pi^2}\alpha\left(\frac{m_p m_r}{m_p + m_r}\right)\frac{E}{U_S} \tag{2.1}$$

where, α is the dimensionless correction factor depending on m_r/m_p, E is the energy of incident ions, U_S is the binding energy of atoms and the ratio $(m_p m_r)/(m_p+m_r)$ is the energy transfer mass factor where the m_p and m_r are the mass of incoming particle and of the target atoms, respectively [158]. From this equation it is clear that the sputter yield depends linearly on the ion energy E.

The sputter yield can also be simulated or experimentally obtained. Depla et al. [160] found a good match between the simulated sputter yield and the experimental data. Experimental results indicate that the number of atoms ejected from the yttrium or zirconium target have a linear dependency on the discharge voltage. The sputter yield obtained experimentally at research group DRAFT[1] for yttrium and zirconium follows the linear equation defined as:

[1]Research Group DRAFT: Design, research and feasibility of thin films, Ghent University.

Y: $\gamma_Y = 8\times10^{-4}V_Y + 2.6\times10^{-1}$

Zr: $\gamma_{Zr} = 1.5\times10^{-3}V_{Zr} + 1\times10^{-1}$

where V is the voltage of Y and Zr. The experimental results of both Y and Zr sputter yields are displayed in Figure 2.6.

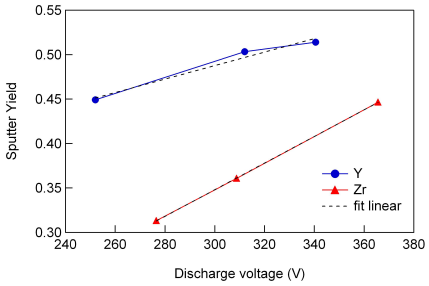

Figure 2.6: Experimental sputter yield for yttrium and zirconium obtained experimentally at DRAFT[1].

Ion Implantation: when the ionized Ar collides with the target, there is a probability that this ion will be trapped into the target. The fraction of implanted ions increases with increasing energy. Moreover, the presence of implanted ions [161, 162] can also influence the sputter yield by changing the surface binding energy per atom. As the sputter process proceeds, the implanted ions may also be resputtered.

Energy and Angular Distribution of the Sputtered Atoms: in the energy distribution described by Thompson [163, 164], it was assumed that there is an isotropic distribution of velocities in the solid. Besides, the particles have to overcome the surface binding energy of the metal to leave the target. The energy distribution of nascent sputter flux is related to the energy and the angular distribution for low energetic bombardments as:

$$N(E,\gamma) = \frac{E}{(E+U_S)^{3-2m}}\cos\theta \tag{2.2}$$

where E is the energy of the sputtered particles, U_S is the binding energy of the atoms, m is a parameter dependent on the energy E (being 0 for low energetic bombardments) and θ corresponds to the angular distribution in a cosine behavior. This equation suggests that the particles are sputtered in a wide range of energies, being most of them sputtered in the order of a few eV. In addition, the function has a maximum for E = U_S/2 and a large tail at higher energies as can be seen in the example of Figure 2.7.

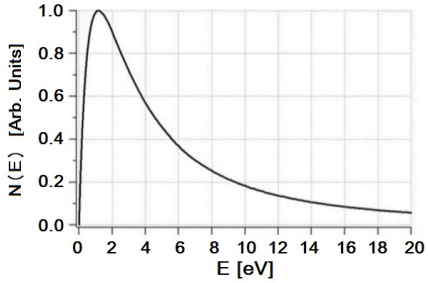

Figure 2.7: Example of the energy distribution of sputtered In by Ar^+ bombardment with an incident energy of 400 eV [165].

The angular distribution defines the spatial distribution of a sputter particle and provides information on the collision cascades in the target. This distribution is dependent on the incident energy [166, 167]. When the incident energy is low, a collision cascade is formed but not yet developed leading to an anisotropic angular distribution. The atoms are then ejected in an under-cosine or heart-shaped type, see Figure 2.8. For high incident energy the distribution takes the over-cosine form. In this case, the probability that recoil atoms are transported perpendicular to the target surface is high.

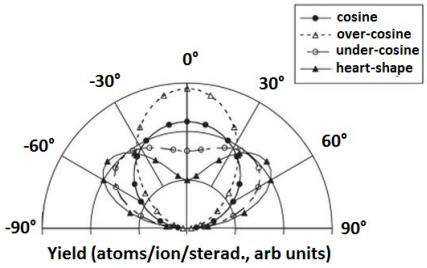

Figure 2.8: Possible angular distributions of a sputtered particle [168].

The ion-atom interaction can easily be simulated, using computational programs, such as: SRIM/TRIM [169] which are based on a Monte Carlo code. Monte Carlo simulations have been extensively used to simulate collision cascades [74, 169–173].

Glow Discharge: schematic drawing of the sputtering process is shown in Figure 2.9. A glow discharge is a partially ionized gas consisting of energetic particles. It is created by applying a potential difference between two electrodes. When a negative voltage is applied, the free electrons are repelled and collide

with the Ar atoms, creating argon ions and new electrons ($Ar + e^- \rightarrow Ar^+ + 2e^-$). The positive ions are accelerated (attracted) towards the target with high speed. The collision of the positive ions with the source material results in removal of particles from the target, which are transported to a substrate and the chamber walls [174]. Secondary electrons are also emitted and accelerated away from the cathode (target), being responsible for the ionization of the gas. Besides ionization, excitation of the argon atoms ($Ar + e^- \rightarrow Ar^* + e^-$) is also possible. The resultant excited atom releases its energy by emitting photons, which is the origin of the glowing of the plasma.

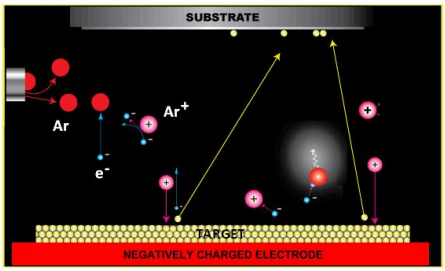

Figure 2.9: Schematic drawing of the sputtering reaction [175].

A potential distribution is created between the cathode and an electrical or insulated object (substrate), as illustrated in Figure 2.10. The plasma in this region is equipotential and its potential vs. ground equals to V_p. The positive potential occurs due to higher velocity of the electrons in relation to the ions. When the plasma is created, both ions and electrons will difuse outwards. Thus, the electrons move faster away from the surface, resulting in a positive net charge, which consequently creates an attractive force on the electrons. Near the edges, a space charge layer (sheath) with a negative potential is generated. When a floating object is inserted into the plasma, the initial flux of electrons to this object will be much higher than the flux of positive ions due to the difference in mass. In this way, the object will be negatively biased. The potential of the object is in equilibrium when it is high enough to repel sufficient electrons to equal the ion and electron flux. This equilibrium potential is the floating potential V_f. As the cathode is already in a high negative potential, a larger potential difference V_d is created.

Finally, the particles are ejected from the cathode towards the substrate (as well as to the other surfaces in the chamber). During the transport other collisions can occur, changing the direction and the energy of the sputtered particles, until the emitted particles are either scattered or adsorbed on a surface.

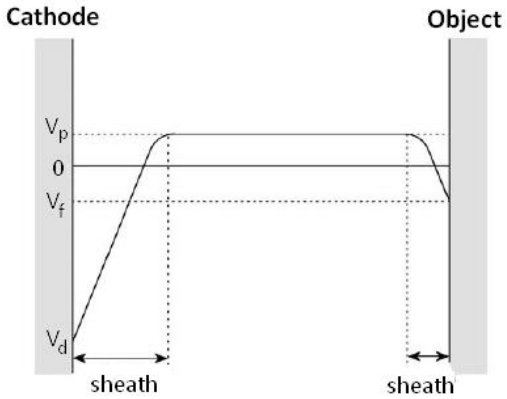

Figure 2.10: Potential distribution in a glow discharge between a cathode and a floating object.

2.2.1 Magnetron sputtering

The fundamental processes involved in sputtering were given above. The principles of magnetron sputtering are illustrated in Figure 2.11. Basically, a magnetic field ($\vec{B}$) is produced by permanent magnets behind the target. Those magnets are arranged with one pole in the center of the target and the other pole formed by a ring around the outer edge of the target. The generated magnetic field is applied parallel to the target surface. When the negative voltage is applied between target and chamber walls, the secondary electrons produced by ion bombardment are repelled away from the target. Due to the magnetic field, these electrons are trapped into semicircular orbits due to Lorentz force. Hence, more Ar^+ ions are produced, the plasma density increases and there is an increase of ion bombardment on the target, resulting in higher sputter rate [176]. Because of the high ion current densities, efficient cooling is necessary.

In a planar magnetron, which is the type of magnetron used in this work, $\vec{B}$ varies in both magnitude and direction over the target surface. There is a central magnetic pole (north) and an annular pole (south) which cause the magnetic field lines between the poles to be circular symmetric, as indicated in Figure 2.11. The horizontal component provides the magnetic trapping and the vertical component prevents the escape of the electrons from the magnetic tunnel. The closed-drift current is parallel to the target and forces the secondary electrons to follow a circular path [177]. The Lorentz force leads the electrons to the region between inner and outer magnets. This region corresponds to the maximum ionization and also to the largest ion current density. Consequently the material removal

concentrates in this region provoking a local erosion of the target, forming the so called race track. The race track can be considered a drawback of this technique, since the target utilization is limited to 30% [178] - 45% [179].

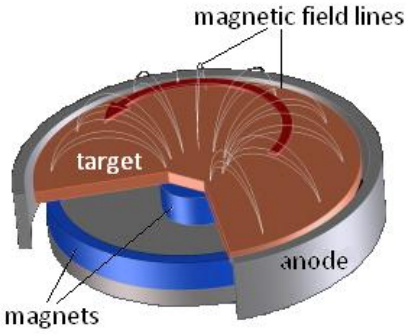

Figure 2.11: Planar magnetron and the magnetic field lines [180].

2.2.2 Balanced and unbalanced magnetrons

In the work of Window [181], a balanced and two different unbalanced configurations (type I and type II), were experimentally observed. These configurations are presented in Figure 2.12. In the balanced magnetron, Figure 2.12a, the magnetic flux lines form closed loops between the magnetic poles. The result of this configuration is a strong confined plasma near the target and a few charged particles reaching the substrate [182]. This configuration is used when low energetic bombardment is required. When high energetic bombardment is needed, i.e. when a modification of the thin film growth is desirable, the unbalanced configuration is preferred. The main difference between both types of unbalanced magnetrons is the position of the strongest magnet, either in the center (type I, Figure 2.12b) or in the outer magnet (type II, Figure 2.12c). The first one gives low ion and electron fluxes at substrates and low self-bias potentials. The latter acts in the opposite way: the field lines are not closed between the center and the outer magnets but instead the lines are directed to the substrate. Besides, some secondary electrons are not captured near the target and higher plasma, away from the cathode, is formed. As a result, this plasma interacts with the growing film on the surface of the substrate [176].

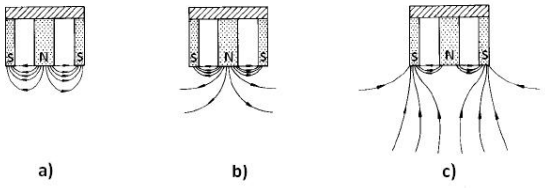

Figure 2.12: Types of magnetrons configurations: a) balanced; unbalanced: b) type I; c) type II [181].

2.2.3 Reactive magnetron sputtering

In reactive sputtering a reactive gas is added to the sputtering system, e.g. oxygen or nitrogen, while using a metallic target as source. As a result, there is a chemical reaction on the surface of the substrate to form a new compound. The reaction takes place on the substrate as well as on the target and chamber walls.

The addition of reactive gas changes the behavior of the sputtering process. Figure 2.13 shows a schematic drawing of a hysteresis loop for target voltage, partial pressure and deposition rate of Al with O_2 as reactive gas. Note that the loop changes as a function of the reactive gas in two different pathways: one for the increasing and another for the decreasing of the reactive gas flow. These different paths form the so called hysteresis loop. When O_2 flow is inserted in the chamber during sputtering, the O_2 reacts with the sputtered Al in all available surfaces of the chamber, e.g. substrate, chamber walls and target. At this point the voltage is constant, the partial pressure remains practically constant due to the oxygen use during the chemical reaction and the deposition rate is high. This region of low flow is denominated *metallic mode*. At a certain O_2 flow, the compound formation dominates at the target surface. Consequently the deposition rate decreases because the surface binding energy of the compound is higher than of the metal. This means that less metallic particles are sputtered to react with the reactive gas at the surface of the substrate. The decrease of the deposition rate results in more available O_2 in the chamber and hence the partial pressure increases. The voltage drop (or increase) is dependent on the material. The change in pressure and in the plasma composition can also influence the behavior of the discharge voltage as described in [183]. The complete oxide formation on the target is called poisoning and the region of high O_2 flow is defined as *poisoned mode*. When the O_2 flow is reduced, the compound is removed from the targe and a reverse effect is observed. However, the amount of O_2 necessary to allow removal of the oxide of the target is lower due to the lower oxide sputter rate. Consequently, the return occurs at lower flows of O_2 [138, 184]. The hysteresis is then defined by the difference between the sputter yield of the metal and of the

oxide. The larger the ratio between the sputter yield of the metal and the oxide, the more pronounced the hysteresis loop will be.

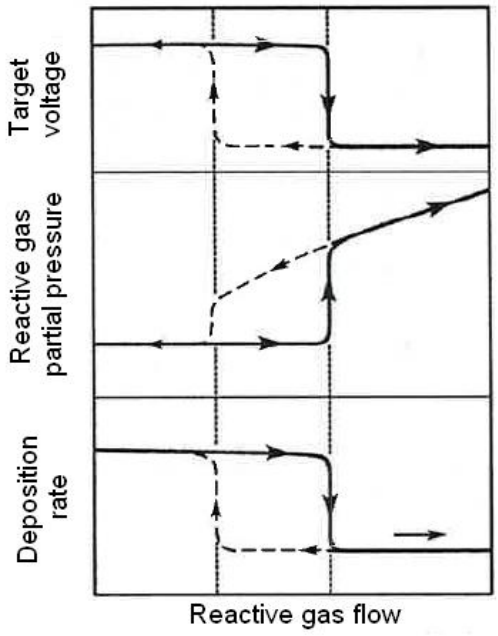

Figure 2.13: Typical reactive magnetron sputtering hysteresis effects for Al/O_2.

The hysteresis effect modeled by Berg et al. [185] takes into consideration the target modification by the reactive gas. In his model the incoming reactive gas is divided in three flows: the gas reacting at the target surface (q_t), at the substrate and chamber walls (q_c) and the gas that passes out through the vacuum pump (q_p). The pumping speed (S) can be determined by the relation between the fraction of gas which does not react (q_p) and the partial pressure in the chamber (p_R) as: $q_p = p_R S$. The variation in partial pressure can be observed in Figure 2.13. Berg's model indicates that the increase of the reactive gas leads to a complex transition region where the slope of the curve is negative. Based on Berg's model, several aspects of the reactive magnetron sputtering are well described. However, the reactive ion-target interactions, e.g. implantation, have not been considered. Depla et al. [186] discusses that the reactive gas not only chemisorbs at the target but that there is an abrupt change on the target conditions due to the ion implantation.

In general, the hysteresis effect is a drawback in the use of reactive magnetron

sputtering. However, the control of the gas flow, partial pressure or the target voltage at the edge between the metallic and poisoned mode allows the deposition of a compound with a high deposition rate.

2.3 Summary

As shown in this chapter, there are plenty of techniques to deposit films on an amorphous or polycrystalline surface. The choice strongly depends on the final result expected from the desired films. PVD techniques are known to provide flexibility to obtain a desired compound.

The DC reactive unbalanced magnetron sputtering (DCMS) was chosen for this work due to its benefits related to the deposition of YSZ thin films, such as, deposition of a metallic target in a reactive environment and the high energetic bombardment, allowing a modification of the thin film growth. Moreover, the flexibility of controlling the deposition parameters allows us to manipulate the microstructure and texture of our YSZ films in an easy way. In order to understand the processes occurring during deposition, some basics of magnetron sputtering were introduced in this chapter and will be further discussed throughout this work.

At this point we understand how the DCMS works. In the next chapter, the mechanisms involved in the film growth will be given. In this way, the trajectory of how the adparticles leave the target, their motion through the gas phase, their collection on a surface and finally their growth will allow us to understand the effects of the growth on the microstructure and texture of the YSZ system.

3 Thin film growth process

In order to understand the growth formation and how the out-of-plane and in-plane alignment can be optimized, a short description about the film growth will be given in this chapter, starting from the atomic level until a fully developed thin film. First, an approach at atomic level will be described. Then, nucleation and crystal growth will be briefly explained. And finally, the film thickening will be discussed, correlating the growth with the thin film microstructure.

3.1 The adsorption process

Adsorption is the first process of the film growth. Basically, in this step molecules or atoms are collected on another surface, e.g. a substrate. This collection depends on the sticking probability on a bare surface since not all the atoms impinging on a surface stick to it. The sticking coefficient is the ratio between the amount of particles adsorbed on a surface and the amount of arriving particles. An adsorbate atom or molecule can interact with the substrate either by chemisorption or physisorption. The difference between both terms is related to the binding strengths and mechanisms involved.

Physisorption is the weakest kind of adsorption. Due to the weaker binding energy there are no true chemical bonds except the attractive force or the so called van der Waals interaction. Hence, the electronic structure of the adsorbate is hardly disturbed. Typical energies vary from 50-500 meV/atom [187]. A physisorption interaction depends on the fluctuating dipole moment induced mutually between

adsorbate and substrate. The characteristic energy diagram of physisorption is shown in Figure 3.1a. This graphic shows that the atoms near the surface are attracted with a physisorption potential energy E_d, which is very low for physisorption. This leads to a weak polarization with the surface.

Unlike physisorption, chemisorption has a strong chemical bond formed between adsorbate and substrate with a strongly disturbed electronic structure. Typical chemisorption energies range from 1-10 eV/atom. A representation of its energy diagram can be seen in Figure 3.1b. First, an atom is in the physisorbed state with energy E_p. At a critical distance, r_p, the atom or molecule can return to the gas phase (desorb back) or migrate over the surface until the chemisorbed potential energy E_c is reached, leading to the chemisorbed state. If the atom is attracted to the chemisorption potential energy E_c, a chemical bond with the surface is formed. This process is associated with an energy difference (E_c - E_p).

For some reactive molecules the adsorption evolves in two stages and it is called dissociative chemisorption. The first stage, consisting in a precursor stage, behaves as a physisorbed atom remaining in a metastable stage where the adsorbate can either re-evaporate or remain on the surface of the substrate until it transforms to a chemisorbed state. The second stage is characterized by the splitting of the molecule and the adsorption of the individual atom. The transition from a physisorbed to a chemisorbed state for reactive admolecules such as H_2 and O_2 is generally thermally activated, meaning that the molecule bond has to be broken.

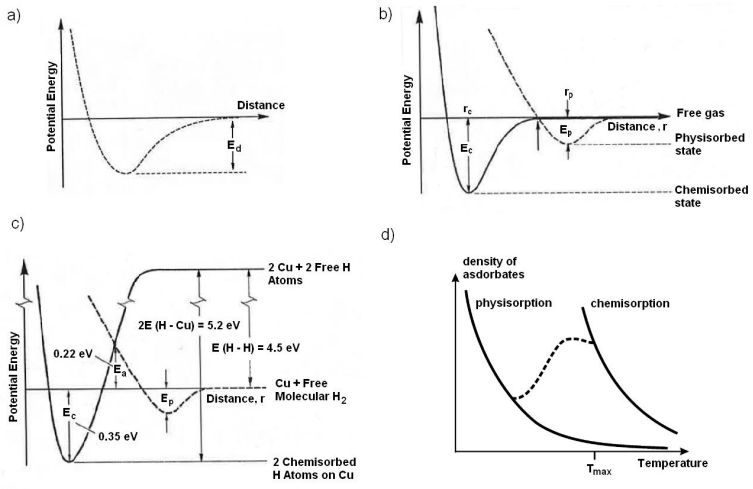

Figure 3.1: Energy diagram of: a) physisorption; b) chemisorption; and c) dissociative chemisorption of an H_2 molecule on a Cu surface; d) typical adsorption isobars [188].

An example of an energy diagram of the dissociative chemisorption is shown in Figure 3.1c for the dissociative H_2 bonding on a Cu surface. The van der Waals interactions create a minimum shallow in the energy curve, E_p, at a large distance from the surface (typically Z $>$ 3 Å [189]). The repulsive forces due to the overlap between electron densities cause a rapid increase of the total energy. In the case where the chemical bond is strong, the energy curve shows a much deeper chemisorption minimum (E_c) at shorter values of Z. The positive amount of energy for higher Z is related to the dissociative chemisorption which in turn is related to the amount of energy that has to be put in the system in order to dissociate a molecule. The characteristics of the dissociative adsorption process are influenced by the crossing point position of the physisorption and chemisorption curve (E_a). This position represents the height of the activation barrier to chemisorption and consequently influences the kinetics of the adsorption.

Figure 3.1d shows the typical adsorption isobars. The full lines represent the equilibrium chemisorption and physisorption isobar and the dashed line is the irreversible chemisorption. At temperatures below T_{max} the molecules are trapped in a physisorbed state. Consequently they cannot overcome the activation barrier to the chemisorbed state. With the increase of temperature, the amount of thermal energy of the adsorbed molecule is such that not only chemisorption can occur but also desorption can take place. In this case the molecules/atoms will desorb from the surface and return to the gas phase.

3.2 Surface processes and film growth

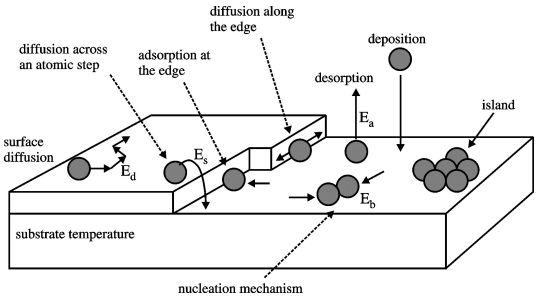

Figure 3.2: Schematic drawing of possible surface interactions occurring on a substrate [190].

The next step of the growing process is the development of a nucleus which leads to the growth of the film. During the deposition, adatoms interact with the substrate and with the atoms that are present on the surface. An interaction

depends on several other factors, such as, the type of substrate, the temperature and the type of adatoms present. Figure 3.2 shows a schematic drawing of several surface processes which are involved in the growing film. Adsorption and desorption were already discussed in the section above. An island is an agglomerate of adsorbed particles and its formation will be briefly discussed in the next section. Interdiffusion and surface diffusion (across an edge or along the edge) are processes which are strongly dependent on the surface mobility of the diffusing species.

3.2.1 Thermodynamic growth modes

The final macroscopic state depends on the process shown in Figure 3.2. Three different film growth modes can be distinguished as illustrated in Figure 3.3. The ML mentioned in the figure below stands for monolayer.

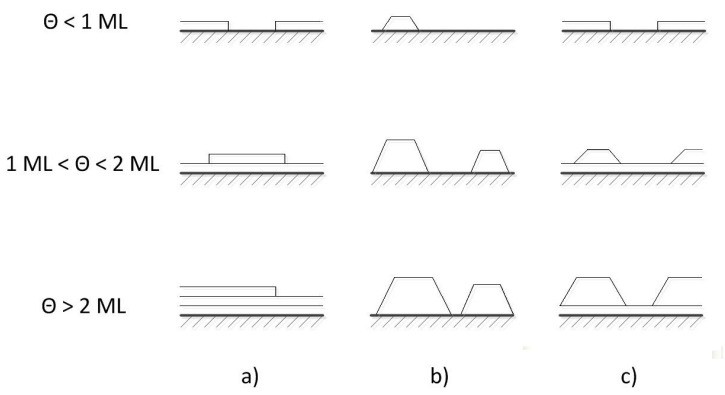

Figure 3.3: Schematic drawing of three different growth modes for different coverage regime (θ) from $0 < \theta < \infty$ ML (monolayer). a) Frank-van der Merve or layer-by-layer growth; b) Volmer-Weber or island growth; c) Stranski-Krastanov or layer plus island growth [191].

- The layer-by-layer mode or Frank-van der Merve growth, Figure 3.3a, is described by atoms being deposited on a substrate with an interaction between adsorbate and substrate which is stronger than between them. The nucleus is formed in 2D, meaning that a layer starts to form. A new layer only starts to grow when the last one is fully developed.

- The second mode is known as island formations or Volmer-Weber growth,

Figure 3.3b. Here the interactions among deposited atoms are stronger than to the substrate, nucleating immediately upon contact.

- The last mode is an intermediate case known as Stranski-Krastanov growth, Figure 3.3c. In this case, there is first a formation of layers followed by island formations. This change can be due to lattice mismatch between the growing layers on the substrate.

A simple distinction among these growths can be made in terms of the surface energy. Therefore, a basic thermodynamic model for homogeneous nucleation from a supersaturated vapor will be given. This surface energy represents the free energy per unit area necessary to create an additional surface. This approach is similar to the analysis used for contact angles as described by Young [192]. The horizontal components of the free energies are in equilibrium when $\gamma_S = \gamma_* + \gamma_F \cos\theta$ where γ_S is the surface free energy of the substrate-vacuum interface, γ_F is the surface free energy of the film-vacuum interface, γ_* is the surface-film interface energy and θ is the contact angle. Figure 3.4 shows a simplified picture of a deposited film and the free energies γ_S, γ_F and γ_*. In the case of Frank-van der Merve growth, the angle between the adsorbate and substrate, θ, is equal to 0 and the free surface energy of the substrate is $\gamma_S \geq \gamma_* + \gamma_F$; in the opposite case, i.e. for Volmer-Weber growth conditions, $\theta > 0$ and the surface energy of the substrate is $\gamma_S \leq \gamma_* + \gamma_F$. The Stranski-Krastanov growth is assumed to be formed due to the occurrence of a lattice mismatch between deposited film and substrate. The interface energy increases and the elastic strain field exceed the adhesion forces, since it is strained to fit the substrate [159].

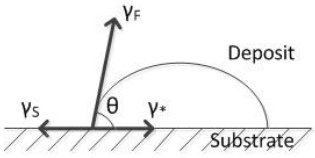

Figure 3.4: Simplified picture of a deposited film where free energies γ_S, γ_F and γ_* correspond to the free surface energy of substrate-vacuum, film-vacuum and surface-film interface, respectively.

The nucleation process in the case of Volmer-Weber takes into account the difference in Gibbs enthalpy, which is the difference in enthalpy when a particle is transferred from the gas phase to the substrate in a non-equilibrium state. In the island growth mode, the ΔG is given by:

$$\Delta G = n\Delta\mu = nkT \ln\left(\frac{p}{p_0}\right) \tag{3.1}$$

where n is the particle number and $\Delta\mu$ represents the chemical potential of the growing deposit [191, 193]. The term (p/p_0) is known as the degree of supersaturation and is one of the driving forces to the formation of a nucleate on a substrate. As a consequence, the nucleation begins when a cluster of atoms reach a critical size. The description of the critical size as a function of the free surface energy can be found in [187].

Naturally, there are other parameters which influence the nucleation process, such as impurities, flux of low-energetic ions, preferential nucleation sites at kinks or steps at a non-perfect surface. As a result, an influence of these factors on the competition between the layer-by-layer, island and layer plus island growth can be expected. Moreover, kinetics also plays an important factor in the nucleation process, leading to a competition between the thermodynamic and kinetic factors (e.g. surface temperature and condensing rate) [194].

3.2.2 Growing of small particles to form a grain boundary

In this work, a YSZ thin film is deposited on an amorphous substrate (glass). This results in a large misfit between the substrate and the YSZ film. As discussed in the work of Mahieu [195] and based on the description of growth modes above, our films will mainly have the Volmer-Weber growth (islands formations). Consequently, we focus on an island type of growth.

One of the main advantages of the growth of a thin film on an amorphous substrate is the control of a specific crystallographic alignment as a function of the change of the deposition variables. In the case of a deposition at low temperatures, the substrate yields the nucleation of islands with random orientations. However, a crystallographic alignment can be developed with the existence of re-structuring grain growth, i.e. an interaction between neighboring islands [196].

After development of the first layers or islands into larger clusters, these clusters grow ruled by two mechanisms, namely, Ostwald Ripening [197] and Smoluchowski ripening (or coarsening) [198, 199]. The first occurs due to the evaporation and diffusion of two-dimensional gas atoms of small islands onto larger islands, through surface diffusional mass transport in order to minimize the surface free energy of the island structure. This results in a growth of larger clusters and a reduction of small ones. The second is caused by coalescence of two islands by contact and subsequent diffusion. Small clusters are faster than the large ones and the rate of coarsening increases when the difference in size increases. So, when it is chemically favorable, two clusters will align and merge resulting in an energetically more stable cluster. Larger cluster formations are developed until there is mutual contact. This contact defines a grain boundary between two or more

different grains. Once the surface is fully covered by external particles, further adsorption will only be possible on existing islands. An adparticle is then still able to diffuse into a grain or between two different ones (surface diffusion process). As a consequence, the final structure and morphology of the film strongly depends on the mobility of the grain boundaries.

3.2.3 Morphology of the film based on the extended structure zone model (ESZM)

Structure zone models identify the evolution of a polycrystalline thin film and describe the relationship between microstructure and deposition parameters. The first model described by Movchan and Demchishin [200] indicates three different zones as a function of the ratio between a certain temperature and the melting temperature (T_m). Zone 1 ($T/T_m < 0.3$) has a columnar structure with voided growth boundaries, zone 2 ($0.3 < T/T_m < 0.5$) presents columnar grains defined by metallurgical grain boundaries and zone 3 ($T/T_m > 0.5$) presents equiaxed grains. The term metallurgical grain boundary means that the reduction in internal energy is achieved by reducing the total area of the grain boundary since either recovery and recrystallization are complete. Thornton [201, 202] extended this concept to thin films growing via magnetron sputtering, taking into consideration the influence of the Ar gas pressure. Figure 3.5 shows the schematic drawing of such a model, where the existence of a fourth termed zone is noticed, namely zone T. More details about the T zone are described below. Revised approaches [134, 203–205] were not meant to suppress former models but to recognize several additional features on the evolution of the growing film.

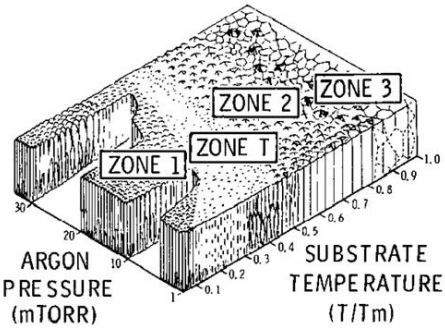

Figure 3.5: Schematic drawing of the structure zone model developed by Thornton [201].

The extended structure zone model (ESZM) suggested by Mahieu [195] not only takes into consideration the homologous temperature T/T_m to describe the structure evolution but also the diffusion processes and other fundamental

phenomena, e.g. nucleation, crystal growth and re-structuring grain growth which depend on the adatom mobility during the growth.

The ESZM can be defined in zones. Zones Ia, Ib and Ic are illustrated in Figure 3.6. At very low temperatures (zone Ia) the adparticles arriving on the surface of the substrate cannot overcome the diffusion barrier and consequently they present limited or no mobility. The lack of mobility results in sticking of the adparticles to the surface, remaining in the same hitting position. Thereafter, a columnar structure separated by voids is created. If a continuous bombardment of energetic species occurs the created voids will be filled in a knock-on event creating a denser structure, characteristic of zone Ib. Note that a transition from Ia to Ib is not dependent on temperature and that the structure remains amorphous. An increase of the temperature (zone Ic) enhances mobility and the adparticles are able to diffuse on the grain forming a crystal habit. The later defines an alternative shape developed from a single basic crystal type. Faceted columnar structure with random orientation is formed and its grains are terminated by planes of lowest crystallographic growth rate. Moreover, there is no competition between neighboring grains; meaning that there is no diffusion from and to another grain and only geometric shadowing can induce overgrowth. Hence, the columns are not longer separated by voids but by grain boundaries.

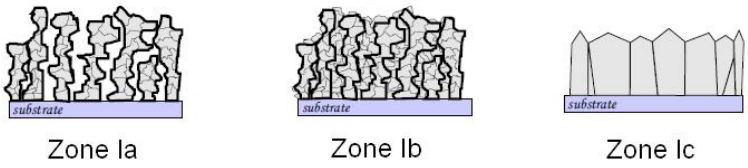

Figure 3.6: Zone Ia: hit-and-stick growth and columnar structure separated by voids; Ib: knock-on event creating a denser structure and Ic: formation of faceted columns [195].

Further increase of the temperature and sufficient mobility allows the growth to occur according to the kinetically determined crystal habit. Therefore, adparticle diffusion is no longer limited by the grain boundaries and diffusion between two different grains is possible. All these crystals will have a specific crystallographic direction and after film thickening, there will be overgrowth. As a result, the remaining grains correspond to the ones with the geometric fastest growing direction perpendicular to the substrate. Those grains are the most tilted facets with respect to the substrate plane. That is why the V-faceted column characteristics of zone T are formed. This characteristic structure is shown in Figure 3.7. The preferential orientation is then defined by the geometric fastest growth direction, the grain with the most tilted facet with respect to the substrate. In the case of YSZ films, the geometric fastest growing direction is the [200] direction. This

direction is normal to the (100) plane in the cubic structure. Another approach presented by [205] suggests that the orientation selection is triggered by anisotropy in diffusivities on different crystallographic planes. Low diffusivity surface 100 are more stable and possess lower potential sites when compared to high diffusivity 111 surface which has longer mean free path and higher probability to move. In this way, 100 grains grow faster. These grains overgrowth high diffusivity grains defining the preferential orientation of the film. Thus, low diffusivity surface is equivalent to the geometric fastest growth direction presented by the ESZM, indicating the equivalence of both approaches.

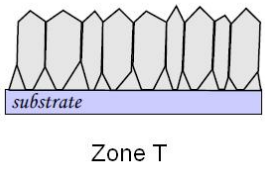

Figure 3.7: V-faceted columns characteristic of zone T [195].

At higher temperatures, the mobility also increases and diffusion between the grains occurs. In addition, atoms that were stable can also become active. This results in re-structurative grain growth which is driven by the differences in the average energy per atom for islands or grains of different sizes. Re-structuring grain growth may initiate and unstable islands are incorporated in stable islands via ripening, island diffusion or grain boundary migration. Consequently, no evolutionary V-shaped overgrowth will be present in the resulting film. Instead, as indicated in Figure 3.8, defined straight columns will be observed on the film. Those columns will aim for the thermodynamic most stable situation, which in this case are the planes with the lowest surface energy parallel to the substrate. This growth favors a polycrystalline film with a particular out-of-plane orientation: this is the [111] out-of-plane orientation for YSZ thin films.

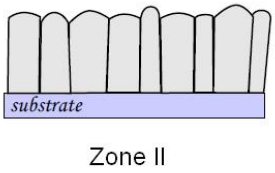

Figure 3.8: Straight columns characteristic of zone II [195].

Either for zone T and zone II the kind of structure growth is strongly related to the deposition process itself. By tuning the deposition parameters, it is possible to obtain a specific orientation. The influence of some deposition parameters on the ESZM of the YSZ system will be discussed in Chapter 5.

At even higher temperatures not only surface diffusion and re-structuring grain growth takes place but also bulk diffusion participates in the growing process. The columnar structure is substituted by crystal grains or equaixed grains, as shown in Figure 3.9. However, Barna and Adamik [204] gave experimental evidence that there is no formation of zone III. This zone occurs if impurities acting as driving force or barriers to the growing process are present. Those impurities can be absorbed and block the surface sites, they can form complexes or other phases with different activation energies and also be blocking points to the grain boundaries avoiding or hindering particles mobility. Moreover, they can create nucleus zones allowing the coarsening and growth of equiaxed grains.

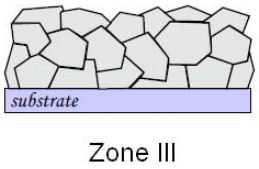

Figure 3.9: Equiaxed grains representative of zone III [195].

3.3 Texture of thin films

In previous sections, a brief description of surface processes and film growth was given. It was also mentioned that the microstructure either in zone T or zone II can be manipulated by controlling the deposition conditions. Therefore, not only the microstructure can be tuned but also the texture.

The texture is defined by the orientation or the lack of orientation of a crystal on a surface. Several crystalline grains when deposited on an amorphous or random oriented substrate form a polycrystalline film. Each one of them together with the corresponding crystallographic orientation constitutes a specific film orientation. When no correlation among the orientation of the grains exists, the resulting film is known to have no alignment, i.e. each grain possesses its own random orientation with no relationship between substrate and film as illustrated in Figure 3.10a. In some cases there is an organization of the grains to a specific direction and the film is called uniaxial aligned, Figure 3.10b. Figure 3.10c not only shows a preferred orientation of the grains perpendicular to substrate (out-of-plane) but also parallel

to the substrate (in-plane). These films are known as biaxial aligned films.

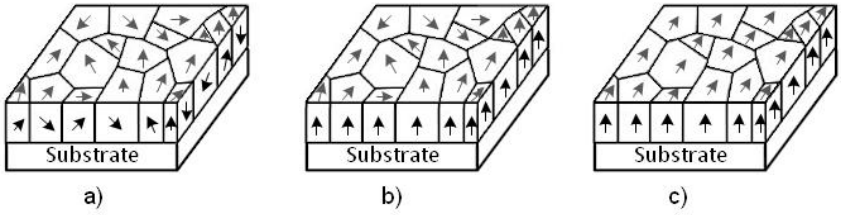

Figure 3.10: Schematic drawing of thin films alignment. a) No alignment and no preferred orientation; b) uniaxial alignment with an out-of-plane preferred orientation and c) biaxial alignment with an in-plane and out-of-plane preferred orientation.

In the next chapters, it will be shown that one of the main characteristics of our YSZ thin films is the interesting feature of biaxial alignment: meaning that our films not only present a preferential out-of-plane orientation, but also an in-plane orientation of the constituent crystallites.

3.4 Summary

The growing of a film is a combination of several deposition steps. Starting with the adsorption where the molecules or atoms first adsorb to a surface via physisorption and chemisorption. Interdiffusion and surface diffusion supports the formation of agglomerations or nucleus sites on the surface forming nucleation. The nucleation growth zones were shown to be formed in three different ways, layer to layer, layer plus island growth and island growth formation. In our work we consider the nucleation to be mainly of islands formations (Volmer-Weber growth) due to the large misfit between the amorphous substrate and the YSZ film. As the film increases in thickness a defined structure is formed. The extended structure zone model identifies the evolution of a polycrystalline thin film and its relation with the deposition conditions. In zone T and zone II, the formed microstructure is strongly dependent on the deposition conditions.

In this chapter it was shown that the films can develop a certain crystal organization and therefore a specific orientation. The YSZ thin film grown in this work presents the interesting feature of biaxial alignment, resulting in an in- and out-of-plane alignment. Moreover, it was discussed that both texture and microstructure can be controlled by the deposition conditions. The next chapter describes in detail the experimental setup used in this work, the deposition conditions changed during the sputtering and the different characterization techniques used to understand the YSZ system.

4

Experimental setup and characterization methods

Chapters 2 and 3 discussed the techniques to deposit thin films and the film growing process, respectively. In this chapter, the experimental setup is described, the deposition conditions are explained and finally the characterization methods used to determine the film characteristics, texture and microstructure are discussed.

4.1 Experimental setup

Yttria-stabilized zirconia thin films were deposited using reactive unbalanced magnetron sputtering. The schematic drawing of the vacuum chamber, denominated Maximus, is indicated in Figure 4.1. Commercial targets of Y and Zr from Kurt J. Lesker were mounted on a water-cooled magnetron inside a vacuum chamber. The targets have a diameter of 2 inches (50.8 mm) and a thickness of 3 mm. The magnetrons were initially positioned 210 mm from each other's center, obtaining an angle of approximately 45° between the target center and the substrate holder. In this way, a flux of Y atom coming from one side and a flux of zirconium atom coming from the other side of the chamber exist. This configuration permits a good control of the composition, creating a compositional gradient along the sample substrate. Since the reaction occurs in a reactive environment, Y_2O_3-ZrO_2 (YSZ) will be formed on the sample surface.

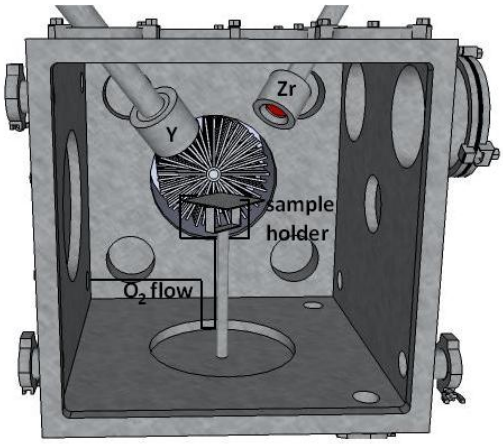

Figure 4.1: Schematic drawing of the vacuum chamber.

The chamber was pumped down via a turbo-molecular and a rotary pump, reaching a base pressure of approximately 10^{-4} Pa. The pressure was measured by a dual gauge, i.e. combination Penning-Pirani, and by a capacitance gauge during deposition. Argon is used as a sputter gas and oxygen as a reactive gas. The flow rate of the sputter gas was controlled by a mass flow controller of 50 cm^3/min and 10 cm^3/min for argon and oxygen, respectively. The reactive gas was introduced in the chamber through a local O_2 inlet flow oriented directly to the substrate. In this way it is possible to maximize film oxidation and minimize target oxidation [125]. The pumping speed was kept constant and equal to 120 L/s.

In order to stabilize the experimental conditions before deposition, a shutter was added in the chamber between substrate and targets. The substrate holder was grounded and it was neither heated nor cooled during deposition. The magnetrons were powered using a DC power supply from Httinger Elektronik.

4.2 Substrates and sample preparation

Amorphous glass (76 mm 22 mm x 1 mm), silicon (100) (10 mm x 10 mm x 0.5 mm) and sapphire (10 mm x 10 mm x 0.4 mm) were used as substrates. The choice is dependent on the film analyses. Due to its amorphous characteristics, glass has its signal easily removed when determining thickness or crystallinity of the film. Silicon, on the other hand, is suitable for sample preparation due to its fragility, being a convenient material for image analyses, such as in transmission electron microscopy. Sapphire substrates were used for optical properties analyses. Sapphire has very low absorption edge and

therefore is suitable to determine high band gap materials.

Glass samples were first cleaned using an ultrasound bath. The substrates were immersed in an acetone/methanol sequence during 5 min for each solution. After dried with N_2 or O_2, the cleaned glass substrate is marked with a line, using a marker pen, in the parallel direction to the length of the glass. This mark is used to determine thickness (see section 4.6.1).

Silicon samples require a different cleaning route, namely RCA clean. Following this route, the silicon wafers are cleaned and a superficial silicon dioxide layer can be grown. In this route three different solutions are used in a sequence. All the solutions have to boil before the immersion of the cut silicon wafers. The first solution is a combination of 90 mL distilled water with 30 mL H_2SO_4 and 30 mL H_2O_2 during 10 min. After cleaning it with distilled water, the cut silicon wafers are immersed in the second solution of 100 mL distilled water with 20 mL NH_3 and 20 mL H_2O_2 also for 10 min. After cleaned with distilled water, they are immersed in the last solution formed by 100 mL distilled water, 20 mL HCl and 20 mL H_2O_2. After the sequence is finished, the cleaned samples are stored in a beaker containing distilled water until they are used.

Before using sapphire as substrate, the substrate was immersed in acetone to remove any residual from its surface.

4.3 Selection of the most suitable method to deposit fully oxidized films

The voltage and deposition rate of Y and Zr change when there is an increase or a decrease of the O_2 flow. Moreover, both trends are noticed to be different for the addition and removal of the reactive gas. This different trend forms a hysteresis loop. This term has already been discussed in section 2.2.3, Chapter 2. The hysteresis loop can be experimentally obtained using a quartz crystal microbalance. This device measures the mass per unit area or the deposition rate, which changes as a function of the addition or removal of a small mass due to film deposition at the surface of the crystal. The hysteresis loop of Figure 4.2 is representative for a target-substrate (T-S) distance of 240 mm and 90 mm with currents of 0.2 A and 0.5 A for Y and Zr, respectively. These T-S distances are selected distances used during the deposition of YSZ films. In Figure 4.2a it is possible to observe the ”negative” contribution of the oxygen flow to the Y discharge voltage, i.e. for a critical O_2 flow the voltage abruptly decreases. The deposition rate also decreases at the same critical O_2 flow. Above 2.5 sccm of O_2 the deposition rate is approximately 0.2 nm/min and consequently the deposition is in poisoned mode. In Figure 4.2b, a ”positive” change in voltage is seen above 2 sccm where the Zr voltage increases with the increase of O_2 flow. Above this

value the deposition is in poisoned mode and consequently the deposition rate decreases. When both magnetrons are operational it is easier to control the O_2 flow at the edge of the metallic mode by observing the Y discharge voltage, since its change is abrupt in comparison with the Zr voltage.

From the results of Figure 4.2 we have two possible ways to deposit fully transparent oxide films. The first is to perform deposition in oxide mode. However, as seen above, this means that the deposition rate is very low and the deposition can take very long before some hundred of nanometers are reached. The second involves the control of the voltage or the partial pressure of the reactive gas. In this way it is possible to deposit fully oxidized films with a high deposition rate during a shorter period of time. Note that the hysteresis loops of Figure 4.2 are measured separately. No hysteresis of the YSZ system was performed because in a dual magnetron system both targets are mutual dependent, i.e. if one of the targets goes to the poisoned mode the second target follows the other's behavior. In our experiments we based on the Y hysteresis loop. Therefore, the flow of O_2 is selected in the transition region from metallic to poisoned mode of Figure 4.2a [206]. In the current work, the voltage is used as indicator to know if either the deposition is in metallic or poisoned mode. As seen in Figure 4.2a a drastic change in voltage from approximately 300 V to 190 V limits the region metallic and poisoned mode.

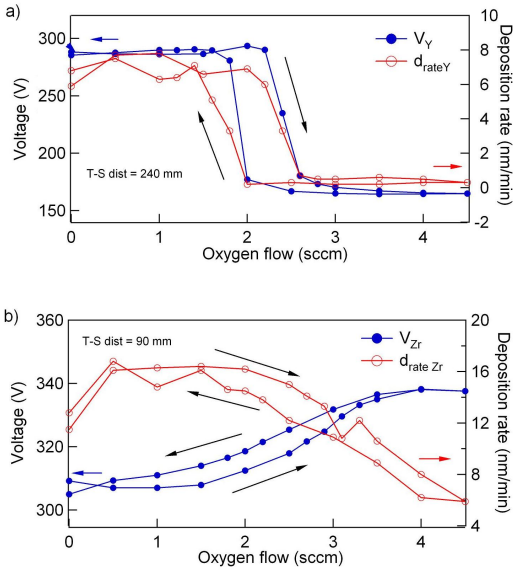

Figure 4.2: Hysteresis loop of voltage and deposition rate in function of oxygen flow, obtained via quartz balance, for: a) yttrium at 0.2 A and; b) zirconium at 0.5 A.

4.4 Deposition conditions

Several deposition conditions were changed namely, the Y T-S distance, chamber pressure, Y current and deposition time. Below, we list the experiments performed using the deposition chamber and the respective deposition condition. All YSZ coatings were transparent and fully oxidized in the cubic phase. A summary of the deposition conditions and the experiments is given in Table 4.1.

Influence of:	**Distance**	**Pressure**	**Current**	**Time**
Y current [A]	0.2	0.2	0.17/0.37/0.58/ 0.77/1.16/1.57	0.2
Zr current [A]	0.5	0.5	0.5	0.5
Y T-S distance [mm]	80-240	80-240	240/100	240/80
Zr T-S distance [mm]	90	90	90	90
Pressure [Pa]	0.5	0.95	0.5	0.5
Ar flow [sccm]	35	70	35	35
O_2 flow [sccm]	2-2.5	1.2-1.4	2-2.5	1.8-2.5
Deposition time [min]	20	20	20	150, 20-120

Table 4.1: Deposition conditions of the experiments.

- Changing Y T-S distance at 0.5 Pa: The compositional variation, more specifically the change in Y content, was ensured by altering the Y T-S distance from 80 to 240 mm, in steps of 20 mm. Other parameters, such as target currents (I_Y = 0.2 A, I_{Zr} = 0.5 A), Zr T-S distance (d_{Zr} = 90 mm) and Ar flow (35 sccm) remained constant. The O_2 flow was controlled keeping the maximum deposition rate and varied between 2 - 2.5 sccm.

- Changing Y T-S distance at 0.95 Pa: The same experiment was performed at 0.95 Pa. In this work, 0.5 Pa is referred to as *low pressure* while 0.95 Pa is referred to as *high pressure*. At high pressure the Ar flow was set to 75 sccm. Other parameters remain constant as reported for the 0.5 Pa experiment. The O_2 flow varied from 1.2 to 1.4 sccm.

- Changing Y current: Current was changed from 0.2 A to 1.6 A with intervals of 0.2 A. A fixed Y T-S distance was selected (240 or 100 mm). The other deposition conditions were kept constant and equal to the ones described for changing Y T-S distance at 0.5 Pa. The O_2 flow varied from 2 to 2.5 sccm.

- Changing deposition time: In this experiment the time was the variable parameter. The other deposition conditions are constant and also similar to the ones described for changing Y T-S distance at 0.5 Pa. The Y T-S

distance, however, is equal to 240 mm or 80 mm and the O_2 flow varied from 1.8 to 2.5 sccm. In most of the experiments, the deposition time was 20 min, except in the experiments with one magnetron (30 min) and where time was the variable parameter, varying from 20 up to 150 min. The flow of O_2 was defined using the information of a hysteresis loop, previously described in section 4.3.

4.5 Measuring YSZ characteristics on the film

First, the thickness and the composition of the deposited YSZ layer on the glass substrate are determined. How this is done will be explained in the coming sections. On the sample substrate, 5 different points were chosen to determine the thickness and 6 different points were selected to determine composition. These points vary as a function of the length of the sample (76 mm), where the 0 mm corresponds to the Y side and 76 mm to the Zr side. These points on the layer/substrate are shown in Figure 4.3. From now on we denominated position on the substrate referring to the combination layer + substrate.

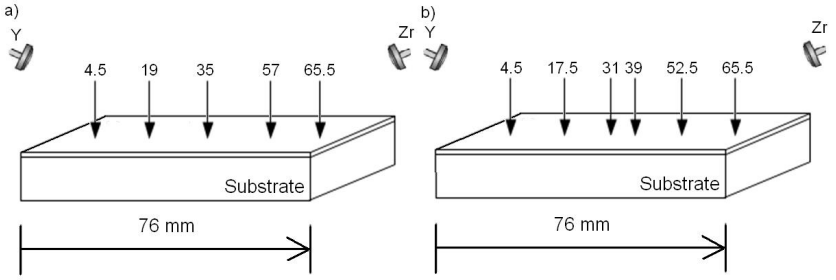

Figure 4.3: Selected positions on the substrate to determine a) thickness and b) composition.

Microstructural and textural analyses were determined using two different sets of samples. The first set (called *set 1* in this text) considers a single point located in the center of the sample, while the second set (*set 2*) considers multiple points spread over the sample. These points are chosen based on a fixed composition, e.g. 10 to 50 at.%Y with interval of 5 at.%Y. As a result we have approximately 50 points with different compositions and Y T-S distances. A schematic drawing of these set of samples is depicted in Figure 4.4.

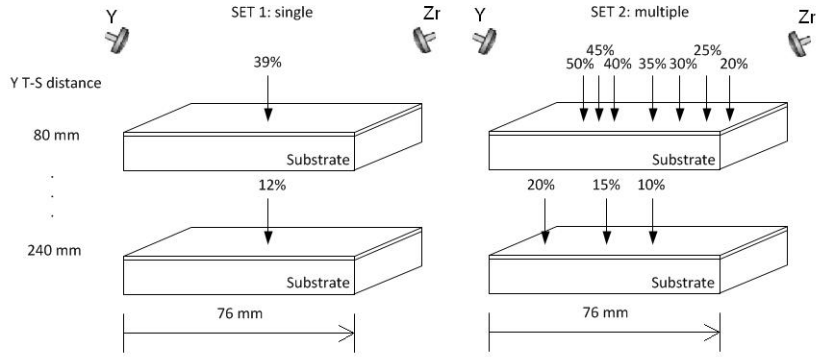

Figure 4.4: Schematic drawing of the two different set of sample: single and multiple points.

4.6 Methodology to obtain the characteristics, texture and microstructure of thin films

4.6.1 Layer thickness

Using the marker on the glass substrate as previously mentioned in section 4.2 and illustrated in Figure 4.5a, it is possible to measure the thickness. After depositions, this line is removed with acetone, forming a step. As a result, a non-deposited region allows obtaining the thickness using a profilometer (Talystep Taylor-Hobson). The measurement probe of the profilometer moves along the sample surface, Figure 4.5b. In this way, the difference between two different heights is converted to an analog signal giving the total thickness of the step [207].

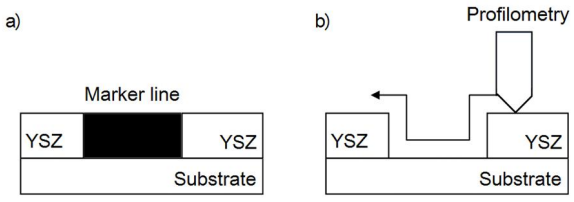

Figure 4.5: Schematic drawing of a) a deposited sample with a marker line and, b) a deposited sample with a step and the trajectory of the profilometer nail.

Another way to measure the thickness is based on the transmittance spectra

using the envelope method developed by Swanepoel [208]. In this model, the wavelength in the infrared region of two maximum or two minimum fringes of the transmittance spectra are considered as well as their respective refractive index. The thickness is then calculated by the equation:

$$thickness = \frac{\lambda_1 \lambda_2}{2\left(\lambda_1 n_1 - \lambda_2 n_2\right)} \tag{4.1}$$

This last approach is only applied for samples used to study optical properties.

4.6.2 Transmittance

Transmittance spectra were obtained using a spectrophotometer (double beam double monochromator UV-VIS-NIR spectrophotometer). The spectra were obtained in the wavelength range varying from 200 to 2000 nm.

4.6.3 Thermal flux

Energy flux determinations were performed using a passive thermal probe [209]. Using this device, the amount of energy arriving on the sample surface can be determined based on the temperature variation during deposition [210]. The thermal probe was positioned in the center of the chamber, replacing the sample holder. Once the deposition starts, the thermal probe starts to heat up due to the impact of the deposition particles on its surface. This difference in temperature is converted to thermal power per area using the software thermal probe measurement and analysis system (TPMAS). The duration of each measurement is approximately 500 s, being dependent on the stabilization of temperature. An example of the obtained image via TPMAS is illustrated in Figure 4.6.

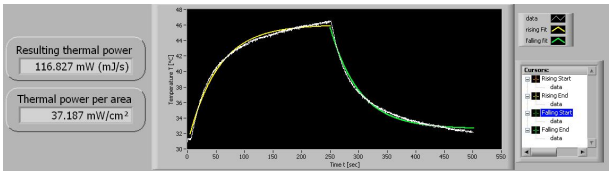

Figure 4.6: TPMAS interface showing the fit of the temperature vs. time and the calculated results of thermal power and thermal power per area.

4.6.4 Composition of the layer

The film composition was measured using energy-dispersive X-ray spectroscopy analysis (EDX) in combination with scanning electron microscopy (SEM) Quantafeg - FEI, with a beam current of 208 μA, an acceleration voltage of 10 kV

and spot size of 5. A region of the sample is focused with SEM before EDAX is performed. With the EDX Genesis software it is possible to determine the amount of Y, Zr and O in the layer, either in atomic or mol percentage. The accuracy of the EDAX was confirmed by measuring some samples at VITO[1] using an electron probe microanalyzer (EPMA) JEOL. It was found that the measurements of EDAX are within the experimental uncertainty of the measurements with EPMA, proving the accuracy of the experimental data and allowing the analysis to be done in the department. In this work the contents are given in atomic percentage. The final composition is defined using the metal ratio of the film, calculated as Y/(Y+Zr).

4.6.5 Micrographs

Since YSZ films are insulating, an ultrathin coating of electrically conducting material, such as gold, is needed in order to prevent the accumulation of electrostatic charge at the surface. Therefore, a very thin layer of gold is deposited on the sample by low-vacuum sputter coating with a current of 5 mA during 15 s. Moreover, a contact with carbon tape is done between the gold layer and the sample holder in order to improve contact.

The SEM images are obtained using a scanning electron microscopy (SEM) (Quantafeg - FEI), with a spot size 3 and acceleration voltage of 20 kV. An example of the SEM image is shown in Figure 4.7. The substrate, the layer and the screw of the sample holder are displayed in this image.

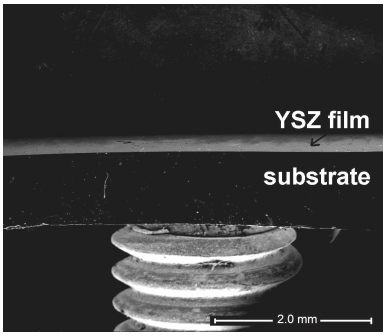

Figure 4.7: SEM image of a sample prepared for cross section.

4.6.6 Compositional gradient on nano scale

In order to perform analyses with annular dark field scanning transmission electron microscopy (ADF-STEM) and scanning transmission electron microscope-energy

[1] VITO: Vision on Technology, Mol

dispersive X-ray analysis (STEM-EDX), samples must be prepared in cross-section using focused ion beam (FIB) milling. The total FIB sample is approximately 5 μm in length. The sample preparation was performed by the Electron Microscopy for Materials Science (EMAT) group in Antwerp. Those samples were further investigated using ADF-STEM and STEM-EDX in order to analyze the yttrium and zirconium distribution. STEM was performed in a FEI Tecnai G2 instrument at 200 kV. The EDX spectrum images were acquired with a Si (Li)-type EDX system by EDAX. Active drift compensation was used through the microscope control software. The local area STEM-EDX spectra acquisition time was 10 seconds. The EDX data was acquired in a 0-20 keV range. The elemental map and quantitative compositional results were generated using the Zr K-line (15.770 keV) and the Y K-line (14.958 keV) using TIA software. A low magnification ADF-STEM image is illustrated in Figure 4.8.

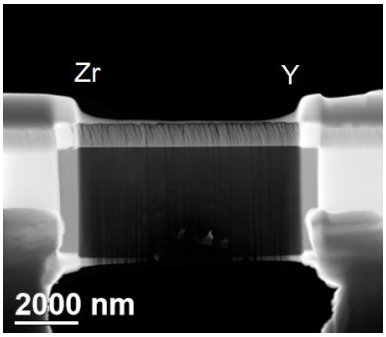

Figure 4.8: Low magnification ADF-STEM images showing YSZ sample prepared by FIB.

4.6.7 X-ray diffraction pattern

The diffraction pattern was obtained via X-ray diffraction (XRD) using CuKα radiation in $\theta/2\theta$ (Bragg-Brentano) configuration with a LynxEye Silicon Strip detector mounted into a D8 discover apparatus (Bruker AXS). A pinhole is attached on the X-ray tube, resulting in a circular 2 mm spot on the sample. The 2θ values vary from 25 to 78°. The obtained diffraction lines are plot in Evaluation (EVA) software in order to obtain parameters like maximum θ, area and full width at half maximum (FWHM) of the diffraction peak. The signal of the glass can easily be corrected by removing the signal background from the obtained spectrum. Moreover, the diffraction spectrum can be compared with a polycrystalline YSZ in order to identify if the diffraction peaks agree with a cubic fluorite type from the JCPDS card file #30-1468.

4.6.8 Rocking curve

An analysis of the full width at half maximum (FWHM) of the diffraction peak determines if this peak in a certain θ can be considered as a preferred orientation. This analysis can be done by looking into the FWHM of the out-of-plane direction via rocking curve [130, 211–213]. Rocking curves were obtained using a Siemens Bruker D5000 X-ray Powder Diffractometer. In this analysis, the detector and the source are kept fixed with an appropriate Bragg angle corresponding to the desired orientation angle, i.e. $\theta[200] = 17.6°$. The sample substrate then rotates or "rocks" in a certain axis, i.e. the ω axis [214]. The distribution corresponding to the specific θ at different rotations reflects the probability of a certain angular range near the Bragg angle θ. The smaller the FWHM value (narrower the diffraction peak) the better becomes the orientation.

4.6.9 Pole figures

Crystal orientations can be determined from pole figures. Pole figures are obtained using XRD with a Sol-X energy dispersive detector. Figure 4.9 illustrates the θ, polar χ and azimuthal φ angles in the pole figures measurement. In this kind of measurement a sample is fixed in a certain 2θ angle, corresponding to a chosen (*hkl*) orientation. Next, the intensity data for various settings of chi (χ) and phi (φ) are collected. A new set of chi values only start after all phi values are measured [215, 216]. The χ was varied from 0° to 80° and the φ from 0° to 360°, both with increment of 5°. The resulting pole figure projects the probability of finding a given (*hkl*) plane as a function of 2θ angle. A combination of two or more pole figures can give us an idea of the three dimensional structure and of its alignment.

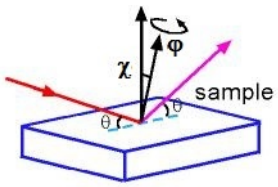

Figure 4.9: Illustration of the θ, polar χ and azimuthal φ angles in the pole figures measurement (Figure from [217]).

Because the visualization of pole figures is not as trivial and direct as the other analyses described above, we will discuss in more details how pole figures can be evaluated.

4.6.9.1 Identification of the preferred orientation using pole figures

Biaxial aligned samples in the cubic phase have two main preferred orientations, an out and in-plane orientation. Thus, a pole figure obtained for two orientations, (111) and (100), will be sufficient to observe the cubic structure as a whole.

Figure 4.10 gives a simple example of a [200] out-of-plane preferred orientation of a YSZ thin film. In Figure 4.10a, a cubic crystal shape of a (100) plane is indicated as well as the [100] direction perpendicular to this plane. The [100] and [200] directions are equivalent and the latter will be used to discuss the preferred orientation of YSZ films. When [200] is the preferred orientation, the correspondent pole figure will have a main peak in the center of the pole which corresponds to the projection of the [100] direction. Moreover, a biaxial aligned thin film presents four peaks when a pole figure is performed in the [111] direction. This can be observed in Figure 4.10b where the perpendicular direction of the (111) plane is located at 55°. The [111] pole of uniaxial aligned films is represented by a circular shape, indicating the random orientation of the projected direction.

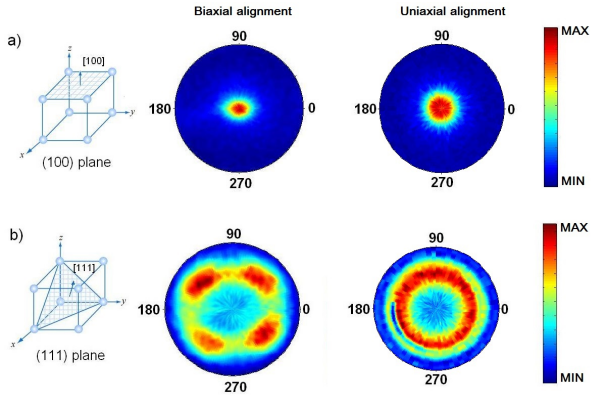

Figure 4.10: Cubic crystal planes and its respective characteristic pole figure for YSZ thin films for biaxial and uniaxial alignment: a) (100) plane; b) (111) plane.

4.6.9.2 Possible influences of the deposition parameters on the alignment of thin films

As described in Chapter 2, sputtering is a flexible technique since the deposition conditions can easily be tuned and controlled. However, it was discussed in Chapter 3 that the growth in zone T and II strongly depend on the applied deposition conditions. These conditions do not only define the zone of growth but also affect the in-plane and out-of-plane alignment of thin films. In order to determine the degree of alignment, the (hkl) peak of the XRD pattern is used.

The degree is defined as the product of the (hkl) peak area and its repestive (hkl) intensity divided by the summation of all observed diffraction peaks of the film under investigation. Previous studies demonstrated the effect of several deposition parameters on the alignment, including the influence of the substrate bias [134], target-substrate distance [117, 157, 218, 219], target-substrate angle [103, 134], pressure [134], film thickness [195, 218, 220], the ratio of Ar/O_2 in the vacuum chamber, the target usage, magnet configurations in the magnetrons, the condition of the chamber walls [195] and the use of other deposition techniques [101]. Table 4.2 provides a summary of the deposition parameters and its influence on the alignment of thin films based on the literature cited above.

Influence of:/ Alignment	**Improves**	**Worsens**
Substrate bias	x (positive bias)	x (negative bias)
Increase of T-S distance	–	x
Increase of T-S angle	x	–
Increase of pressure	–	x
Increase of film thickness	x	–
Increase of Ar/O_2 ratio	–	x
Target usage	x	–
Magnet configurations (unbalanced)	x	–
Deposited material on chamber walls	x	–

Table 4.2: Summary of the deposition parameters which affects the alignment on thin films.

In fact, it is not the objective of this work to study the influence of each of these deposition parameters on the biaxial alignment of thin films. However, as some deposition conditions are varied in this work, their influence on the alignment of YSZ thin films will also be demonstrated. An overview on the influence of pressure and thickness is given in Appendix A.

4.7 Summary

In this chapter the focus is given to the experimental setup and the methodologies used to determine the different characteristics and properties of YSZ thin films. During this work a dual unbalanced reactive magnetron sputtering is used to grow YSZ films on either glass, silicon or sapphire substrates. The description of how the samples were prepared and the reason of choosing different substrates was explained. Before deposition, the hysteresis loops of Y and Zr were obtained in order to identify the point of the highest deposition rate to deposit fully oxidized thin films.

During this work, several analyses techniques were employed in order to study the characteristics of YSZ thin films. These techniques and the procedures involved were briefly discussed. Since pole figure analysis is not trivial, a description of how to identify the directions was introduced.

To finalize this chapter it was shown based on literature review that deposition conditions can alter the alignment of thin films. As described in this chapter, other deposition conditions also influence the alignment but they were not yet experimentally shown. In Chapter 5 the effect of different deposition conditions on several characteristics of the film, microstructure and texture will be discussed.

5

Tuning the YSZ system

The deposition conditions, mentioned in Chapter 3, affect the microstructure and texture of the growing film. Previous studies reported that microstructure and texture can be influenced by the substrate temperature [221], the total pressure [102, 119, 135, 222], as well as other deposition variables [134, 205]. Therefore, to study the influence on the thin film characteristics some deposition conditions were varied, namely, the target-substrate (T-S) distance, the gas pressure, the deposition time and the target discharge current (see Table 4.1, Chapter 4 for more details).

This chapter consists in five different parts. In Part I the influence of the deposition conditions on some selected thin film characteristics (thickness, composition, grain size and lattice parameter) is reported. Simulations to predict the composition and film thickness using a Monte Carlo code are discussed in Part II. The effect of the deposition conditions on the microstructure is discussed in Part III. Part IV discusses the texture being influenced by the deposition conditions. Finally, in Part V the relationship between grain and columnar tilt is described.

5.1 Part I: Influence of the deposition conditions on the characteristics of YSZ thin films

5.1.1 Thickness, composition, grain size and lattice parameter as a function of the position on the substrate

As discussed before, the thin film characteristics depend on the deposition conditions. However, under the conditions used in this work, i.e. dual reactive magnetron sputtering on a non-rotating substrate, the film properties will also vary as a function of the position on the substrate since the deposition is not homogeneous. To illustrate this point in a qualitative way, a schematic drawing of the material flux arriving on the sample substrate is shown in Figure 5.1 for two different Y T-S distances (a) 240 mm and (b) 80 mm. The flux of Zr in the direction of the substrate remains the same as both the target substrate distance and the applied power to the Zr magnetron are constant. The change of the Y T-S distance, on the other hand, affects the number of collisions of the sputtered atoms. When the T-S distance becomes shorter, the probability for collisions decreases in comparison with larger T-S distances. Therefore, at shorter distances the atoms will scatter less and the amount of Y atoms arriving on the substrate will increase. The schematic drawing shows also another important effect related to the inclined target (45° in relation to the substrate). Due to this inclination, the distribution of arriving particles is different because the total effective distance between target and substrate varies as a function of the substrate length. As a consequence, the distribution of the arriving atoms will be modified.

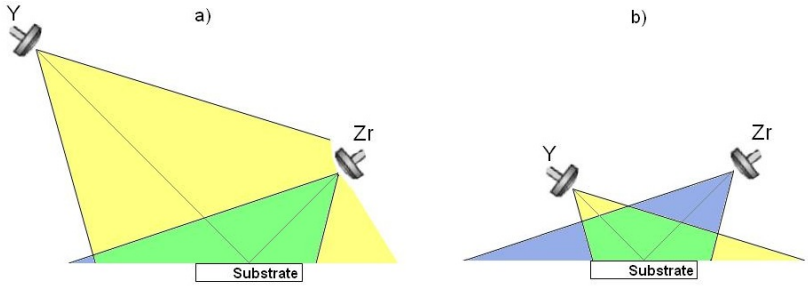

Figure 5.1: Schematic drawing of the incoming material on the substrate. a) Representation of a Y T-S distance of 240 mm and b) 80 mm. Distances considered from the center of the Y target to the center of the glass substrate.

The same reasoning can be done at high pressure, meaning that the effect of Y T-S distance is similar. However, the probability of collisions between emitted particles and gas increases at higher pressures leading to a deviation of the particles

from its original path due to increase of scattering. In a first approximation, the current only affects the number of atoms arriving on the substrate.

In the following paragraphs the effect of different deposition parameters (Y T-S distance, argon pressure, and discharge current) on the film thickness, composition (content of Y), average size of the constituent grains and the average lattice parameter will be discussed for different positions on the substrate.

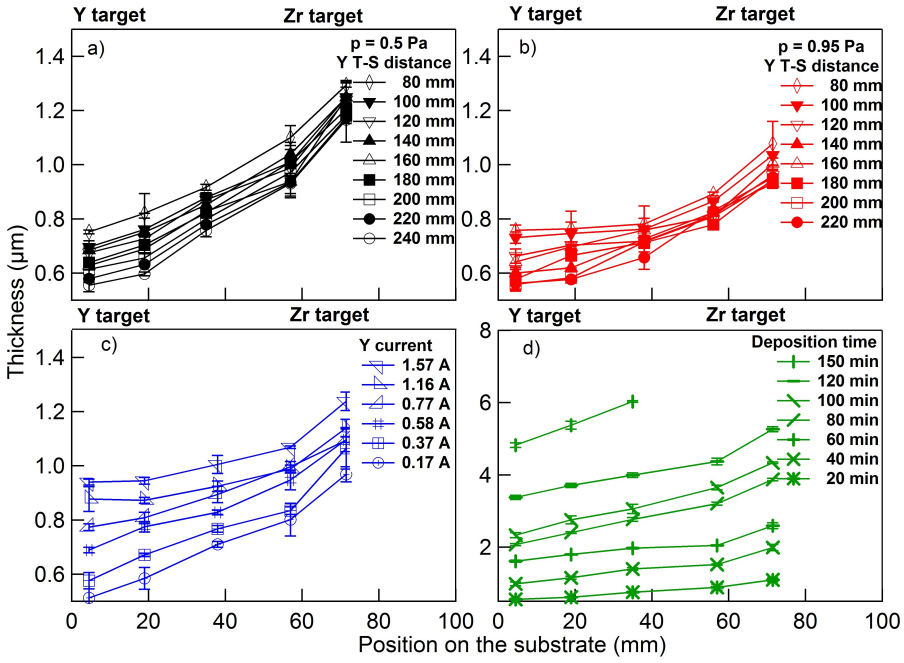

Figure 5.2: Thickness as a function of the position on the substrate when changing a) Y T-S distance at 0.5 Pa; b) Y T-S distance at 0.95 Pa; c) Y target current at 0.5 Pa, and d) deposition time at 0.5 Pa. Both plots c) and d) are deposited at a fixed Y T-S distance of 240 mm. Plots a), b) and c) are deposited during 20 min.

The first thin film property to be discussed is the film thickness. Figure 5.2 shows the thickness along the substrate for different experimental conditions. The thickness is measured by profilometry as discussed in Chapter 4. In this context, it is important to mention that film delamination occurs when the film thickness becomes larger than 6 μm. In general, along the substrate the thickness increases from the Y side (left) to the Zr side (right). The latter can be understood when considering the power on both cathodes. The Y source has a lower power (50 W, 0.2 A) as compared to the Zr source (150 W, 0.5 A). As the sputter yield and discharge voltages are comparable between both materials, more Zr atoms

are sputtered than Y atoms, explaining the observed trend. The top panels of Figure 5.2 (a and b) show the change in film thickness as a function of the position on the sample for two series of experiments at two different pressures. In both series the distance between the center of the Y target and the substrate center (T-S distance) is modified. The main effect is a decrease of the thickness at higher pressure. The reduction of the deposition rate can be understood from the scattering of the sputtered atoms. The number of collisions before reaching the substrate depends on the mean free path defined by the pressure and the distance between target and substrate. Therefore, the increase of the scattering will be easily noticed for a target located far from the substrate, i.e. the Y target located at 240 mm. This explains that the deposition rate decreases more for the Zr side as compared to the Y side.

The bottom panels of Figure 5.2 (c and d) show the sample thickness as a function of the discharge current of the Y target and the deposition time. Evidently, the sample thickness increases with time and current. Therefore, it is more interesting to analyze the data in another way, i.e. to study the deposition rate as a function of the substrate position. The deposition rate as a function of the deposition time is shown in Figure 5.3a. It is clear that the deposition rate remains constant, which is an important conclusion as it shows the stability and reproducibility of the process. In Figure 5.3b, the deposition rate as a function of the discharge current (or power) is shown. An almost linear increase of the deposition rate is noticed as a function of the applied power (or used current). The slope of the fitted line decreases as a function of the position on the substrate, i.e. a higher slope is found for a point closer to the Y target.

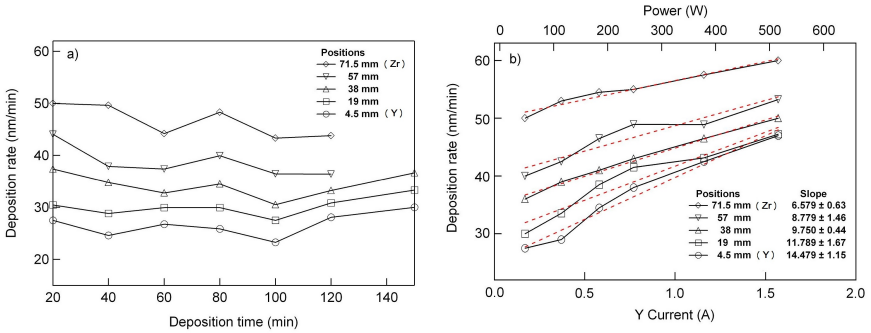

Figure 5.3: The deposition rate is evaluated at several positions on the substrate when changing: a) deposition time and b) current.

The choice for dual reactive magnetron sputtering in this work is based on the flexibility to change the composition. This is illustrated in Figure 5.4, showing the

Y metal ratio as a function of the same deposition conditions as discussed above. The metal ratio, defined as the percentage of Y on the total number of metal atoms in the film, was obtained by SEM-EDX.

As expected, a higher Y content is noticed at shorter Y T-S distances and higher Y current. From the schematic drawing shown in Figure 5.1, the overall trend of the Y content can be understood. Closer to the Y target, the Y content is higher as the path between target and substrate is shorter. When changing the T-S distance, the composition at the Y side of the substrate changes more as compared to the Zr side. As discussed for the thickness measurements (see above), this behavior can be understood from the higher power on the Zr target, and therefore the composition is dominated by the flux of Zr atoms.

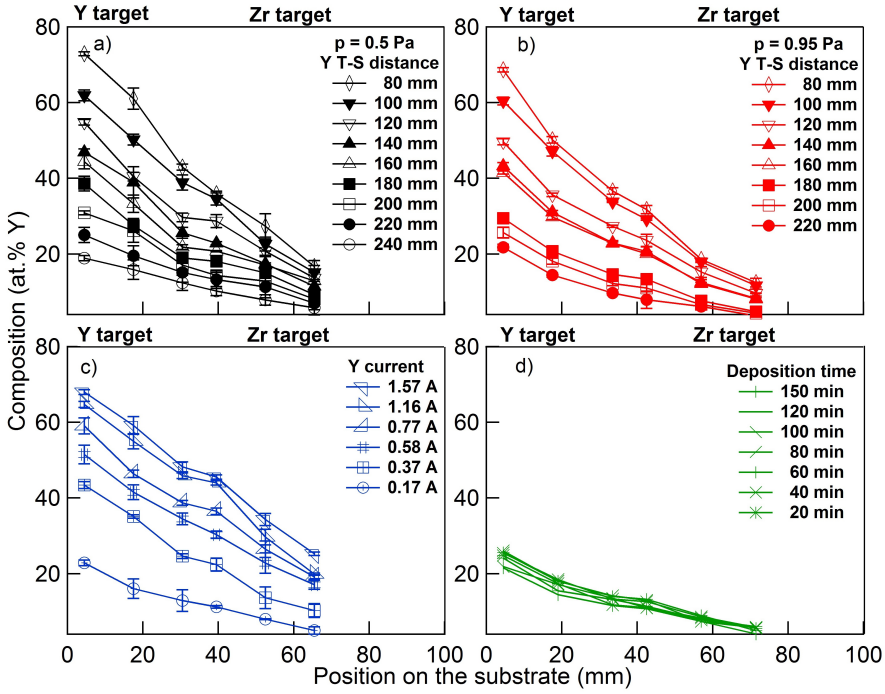

Figure 5.4: Composition as a function of the position on the substrate when a) changing Y T-S distance at 0.5 Pa; b) changing Y T-S distance at 0.95 Pa; c) Y target current at 0.5 Pa, and d) deposition time at 0.5 Pa. Both plots c) and d) are deposited at a fixed Y T-S distance of 240 mm. For the experiments as a function of the deposition time, the current was fixed at 0.2 A.

The same effect can be seen at high pressure, Figure 5.4b. Although the values of the Y content decrease little with the increase of pressure, the total

compositional variation is not the same, i.e. the slope is different at high pressure when compared to the results of Figure 5.4a. This can be related to the decrease in voltage and the increase in scattering. The effect of the pressure is mainly due to the lowering of the discharge voltage at higher pressures [171, 183, 223, 224], reducing the sputter yield of the target material.

Important in the context of this work, is the reproducibility of the composition. Figure 5.4d shows the composition measured under the same conditions, but for different deposition times. Clearly, the variation of the composition is small when comparing one deposition series with another.

Combining the latter results, with the results for the low pressure experiments at a Y T-S distance of 240 mm, and the results of the current experiment at 0.2 A, it is possible to quantify the error on the composition. Figure 5.5 shows in (a) the comparison between the compositions of three experiments at 0.2 A and (b) the relative error, i.e. the ratio of the absolute error to the measured compositional value for each position on the substrate. Figure 5.5b indicates that the relative errors show only little variation with the position on the substrate. In average, for the three plots shown in Figure 5.5b, the relative error is 12 %.

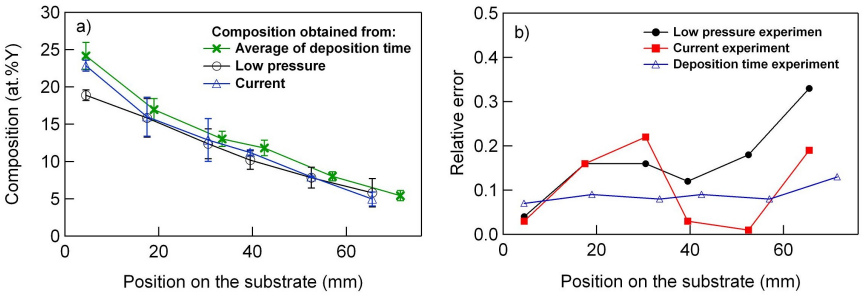

Figure 5.5: a) Comparison between the compositions obtained when deposition time, pressure and current are changed; b) Relative error as a function of the position on the substrate.

The deposition conditions have also an influence on the grain size and on the lattice parameter. For each sample an XRD pattern was measured in Bragg-Brentano configuration. A full discussion of these XRD pattern will be treated in Part III (5.3). In this part we focus on the grain size and the lattice parameter which can be retrieved from these XRD diffractions. Indeed, the mean grain size (κ) can be calculated from the Debye-Scherrer equation, [225,226] using the full width at half maximum and the θ angle of the diffraction peaks obtained via XRD. The Debye-Scherrer equation is given by:

$$\kappa = \frac{K\lambda}{B\cos\theta} \tag{5.1}$$

where K is a shape factor of the average grain (0.9), λ is the X-ray wavelength of the X-ray source Cu Kα (1.5406 Å), B is the full width at half maximum of the diffraction peak in radians equivalent to the height half-way between background and the peak maximum and θ is the respective Bragg angle. This equation suggests that a narrower diffraction peak results in a larger grain size. The analysis was performed using the (200) Bragg reflection. Since the [200] is the preferred orientation of the YSZ films, the measured grain size represents the grain size in the perpendicular direction [227]. The analysis was repeated for the (111) Bragg reflection, and the comparison between both analyses is discussed later in this chapter.

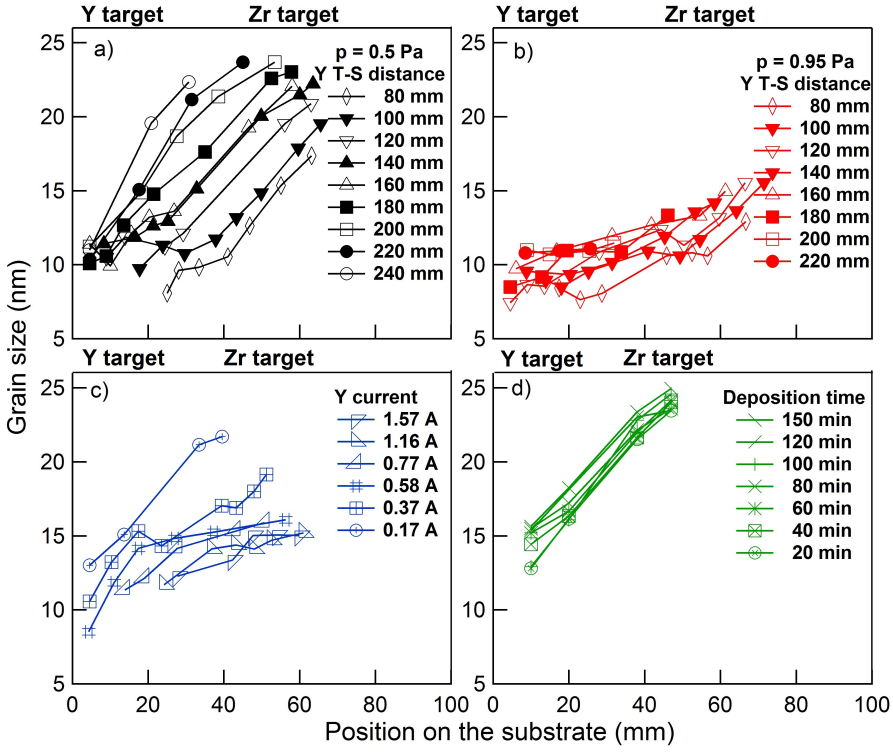

Figure 5.6: Grain size as a function of the position on the substrate for the following deposition conditions: a) Y T-S distance at 0.5 Pa; b) Y T-S distance at 0.95 Pa; c) current at 0.5 Pa and d) deposition time at 0.5 Pa.

The lattice parameter of YSZ is calculated using Bragg's law. In this way, the

length of the cubic unit cell can be quantitatively determined [228]. The lattice parameter of a reflection *hkl* was obtained using the θ-values of the XRD data as described in [71, 229]. The equation to calculate the lattice parameter is given by:

$$a = \frac{n\lambda(h^2 + k^2 + l^2)^{\frac{1}{2}}}{2\sin\theta} \tag{5.2}$$

where, a is the lattice parameter, n is the order of diffraction, λ is the wavelength of the incident wave Cu Kα (1.5406 Å), *hkl* are the Miller indices of the orientation and θ is the angle between the incident ray and the scattering planes.

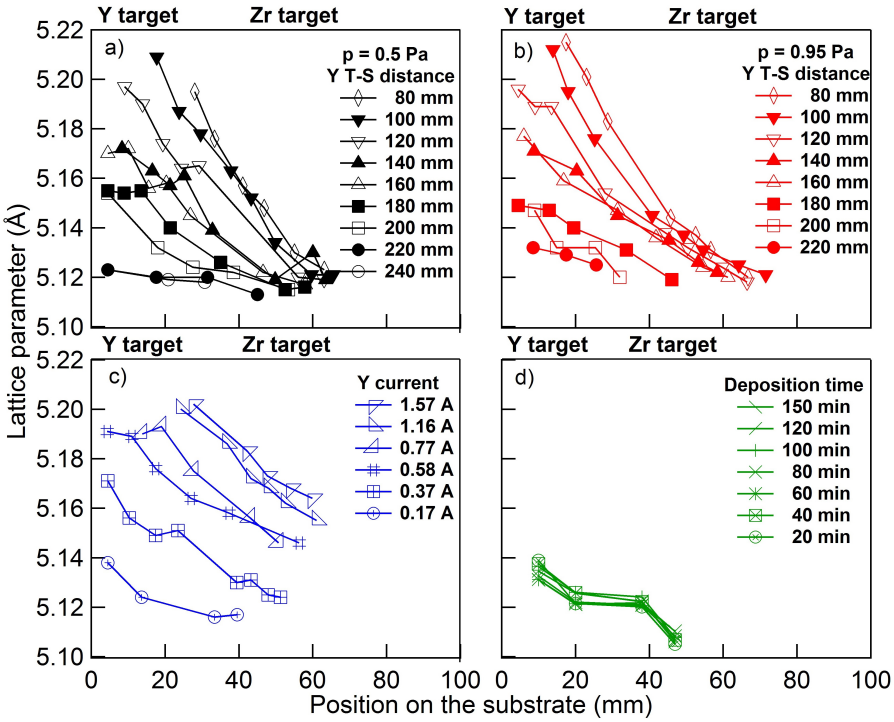

Figure 5.7: Lattice parameter as a function of the position on the substrate for the following deposition conditions: a) Y T-S distance at 0.5 Pa; b) Y T-S distance at 0.95 Pa; c) current at 0.5 Pa and d) deposition time at 0.5 Pa.

The obtained grain size from equation 5.1 as a function of the position on the substrate, lead us to the results displayed in Figure 5.6. In general we observe that the grain size increases along the sample substrate at a fixed Y T-S distance, being smaller in the regions enriched with Y and larger in the regions rich in Zr.

Comparison between the experiments performed at low pressure (Figure 5.6a) and at high pressure (Figure 5.6b) shows that the pressure has a strong influence on the grain size. Nevertheless, also at high pressure, the grain size increases when moving from the Y side to the Zr side of the substrate. Figure 5.6c shows the grain size at different position on the substrate as a function of the current, indicating an increase of the grain size as a function of both current and position on the substrate. For sake of completeness, Figure 5.6d shows the grain size as a function of the deposition time. Despite of the strong variation in thickness (see Figure 5.2d), the variation of the grain size is small which agrees with the fact that the film grows in zone T and therefore no competition in the grain, allowing its growth, is expected.

The plot of the lattice parameter as a function of the deposition conditions is displayed in Figure 5.7. The lattice parameter decreases with the increase of the position on the substrate and current as well as with the increase of Y T-S distance. The lattice parameter as a function of the pressure (see Figure 5.7a and b) indicates a similar reduction in values at a specific Y T-S distance. The main difference between both is the inclination of this reduction, which seems to be stronger at higher pressures. This can be associated to the thickness or to the Y content which are both smaller than the ones found at lower pressure. As displayed in Figure 5.7c, the increase of current leads to a proportional increase of the lattice. Again the good reproducibility is illustrated in Figure 5.7d.

5.1.2 Relations between deposition conditions and YSZ characteristics

From the results shown in the previous paragraphs (see Figure 5.2, 5.4, 5.6 and 5.7), it is clear that the deposition time only affects the film thickness, but has no influence on the composition, grain size and lattice parameter. This leaves us with 3 deposition parameters affecting the composition, grain size and film thickness. These film properties do vary along the substrate due to the dual magnetron configuration. Apart from the possible influence of the deposition parameters on the film properties, it can be expected that some of these properties are interconnected. For example, a change of the film composition will affect the lattice parameter. It is therefore necessary to distinguish between trends originating from interconnected film properties and trends resulting from deposition conditions. With this goal, it is instructive to re-analyze the data in several ways. A first approach is to plot the film properties not as a function of the position along the substrate, but as a function of the deposition conditions for fixed substrate positions. The result of this approach is shown in Figure 5.8.

For larger Y T-S distances the Y content, the film thickness and the lattice parameter decrease while the grain size increases. The effect of the T-S distance on the thickness is quite small. Comparing the experiments at low and high

pressure the following conclusions can be drawn. At higher pressure the values of the studied film characteristics are smaller and/or the variation as a function of the Y T-S distances is reduced. Current affects the composition, thickness and lattice parameter by increasing their values when Y T-S distance increases. On the contrary, the grain size decreases with the increase of Y T-S distance.

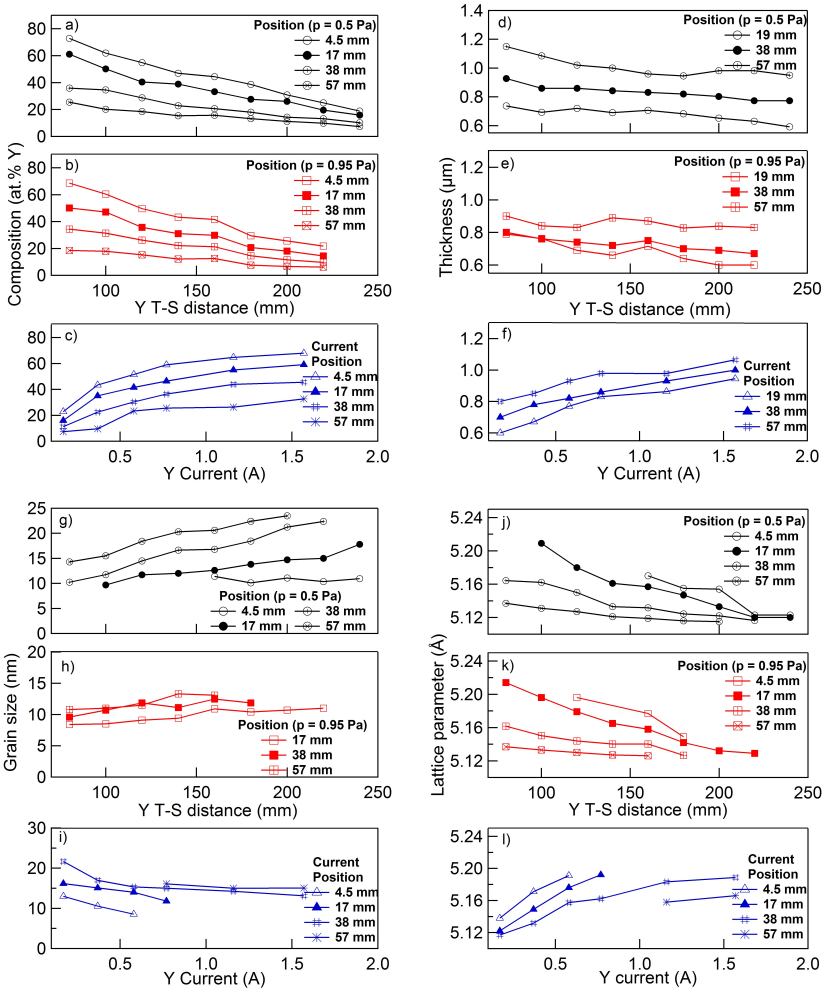

Figure 5.8: Composition, thickness, grain size and lattice parameter variation at a fixed position on the substrate as a function of: a;d;g;j) Y T-S distance at low pressure; b;e;h;k) Y T-S distance at high pressure; c;f;i;l) current at low pressure.

An alternative approach, to analyze the influence of the different deposition

conditions, is to study the trends for a fixed film thickness. The results in Figure 5.9 indicate the same trends as shown in Figure 5.8. From the presentation of the results in section 5.1.1, it was clear that the film thickness does not affect the lattice parameter, composition and grain size. The analysis discussed here allows concluding that the observed trends are the result of an implicit relationship between the different film properties. Indeed, to change the film thickness at a fixed deposition parameter, it is necessary to select a different position on the substrate, which affects the composition.

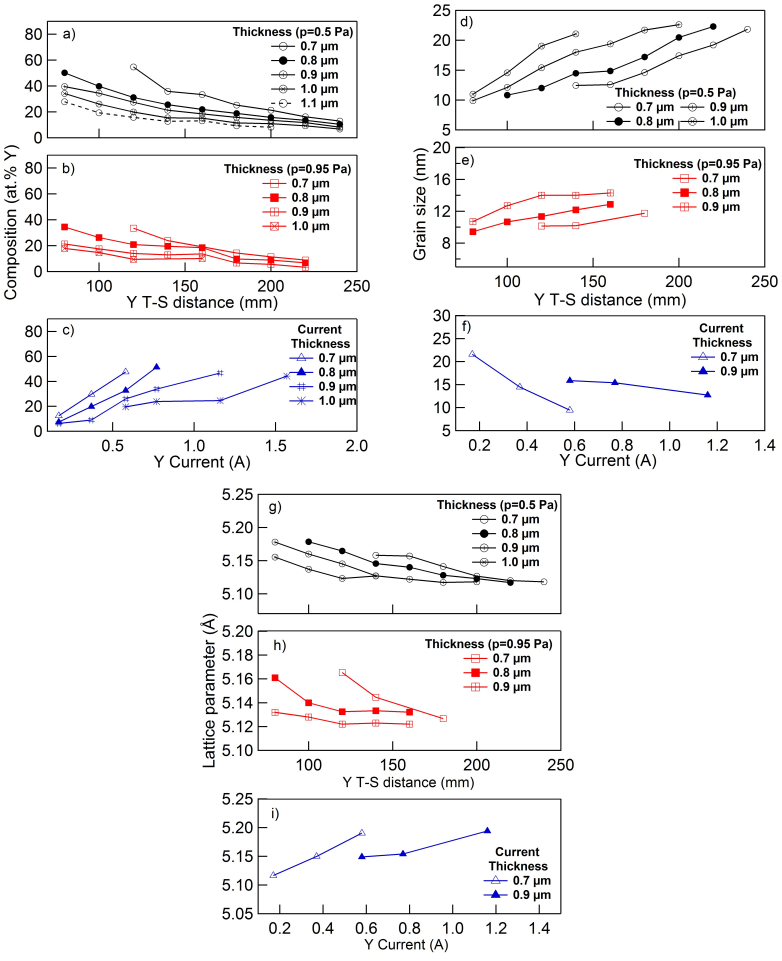

Figure 5.9: Composition, grain size and lattice parameter variation at a fixed thickness as a function of: a;d;g) Y T-S distance at low pressure; b;e;h) Y T-S distance at high pressure; c;f;i) current at low pressure.

The last approach is a plot (see Figure 5.10) of the behavior of thickness, grain size and lattice parameter as a function of the deposition conditions at a fixed composition (15, 20, 30, 40 and 50 at.%Y). In Figures 5.10f and i only three and two compositions are considered because other compositions would not allow us to have enough points to observe a trend.

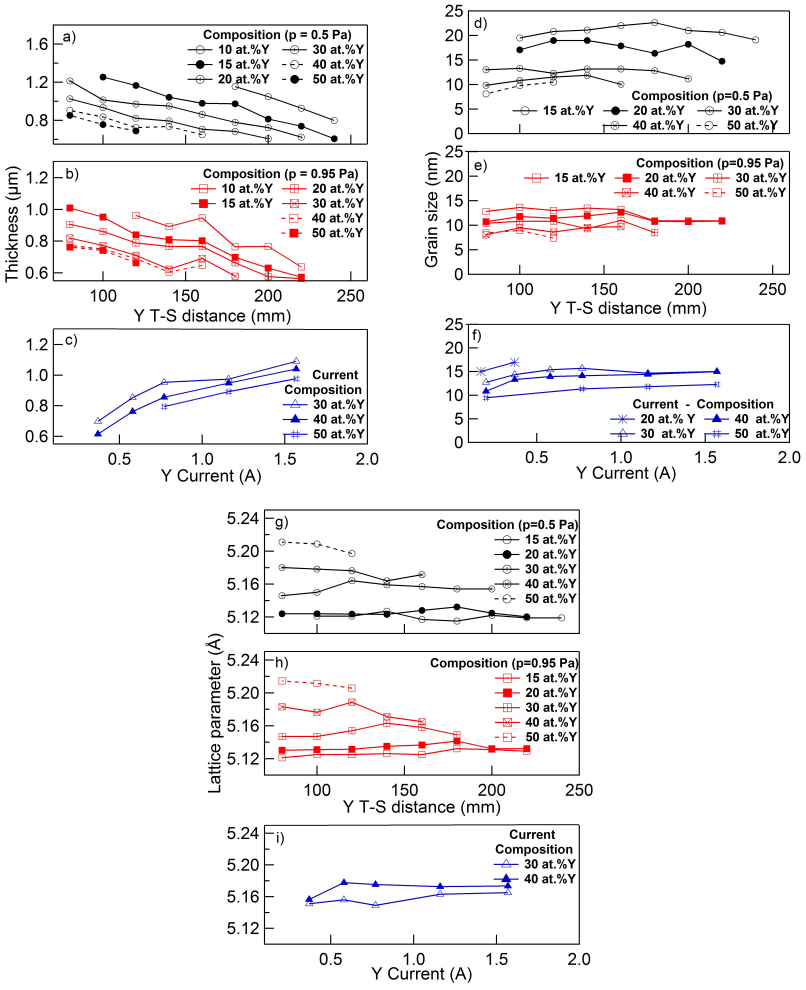

Figure 5.10: Grain size and lattice parameter at a fixed composition as a function of: a;d;g) Y T-S distance at low pressure; b;e;h) Y T-S distance at high pressure and c;f;i) current at low pressure.

Figure 5.10a to c shows the variation of the thickness for fixed composition.

As stated before, this result finds its origin in the implicit relationship between film thickness and composition, and is therefore not a real trend. More important are Figures 5.10d to i. When plotting the grain size and the lattice parameter as a function of the T-S for fixed compositions, we obtain a constant value for both grain size and lattice parameter as a function of Y T-S distance. The values for the grain size are smaller at higher pressure. However, it remains constant with the variation of Y T-S distance. For the discharge current the overall effect is quite small, and perhaps not significant. So, at constant pressure and discharge current, only the composition of the YSZ thin film is crucial to the definition of the lattice parameter and the grain size.

The above conclusion is important as it proves that dual reactive magnetron sputtering, without substrate rotation, allows to study the influence of the composition on the YSZ thin film properties and the compositional gradient on the sample without hidden effects of T-S distance on the studied film properties (grain size and lattice parameter).

5.1.3 Grain size and lattice parameter as a function of composition

Based on the conclusions given above, we will study in this section the effect of pressure and current on the relationship between grain size and composition. As the lattice parameter is only affected by the composition, it is possible to summarize all results in one overview plot, and make a full analysis of the data.

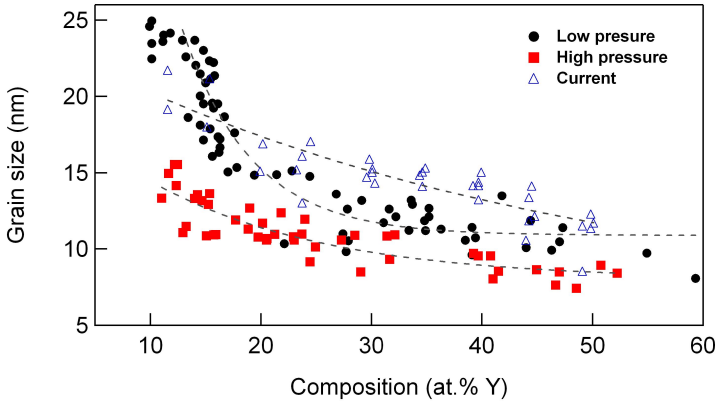

Figure 5.11: The average grain size of YSZ thin films as a function of the Y content for different deposition conditions. The fit corresponds to an exponential decay behavior.

Figure 5.11 shows the grain size as a function of the composition. This graph

shows that the grain size decreases exponentially with the increase of Y content, independent of Y T-S distance and current.

The equations ruling the exponential behavior as a function of composition are: Low pressure:

$$\kappa = 10.891 + 104.21exp(-0.158C) \tag{5.3}$$

High pressure:

$$\kappa = 7.983 + 12.277exp(-0.064C) \tag{5.4}$$

Current:

$$\kappa = 5.479 + 18.313exp(-0.0215C) \tag{5.5}$$

where C is the composition given in at.% of Y. These equations are a simple exponential fit of the results of Figure 5.11 and they will be used in Chapter 6, where the value of the grain size at different compositions is needed.

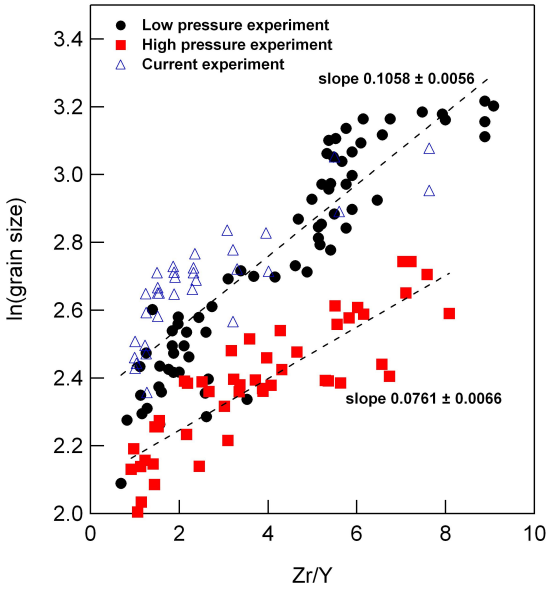

Figure 5.12: Natural logarithm of the grain size varying as a function of the ratio between Zr and Y. Note the two similar trends indicating the influence of the pressure on the results.

An assumption for the exponential reduction of the grain size can be explained by Y acting as a dopant (behaving as an impurity on the structure). As a consequence, high content of Y inhibits the mobility during growth hindering the grain to grow. In the work of Boulouz [128] a similar behavior was discussed, stating that the decrease can be explained by Y acting as an inhibitor on the surface

mobility of the Zr adatoms. To study this effect in more detail the following reasoning was followed.

If Y is acting as an inhibitor, the metal ratio is not a good measure for its effect because the addition of Y does not vary linearly. Indeed, for a metal ratio of 10 at.%, one Y atom can affect 9 Zr atoms, or a ratio of 9/1, while for 20 at.% there are 2 Y atoms for each 8 Zr atoms, resulting in a ratio of 4/1. Therefore, the (natural logarithm of the) grain size is plotted as a function of the Zr/Y ratio as shown in Figure 5.12. As the effect of the discharge current on the grain size is small, and as these experiments are performed at low pressure (0.5 Pa), the data of both experiments were treated together for the linear fit. Comparing the slope for the high and low pressure experiments, an almost equal behavior is noticed. This indicates that the compositional influence of the grain size is for both experiments the same. The difference between the low and high pressure experiment can be explained from the lower energy at high pressure of the sputtered atoms when arriving at the substrate [135, 227].

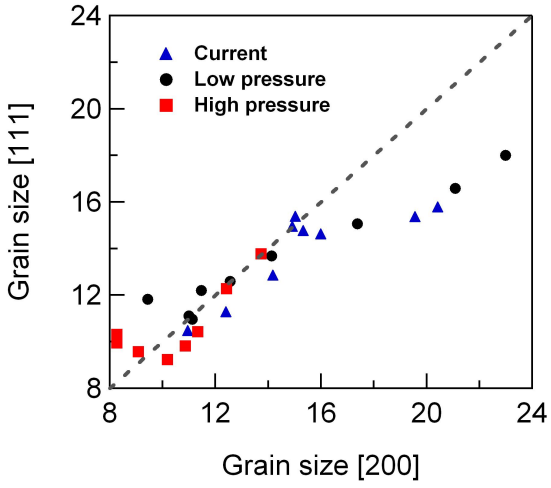

Figure 5.13: Comparison between the grain sizes obtained in the [200] and [111] direction at a) low pressure; b) high pressure and c) different currents.

Important in this context is the determination of the grain size which is based on the use of one crystallographic orientation, i.e. the [200]. To exclude any possible effect of the analysis, the analysis was repeated for the [111] direction. The 1:1 relation between the grains in the [111] and [200] direction are given in Figure 5.13. Note that for all deposition conditions, the grains are equivalent in the region of low grains values (or high content of Y), indicating that the fractions of [200] and [111] are significant to calculate the grain size. On the other hand,

for large grains there is a discrepancy in the 1:1 relation which can be attributed to a broadening of the intensity peak in the [111] direction since the grain are [200] preferential oriented, as it will be discussed in Part III (5.3). As a result, the comparison between both measurements suggests the use of the [200] direction to determine the grain.

One might wonder about the presence of microstrains in these YSZ thin films due to the large range of composition and thus lattice spacing gradient. This effect would induce a broadening of the XRD peak, and consequently the values calculated above for the grain size could be erroneous. In order to determine if the microstrains affect significantly these films, resulting in different grain sizes, an analysis based on the use of a Voigt function [230] was performed for the samples with different discharge currents. Results indicate that the contribution of microstrains is small. As a result, the difference between the obtained grain size with and without microstrain is not significant. Therefore, it is possible to consider the values of the grain size exclusively from Debye-Scherrer equation as proposed above. Further details about the calculation of the grain size and microstrain can be found in Appendix B.

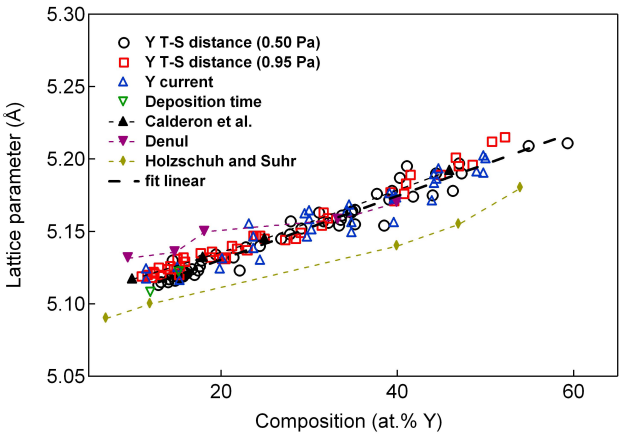

Figure 5.14: Lattice parameter of YSZ thin films obtained for several deposition conditions. The data follow a linear behavior and are in agreement with Vegard's law and literature.

The lattice parameter was also proved to be mainly influenced by composition and its plot for all deposition conditions is shown in Figure 5.14. Note that the lattice varies linearly with the increase of Y content. The linear trend observed in the graph follows the empirical rule of Vegard's law [7], which states that a linear relation between the lattice parameter and the concentration of the constituent

elements exists. In addition, the obtained lattice parameters are in agreement with the data obtained from literature [45, 50, 52, 128, 231–233]. In the work of Holzschuh and Suhr [50], for example, it was shown that the increase of Y content from 3.5 to 80 % causes the lattice parameter to increase from 5.08 to 5.27 Å. The smaller lattices encountered in their work is mainly to the deposition temperature of 500 °C which allows the growth of the grain size and consequently the decrease of the lattice parameter. Figure 5.14 shows the comparison between our results and the work of Holzschuh and Suhr [50], Denul [231] and Calderon et al. [233]. From these results we observe that independent of any deposition condition the change of the lattice is ruled by the content of Y in the film.

By analyzing the results displayed in Figure 5.14 we can affirm that:

- There is a linear trend between lattice parameter and composition being defined as:

$$a = (5.087 \pm 0.00189) + (0.0021 \pm 6.31 \times 10^{-5})C \tag{5.6}$$

  where the lattice parameter of the pure cubic ZrO_2 structure is 5.087 Å, in agreement with literature [50, 234]. The value of the slope 0.0021 identifies the difference in ionic radius between Y and Zr. The reported ionic radii are 0.9 Å (Y) and 0.72 Å (Zr) [235], giving a difference of 0.18 Å. Reminding that the composition in this linear equation is given in percentage, we have a slope of 0.21 which is very close to the difference in ionic radius between both elements. Moreover, the fit done for all points with different deposition conditions has an R-squared of 0.978, significant for 139 points.

- The absence of stress can be reviewed from the linear trend. Indeed, the first indication of strain is a deviation between measured data and the linear equation based on Vegard's law [236–238]. Based on the work of Janssen [239] about the development of stress in zone T growth, it is believed the existence of stress due to the insertion of a bigger ion in the zirconia lattice. However, since our plot shows a nice linear trend up to 60 at.% Y, another mechanism is considered to take place in order to relieve this compressive stress. More details about this mechanism will be given in Chapter 6.

5.1.4 Summary and conclusions of Part I

In Part I, it was shown how the deposition conditions affect the characteristics of the YSZ system. Target-substrate distance, pressure and current affect the YSZ characteristics in a specific manner. However, analyses of each deposition condition on the YSZ characteristics becomes complex to obtain due to the mutual dependence of the YSZ characteristics. A solution to the analyses is to fix thickness and composition in order to study each of these YSZ characteristics.

Thickness and composition were shown to be related, being mutually controlled. This means that a range of thickness can be deposited with a certain value of composition and vice-versa.

The grain size and lattice parameter were also shown to be influenced by the deposition conditions. However, this influence was identified to be directly related to the composition. By following an exponential decay we observed that grain size increases with the decrease of Y content. The Y in the lattice was suggested to act as a barrier inhibiting the growth of the crystallites. The same behavior was found either for the change of Y T-S distance, pressure or current. The data of the experiments with current were shown to be complimentary to the experiments at low pressure. The increase of pressure, on the other hand, presents smaller crystallites due to the lower energy of the sputtered atoms.

Following the same reasoning, the lattice parameter was also analyzed as a function of the composition. The YSZ system was demonstrated to have a linear trend with the increase of the Y content, which agrees with literature. Hence, our results agree with the empirical rule of Vegard's law in the whole region of composition, i.e. varying from contents of 10 up to 60 at% Y.

In Part I, we demonstrated that the composition can be tuned by changing the deposition conditions, confirming that magnetron sputtering is a flexible technique where the deposition conditions can easily be tuned to acquire the desired film. In addition, it was shown that DCMS presents good reproducibility. Another approach suggests the control of the composition value by using a simulation tool. In this way, no extra experimental measurement is necessary to determine a specific value. Therefore, Part II (5.2) describes how the tuning of the simulation tool agrees with our experimental results.

5.2 Part II: Comparison of experimental data to simulation results

The film thickness and the film composition depend on the number of yttrium and zirconium atoms which arrive at the substrate. The latter can be calculated by applying the so-called particle trajectory Monte Carlo code. This type of code follows a sputtered atom from the target towards the substrate, and describes the collision between the sputtered atom and the atoms present in the vacuum chamber. A home-built code, SIMTRA [240] was used to perform the simulations. These simulations have taken several assumptions in consideration likewise defined in [173]. The following assumptions are used in this part:

- The sputtered particles are neutral atoms in the ground state, traveling from the target to their final position;
- Their path is only affected by elastic collisions with the gas atoms;
- The gas is homogeneous and in thermal equilibrium with temperature;
- The interaction potential is defined by a Molière screening function.

Apart from the input of the deposition geometry, the initial conditions of the sputtered atom must be described. The starting point of the trajectory, i.e. the place of ejection of the sputtered atom, is sampled from the race track or the ion current distribution. These are sampled from the energy distribution and the angular distribution of the sputtered atoms. Especially the latter distribution is not well described in literature as it depends not only on the target/ion combination but also on the target surface condition as shown by Boydens et al. [241]. In this part, we will tune the angular distribution of sputtered Y and Zr atoms to reach the best fit between the simulated and the measured sample composition. The optimized angular distribution will be used to calculate the expected film thickness. However, the film thickness does not only depend on the number of arriving atoms, but also on the growth conditions which can induce porosity. The latter will be discussed in detail in this part.

5.2.1 Geometrical configuration

As discussed before, a dual reactive magnetron sputtering is used in this work. The position of the magnetrons in the framework of the vacuum chamber was accurately measured and implemented in SIMTRA. The chamber geometry, targets and substrate are shown in Figure 5.15.

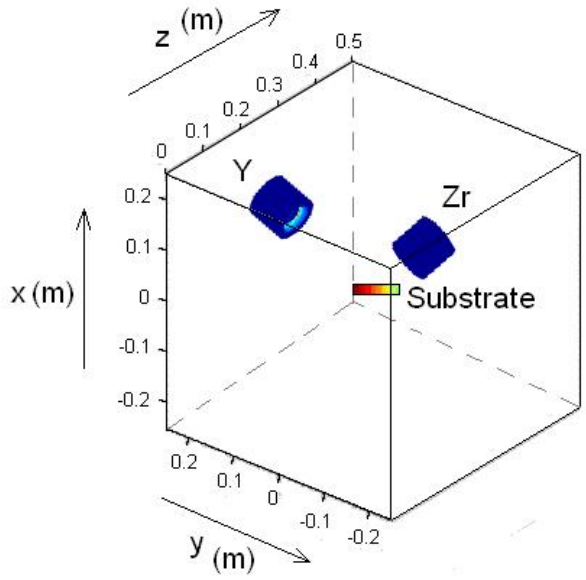

Figure 5.15: Chamber dimensions, targets and sample substrate defined for the simulations in SIMTRA.

5.2.2 Obtaining sample composition

The equation that allows determining the flux of metal atoms (F_M) arriving on the substrate is defined by:

$$F_M = I\gamma_M f_M \tag{5.7}$$

where I is the ion current, γ_M is the sputter yield of the metal and f_M is the metal fraction arriving on the substrate determined via simulations. In this section we will describe how these variables were obtained.

- The ion current (I): The amount of ions bombarding the target vary as a function of the discharge current and of the ion-induced secondary electron emission (ISEE) yield. The latter is defined by the number of secondary electrons emitted by the cathode per incident ion. The ISEE values are tabled and the respective values for Y and Zr are 0.178 and 0.121 [183]. The total number of incident ions is obtained from:

$$I = \frac{I_{dM}}{e(1 + ISEE_M)} \tag{5.8}$$

where I_{dM} is the discharge current of the metal and e is the electron charge.

- Sputter yield (γ_M): The sputter yield can be simulated or experimentally obtained. The experiments consist in determining the amount of material emitted during a certain period of time, which can take up to several hours. The value of the sputter yield is determined from the material loss prior and after deposition. The equation that describes the sputter yield obtained experimentally is given below:

$$\gamma_M = \frac{\#sputtered_{atoms}}{\#incident_{atoms}} = \frac{\Delta m N_A}{M_M} \frac{e(1 + ISEE)}{I_{dM}} \tag{5.9}$$

  where Δm is the difference in mass, M_M is the molar mass of the metal and N_A is the Avogadro's constant. The number of incident ions is obtained from equation 5.8.

  The sputter yield used in this work follows the experimental data shown in Figure 2.6, Chapter 2.

- Fractions of Y and Zr (f_M): The fractions (f_M) of both metals are obtained via SIMTRA. When both fluxes f_{Zr} and f_Y are known, it is possible to calculate the metal fraction or the sample composition as

$$Composition = \frac{f_Y}{f_{Zr} + f_Y} \tag{5.10}$$

5.2.3 Optimizing the simulations

As stated before the simulations were optimized through a change of the angular distribution of the sputtered atoms. In a first series of simulations, both the energy distribution and the angular distribution were taken from SRIM [169]. In SRIM the angular distribution follows a cosine distribution.

Two simulations using SIMTRA are performed to obtain the fractions of Y and Zr. SIMTRA allows the simulation of only one target as source. That is why, the first simulation considers the Y target as the source (sputtered particles) and the Zr target as an object. In the second simulation Zr is considered as a source. For each of these simulations 10^6 particles were simulated. Note that each Y T-S distance requires a new simulation either for Y and Zr. Although the Zr T-S distance remains fixed, we repeated the simulation changing the Y T-S distance of the object (Y target). The simulated fractions for Y and Zr are given in Figure 5.16. This figure shows that the fraction of Y increases with the decrease of Y T-S distance, as expected from the experimental results. The fraction of Zr is invariable, being independent of the Y T-S distance of the object. This let us conclude that the position of the Y as an object does not influence the Zr deposition distribution.

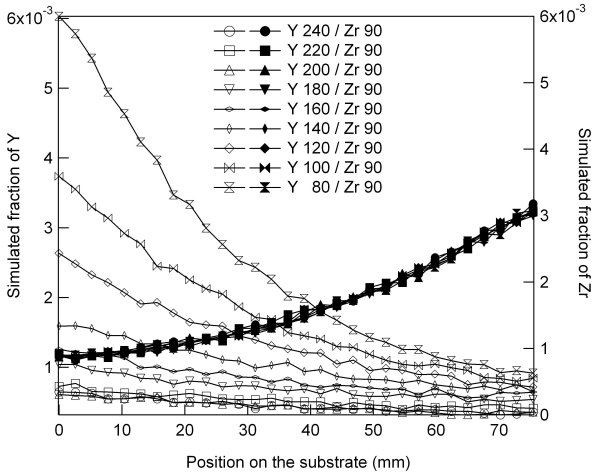

Figure 5.16: Fraction variation of Y and Zr simulated via SIMTRA along a full glass substrate.

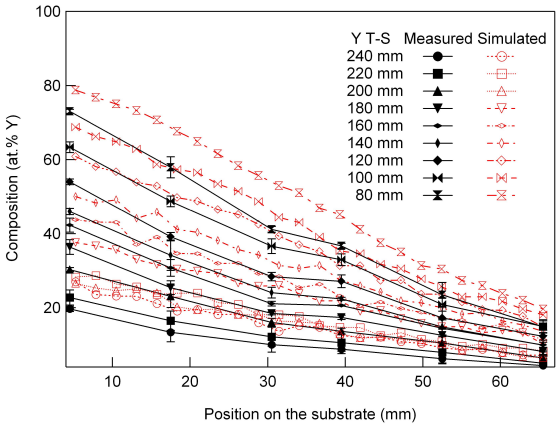

Figure 5.17: Comparison between compositions obtained experimentally and simulated using a cosine angular distribution.

The Y compositional variation is illustrated in Figure 5.17. In this plot the measured data is given by the closed markers and full lines while the simulated data is indicated by the open markers and dashed lines. The same symbols were used for a given Y T-S distance. Initially, it is observed that the relation between experimental and simulated data is acceptable since the trends are very similar. However, there are two factors which inhibit the use of this simulated data. First,

the maximum quantitative error obtained between both data is rather large. The average percentage error is calculated by taking the average of the difference between all measured and simulated composition divided by the simulated data. Using a cosine angular distribution the average error is 18 %, which is rather big for an ideal fit. Second, it is noticeable that the values between simulated and experimental differs by a Y T-S distance, i.e. the simulated data of a certain Y T-S distance agrees with a higher Y T-S distance of the experimental data, indicating that the fit between both results is not ideal. A way of solving the difference between measured and simulated data involves the modification of the angular distribution. This approach will be discussed below.

In order to improve the fitting between measured composition data and simulation, the angular distribution of both Y and Zr were changed. The angular distribution has been already introduced in section 2.2, Chapter 2. This distribution is dependent on the angle of incidence, the ratio between the masses of the ion and target and the incident energy which varies its shape [166, 167, 242]. If the incident energy is low, the particles are ejected in an under-cosine (or heart-shape) type, while if the incident energy is high, the particles are ejected in an over-cosine shape. The target morphology which is dependent on the sputtering yield of the material also contributes to the modification of the angular distribution [241]. The equation proposed by Yamamura et al. [242] to describe the angular distribution is given by:

$$s(\theta) = \cos\theta(1 + B\cos^2\theta) \tag{5.11}$$

where B is the fitting parameter and θ is the ejection angle. The analytical equation to describe the angular distribution in SIMTRA is proportional to [173]:

$$s(\theta) \propto \sum_{i=0}^{5} c_i \cos^i\theta \tag{5.12}$$

where c_i are fitting parameters which can be defined in SIMTRA. In order to see the effect of the angular distribution in our compositional variation we simulate the transport of particles with different angular distributions using the model of Yamamura. In SIMTRA c0 to c5 are user defined, in our simulations c0, c2, c4 and c5 equals to 0 while c1 = 1 and c3 is variable. The B in equation 5.11 corresponds to c3 in SIMTRA. The c3 parameter is varied from -2 to 2 in intervals of 0.5 for the simulations changing Y T-S distance as well as the simulations changing Zr T-S distance. Therefore, at this point SRIM is no longer used and instead we use the energy distribution of Thompson [163].

The composition of the YSZ film is simulated for each pair of c3 parameter [$c3_Y$, $c3_{Zr}$]. The ideal fit occurs when the comparison between experimental and simulated data is equal. We can compare the results by calculating the area between both curves, i.e. a curve for the resultant equation of the experimental

and simulated results and another curve for the ideal case (a 1:1 relation where y = x). The function describing the comparison between both data is defined by a linear trend, i.e. y = ax + b. The error between the simulated and experimental data is obtained by considering the difference in area of both functions divided by the maximum composition (M). A schematic drawing of these areas is illustrated in Figure 5.18.

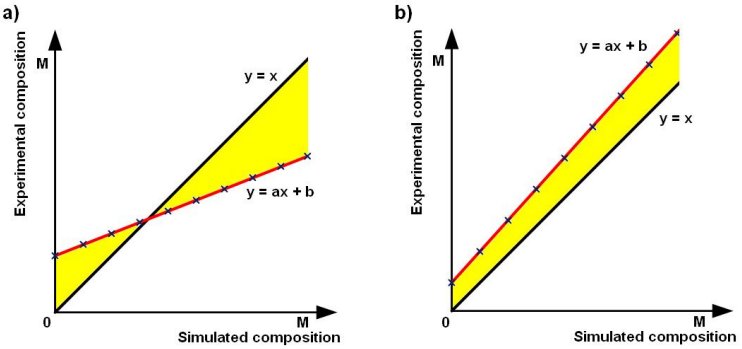

Figure 5.18: Areas defined by a 1:1 function and a linear function of the experimental and simulated data. Situation (a) illustrates an interception between both functions while (b) illustrates no interception.

Figure 5.18a shows the situation where the interception between both functions occurs within the composition range defined by 0 to M, i.e. when y = b/(1-a). Under these conditions the error is calculated using the equation below:

$$Error = \frac{\int_0^{b/(1-a)}(ax+b)dx - \int_0^{b/(1-a)} xdx + \int_{b/(1-a)}^{M} xdx - \int_{b/(1-a)}^{M}(ax+b)dx}{M} \tag{5.13}$$

In the situation illustrated in Figure 5.18b, the error is simply obtained by the difference of the areas of both functions, given as:

$$Error = \frac{\int_0^{M}(ax+b)dx - \int_0^{M} xdx}{M} \tag{5.14}$$

From these results, a [9,9] matrix is created. If the fit is ideal, the difference in area is null. Therefore, very low values in the matrix represent the best fit between experimental and simulated results. The matrix is plot in a contour plot as illustrated in Figure 5.19. For better visualization of the data, the matrix is plot in logarithmic scale. The contour plot suggests that there are two regions of minimum corresponding to [$c3_Y$, $c3_{Zr}$] equal to (-0.5,0) and (-0.5,2). A negative value of c3

indicates that the angular distribution has a heart-shape, while a positive c3 value is characteristic of an over-cosine distribution. Therefore, these results suggest that the angular distribution of Y has a heart-shape while the angular distribution of Zr follows either a cosine or an over-cosine form.

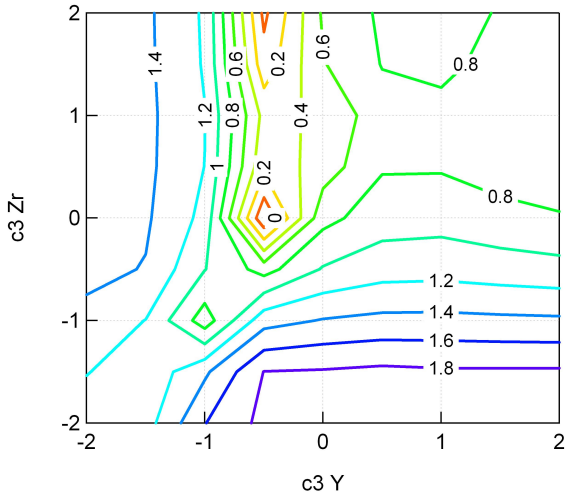

Figure 5.19: Contour plot of the c3 constant values varying from -2 to 2 in intervals of 0.5 either for simulations with Y and Zr. The regions of minimum indicate the best fit between experimental and simulated data.

In order to improve the simulation, we can also add the effect of re-deposition, i.e. consider the amount of Y sputtered present on the Zr target and vice-versa. Therefore, simulations with SIMTRA are repeated. We considered that Y particles are emitted from the Zr target under the conditions of the Zr target (Zr T-S distance and current). Analogously, the amount of Zr being emitted from the Y target is considered under the conditions of the Y target. Then, the new fractions of re-deposited Y and Zr are calculated and added to the fractions of the emitted Y and Zr. Next, the [9,9] matrix is obtained and displayed in a contour plot. The contribution of re-deposition on the contour plot is illustrated in Figure 5.20. Note that the region of minimum is the same as shown in Figure 5.19 and therefore it is possible to conclude that the effect of re-deposition on the simulation does not affect the results.

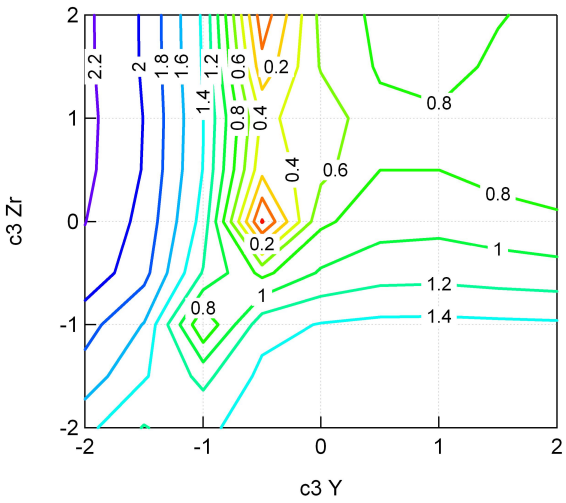

Figure 5.20: Contour plot of the c3 constant values varying from -2 to 2 in intervals of 0.5 either for simulations with Y and Zr. In this plot the re-deposited particles are taking into consideration in the simulation.

Another approach involves the change of the target positions on the simulations, i.e. the Y target substitutes the position of the Zr target and vice-versa. As the chamber is considered to be symmetric, no difference between the values of the contour plot should be seen. The geometric values to be added in SIMTRA are not copied from the original simulation input but they are once more measured from the chamber. Thereon the simulations are repeated changing the parameter c3 of the angular distribution with the same intervals mentioned above (from -2 to 2, in intervals of 0.5). The contour plot for this configuration is given in Figure 5.21a. This plot indicates only one minimum at (-0.5,1) indicating the best fit between experimental and simulated data. However, the region of minimum fits exactly between the two minimum indicated in Figure 5.19, suggesting that the best fit should be encountered in this region. Besides, it is also an indication of the chamber symmetry since the change of the target position leads to the same region of minimum. If we combine both images (Figure 5.19 and 5.21a) by taking their average, it is possible to observe the region of minimum deviation. This representation is illustrated in Figure 5.21b. Note that the region of minimum deviation is delimited by a fixed c3 value for Y and a certain range of c3 for Zr. This indicates that the fit between measured and simulated is strongly affected by the change on Y T-S distance and therefore a specific c3 is necessary to have a good fit of the data. On the other hand, since the Zr T-S distance remains constant, a variation of its c3 parameter leads to the same result, being less

sensitive to the change of $c3_{Zr}$. Therefore, considering the c3 values obtained, it is concluded that the Y target has a heart-shape distribution ($c3_Y$ = -0.5), while for Zr target the angular distribution varies from a cosine to an over-cosine distribution ($c3_{Zr}$ = 0 → 2).

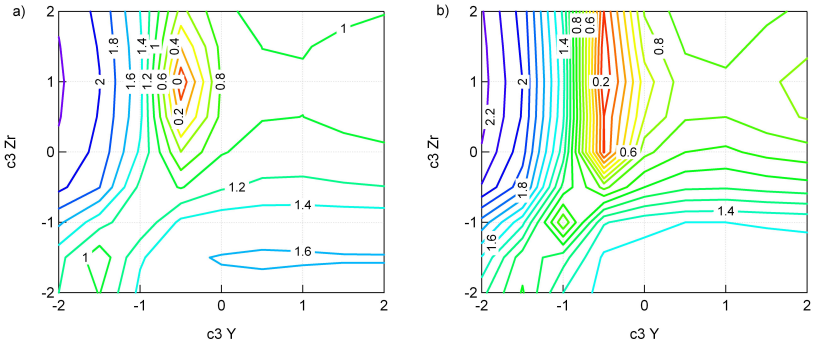

Figure 5.21: Contour plot of the c3 constant values varying from -2 to 2 in intervals of 0.5. a) On this simulation the position of Y and Zr on the simulated chamber are changed. The region of minimum indicates the best fit between experimental and simulated data. b) Contour plot resultant of the combination between both simulations (without and with inversion of targets). The region of minimum is delimited by a fix $c3_Y$ value (-0.5) and a variable $c3_{Zr}$ (from 0 to 2).

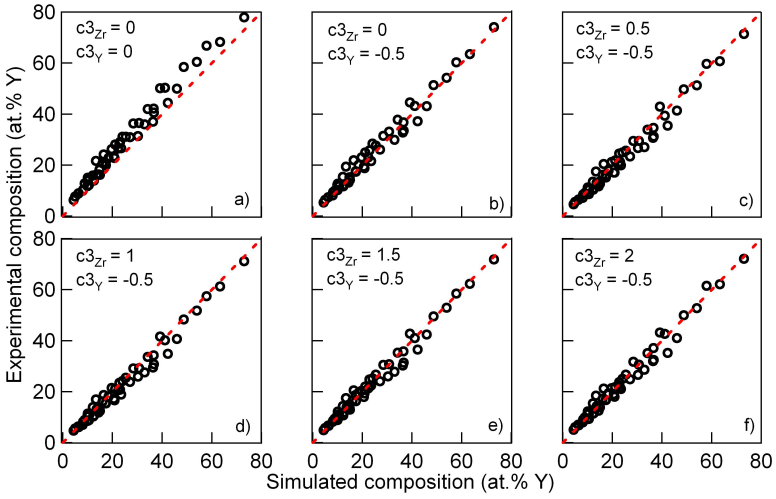

Figure 5.22: Comparison between experimental and simulated composition for [$c3_Y$,$c3_{Zr}$]: a) (0.0); b) (-0.5,0); c) (-0.5,0.5); d) (-0.5,1); e) (-0.5,1.5) and f) (-0.5,2).

The best fits between experiment and simulation are shown in Figure 5.22 together with the SRIM results (Figure 5.22a). These results confirm that the angular distribution obtained via SRIM does not match the simulated and experimental results and therefore the tune of the c3 parameters via SIMTRA becomes necessary.

As pressure and current influence the discharge voltage, a possible change of the angular distribution could be expected. However, the effect of both parameters on the discharge voltage is, under the given conditions, quite small. Nevertheless the effect of both parameters on the fitting procedure was investigated. Figure 5.23a shows the results of the optimization for the current experiments in the interval of -2 to 2, while Figure 5.23b shows the optimization for the high pressure experiments in the interval from -1 to 1. As can be concluded by comparing these results with the results in Figure 5.19, 5.20 or 5.21 a minimum is found at the same values of c3.

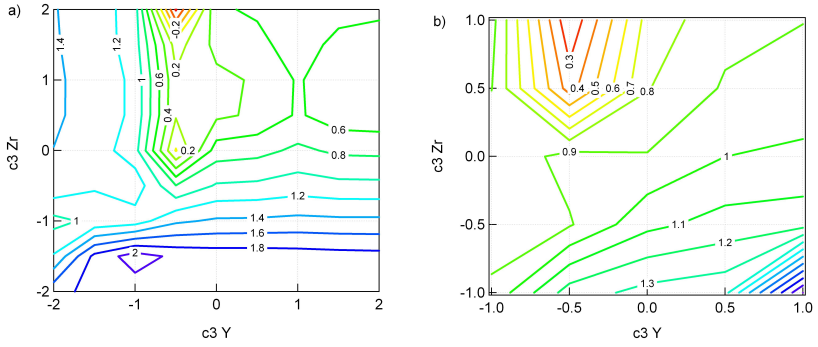

Figure 5.23: Contour plot showing the c3 parameter variation in Y and Zr under certain conditions: a) changing discharge current and b) high pressure.

It is clear from the above analysis, that there is no statistically significant difference between the results within the defined minimum. Therefore, we have selected for further discussion the values (-0.5,0) for the c3 parameters in the simulations. For sake of completeness, the simulated and the experimental composition for the low pressure experiment is shown in Figure 5.24. Despite the small differences between some of the data points, the trend is good, and allows to predict the composition at any point on the substrate at any Y T-S distance without further experimental work. The systematic deviation encountered at small positions on the substrate and higher Y T-S distance can be associated to the mean free path between Y target and substrate. The measured Y contents present smaller values, indicating that the particles are deviated and spread away from the substrate. For larger positions on the substrate this influence is barely noticed

because of the short Zr T-S distance. The same occurs at shorter Y T-S distance. Using the simulated composition the film thickness can be calculated.

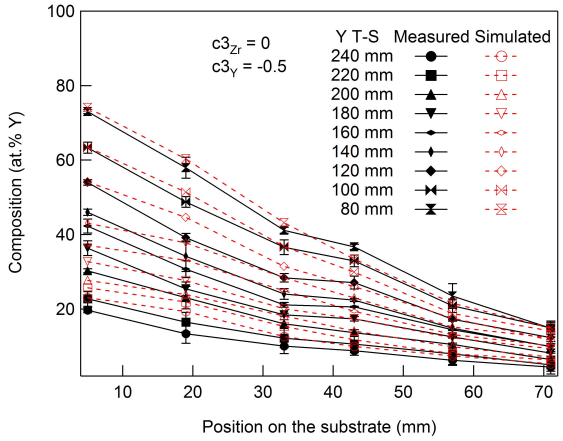

Figure 5.24: Comparison between compositions obtained experimentally and simulated with an angular distribution defined by $c3_Y$ = -0.5 and $c3_{Zr}$ = 0.

5.2.4 Obtaining thickness and porosity based on SIMTRA

Based on the flux of both Y and Zr, it is possible to calculate the deposition rate and consequently to obtain the simulated film thickness. The deposition rate can be quantified from the sputtering yield and the incident ions rate [168]. The simplified equation is given below:

$$d_{rate} = \frac{(f_{Zr} + f_Y) M_{YSZ}}{\rho_{YSZ} N_A} \tag{5.15}$$

where M_{YSZ} is the molar mass of YSZ, ρ_{YSZ} is the film density and N_A is the Avogadro's constant.

The thickness value is obtained by multiplying the deposition time of these samples by the deposition rate obtained in equation 5.15. As the film density (ρ_{YSZ}) depends on operating conditions and structure of the films and therefore, it is not known, equation 5.15 is used with the theoretical density. However, it is possible to calculate the film density from the film characteristics. Thus, the density is calculated from the mass and the volume of the unit cell. The mass takes into consideration the number of atoms of Y, Zr and O in the lattice while the volume is calculated as a function of the lattice parameter which varies with the content of Y. The latter can be obtained by using Vegard's law as shown in Figure 5.14. Figure 5.25 shows the simulated thickness compared with the

calculated thickness from Figure 5.2a. The simulated density is smaller than the measured density, which is expected since the simulations do not take in consideration the real density of the YSZ layer. The high density values at small positions on the substrate are physically not possible and therefore not taken into consideration in this analysis.

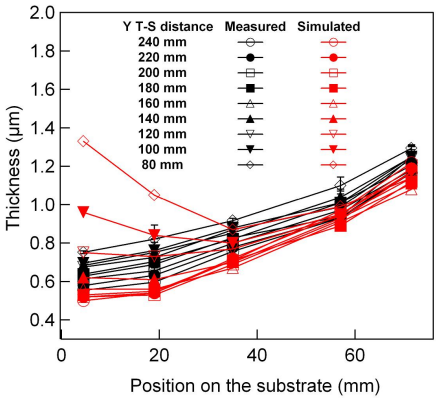

Figure 5.25: Comparison between measured and simulated thickness corrected by the calculated density.

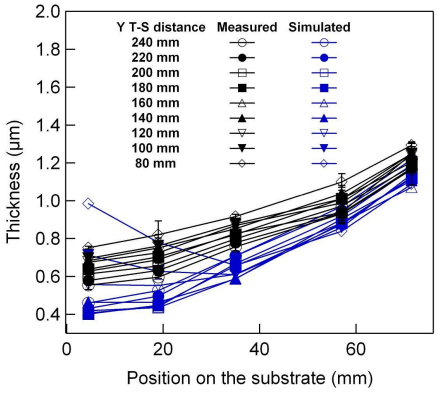

Figure 5.26: Comparison between measured and simulated thickness corrected by the difference in thickness due to the inclination angle of the microstructure.

Further in this work, it is shown that the film possesses a columnar structure with a certain inclination as a function of the content of Y. A full description of this

columnar structure is given in Part III (5.3). As the inclination is not included in the SIMTRA results, a correction is need to compare them with the experimental values. This correction is just the cosine of the experimentally observed inclination angle of the columns. This result is shown in Figure 5.26.

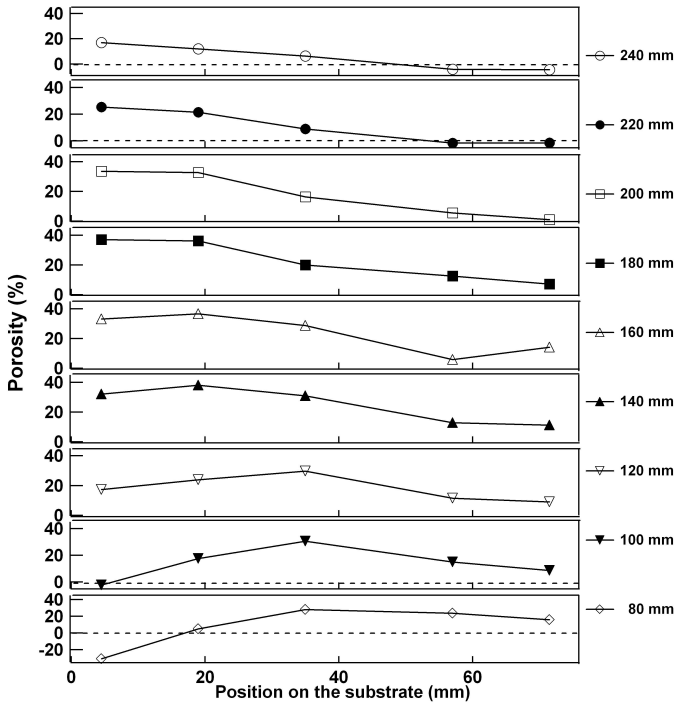

Figure 5.27: Porosity obtained from the ratio between measured and simulated data. The variation is seen along the substrate as well as the Y T-S distance.

In general, the simulated thickness is smaller, indicating that those films are porous. The ratio between the measured and the simulated thickness, defined by 1-t_s/t_m, gives us an idea of the porosity of the film. The porosity as a function of the position on the substrate and Y T-S distance is shown in Figure 5.27. Due to the error on the measured and simulated film thickness, some values are negative which is of course meaningless. Nevertheless, some trends can be concluded from this calculation. At a fixed substrate position, the porosity decreases with increasing the Y T-S distance. As discussed in Mahieu et al. [243], under a given condition, the momentum transfer of sputtered atoms and the reflected neutrals influence the film density. Increasing the Y T-S distance will lower the momentum flux of the sputtered atoms due to the collision with the atoms in the gas phase.

However, the momentum transfer of sputtered atoms, which is the ratio between the moment flux and the deposition rate, increases due to the low variation in deposition rate. In this way, the increase of the momentum transfer of sputtered atoms improves the film density. Also the trend in porosity over the substrate can be understood from this reasoning. At large Y T-S distance (e.g. 240 mm) the Zr target is much closer as compared to the Y target, and therefore it can be expected that the porosity on the right hand side (Zr side) of the substrate is smaller. At smaller Y T-S distances (e.g. 80 mm) both targets are closer to the substrate, and therefore a maximum of porosity is noticed in the middle of the sample, i.e. at a position far from both magnetrons.

5.2.5 Summary and conclusions of Part II

In Part II, it was shown that simulation is a strong tool to obtain the composition of the film based on the fraction of metals arriving on the substrate. In addition, it allows us to predict the results of the deposition phenomena occurring during sputtering. By changing the settings in SIMTRA, such as the angular distribution it is possible to tune the simulation results. This tuning indicated that there is a certain region of c3 values capable to fit the experimental and simulated composition values with an error of approximately 10 %. Interestingly, it was shown that a variation of the $c3_{Zr}$ is allowed from a cosine to an over-cosine distribution without changing the error, while the c3 parameter of Y is very sensitive to its variation, suggesting that the angular distribution of Y is defined by a heart-shape distribution.

After the tuning of the c3 parameter, the thickness was also obtained. However, a big discrepancy was noticed between the simulated and experimental results because the thickness is strongly influenced by several other factors, such as the effective density or the film growth angle. Using the ratio between experimental and simulated thickness it is possible to calculate the porosity of the films. The porosity is seen to vary significantly with the position on the substrate likewise with the Y T-S distance.

In summary, the use of simulation helps to determine the characteristics of the film with no further experimental measurements. As the angular distribution for our system is defined, further simulations can be easily performed with a high confidence being justified by the significant fit between simulations and experimental data.

Up to now we have not yet reported the effect of the deposition conditions on the microstructure and texture. Therefore, in Part III (5.3) and IV (5.4) we discuss in details how these deposition conditions can affect the growth and the crystallography of the YSZ system.

5.3 Part III: Microstructural analysis on YSZ thin films

In Part I (5.1) we described the effect of the deposition conditions on some of the characteristics of YSZ. However, the deposition conditions, as mentioned in Chapter 3, can also influence the texture and microstructure of thin films. The influence of the deposition conditions on the microstructure will be the topic of Part III. Based on SEM cross section images, it is possible to evaluate the YSZ columnar growth. A correlation between the growth zone model and the obtained results is described. The deposited films present a tilt of the [200] direction when the content of Y increases. Moreover, the geometric effect on the tilt is investigated by changing the angle of the substrate. In this way, it is possible to understand the effect of the deposition geometry on the columnar growth.

5.3.1 Preferred orientation of YSZ thin films

To start the discussion, we first focus on the texture of a low content YSZ thin film. Therefore, a thin film was deposited at a Y T-S distance of 240 mm, and a total pressure of 0.5 Pa. If the center of the sample is considered, the resultant film has a thickness of 0.85 μm and a composition of 8 at.% Y, see Part I (5.1). The diffraction pattern (Bragg-Brentano configuration) is shown in Figure 5.28, together with the reference diffraction pattern of a polycrystalline YSZ film (JCPDS card file #30-1468). From this measurement, the [200] preferential out-of-plane orientation is clear, which agrees with literature results [118, 130].

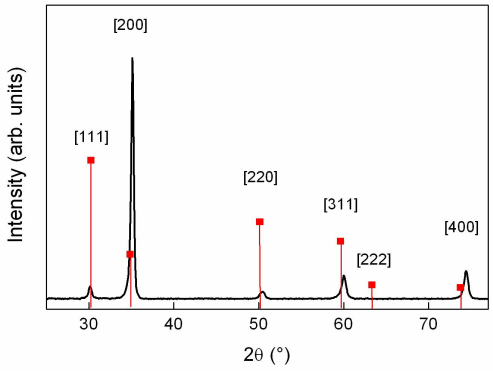

Figure 5.28: YSZ thin film with a [200] out-of-plane preferred orientation. The reference diffraction peak of the cubic fluorite type is taken from the JCPDS card file (#30-1468).

The small shift of the Bragg reflections for the measured sample as compared to the reference can be attributed to the difference in composition. Calculating the lattice parameter of the deposited film leads us to 5.103 ± 0.009 Å (see Figure 5.14), agreeing with 5.1, 5.12, 5.14 Å reported in literature for the same content of Y [125, 182, 211].

To evaluate the level of alignment, a rocking curve (see Figure 5.29) was measured. A full width at half maximum (FWHM) of 17° was obtained, which is consistent with the values obtained in literature [130, 211, 244], confirming the out-of-plane preferred orientation of the YSZ thin film.

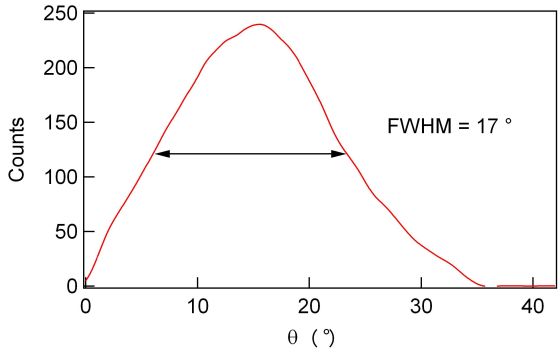

Figure 5.29: Rocking curve of the 8 at.% Y. The FWHM of 17° is coherent with the results of literature [130, 211, 244], suggesting that [200] is the preferred orientation of YSZ at this composition.

From these results, it is possible to conclude that YSZ films with 8 at.%Y are [200] out-of-plane preferential oriented. Moreover, it is observed that the film presents the cubic structure. In order to observe the film growth and the influence of the deposition conditions on the microstructure, SEM cross section images become necessary and the results will be discussed in detail in the next sections.

5.3.2 Influence of the deposition conditions on the microstructure of YSZ thin films

5.3.2.1 Development of a columnar structure during film growth and correlation to the zone model

Chapter 3 described the film growth based on the extended structured zone model (ESZM). In order to observe the influence of the deposition conditions on the microstructure, the SEM cross sections and surface images of several YSZ films deposited at different conditions were obtained. Figure 5.30a to e presents the

SEM cross section images of YSZ films deposited at 0.5 Pa with Y T-S distances of 240 mm to 80 mm in intervals of 40 mm and the surface view (Figure 5.30f) of a sample with a Y T-S distance of 200 mm.

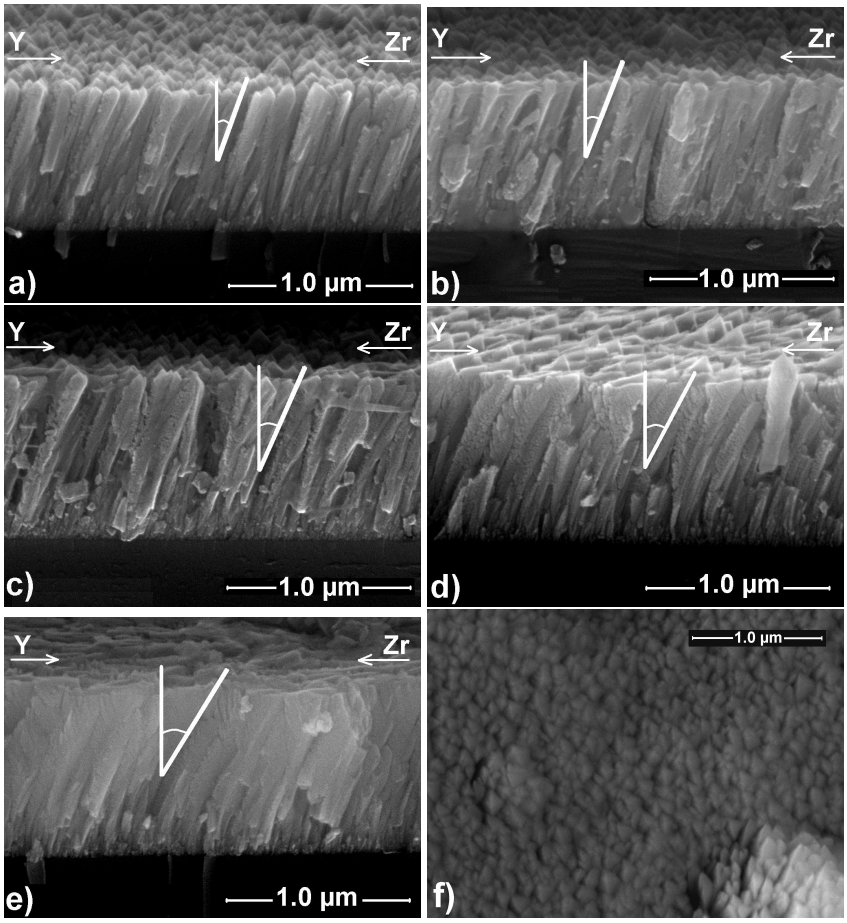

Figure 5.30: Cross section SEM images of YSZ samples with Y T-S distance varying from 240 to 80 mm in intervals of 40 mm: a) 240 mm (12 at.%Y), columnar tilt 10.9 ± 1.73°; b) 200 mm (17 at.%Y), columnar tilt 17.1 ± 2.2°; c) 160 mm (24 at.%Y), columnar tilt 25.9 ± 2.62°; d) 120 mm (29 at.%Y), columnar tilt 29.1 ± 1.91°; e) 80 mm (39 at.%Y), columnar tilt 30.3 ± 2.4°. The microstructure is characteristic of zone T growth. f) Surface image of a sample with Y T-S distance = 200 mm indicating the pyramidal surface.

A columnar structure is clearly observed in the cross sections of Figure 5.30a to e. On the bottom of the columns small columns characterize the overgrowth. This characteristic was already shown in Chapter 3 to be related to zone T based on

the ESZM. Similar columnar structures formed due to shadowing have also been reported in literature [101,125,130,182,220,221,244,245]. The V-shaped facetted column characteristics of zone T are clearly identified as well as the pyramidal surface structures (surface image, Figure 5.30f).The surface structure can also be explained from the columnar tilt. The crystallite habitus is a squared based pyramid showing the (111) facets, or stated differently a $\{111\}$ crystal form. At low Y content (Figure 5.30a) a clear "roof-like" surface structure is noticed which is defined by the crystal habitus. As the crystallites tilt at higher Y contents, a flatter surface structure is noticed, since the surface is defined by the (111) facets which become more parallel to the substrate.

The columns are clearly tilted. In addition, based on the analysis of several samples, it is clear that the columns tilt towards the Zr source. This inclination can be obtained by measuring the angle formed between the normal and the inclined column, as indicated in the cross section images (see Figure 5.30a to e). Using Meazure program [246], we consider several columns in order to obtain their respective tilts. Therefore, the angles shown in this section are the average of these tilts. Furthermore, the columnar tilt increases with the increase of Y content in the film. The obtained values for composition and angles of samples of Figure 5.30 a to e are: (a) 12 at.%Y and 10.9 ± 1.73°; (b) 17 at.%Y and 17.1 ± 2.2°; (c) 24 at.%Y and 25.9 ± 2.62°; (d) 29 at.%Y and 29.1 ± 1.91° and (e) 39 at.%Y and 30.3 ± 2.4°.

The SEM images corresponding to depositions performed at high pressure (0.95 Pa) are illustrated in Figure 5.31. Figure 5.31a and b show the columnar structure at Y T-S distance of 220 mm and 100 mm, respectively. Figure 5.31c shows the film surface. At high pressure an inclined V-shape growing in zone T is present. This inclination can be related to the mobility of adparticles and the flux of material arriving on the substrate. The increase of mobility also affects the sample surface and as a consequence the pyramidal surface has a more rounded shape. Furthermore, for these conditions, a thicker columnar structure is observed in the film. This can be related to the amount of energy per adparticle delivered to the growing film which is higher than at low pressure. As a consequence, the increase of pressure results in an increase of the mobility of the adparticles. More details about energy analyses will be given in the next section.

Comparing Figures 5.31a and b the same tilt angle is observed, (a) 28.3 ± 1.39° and (b) 28.3 ± 2.27°, even though the contents of Y are different for both examples. It is possible to conclude that pressure eliminates the influence of composition on the columnar tilt.

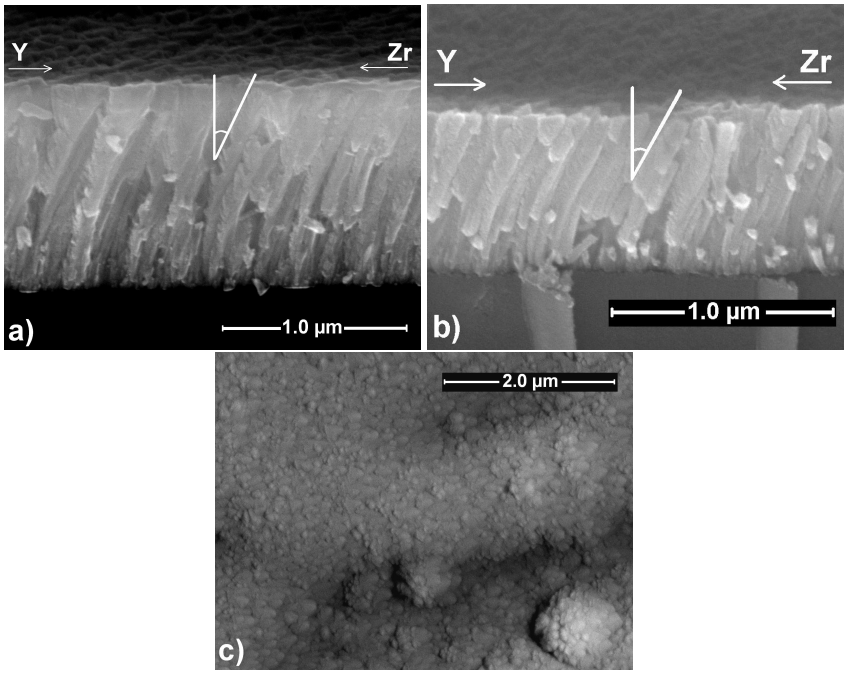

Figure 5.31: SEM images of YSZ thin films deposited at high pressure (0.95 Pa). Cross section view of Y T-S distance: a) 220 mm (9 at.% Y), columnar tilt 28.3 ± 1.39°; b) 100 mm (31 at.% Y), 28.3 ± 2.27°. The columnar tilt is the same although both samples have different content of Y. c) Surface image of a sample with Y T-S distance = 220 mm indicating a more rounded pyramidal shape.

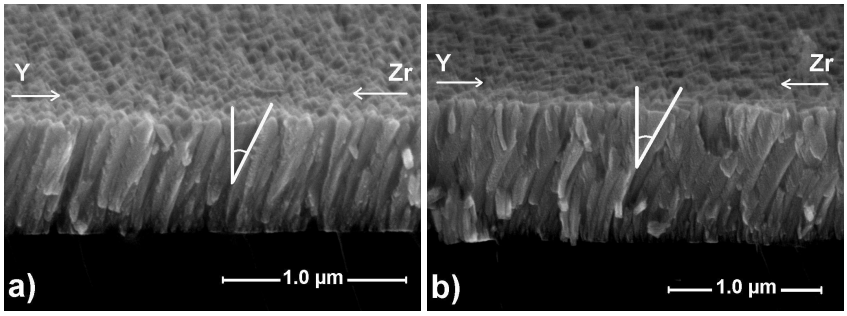

Figure 5.32: SEM cross section for samples deposited at different currents: a) 0.37 A (24 at.% Y), columnar tilt 24.4 ± 1.91° and b) 1.16 A (44 at.% Y), columnar tilt 29.1 ± 1.81°. The tilt increases with the increase of the Y content.

The change of current, represented in Figure 5.32, acts in a similar way to the change of Y T-S distance at low pressure, i.e. the increase of Y content due to the change in current rises the columnar tilt from (a) 24.4 ± 1.91° in sample 0.37 A with 24 at.% Y to (b) 29.1 ± 1.81° for sample 1.16 A with 44 at.% Y. Both images show a columnar growth in zone T defined by overgrowth and a V-shaped facetted column.

The effect of deposition time is no longer discussed because time only affects the variation of thickness with no significant variation in the microstructure of the films. However, the SEM cross section images related to the change in thickness can be found in Appendix C.

Figure 5.33 shows the influence of the composition on the columnar tilt based on the similar analyses as discussed above. Note that there is a variation of the columnar tilt as a function of composition when either Y T-S distance or current is changed at low pressure. This increase of the columnar tilt seems to grow in a asymptotic way reaching a maximum of 30° at low pressure and approximately 28° when current is changed. Until 24 at.%Y the columnar tilt of both experiments seem to be similar. The columnar tilt presents no variation at high pressure and its value is constant at 28°. Of course, the presented result must be treated with some care, as we here implicitly assume that the tilt is defined by the composition. The number of studied sample is insufficient to make a statistically significant conclusion. However, in Part IV (5.4), a more in-depth analysis will be performed based on pole figures, allowing to draw this conclusion. Moreover, as discussed in Part I (5.1), the influence of most deposition parameters (except pressure) was minor as compared to the influence of the composition.

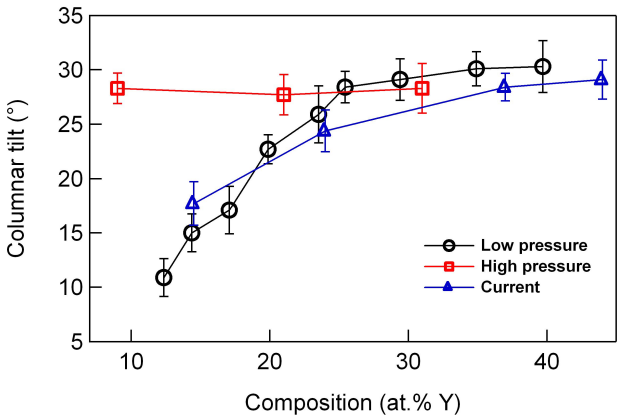

Figure 5.33: Columnar tilt as a function of the composition for samples deposited at different Y T-S distances at low and high pressure and at different currents at low pressure.

5.3.2.2 Energy analyses on YSZ thin films

To pinpoint the growth model for YSZ films, the thermal flux towards the growing film was examined under different growth conditions. Figure 5.34 shows the variation in thermal flux, the flux of metal particles and the energy per deposited atom (EPA) versus Y T-S distance at different deposition conditions, namely, low pressure, high pressure and current using set 1 of samples (points obtained from the center of the sample as described in section 4.5, Chapter 4). No energy analysis was performed with different deposition times because of its equivalence with the results of Y T-S distance of 240 mm deposited at low pressure.

The thermal flux, given in $mW.cm^{-2}$, determines the increase of temperature on the substrate due to the particle bombardment on the sample surface. Its value was obtained using a thermal probe, which use has already been introduced in Chapter 4. The flux of metal particles given in $cm^{-2}.s^{-1}.at^{-1}$, on the other hand, was not obtained experimentally but it is defined considering the specific mass, composition and thickness of the film [168], being calculated from equation 5.16:

$$F_M = \frac{R_d N_A}{\left[\left(\frac{f_Y}{2}\frac{M_{Y2O3}}{\rho_{Y2O3}}\right) + \left(f_{Zr}\frac{M_{ZrO2}}{\rho_{ZrO2}}\right)\right]} \tag{5.16}$$

where N_A is the Avogadro's constant, R_d is deposition rate (thickness of the sample related to a specific composition divided by deposition time), f_Y and f_{Zr} are the atomic fractions of metallic Y and Zr, respectively, M is the molar mass and ρ is the density of both oxides. And finally the energy per deposited atom ($eV.at^{-1}$) is the energy expressed as the measured thermal flux normalized to the calculated flux of metal particles.

First, we discuss the thermal flux of Figure 5.34a for different Y T-S distances deposited at low pressure (0.5 Pa), at high pressure (0.95 Pa) and for different currents deposited at 0.5 Pa with a fixed Y T-S distance of 240 mm. At low pressure, represented by the open circles, a decrease in thermal flux is observed until Y T-S reaches approximately 140 mm, remaining constant within the measurement error tolerances. Therefore, only a minor influence of the distance exists. This can be explained based on the magnetrons position. Given that one source (zirconium) is close to the substrate (90 mm), the effect of the other source (yttrium) is minimal, except when the distances are nearly equal resulting in a small increase of the energy flux. The reason for the small increase was attributed to the power of the closest magnetron, approximately 150 W, while the power of the moving magnetron was approximately 55 W (current of 0.2 A), eliminating the inverse square effect of the distance [247].

The thermal flux at high pressure has practically the same behavior as described above when changing Y T-S distance, i.e. there is a constant value at higher T-S distance and a slight increase at smaller T-S distances. It can be assumed that

the thermal flux towards the sample will not significantly change with pressure as the major contribution comes from electrons [247]. However, the changes in ionization efficiency in the plasma and in the energy absorption rate of the gas can alter the behavior of the thermal flux. Ekpe and Dew [210, 248] found a linear increase of the thermal flux with power and pressure for aluminum. But at low powers in the range of 50-150 W the change in thermal flux is not significant. Therefore, there is only a minor influence from pressure and distance.

An increase of the discharge current increases the thermal flux. From the plot of Figure 5.34a, it is clear that the current affects the thermal flux linearly, which it is expected since the power also increases linearly [210].

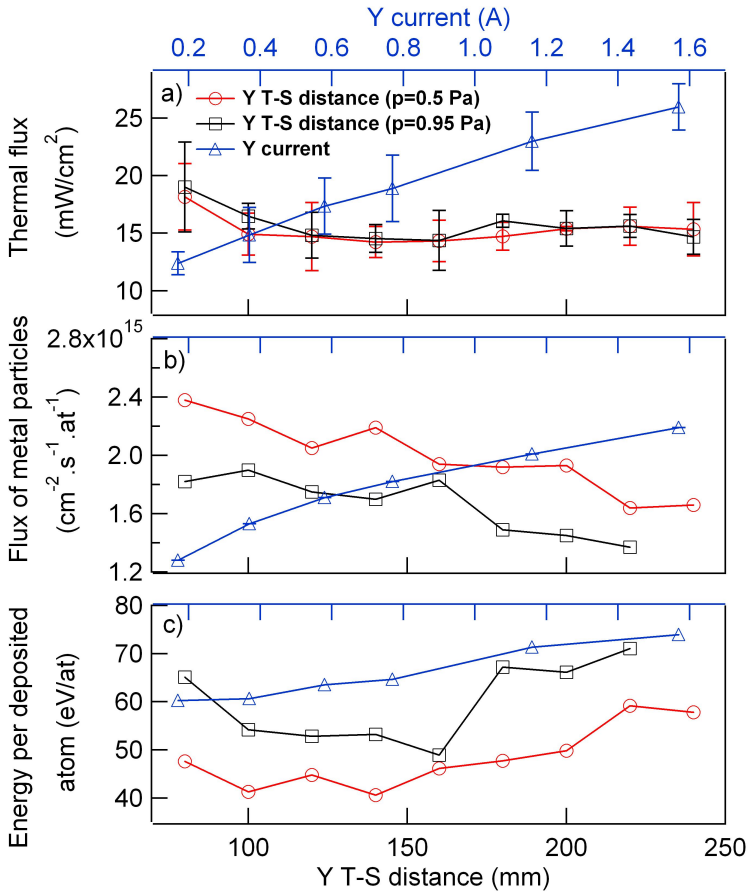

Figure 5.34: a) Thermal flux; b) Flux of metal particles; c) Energy per deposited atom vs. Y T-S distance for samples deposited at 0.5 Pa (circular markers) and 0.95 Pa (square markers) and vs. current for samples deposited at 0.5 Pa (triangle markers).

The flux of metal particles, Figure 5.34b, is not only related to the Y T-S distance but also to the gas pressure and target current. With the change of Y T-S distance to higher values, the flux of metal particles reduces for both experiments at low and high pressure. This can be related to the smaller solid angle and the increase of gas scattering when changing Y T-S distance to higher values, as described in Part I (5.1). Furthermore, the effect of the pressure is mainly due to the lowering of the discharge voltage at higher pressures [160, 171, 183, 223, 224], reducing the sputter yield of the target material. The current, on the other hand, has an opposite effect, meaning that the flux of metal particles increase with the increase of current. As this flux is calculated based on the deposition rate, it is evident that the flux increases with the increase of current.

Two hypotheses can be proposed to explain the textural change of thin films. One is based on the mobility of the arriving species defining the growth zone in the extended structure zone model. The mobility is defined by the total energy per deposited atom (EPA) [210, 248, 249], which is the ratio between the thermal flux and the flux of metal particles, as already mentioned above. This relationship provides more information on the possible effect of energy on the film growth mechanism. As illustrated in Figure 5.34c, it is possible to see the increase of the total energy per deposited atom for all deposition conditions. This increase can be understood from the almost constant energy flux and the lowering of the deposition rate when changing Y T-S distance and from the ratio between both increasing slopes when changing the current. The ratio between the EPA of the maximum and the minimum values, 1.5, 1.4 and 1.3 for experiments changing Y T-S distance at 0.5 Pa, 0.95 Pa and changing current, respectively, are not sufficient to cause a transition from zone T to zone II [157, 250]. In fact, as shown previously by our research group [157, 250], a textural change could be explained by a transition from zone T to zone II growth. For this kind of transition to happen, the mobility, and therefore the EPA, must drastically increase. Typically, the EPA changes over an order of magnitude. The reason for this drastic increase is due to target poisoning reducing the deposition rate substantially. In this study, target poisoning was prevented by the use of a local oxygen inlet resulting in a minor variation of the deposition rate. Therefore, based on the EPA, no textural change is expected.

Another hypothesis for the textural change of the thin film is based on previous work published by our group [250] where it was demonstrated that the nature of the adsorbing reactive gas species (atomic oxygen or molecular oxygen) also influence textural evolution. At high concentrations of atomic oxygen in the plasma, YSZ thin films can grow [220] while a [200] out-of-plane orientation is observed at low atomic oxygen concentrations. Since our samples are deposited in metallic mode there is a very low oxygen plasma concentration and no change in preferred orientation and/or microstructural change is expected.

5.3.2.3 Influence of different substrate angle on the columnar tilt

The configuration of the deposition setup is of fundamental importance for the growth of YSZ thin films. To further clarify the correlation between the geometric configuration and the columnar tilt, depositions with different substrate angles were performed. Deposition conditions were kept the same as in the experiments changing Y T-S distance at 0.5 Pa. In fact, these experiments are the reference since there is no inclination of the substrate (0° tilt). The inclinations of the substrate were defined at +7.4° and -7.4°. The schematic drawing of the different substrate angles is represented in Figure 5.35. The positive sign indicates a clockwise tilt, i.e. towards the Zr target, while the negative indicates an anticlockwise tilt, i.e. towards the Y target.

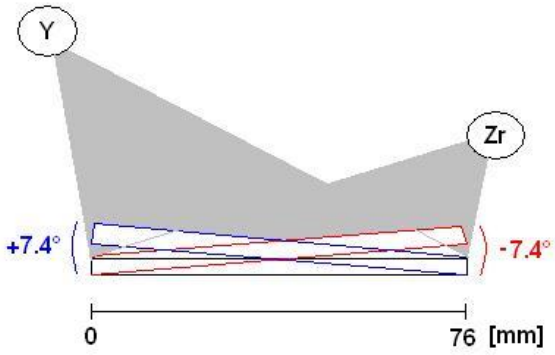

Figure 5.35: Schematic drawing of the substrate inclinations used to determine the geometrical influence on the columnar growth of the YSZ films. The positive sign indicates a clockwise tilt of +7.4° in the direction of the Zr target while the negative sign indicates an anticlockwise tilt of -7.4° in the direction of Y target.

Our analyses are performed using SEM cross section images of the different substrate angles. As seen previously in section 5.3.2.1, the growth of YSZ films is characterized by columns and the columnar tilt is obtained via the visual tilt of the SEM images.

When the substrate angle is changed, the position of the Y and Zr targets is different from the initial one (substrate angle = 0°). This leads to different starting angles and consequently to a different columnar tilt. This difference in the starting angle can be seen in the SEM cross section images of Figure 5.36. These samples were deposited with a Y T-S distance of 200 mm. The corresponding Y content in samples +7.4°, 0° and -7.4° are 9 %, 16 % and 15 %, respectively. Turning the substrate away from the Y source (+7.4°, Figure 5.36a) results in a smaller columnar tilt (11.8 ± 0.7°) when compared to the non-inclined substrate

(0°, 17.7 ± 1.4°, Figure 5.36b). The opposite is noticed when the substrate is inclined towards the Y source (-7.4°, Figure 5.36c): a columnar tilt of 23.9 ± 2° is observed. The columnar tilt difference (on average 6.05°) is within the error equal to the inclination angle, being symmetric to the non-inclined substrate.

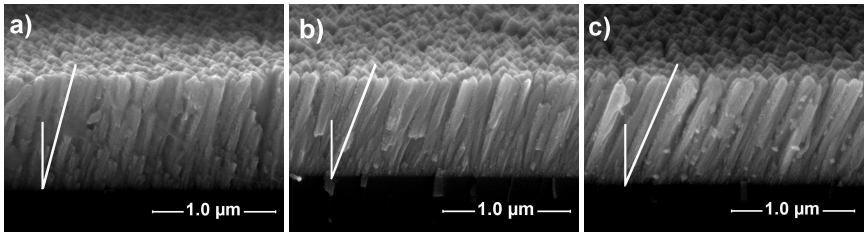

Figure 5.36: Cross section images of different substrate angles deposited with a Y T-S distance of 200 mm. The substrate angles are: a) +7.4° (inclined to Zr target), columnar angle 11.8 ± 0.7°, 9 at.% Y; b) 0°, columnar angle 17.7 ± 1.4°, 16 at.% Y; c) -7.4° (inclined to Y target), columnar angle 23.9 ± 2°, 15 at.% Y.

In the same way we can compare the SEM cross section images of Y T-S distance of 80 mm displayed in Figure 5.37. The obtained columnar angles are 26.6 ± 2.5°, 30.3 ± 2.4° and 30.9 ± 2.7° for substrates angles of +7.4°, 0° and -7.4°, respectively. Due to the inclination of the substrate the composition is also affected. The content of Y of the samples below are obtained in the center of the sample and the respective values are (a) 23 %, (b) 39 % and (c) 42 at.% Y. This can be understood by the direction of the material flux. When the substrate is inclined to the direction of Zr, more Zr particles are normally oriented to the sample surface in comparison to Y particles. Therefore, less Y is present on the total composition. The contrary is also true and as a consequence more Y is present on the layer when the substrate is inclined to the direction of Y source.

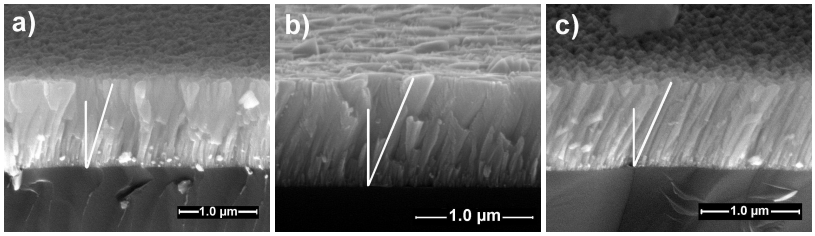

Figure 5.37: Cross section images of different substrate angles deposited with a Y T-S distance of 80 mm. The substrate angles are: a) +7.4° (inclined to Zr target), columnar angle 26.6 ± 2.5°, 23 at.% Y; b) 0°, columnar angle 30.3 ± 2.4°, 39 at.% Y; c) -7.4° (inclined to Y target), columnar angle 30.9 ± 2.7°, 42 at.% Y.

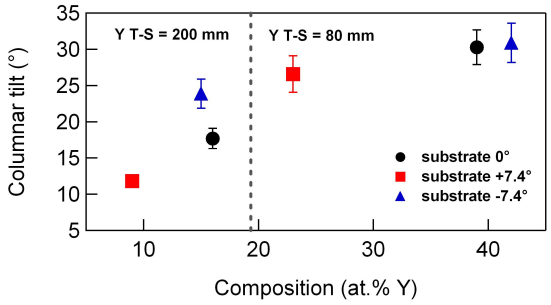

Figure 5.38: Representation of the columnar tilt of the images shown in Figures 5.36 and 5.37 as a function of the content of Y.

Figure 5.38 displays the columnar tilt of Figures 5.36 and 5.37 as a function of the content of Y. In conclusion, Figure 5.38 demonstrates that the change of tilt is related to the geometry since the columnar tilt is dependent on the substrate angle and composition. A change of the substrate angle might alter the starting angle of the tilt but does not change the columnar behavior of the tilted growing film at higher Y concentrations, because the maximum angle of curvature of the columns reach a limit at higher content of Y.

5.3.3 Summary and conclusions of Part III

In Part III, the influence of the deposition conditions (distance, pressure and current) on the microstructure was studied. Based on SEM images and correlating the results with the extended structured zone model, it was identified that our samples grow in zone T with a well defined facetted V-shape columns. Interestingly, a tilt of the columns was noticed when the content of Y increases (decrease of Y T-S distance) at low pressure or when the Y current was increased. This tilt follows the direction of the Zr source. At high pressure, the tilt is independent of Y T-S distance or composition. Energy analyses were also executed and corroborated with the conclusions found via SEM images.

The results attested that the geometrical configuration of the deposition setup plays an important role on the tilt. Therefore, the influence of the chamber's geometry was analyzed in detail by changing the substrate angle. The columnar tilt at high Y content are not affected by the substrate angle but varies as a function of the content of Y. At low content of Y, on the other hand, the substrate angle leads to different tilt angles. Moreover, the change on the substrate angle also changes the amount of Y on the film, which depends on how the substrate is oriented. A next step is to determine the influence of the deposition conditions on the grain tilt (texture) and the relations involved between grain and columnar tilt.

5.4 Part IV: Textural analysis on YSZ thin films

The microstructure of the YSZ system was explained in Part III (5.3). Part IV focuses on the influence of the deposition conditions on the texture of the YSZ thin films. In addition, two methods are proposed in this part to obtain the grain tilt, one based on the analyses of pole figures/polar plot and the second using XRD/polar plot.

5.4.1 Texture determined via pole figures

Based on the SEM results and the energy analyses from Part III (5.3), it is observed that YSZ films grow in zone T with a columnar microstructure. Moreover, a columnar tilt develops with the increase of composition when deposited at 0.5 Pa independently of the type of deposition condition. At high pressure, on the other hand, a constant columnar tilt was observed. In order to analyze in detail the crystallographic orientation of the structure, pole figures were measured. A description of this method and its interpretation was already given in Chapter 4.

Figure 5.39 illustrate the (111) and (100) pole figures obtained for set 1 (see Chapter 4, section 4.5) of samples deposited at 0.5 Pa. The first column indicates the (111) pole figure, followed in the middle by the (100) pole figure and the last column represents the schematic drawing of the cubic structure from a crystallographic software (CaRIne v3.1) [251]. The use of the schematic drawing of the lattice demonstrates how the cubic lattice should be positioned in relation to the substrate normal. The [200] direction is indicated by the white atom in the schematic drawing. The Y and Zr magnetrons are positioned on the left and right hand sides of the plotted poles and their positions are indicated in the figure.

Biaxial alignment of the YSZ thin films can also be observed in these images. At low concentrations of Y (or high T-S distance, Figure 5.39a the [200] is identified as the out-of-plane preferred orientation with a clear peak in the center of the (100) pole. The four [111] peaks at 55° are identified in the (111) pole figure, confirming the biaxial alignment of the films. As the Y content increases (decrease of T-S distance) there is a tilt of the out-of-plane preferred orientation from [200] to [111], which can be observed by the movement of the [200] direction either in the (100) pole likewise in the schematic drawing. This tilt represents the grain tilt. It is possible to quantitatively determine this tilt from the [200] direction in CaRIne when compared to the pole figures results. The following grain tilts are obtained: 5.8, 12.5, 21.7, 35.7, 39.3, 41.6, 43.5° for Figure 5.39a to g, respectively.

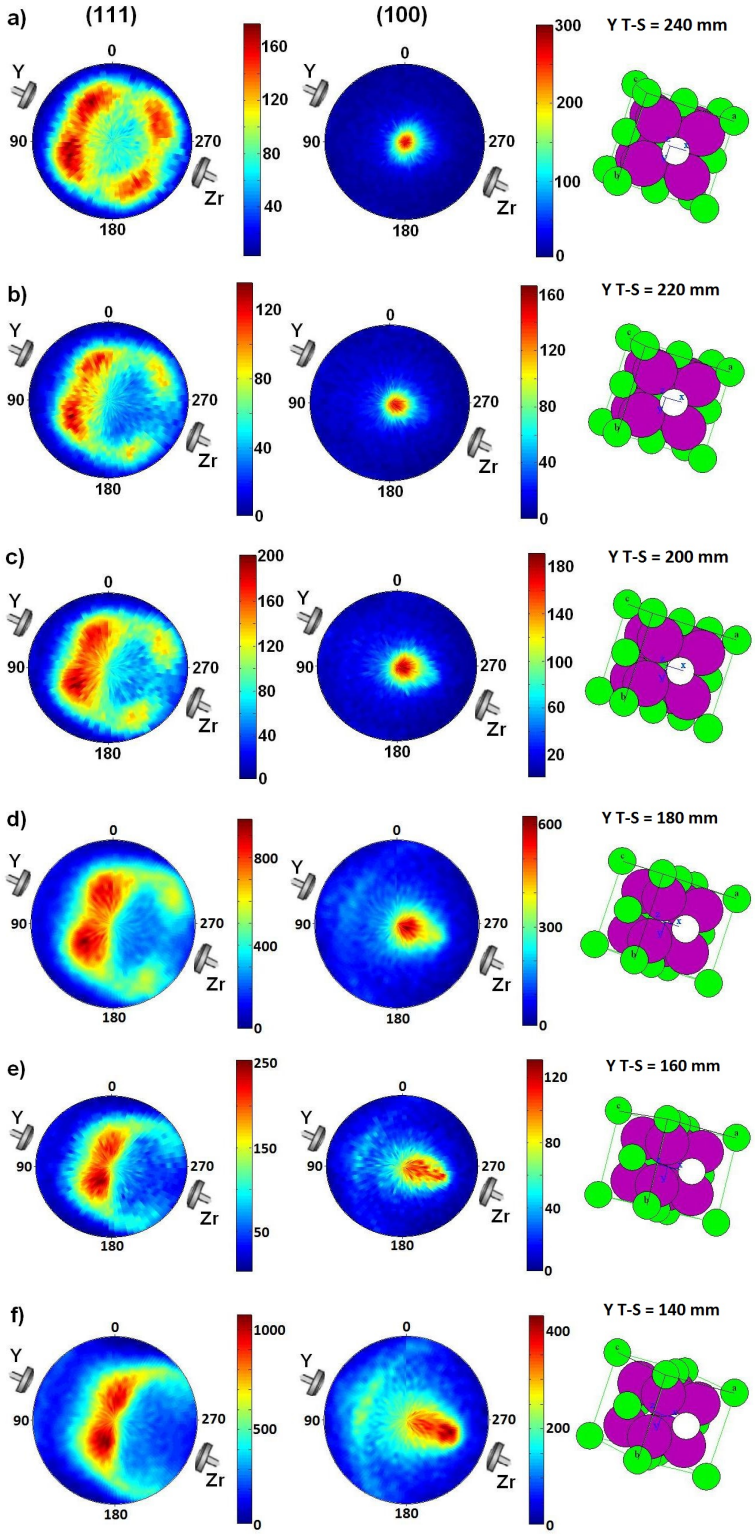
a)
(111)
(100)
Y T-S = 240 mm
b)
Y T-S = 220 mm
c)
Y T-S = 200 mm
d)
Y T-S = 180 mm
e)
Y T-S = 160 mm
f)
Y T-S = 140 mm
0
90
180
270
Y
Zr

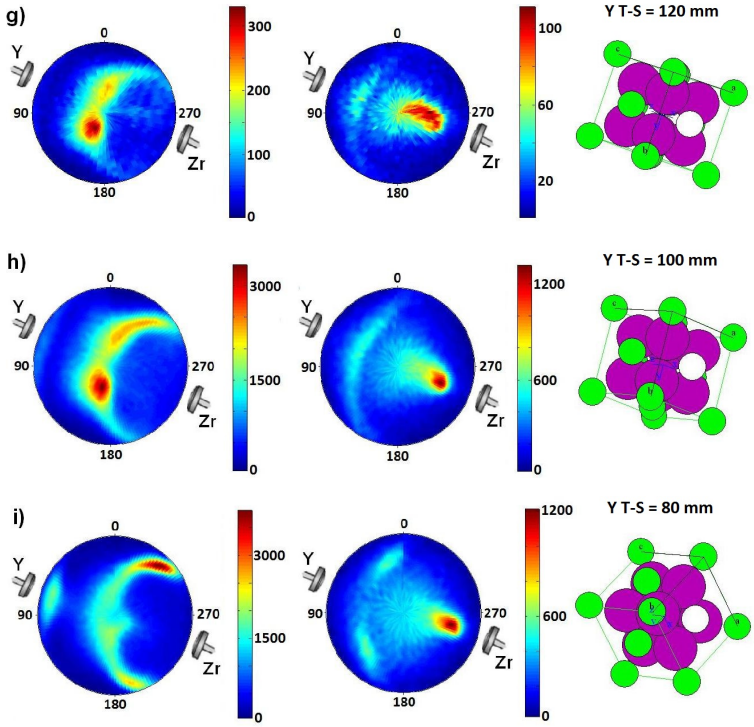

Figure 5.39: Pole figures for YSZ films deposited at 0.5 Pa. The respective Y T-S distances and compositions are: a) 240 mm (12 at.% Y); b) 220 mm (14 %); c) 200 mm (17 %); d) 180 mm (19 %); e) 160 mm (24 %); f) 140 mm (26 %); g) 120 mm (29 %); h) 100 mm (35 %); i) 80 mm (39 %). The first and second columns indicate the (111) and (100) pole figure, respectively, followed by the schematic drawing of the cubic structure. The white atom in the schematic drawing corresponds to the [200] direction.

The tilt noticeably follows the Zr source, as indicated in the SEM images (Figure 5.30). Intriguing, starting from Y T-S distance of 120 mm (29 %) there is also a rotation of the lattice, identified by the [111] peak with higher intensity. As soon as the Y T-S becomes smaller than 120 mm this rotation is clearer. Note that for higher contents of Y (39 %) and minimal Y T-S distance (80 mm) (Figure 5.39g), the YSZ film does not reach a pure [111] out-of-plane preferred orientation but it still presents a strong tilt of the [200] orientation. The rotation is identified by the three peaks in the (100) plane. The change in tilt goes in agreement with the conclusions of Part III (5.3), confirming that no zone transition occurs when the content of Y increases or the Y T-S distance decreases.

Figure 5.40 illustrates the pole figures at high pressure of three different Y T-S samples deposited at (a) 220 mm, (b) 140 mm and (c) 100 mm with compositions

of 9 %, 23 % and 31 %, respectively. Similar to Figure 5.39, the first column indicates the (111) pole, followed by the (100) pole and finally the schematic drawing of the cubic structure from CaRIne [251].

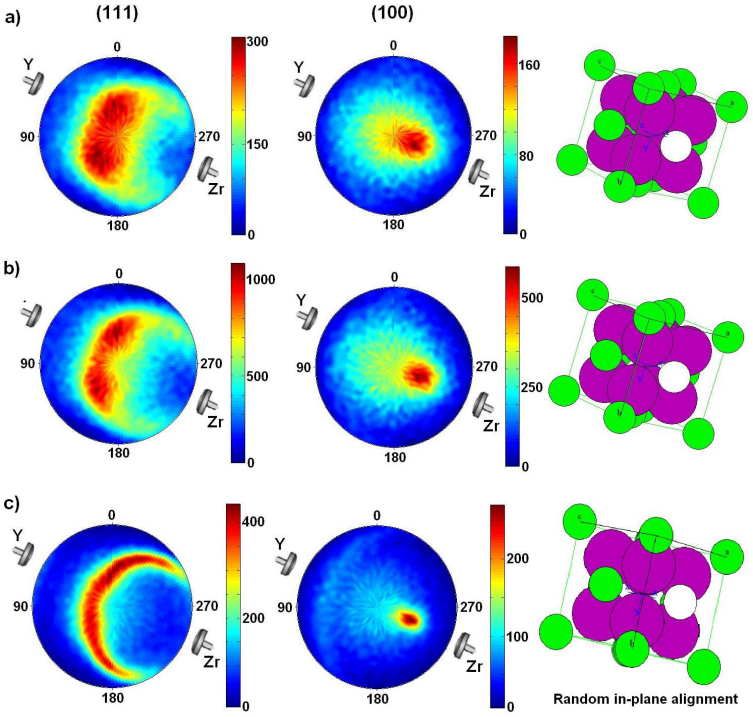

Figure 5.40: Pole figures for YSZ films at high pressure. The respective Y T-S distance and compositions are: a) 220 mm (9 at.% Y); b) 140 mm (23 %); c) 100 mm (31 %). The first column indicates the (111) pole figure, followed by the (100) pole and the third represents the schematic drawing of the cubic structure.

Comparing the results of Figure 5.39 and Figure 5.40, the first difference is that the biaxial alignment worsens. The pressure is one of the factors that affect the biaxial alignment as seen in section 4.6.9.2, Chapter 4 and shown in Appendix A. It is noticeable that the peaks in Figure 5.40 are less intense and also broader than the poles at low pressure. The next remark is that at higher pressure the orientation is independent of Y content and Y T-S distance since there is no variation of the tilt on the [200] direction and the grain tilt is confined in the region between 35-40°. These poles indicate a [200] preferred orientation tilted in the direction of Zr (right hand side of the pole figure). There are two [111] peaks located very close to the center of the pole. The other two less-intense peaks, on the right hand

side of the pole, indicate that the cubic structure is tilted. The variation seen in the pole figures can be attributed to the small differences on the position of the substrate on the sample holder during deposition or even the orientation of the sample during measurement. At high Y content (above 30 % Y, Figure 5.40c the film loses its biaxial alignment becoming uniaxial aligned. This loss can be related to the mobility of the adparticles and also to the angular spread of the incoming material [134]. At higher pressure the arrival angle of the adparticles is strongly influenced by collisions with the gas atoms, changing their direction towards the film surface and resulting in a less-defined directed flux of the arriving atoms. As the Y T-S distance is small and the angular spread is large, the scattered adatoms, which arrive with different directions and orientations, are immediately adsorbed on the film surface, resulting in a random alignment and consequently in lost of the in-plane preferred orientation. In Figure 5.40c, it is observed that the out-of-plane preferred orientation remains [200] and that there is a semicircular shape present in the (111) pole. This semicircular shape represents the contribution of all cubic [111] directions randomly oriented, i.e. a fiber texture.

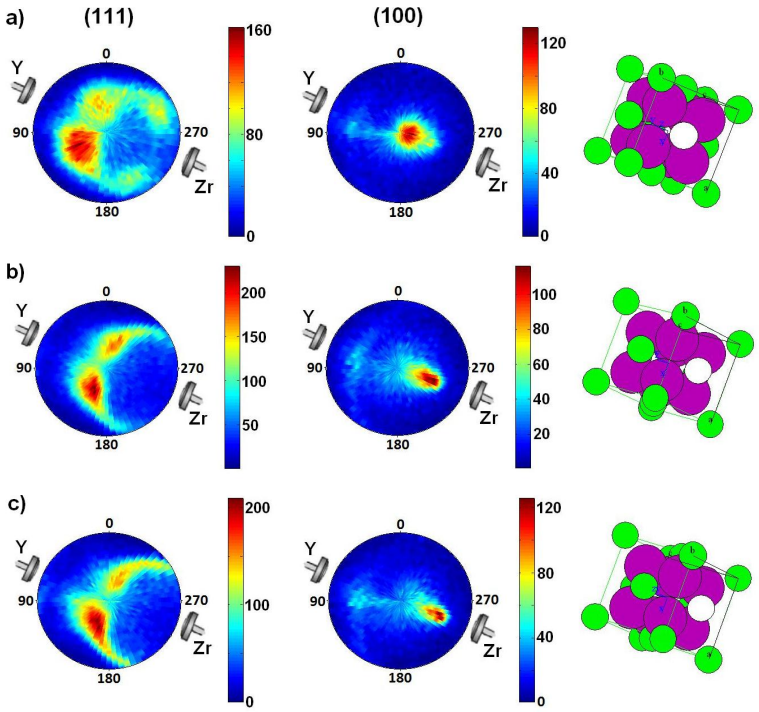

Figure 5.41: Pole figures showing the grain tilt at currents equal to: a) 0.37 A (24 %); b) 0.77 A (37 %); c) 1.16 A (44 %).

In order to identify the grain tilt as a function of the discharge current, pole figures at three different currents 0.37, 0.77 and 1.16 A are shown in Figures 5.41a, b and c, respectively. The correspondent Y contents are 24 %, 37 % and 44 at.%. In pole Figure 5.41a there is a small tilt of the [200] direction. This tilt increases when current goes to 0.77 A, identified by the two main [111] peaks close to the center of the pole, indicating the translation of the tilt. At even higher currents, the grain tilt increases. However, at 1.16 A (Y T-S distance 240 mm) there is no rotation of the lattice in contradiction to the results demonstrated for T-S distance 120, 100 and 80 mm at low pressure (Figure 5.39g to i).

The absence of the rotation at high currents cannot be related to the content of Y in the film since this effect is not distinguished at high content of Y. Although the energy per deposited atom is higher than in the case of low pressure (see Figure 5.34a) no rotation is identified at high currents and therefore this energy has also no influence on the rotation. Another possibility is to consider the Y T-S distance. Figure 5.42 shows the pole figure at 160 mm deposited with a current of 0.77 A. Note that at this current the structure is clearly rotated. This can be seen in the (100) pole where three different peaks can be identified. Therefore, it is possible to concluded that the rotation of the lattice is Y T-S distance related. In Part V (5.5) we will use a simulation tool to analyze how the tilt and the rotation of the lattice are influenced by the compositional variation and Y T-S distance.

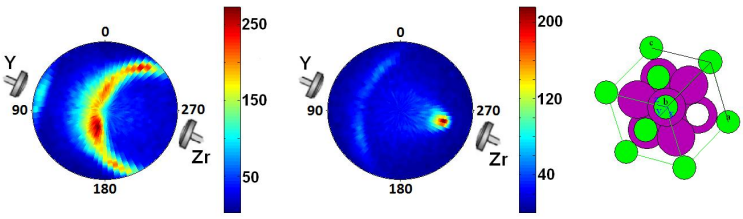

Figure 5.42: Pole figures of a sample deposited at 0.77 A with a Y T-S distance of 160 mm. The rotation of the lattice is in evidence, showing that this effect is geometrically related.

In summary, pole figures are shown to be a straightforward tool to identify the tilt of the [200] direction. A way to represent the results obtained via pole figures includes the use of polar plot. The stereographic positions of the main orientations in a cubic structure are identified by using CaRIne [251] in combination with the pole figure data of the computational program TexEval (version 2.4) from Bruker AXS.

In order to prove the equivalence between polar plot and pole figure we consider the example of a sample deposited at low pressure with a tilt of 12°. Figure 5.43a represents the pole figure of this tilt obtained via pole figure, followed by Figure 5.43b where the stereographic projection of the main directions of

the cubic structure is shown in CaRIne software [251] and finally Figure 5.43c illustrates the position on the polar plot based on CaRIne. Following the cross marker it is clear the concordance of the grain tilt obtained via pole figure and polar plot. As a result, the azimuthal angle of the polar plot can be considered as the position of the [200] direction. Hence, it gives the value of the grain tilt of the YSZ system.

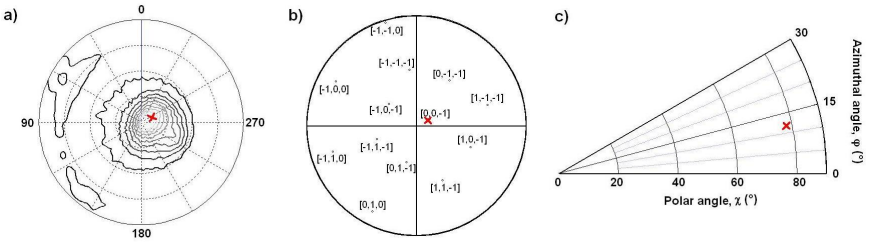

Figure 5.43: Representation of the calculated angle $\varphi = 12°$ and $\chi = 78°$ in a) pole figure; b) stereographic projection via CaRIne and c) a polar plot based on CaRIne.

Since the azimuthal angle gives the value of the grain tilt, the polar plots of the pole figures discussed above can be summarized in Figure 5.44.

The interpretation of the polar plot based on the pole figures is given below. Figure 5.44a shows the representation of the polar plot for the pole figures of Figure 5.39. The polar plot indicates a [200] out-of-plane preferred orientation at low content of Y. As soon as the content of Y increases, an arc is formed from [200] to [111] and the azimuthal angle also increases indicating that the tilt grows. The azimuthal angle gives the grain tilt of the lattice. At approximately $\varphi = 32°$ and 35 at.% Y there is a discontinuity (gap) in the arc which is associated to a rotation of the lattice based on the content of Y and pole figures above. As the content of Y increases, the lattice continues tilting until the grain tilt is approximately $\varphi = 45°$.

Figure 5.44b illustrates the polar plot at high pressure. Note that the grain tilt is confined in the region from $\varphi = 33°$ to 45°, indicating that tilt of the [200] remains practically constant. Moreover, there is no variation of the tilt as a function of the change in composition. The effect of current, represented in Figure 5.44c, shows the same behavior as in Figure 5.44a, i.e. there is a variation of the grain tilt as a function of composition from $\varphi = 13°$ ($\chi = 82°$) to $\varphi = 45°$ ($\chi = 58°$).

The main disadvantage of the use of pole figures is related to the acquisition time. The acquisition time of each particular position requires long periods of time. Another convenient tool to identify the crystallographic orientation of thin films is based on the XRD ($\theta/2\theta$). The main advantage of XRD ($\theta/2\theta$) in comparison with pole figures is the operation time. For example, a full spectrum varying from

20 to 75° takes approximately 30 minutes while a pole figure measurement of two different planes takes up to 2 hours. Therefore, in the following section, we discuss the results obtained via XRD diffraction peaks.

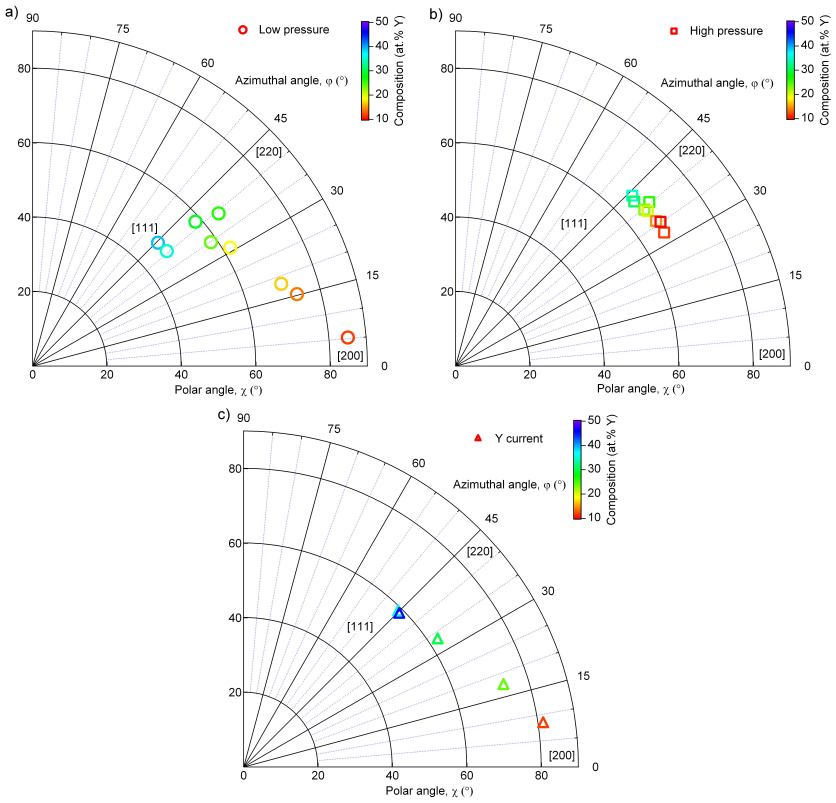

Figure 5.44: Polar plot showing the angles obtained from pole figures for different deposition conditions: a) Y T-S distance at 0.5 Pa; b) Y T-S distance at 0.95 Pa and c) changing Y current at 0.5 Pa.

5.4.2 Fictional zone transition based on XRD (θ/2θ) results

Figure 5.45 shows the XRD diffraction patterns when changing deposition conditions: (a) Y T-S distance at 0.5 Pa; (b) Y T-S distance at 0.95 Pa and (c) Y current at 0.5 Pa. The Y T-S distances or current as well as their respective compositions are indicated in each graph. In order to compare the patterns, the XRD intensities were normalized to their respective thickness values.

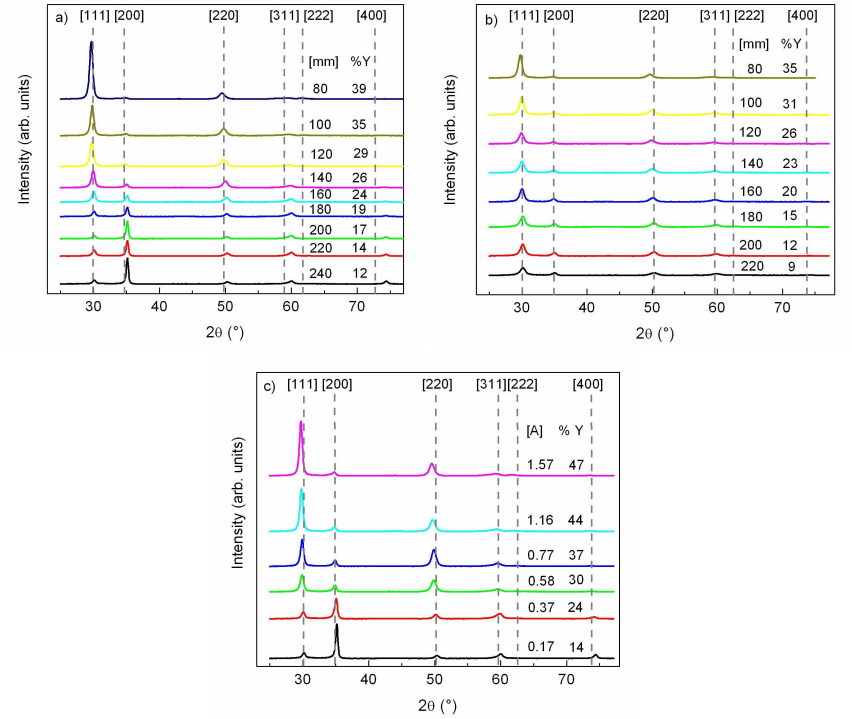

Figure 5.45: Diffraction lines of YSZ samples with a) different T-S distances at 0.5 Pa; b) different T-S distances at 0.95 Pa and c) different Y current at 0.5 Pa.

Note that the XRD diffraction patterns of Figure 5.45a and c indicate a transition from [200] to [111], while Figure 5.45b indicates that the film growths with a [111] preferential direction. The change from [200] to [111] could then be explained by a transition from zone T to a zone II growth, which based on the XRD can be observed starting at 24 at.% Y where the [111] intensity increases while the [200] intensity decreases. Also, a small contribution of [220] appears with the increase of Y content. For even smaller Y T-S distances, and hence higher contents of Y, the [111] intensity significantly increases. The same behavior can be observed in Figure 5.45c. When the current increases, there is a transition from [200] to [111] with a contribution of the [220] direction at higher currents. However, based on the SEM cross images shown in Part III (5.3) and the pole figures of previous section, it is known that our films grow in zone T with a [200] out-of-plane preferred orientation and that a tilt of the [200] occurs with the increase of composition. Therefore, the results obtained via XRD do not indicate the real crystallographic orientation of the YSZ film deposited by dual magnetron sputtering but they are the result of the tilt of the (200) lattice plane.

The $\theta/2\theta$ configuration measures only the planes parallel to the substrate. Due to the tilt, other crystallographic planes, i.e. (111) and (220) become parallel and visible to the θ configuration setup. With this knowledge, it is possible to calculate the crystallographic orientation based on the $\theta/2\theta$ measurements. This misinterpretation of XRD patterns is what we call as the "fictional zone transition" [252].

In order to plot the XRD data in a polar plot, it is necessary to obtain some vectors based on the XRD diffraction. The orientation of a crystal with known unit cell dimensions can be represented in a polar plot by measuring the angles between the crystal faces and a resultant vector. For each sample, a resultant vector was calculated using the fractions of the stereographic projections of the [111], [200] and [220] directions, which correspond to the highest intensity peaks of the XRD data (see Figure 5.45). This vector will have a resultant point in the triangular plane formed by these directions. These directions are situated in the first quadrant of the polar plot as also indicated in Figure 5.46. The resultant vector has two angle components, namely a polar (χ: 0-90°) and an azimuthal (φ: 0-360°) angle. For example, a single crystalline with [200] out-of-plane preferred orientation would have its resultant vector at $\varphi = 0°$ and $\chi = 90°$.

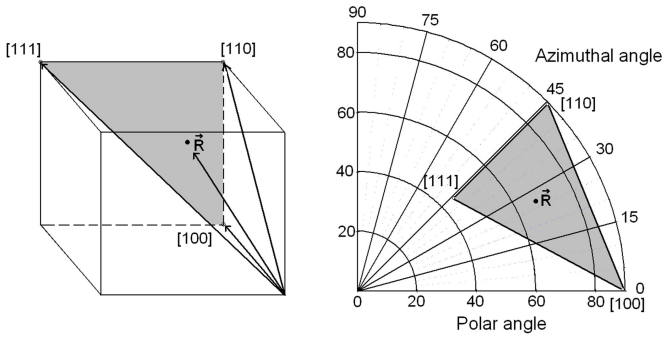

Figure 5.46: Schematic representation of the three vectors obtained from three main directions of the XRD data. The resultant vector resulting from these vectors will be contained in the triangle formed in the first quadrant of a polar plot.

Figure 5.47 shows the representation of those resultant vectors for all deposition conditions using set 2 of samples. The color scale indicates the composition as a function of the Y content. The polar plot can be interpreted in two ways: 1°. as the contribution of the fraction of the different oriented crystals and 2°. as the result of the tilting of the crystals. Therefore it is important when working with a dual magnetron sputtering, to be aware of this when conclusions are made based on XRD ($\theta/2\theta$), in order to avoid misleading information. Using

Figure 5.47a we discuss both interpretations:

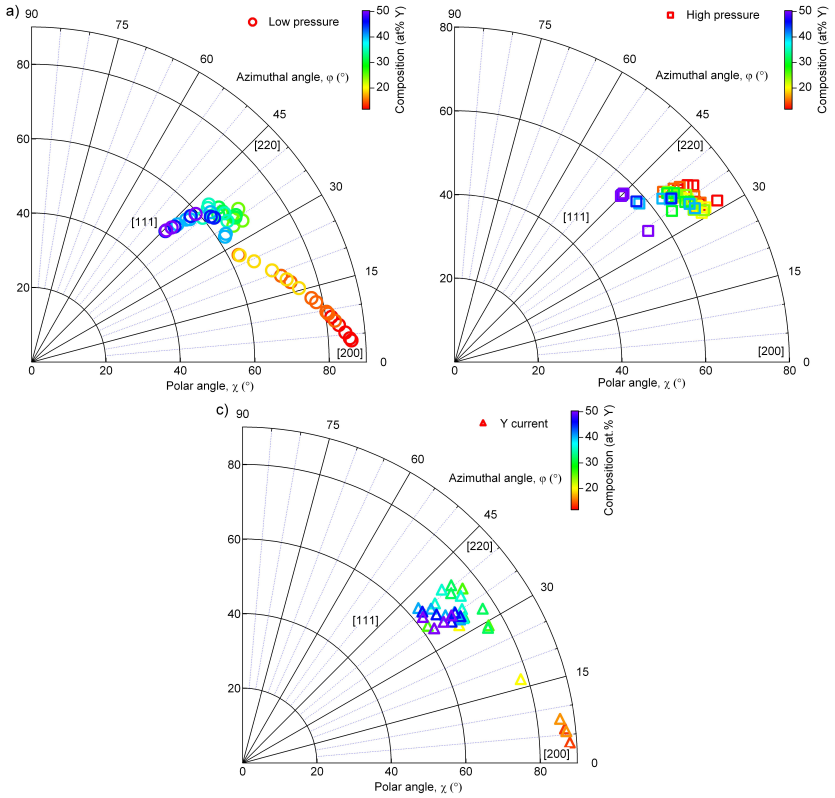

Figure 5.47: Polar plot of the resultant vector calculated for several points at different Y T-S distances based on XRD results obtained using set 2 of samples for a) Y T-S distance from 80 to 240 mm at 0.5 Pa; b) Y T-S distance from 80 to 220 mm at 0.95 Pa and c) changing current from 0.17 to 1.57 A at 0.5 Pa. The color scale shows the compositional variation. Note that the arc behavior is equivalent to the arc shown in the polar plot of Figure 5.44 indicating the equivalence for both pole figures and XRD results.

- 1°: At low pressure, the preferred orientation for low contents of Y or high T-S distance is [200]. With the increase of Y content, a transition from [200] to [111] direction can be seen. In between both, an arc is formed in the direction of [220] from $\chi = 85°$ and $\varphi = 5°$ to approximately $\chi = 45°$ and $\varphi = 45°$. A gap towards the [220] direction can be seen around $\chi = 60°$ and $\varphi = 30°$, representing its contribution. The film becomes [111] preferentially oriented at elevated Y contents. Note that this interpretation describes the

XRD of Figure 5.45a;

- 2°.: The tilt varies from an azimuthal angle of $\varphi = 3°$ at low content of Y up to $\varphi = 30°$ at 25 at.%Y. The gap at $\varphi = 30°$ indicates the rotation of the structure. Then, the tilt continues up to approximately $\varphi = 45°$ at 50 at.%Y.

Figure 5.47b shows the polar plot at high pressure. The [200] is strongly tilted. Moreover, it is clear that the tilt remains confined in a certain region and consequently the film growth is independent of Y content or Y T-S distance. Based on the azimuthal angle of the polar plot we obtain a grain tilt between 30° to 45°. The large interval of the azimuthal angles can be explained by the worsening of the alignment (see Figure 5.40) which gives a large interval of the azimuthal angle.

As described for Figure 5.44c, current has a similar effect as Y T-S distance at low pressure, meaning that the content of Y changes the grain tilt of the lattice. Since the Y variation is not so strong as in the case of Y T-S distance, (see Figure 5.4), the final grain tilt due to the change of current (Figure 5.47c) is lower than in Figure 5.47a. The variation of Y along the sample can also be identified in the arc. As the difference between the contents of Y in the lattice is smaller, the total tilt of the grain becomes also smaller dislocating the arc to higher polar angles.

By comparing the results of the polar plots of Figure 5.44 and 5.47, it is concluded that both results are equivalent and the plots overlap each other. In addition, the advantage of using XRD ($\theta/2\theta$) is that much more data can be obtained in a short period of time with a higher accuracy than when using pole figures.

5.4.3 Influence of the deposition conditions on the grain tilt

In Part III (5.3) a full analysis of the deposition condition on the columnar tilt was limited due to the restricted amount of data available. As a result, we assumed that the columnar tilt varied as a function of the composition. Using the results of the XRD ($\theta/2\theta$), it is possible to discuss the relation between deposition conditions and the grain tilt.

Figure 5.48 considers the change of grain tilt as a function of the deposition conditions (a to c), position on the substrate (d to f) and composition (g to i). Figures 5.48a to c shows the variation of the grain tilt as a function of the Y T-S distance at low and high pressure as well as a function of the discharge current. At low pressure, there is a great interval of tilt at each Y T-S distance, suggesting that the tilt is independent on the Y T-S distance. At high pressure (Figure 5.48b), the grain tilt variation has a maximum of 5°. Moreover, the tilt values remain in the range of 40° independent on the Y T-S distance. Finally, the change of current (Figure 5.48c) shows a combination of both effects as described above. At low

current, there is a large variation of the value of the grain tilt. Starting at 0.77 A the variation in tilt is reduced to 5°. With further increase of current, the average grain tilt slightly increases from 30° to approximately 40°.

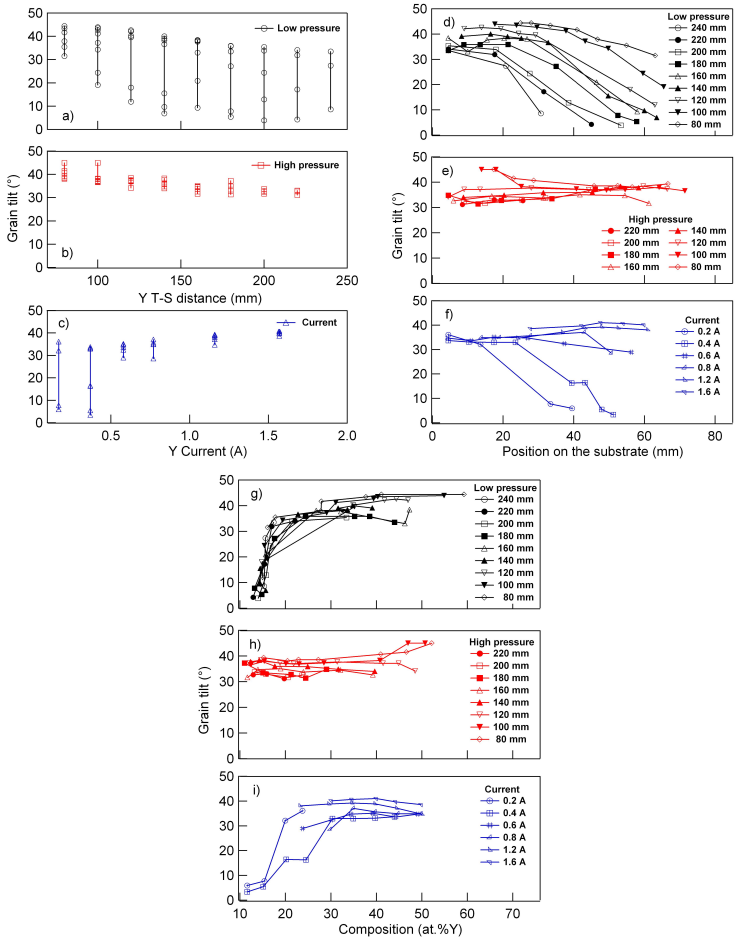

Figure 5.48: Influence of deposition conditions, position on the substrate and composition on the grain tilt: a; d; g) Y T-S distance at low pressure; b; e; h) Y T-S distance at high pressure and c; f; i) Current at low pressure.

Figures 5.48d to f show the grain tilt variation along the sample substrate at different deposition conditions. At low pressure there is a decay of the grain tilt as soon as the position of the substrate gets closer to the Zr side. From the results of Part I (5.1), it was discussed that a straight dependence as a function of the position on the substrate it is not possible to obtain because composition, thickness, grain

size and lattice parameter were shown to vary as a function of the position on the substrate. However, from Figure 5.48e, referring to experiments at high pressure, it is clear that the grain tilt is completely independent of any deposition conditions as well as any film characteristic. This is concluded from the constant values of the grain tilt along the sample. Current, on the other hand, has a similar behavior than seen in Figure 5.48d up to a current of 0.77 A. Above this value, the grain tilt is invariable at approximately 40°.

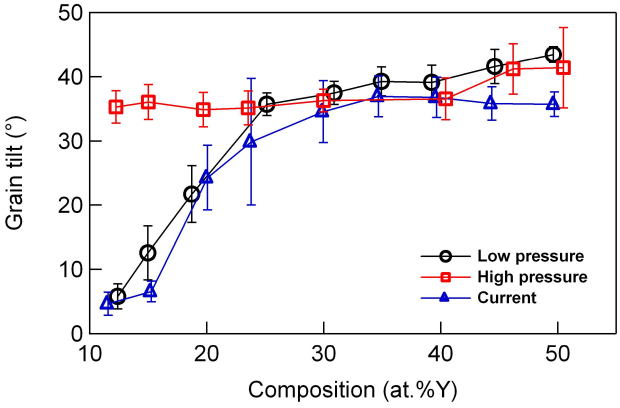

Figure 5.49: Grain tilt as a function of composition for different Y T-S distance at different pressures and current.

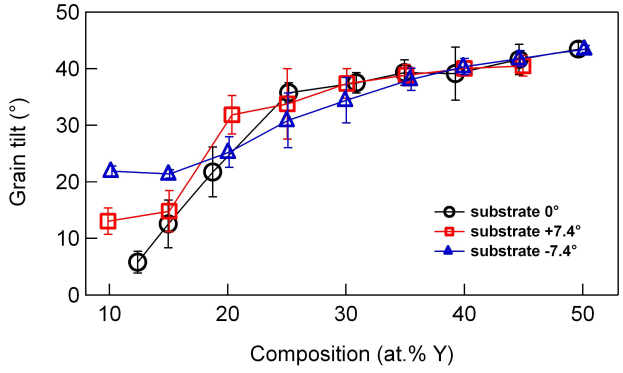

Figure 5.50: Grain tilt vs. composition showing the influence of the change of the substrate angle on the grain tilt.

The influence of the composition on the grain tilt can be evaluated in Figures 5.48g to i. At low pressure, there is a drastic increase of the grain tilt at very small variation of composition. Starting at 25 at.%Y the slope of the curve changes and the grain tilt varies little. In fact, it seems that the tilt reaches a constant value with a maximum of approximately 40°. High pressure shows once more a constant value independent of the content of Y. And current has a similar behavior as shown at low pressure. However, the grain tilt seems to have a smaller value in comparison with the ones at low pressure.

In summary, the results shown in Figure 5.48b, e and h indicate that the grain tilt at high pressure is independent of any deposition condition as well as YSZ characteristic due to the different orientations, directions and energies of the arriving atoms which eliminate the effect of the variation of the content of Y on the tilt. Experiments performed at low pressure with the change of Y T-S distance and discharge current are independent of the deposition conditions but vary as a function of the YSZ characteristics, which are somehow interconnected. At this moment we consider the influence of the composition to explain the behavior of the tilt.

Similar to the columnar tilt, the grain tilt can also be plot as a function of the composition. Figure 5.49 shows the grain tilt for the experiments changing Y T-S distance at low and high pressure as well as the results when varying discharge current. Not surprisingly, the experiments changing Y T-S distance and current at low pressure have an identical behavior as seen for the columnar tilt (Figure 5.33). Up to 24 at.%Y both tilts are equivalent while at contents higher than 24 at.%Y a small difference is noticed. On the other hand, the experiments at high pressure show the constant value of grain tilt independent of the composition, which agrees well with the results obtained above and from the SEM images of Part III (5.3).

Based on the results shown in section 5.3.2.3, we can also analyze the influence of the substrate tilt on the grain tilt. Figure 5.50 shows the grain tilt as a function of Y content. Note that the sample with a substrate angle of 0° is the same as the curve presented at low pressure in Figure 5.49. Below 25 at.% Y there is a change in the grain tilt for different substrate angles. These data were analyzed by statistic t-tests demonstrating significance for low pressures. Above 25 at.% Y, there is a change in curve slope without significant angular differences, meaning that the substrate inclination has no influence on the final grain tilt.

The grain tilt was also shown to vary as a function of the composition as well as with the chamber geometry. Moreover, the behaviors of the columnar and the grain tilt seem to be similar. That is why, we describe in the last part of this chapter (Part V) the comparison between the columnar and the grain tilt and their relations.

5.4.4 Summary and conclusions of Part IV

Since a columnar tilt was observed we investigated the grain tilt by checking the crystallography of these films via pole figures. At low pressure, it was observed that the [200] preferred orientation tilts when Y content increases. At contents of approximately 35 at.% Y not only a tilt is noticed but also a rotation of the lattice. Similarly, the increase of content as a function of the current also demonstrated a change in tilt. However, no rotation was identified. By changing the Y T-S distance to 160 mm, the effect of rotation was noticed. The pole figures at high pressure showed a constant grain tilt. However, at high content of Y the film becomes uniaxial aligned. This is related to the increase in probability of collisions and scattering between adatoms and Ar, which influences the transport of particles to the substrate.

Another way to determine the crystallography of thin films is using XRD ($\theta/2\theta$). However, the XRD patterns of the YSZ indicated a fictional zone transition which does not agree with the results obtained in Part III (5.3). In the presence of a tilt of the cubic lattice, the XRD identifies other directions which do not represent the real out-of-plane preferred orientation. When working with a dual magnetron sputtering, it is important to be aware of the use of a XRD/polar plot to avoid misleading information. Once the right interpretation is used, this technique becomes very simple and accurate. It can lucidly depict possible influences of different crystallographic orientations. Above all it is less time consuming, allowing us to obtain more information in a shorter period of time compared with polar plot based on pole figures.

An analysis of the influence of the deposition conditions on the grain tilt suggested that at low pressure the grain tilt varies as a function of the composition. The behavior of the curve is similar to the columnar tilt described in Part III (5.3). A correlation between grain tilt and composition was done and further investigation of columnar and grain tilt will be discussed in Part V (5.5). Once again we use SIMTRA to determine how the particles are distributed along the sample surface. In this way, we expect to determine the reasoning for the rotation of the lattice at high content of Y as well as the deposition conditions involved in this phenomenon.

5.5 Part V: Relations between grain and columnar tilt

Comparing the results of Part III (5.3) and IV (5.4), it is possible to determine the relations between columnar and grain tilt. In Part V, the relations between columnar and grain tilt will be discussed. In addition, the differences encountered for both tilt will be explained in two different sections. The first leads with the difference encountered between grain and columnar tilt while the second explains the development of the rotation along the sample substrate.

5.5.1 Comparison between grain and columnar tilt

The comparison between grain and columnar tilt at different deposition conditions is illustrated in Figure 5.51.

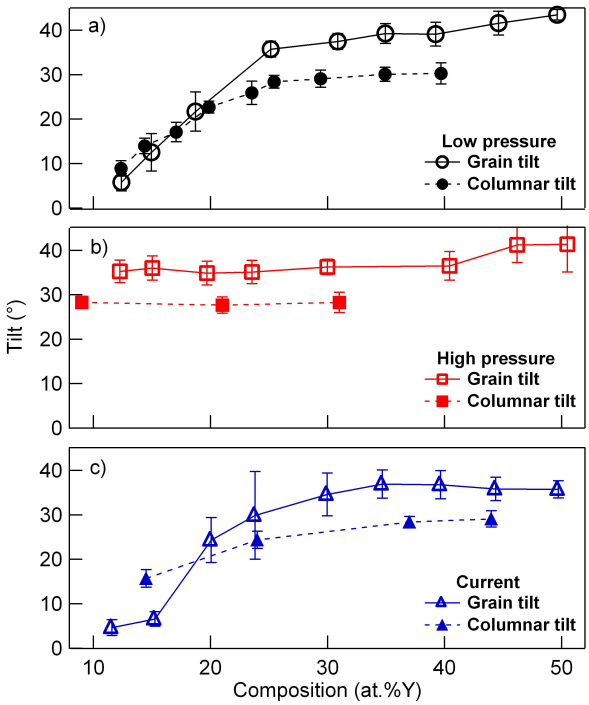

Figure 5.51: Comparison between columnar and grain tilt for different deposition conditions. The grain tilt evaluated from XRD ($\theta/2\theta$)/ polar plot (Figure 5.49), and the columnar tilt obtained from SEM cross section images (Figure 5.33). Both tilts are displayed as a function of the composition measured by SEM-EDX.

The grain tilt in Figure 5.51 is represented by open markers and full lines while the columnar tilt is indicated by closed markers and dashed lines. The deposition conditions under discussion are: (a) Y T-S distance at low and (b) high pressure and (c) current at low pressure.

As Figure 5.51a shows that the grain tilt and the columnar tilt are identical until 20 at.% Y. The grain tilt of Figure 5.51c also seems to follow this linear trend up to 20 at.%Y. Unfortunately, we do not have enough data to compare it with the columnar tilt at low contents of Y. In addition, it is observable that the average tilt values when changing current are slightly smaller than in Figure 5.51a, which can be attributed to the influence of different YSZ characteristics. In addition, it is observed that above 20 at.%Y there is a discrepancy in the columnar and grain tilt value for all the experiments. As explained in Part III (5.3) and IV (5.4) the effect of pressure is independent on the variation of the deposition conditions and YSZ characteristics (see Figure 5.51b).

In a similar way, we can compare the grain and columnar tilt data for the experiments with different substrate angles (0°, +7.4° and -7.4°) from section 5.3.2.3 and 5.4.3. This comparison is displayed in Figure 5.52.

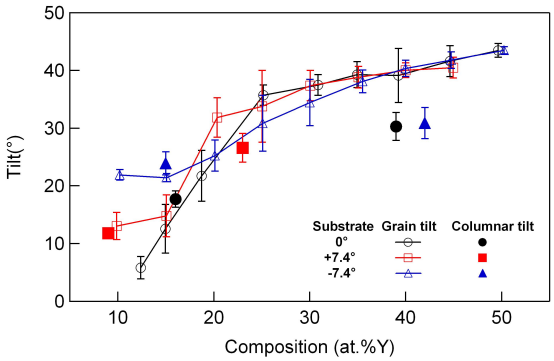

Figure 5.52: Comparison between columnar and grain tilt for the experiments with different substrate angles (data from Figure 5.38 and Figure 5.50).

At low content of Y (< 20 at.% Y), the grain tilt falls within the uncertainty of the columnar tilt obtained in the SEM image of Figure 5.36. This means that in this range of Y content, the columnar tilt is equivalent to the grain tilt. At high content of Y (40 at.%Y), the angles encountered are practically the same (30.3 ± 2.4° and 30.9 ± 2.7°, respectively) indicating that the columnar tilt reaches a maximum of 30°. However, starting at 25 at.% Y we observe a difference in the tilt values between columnar and grain tilt.

The equivalence at low content of Y can be understood from the idea that

the grains are building blocks of the columns. Thus, the tilt variation can be understood by considering the insertion of Y_2O_3 in the ZrO_2 structure. This is schematically indicated in Figure 5.53. Due to the difference in ionic radius between Y and Zr (0.9 and 0.72 Å, respectively), it is possible to consider the tilt as a result of deformed lattices stacked on the top of each other. A similar behavior has also been observed in the work of Saraiva et al. [253] where both tilts were shown to be equivalent.

This deformed cubic structure is a consequence of the compositional gradient between two extremes of the lattice. The deformation increases with the insertion of Y^{3+} in the lattice, meaning more Y in the film. Thus, the tilt formation can be related to three YSZ characteristics, namely: lattice parameter, grain size and content of Y. The lattice and the grain size are both altered as a function of the composition as seen in Figures 5.11 and 5.14. And the content of Y is directly affected by the insertion of yttria in the lattice. A proposed model for the average grain tilt is developed and it will be discussed in detail in Chapter 6.

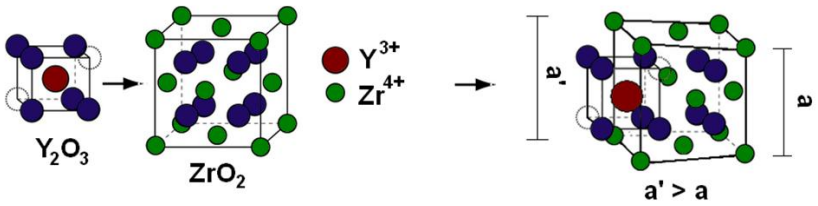

Figure 5.53: Schematic drawing of YSZ lattice: insertion of Y_2O_3 in the ZrO_2 lattice and its deformation generated by the insertion of a higher ionic radius element (Y^{3+}).

The tilt originated from the deformation of the lattice can also explain the behavior of the columnar tilt. As a result, the tilt towards the Zr source is due to the difference in ionic radius. Consequently the columns shown in the SEM cross section images of Part III (5.3) tilt towards the source with the smallest ionic radius, which in this case is the Zr source.

The rotation of the lattice seems to be related to the difference in angle between columnar and grain tilt. Therefore, it is necessary to further understand the nature of both effects. First, we discuss the difference between grain and columnar tilt based on the [111] peak of pole figures. SEM cross section images are also used in order to corroborate with our conclusion. Second, we used the data obtained via SIMTRA to study the effect of the chamber geometry on the particles distribution along the sample substrate. Based on these results it is possible to observe how the tilt and rotation develops along the sample. In order to make these analyses simpler we consider the values of the experiments at low pressure (changing Y T-S distance) because we dispose of more data in comparison to the other experiments.

5.5.1.1 Analyzing the rotation of the tilt

First, we consider the rotation of the lattice. Several representations can be used to determine the orientation distributions, for example plotting as a function of Euler angles or Rodrigues vectors [254]. However, the objects imaging in three dimensional space is not trivially obtained and therefore a visualization of the lattice rotation is complex. Another way to estimate the rotation consists in using the phi and chi values of the [111] peak. The [111] peak is obtained from the pole figure plot using the program TexEval 2.4 (Bruker AXS). Figure 5.54 illustrates the chi and phi values of the [200] and one [111] peak of the samples deposited at low pressure. The [111] peak displayed in this figure corresponds to the peak with the highest intensity represented in the third quadrant of a polar plot. The [200] peak is situated in the first quadrant of the polar plot.

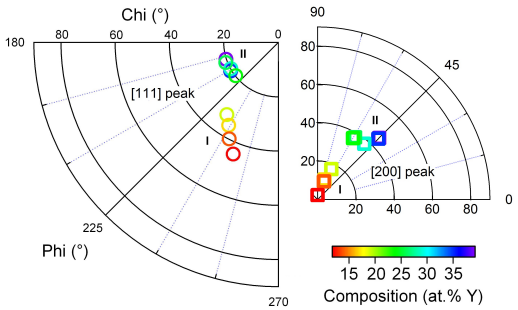

Figure 5.54: The tilt and rotation of the lattice is represented by the [200] and [111]. The [111] peak represents the peask with the highest intensity. The group defined by I indicates a pure tilt of the lattice. The gap between both groups in the third quadrant ([111] peak) corresponds to the lattice rotation. The further variation in phi (group II) indicates a further tilt of the lattice.

In Figure 5.54, two groups can be distinguished: group I and II. Group I corresponds to a pure tilt of the lattice. The total tilt can be observed in the translation of the [111] peak (phi, chi) from (248, 45) to (235, 33) or easily calculate from the translation of the [200] peak from (90, 2) to (66,17) where the tilt value is obtained from the square route of the quadratic difference between both cooridinates, given a tilt of approximately 30°. Starting at 24 at.% Y there is a gap between the values of group I and II. This characterizes the rotation of the lattice. Naturally this hypothetic value of composition (24 at.%Y) is based on the available experimental results. Unfortunately a precise value of composition and Y T-S distance cannot be given since the composition variation from this value and the following one is of ±2 at.%Y. The rotation is defined by the value of the chi axis on the third quadrant, i.e. [111] peak, and is equal to 12°, which corresponds

to the difference between grain tilt and columnar tilt as indicated in Figure 5.51. The variation in phi (seen in group II) suggests a further increase of the tilt while the constant chi indicates no further rotation. In summary, there are two groups with a pure tilt which varies as a function of the Y concentration, but the high Y content species are rotated in comparison with the low content. As a result, we notice a discrepancy between the measured tilt by SEM and the one obtained via XRD.

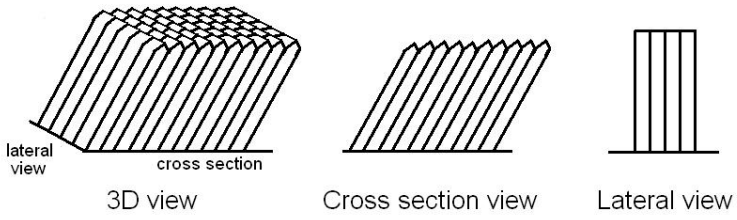

Figure 5.55: Columnar structure represented in 3D, cross section and lateral view.

It is also possible to analyze the behavior of the columnar tilt. The columnar structure, in a cross section view, shows the tilt variation. When this image is seen in a lateral view, the tilt is no longer identified since it is a projection image. The 3D, cross section and lateral view are schematically indicated in Figure 5.55.

Therefore we compare the cross section images of Figure 5.30 with their respective lateral view. The lateral views are displayed in Figure 5.56. In the lateral view images, the samples deposited with a Y T-S distance of 240 mm and 200 mm present low inclination of the columns (4.38 ± 1.54° and 5.56 ± 2.06°, respectively). Sample 160 mm shows a larger tilt in the lateral image (12.5 ± 3.26°) which is attributed to the start of the rotation. The tilt increases with the decrease of the Y T-S distance. For samples 120 and 80 mm a clear tilt is noticed, 14.34 ± 3.06° and 14.16 ± 2.34°, respectively. This trend indicates that the difference between both values of tilt at higher content of Y can be attributed to the 3D growth of the film which cannot be observed by a 2D SEM cross section image. This conclusion is strongly supported by the rotation on the [111] peak in the pole figure at contents of Y superior to 20 at.%, as indicated in pole figure of Figure 5.39d.

However, another contribution for the difference between columnar and grain tilt can be also related to the error involved in the columnar tilt angles obtained via SEM images. At high concentrations, the bending resembles a more curved shape rather than a straight tilt which increases the error when quantifying the columnar tilt angle.

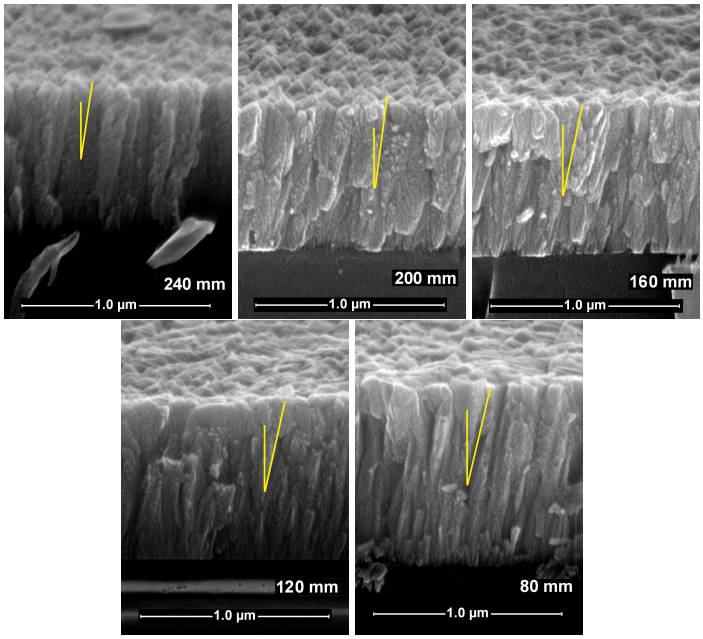

Figure 5.56: Lateral views of the columnar structure for samples 240 mm (4.38 ± 1.54°), 200 mm (5.56 ± 2.06°), 160 mm (12.5 ± 3.26°), 120 mm (14.34 ± 3.06°) and 80 mm (14.16 ± 2.34°) showing the variation from a non inclined to an inclined structure due to the lattice rotation.

5.5.1.2 Analyzing the rotation of the lattice along the substrate

In section 5.4.1, we observe that no rotation of the lattice was identified for Y T-S distances of 240 mm when current was changed. Instead the rotation was noticed at a Y T-S distances of 160 mm when deposited at currents above 0.77 A. Therefore, energy per deposited atom and composition were indicated to have no influence on the rotation. Since the rotation was identified when Y T-S distance decreases, it is believed that the rotation is geometrically related. If the effect of geometry is involved it is possible to simulate it and eventually understand the factors influencing this rotation. Therefore, SIMTRA simulations at different Y T-S at low pressure were performed. As defined in Part II (5.2), a fixed c3 constant of (-0.5, 0) for the angular distribution is used, which corresponds to one of the best fits between experimental and simulated data. The simulation was performed for $1{\times}10^8$ particles with a mesh of 60×60 on the substrate surface (76 mm × 22 mm).

From the simulations we can determine how the content of Y along the substrate varies. Figure 5.57 illustrates the contour plot of the simulated compositional variation for Y T-S distances varying from 80 to 240 mm in intervals

of 20 mm. The color bar corresponds to the total amount of Y (at.%) in the YSZ thin film. In addition, some composition values are also indicated on the contour plot. The position of Zr and Y source are indicated on the top and bottom of Figure 5.57a. This method of plotting remains the same for the other simulations. At low Y T-S distances the direction of the flux of Y and Zr can be observed by the contour lines towards both sides. Moreover, there is a region where both fluxes encounter, which is around 30 to 50 at.%Y (see Figure 5.57a and b). At larger Y T-S distances the amount of Zr is higher and consequently there is dominance of its flux along the sample substrate. As a result, the curvature representing the flux of Zr is easily identified when the content of Y is smaller (Figure 5.57f to i).

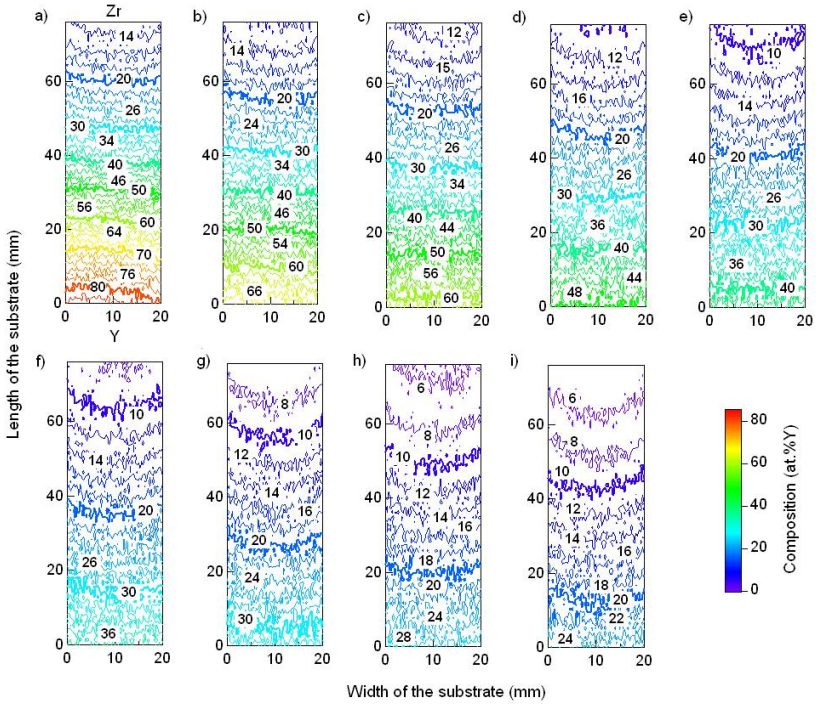

Figure 5.57: Simulation of the deposition surface at different Y T-S distances. From a to i: Y T-S equal to 80, 100, 120, 140, 160, 180, 200, 220 and 240 mm, respectively. The color gradient corresponds to the total amount of Y on the YSZ thin film.

From the simulations shown in Figure 5.57, it is possible to observe that the flux of material is symmetric, i.e. Y and Zr flux are oriented at opposite sides on the substrate and therefore, no geometrical effect can be identified that would indicate the rotation of the tilt. Therefore, we associate the simulated images with pole figures in order to understand how the lattice behaves due to the variation of

the Y content on the film. For this analysis we consider two full YSZ samples at different Y T-S distance (80 mm and 100 mm). Some points are selected along the length of the YSZ film as indicated in Figure 5.58a. Next, the pole figure of each of these points is obtained. The point equal to 0 on the substrate corresponds to the position closer to the Y source. In the same way we can define the same points on the simulation image. This image is shown in Figure 5.58b. Note that the contour plot was limited to discrete values of composition for better visualization. The x and y axis correspond to the dimensions in mm of the substrate.

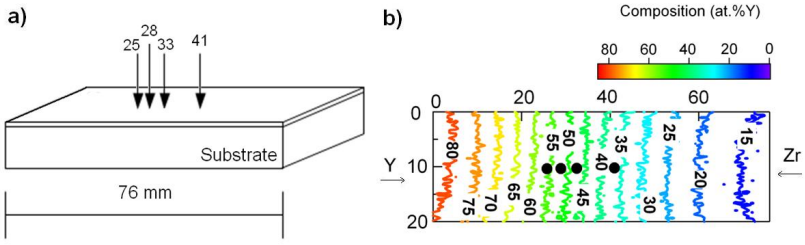

Figure 5.58: a) Selected distances from an YSZ sample deposited with a Y T-S distance of 80 mm. The marked points are given in mm. b) Selected distances are indicated on the simulated image. The x and y axis are given in mm and correspond to the dimensions of the glass substrate.

The (111) pole figures of the selected points indicated in Figure 5.58 are shown in Figure 5.59. From the results obtained for samples deposited at 80 mm, we observe that at contents of 32 at.% Y (Figure 5.59a) there are still two main [111] peaks near the center of the pole, indicating the tilt of the cubic lattice in the direction of Zr source. However, the high intensity of the [111] peak suggests that the rotation already started. Above 46 at.%Y (samples b to d) it is possible to identify the rotation of the lattice. In addition, the rotation seems to remain constant, which agrees with the conclusions presented in group II of Figure 5.54. Based on these results, a quantitative value of the rotation cannot be determined because the interval between values is still too large. In order to determine the start of the rotation, a larger region of compositional variation was chosen in order to detect quantitatively the rotation.

The same approach was followed for samples deposited with a fixed Y T-S distance of 100 mm. This distance was chosen because the variation in composition along the film is smaller than at 80 mm. Thus, the acquisition of pole figures at a fixed position is more accurate. The representations of the positions on the substrate as well as the positions on the simulated image are shown in Figure 5.60.

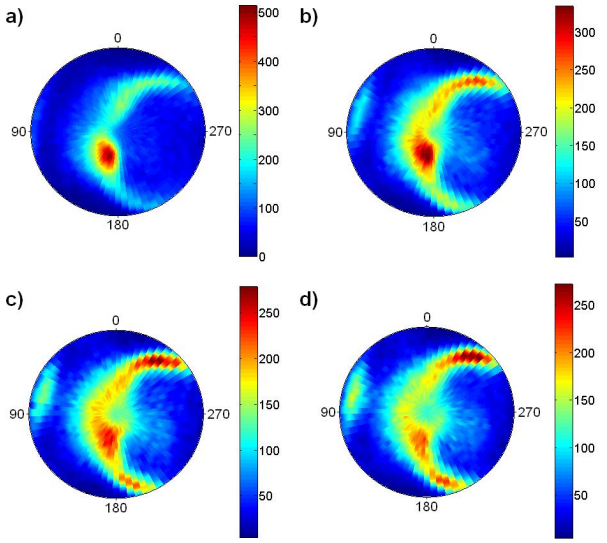

Figure 5.59: Rotation of the cubic lattice along an YSZ sample (Y T-S distance = 80 mm). Position on the substrate: a) 41 mm (32 %); b) 33 mm (46 %); c) 28 mm (50 %) and d) 25 mm (55 %Y).

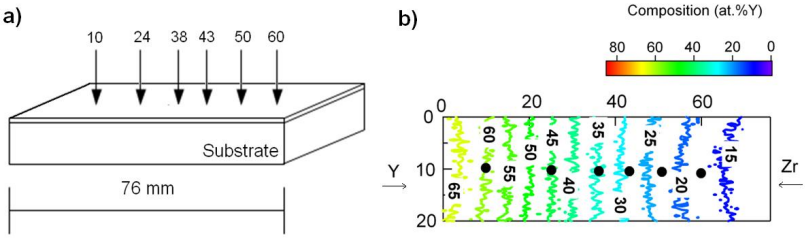

Figure 5.60: a) Selected distances from an YSZ sample deposited with a Y T-S distance of 100 mm. The marked points are given in mm. b) Selected distances are indicated on the simulated image. The x and y axis are given in mm and correspond to the dimensions of the glass substrate.

Figure 5.61 illustrates the (111) pole figure from the selected distances shown above. The position of the peaks can be correlated with the compositional variation shown in Figure 5.60b. Note that the rotation appears along the sample deposited at a fixed Y T-S distance. Figures 5.61a to c (60, 50 and 43 mm) indicate four [111] peaks, which corresponds to compositions lower than 30 at.% Y. Figure 5.61d (38 mm, > 35 at.% Y), the four peaks are no longer identified, being replaced

by two peaks with one high intensity [111] peak. Samples (e) and (f) (24 mm and 10 mm with the respective compositions of 48 % and 58 %) clearly show the rotation, being represented by three main intensities along a semi circle and a low intensity peak on the left hand side of the pole, the latter starting to be formed already in sample (d). Despite of the different content of Y in samples (e) and (f), no difference in the rotation can be noticed in agreement with the results discussed above for Y T-S distance of 80 mm. Therefore, it is possible to conclude that the rotation begins at 20 at.%Y (sample b) reaching a full rotation at approximately 48 at.% Y (sample e).

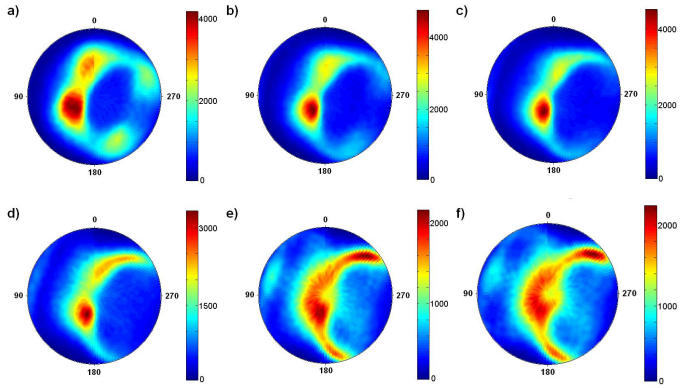

Figure 5.61: Rotation of the cubic lattice along an YSZ sample (Y T-S distance = 100 mm). Position on the substrate: a) 60 mm (14 %); b) 50 mm (20 %); c) 43 mm (28 %); d) 38 mm (35 %); e) 24 mm (48 %) and f) 10 mm (58 %Y).

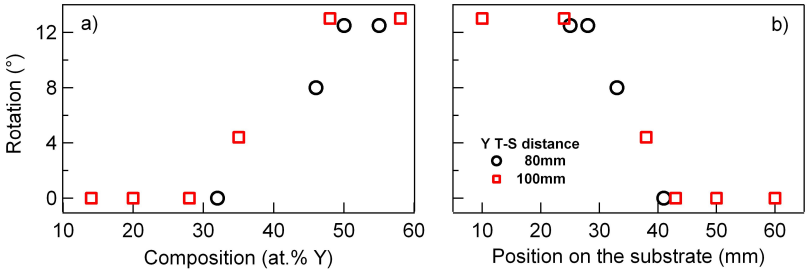

Figure 5.62: Rotation obtained for two different Y T-S distances (80 and 100 mm) as a function of the composition and the position of the substrate.

Simplifying the description given for Y T-S distance of 80 and 100 mm we

can plot the rotation as a function of the composition as well as a function of the position on the substrate. This representation is given in Figure 5.62. First of all, it is important to emphasize that the variation in tilt in group I of Figure 5.54 considers no rotation of the lattice and therefore the rotation is null up to 28 at.% Y in Figure 5.62a and above 40 mm in Figure 5.62b. Note that with a Y T-S distance of 80 mm, the rotation starts at 32 at.% Y and a position of 41 mm and it has a maximum of 12° at 50 at.% Y and 28 mm. When the Y T-S changes to 100 mm there is a small dislocation of the values from 28 at.% Y and 43 mm to 48 at.% Y and 24 mm, which is related to the increase of the Y T-S distance.

Based on these results we observe that a fixed low Y T-S distance is not the main component to generate the rotation but the content of Y does play an important role on the rotation. This effect explains why the high content of Y at high Y T-S distance (see Figure 5.41) was not able to rotate the lattice. Therefore, we conclude that only a combination between geometry of the chamber and content of Y results in the rotation of the lattice.

5.5.2 Summary and conclusions of Part V

The comparison between grain and columnar tilt suggests that there is a linear equivalence of angles up to approximately 25 at.% Y. The insertion of an element of large ionic radius in the ZrO_2 lattice creates a deformation of the lattice. As a result, a column is formed by the addition of several grains on the top of each other. This results in the equivalence between columnar and grain tilt. The effect of pressure, on the other hand, was shown to eliminate the dependency of any YSZ characteristic on the tilt. Above 25 at.%Y, a difference between both tilts is noticed. Using the [111] peak of the pole figure we observed that the difference between grain and columnar tilt is 12°. This difference was shown to occur due to a rotation of the lattice. Using SEM images of a lateral view, it was observed that the columns are tilted at high content of Y. This indicates that the rotation induces a 3D growth which cannot be observed in a 2D cross section image. The development of the rotation was explained using pole figures. The rotation was identified to be triggered by Y T-S distance and also by the content of Y.

Taking into consideration the conclusions described above, we can conclude that the grain tilt varies as a function of the YSZ characteristics such as: composition, lattice parameter and grain size. Therefore, the relations between these characteristics should be further analyzed. Thus, it becomes necessary to understand the phenomena involved at nano scale, i.e. along a particular column of the film. In addition, the proposal of a stress model to predict the tilt of the grains based on the characteristics of YSZ films will be discussed in Chapter 6.

6

Macroscopic modeling of the nano-scale behavior

In Chapter 5, the preferred orientation of YSZ thin films was studied as a function of Y T-S distance, pressure and current. Using the crystallographic and microstructural information of those YSZ thin films, it was observed that they remained in zone T. Hence, a particular columnar tilt develops as soon as the yttrium content increases. In this chapter a model will be developed to explain the observed tilt. The structure of this chapter will consist of two parts:

The first part of this chapter discusses a quantitative analysis performed at the nano scale, taking into consideration the behavior of the compositional gradient in a single column. The latter is obtained via scanning transmission electron microscope-energy dispersive X-ray analysis (STEM-EDX). Next, a correlation between the macroscopic level (from Part III to V (5.3 to 5.5), Chapter 5) and the nano scale is developed. This correlation suggests that the variation of composition within a single YSZ column can be calculated from the macroscopic compositional variation. Based on this correlation, it is possible to calculate the observed tilt from measurements at the macroscopic scale using a simple stress model.

The second part of this chapter deals with a similar analysis. In this case the full length of YSZ samples is considered. In this way, the full compositional gradient developed along the layer can be evaluated with the stress model. Finally, a study about the columnar tilt along the full sample will also be discussed.

6.1 Using macroscopic scale to determine nano scale characteristics

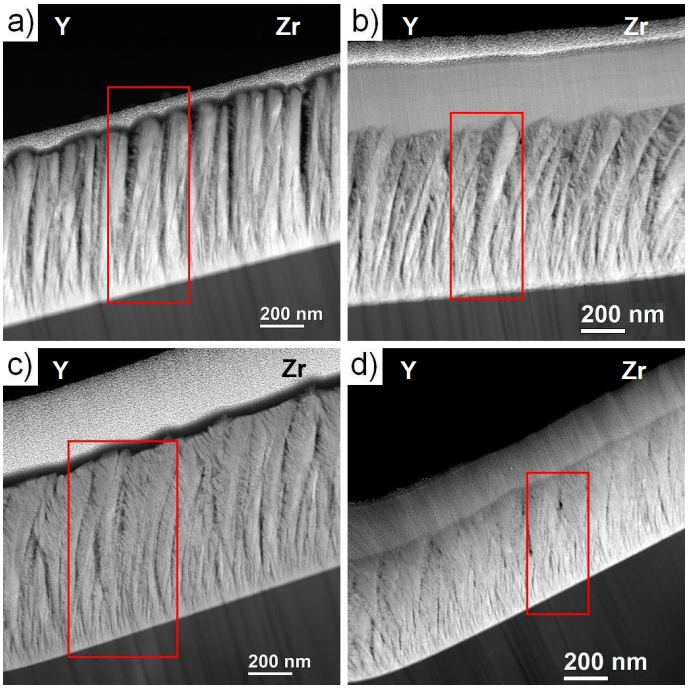

Figure 6.1: ADF-STEM images of four different samples with the following Y T-S distances: (a) A: 240 mm; (b) B: 160 mm; (c) C: 120 mm and (d) D: 90 mm deposited at low pressure. The marked rectangle indicates the region of STEM-EDX mapping. Y and Zr on the figures indicate the direction of the material flux.

The dual magnetron configuration induces anisotropy in the flux of material towards the substrate. As demonstrated in the work of Radnóczi et al. [255] and Saraiva et al. [253] for AlInN and Mg(M)O (where M = Mg, Al, Cr, Ti, Zr and Y), respectively, the deposition strategy will induce a compositional gradient over the constituting crystallites. The quantitative compositional gradient along the columns is obtained via TEM analysis in combination with ADF-STEM and STEM-EDX as described in section 4.6.6, Chapter 4. Figure 6.1 shows the ADF-STEM images of four different samples with the following Y T-S distances: (a) 240 mm; (b) 160 mm; (c) 120 mm and (d) 90 mm deposited at low pressure. For further discussion we label them as A (240 mm), B (160 mm), C (120 mm) and D (90 mm). The investigated area is highlighted by the red rectangle. Y and Zr on the figures indicate the direction of the material flux. The V-shaped facetted

columns are well defined and correspond to the microstructure exhibited in the SEM images shown in Figure 5.30, Chapter 5. A flatter surface when the content of Y increases is also noticed. Moreover, the porosity formed between the columns can be observed. The silicon substrate is indicated by the darker region beneath the columns. The top layer above the columns is the protective layer deposited while preparing the sample via FIB.

Figure 6.2 shows the color map representation of the STEM-EDX images for the highlighted area shown in Figure 6.1. It is possible to distinguish the enrichment of Y on one side of the column. The Y concentration is indicated by the color bar. In order to obtain the composition coordinates on a column, the data collected via STEM-EDX is used. Each pixel in this mapping corresponds to a determined content of Y.

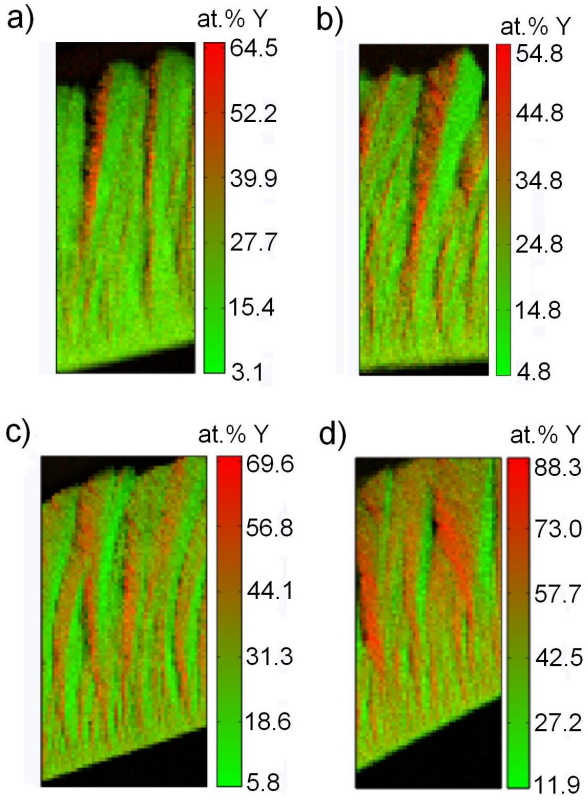

Figure 6.2: Color map of the Y distribution along the columns in YSZ thin films of the highlighted areas of Figure 6.1. The color bar represents the amount of Y in at.% in the column, higher contents of Y are indicated by the red color.

The compositional gradient within the columns is defined by high and low content of Y, as depicted in the color map of Figure 6.2. It is also possible to quantitatively determine the amount of Y present in the columns by overlapping the STEM-EDX mapping with the images of ADF-STEM (Figures 6.1 and 6.2). This overlapping can be better visualized in Figure 6.3 for samples A, B, C and D. The contour plot based on the composition coordinates of each pixel of the STEM-EDX mapping overlays the ADF-STEM images. The resulting image allows the precise determination of the composition over each of the columns.

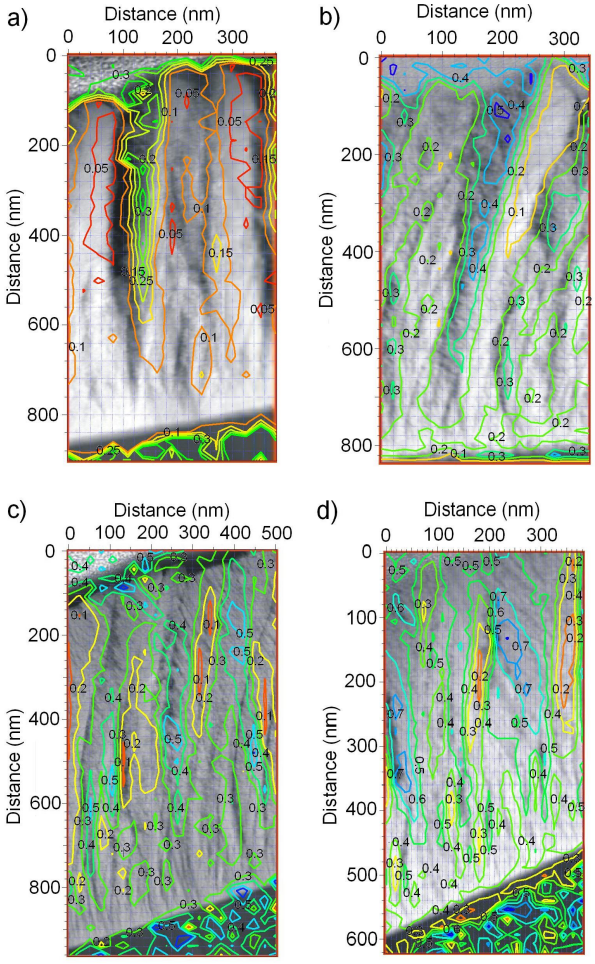

Figure 6.3: Contour plot of the STEM-EDX mapping over the ADF-STEM image. This overlapping allows the compositional determination along the columns for samples: a) A; b) B; c) C and d) D.

The difference in Y content observed from Figures 6.2 and 6.3 defines a compositional profile. An example of a composition profile within a column as a function of the distance for sample A, B, C and D is shown in Figure 6.4.

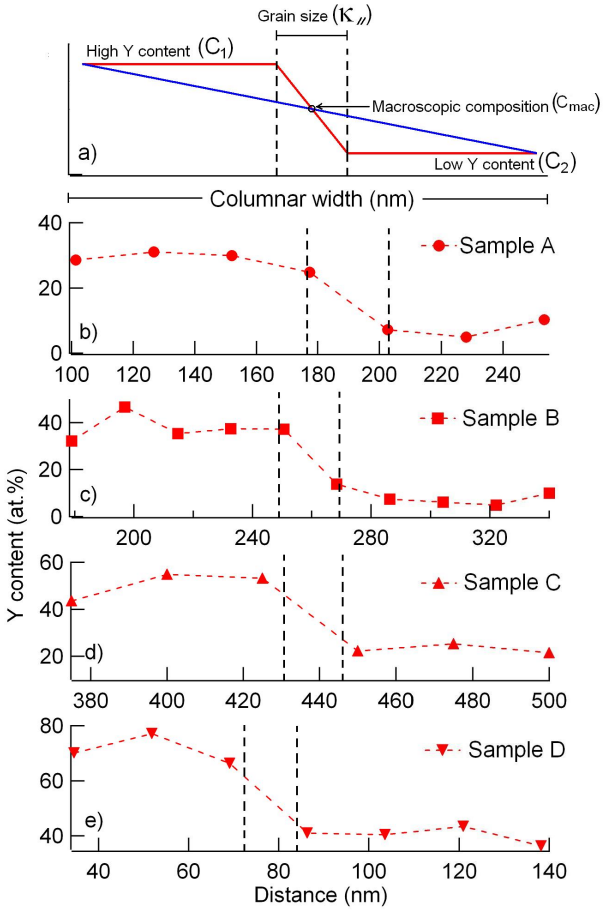

Figure 6.4: a) Schematic drawing of the compositional profile indicating the high content of Y (C_1), low content of Y (C_2), the average in composition which corresponds to the macroscopic composition (C_{mac}) and the region of transition between high and low content delimited in the x axis by the grain size ($\kappa_{//}$). Compositional profile within a column of the YSZ samples with Y T-S distance equal to: a) A (240 mm); b) B (160 mm); c) C (120 mm) and d) D (90 mm).

The compositional profile within a column is schematically represented in Figure 6.4a. Based on several analyses, it is concluded that the composition changes over a distance much smaller than the corresponding columnar width.

Moreover, these distances agree with the distance of a grain size ($\kappa_{//}$) parallel to the substrate. In Chapter 5, the grain size was determined (from $\theta/2\theta$ measurements), but the obtained values are valid for the out-of-plane orientation. Therefore, a few samples were measured with grazing angle XRD [256] (at 1°), and as Figure 6.5 shows, similar values are found for the grain size parallel to the substrate, indicating that the grains have a symmetric shape. In the following, we assume that the grain size determined in Chapter 5 can be used for the calculation of the compositional gradient.

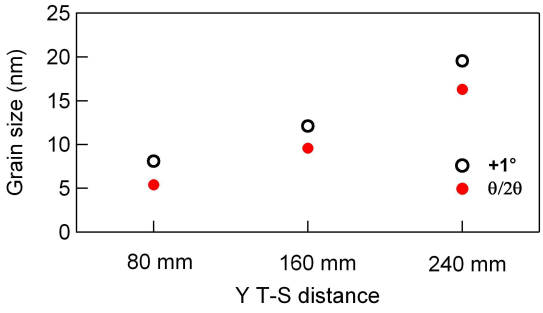

Figure 6.5: Grazing angle XRD for samples deposited at three different Y T-S distances with no inclination ($\theta/2\theta$) and with a grazing of 1°.

The compositional gradient along a column is considered to be the difference in composition between high (C_1) and low content (C_2) of yttrium divided by the corresponding average grain size being equal to 25, 22.7, 12.1 and 11.5 nm for samples A, B, C and D, respectively. These grain sizes are indicated by the dashed lines between high and low content of Y in Figures 6.4b to e. The grain size of Figures 6.4c and d are smaller than the interval between points due to the limitation of the measurement. In summary, the compositional gradient within a column is given by:

$$\frac{\partial C}{\partial x} = \frac{C_1 - C_2}{\kappa_{//}} \tag{6.1}$$

The analysis based on ADF-STEM and STEM-EDX reveals three interesting findings:

- The first finding is related to the ratio between the maximum and the minimum Y content on a column. Taking 12 different locations within the columns of each sample of Figure 6.2 we can calculate the average ratio ($R = C_1/C_2$). The R of samples A, B, C and D is 3.048 ± 0.764, 3.601 ± 0.862, 3.772 ± 1.803 and 2.708 ± 0.511, respectively. Hence,

this ratio between both compositions is approximately 3/1 and seems to be independent of the T-S distance. This can be understood from the fact that the flux of atoms from the Y source remains the same, independently of T-S distance. This means that, the proportion of Y on the left hand side of the column increases likewise the amount of Y on the right hand side. As a consequence, the ratio between both sides of the column remains constant.

It is possible to have an idea of the value of this ratio by using the Tangent Rule [257]. This rule assumes that adatoms will impinge on a substrate with a certain angle and with a certain probability. The ratio probability (R) can then be calculated by simple geometry as indicated in equation 6.2:

$$R = \frac{3cos\alpha + \sqrt{3}sin\alpha}{3cos\alpha - \sqrt{3}sin\alpha} \tag{6.2}$$

where α is the incident angle. A schematic drawing of the incoming material on the surface is depicted in Figure 6.6.

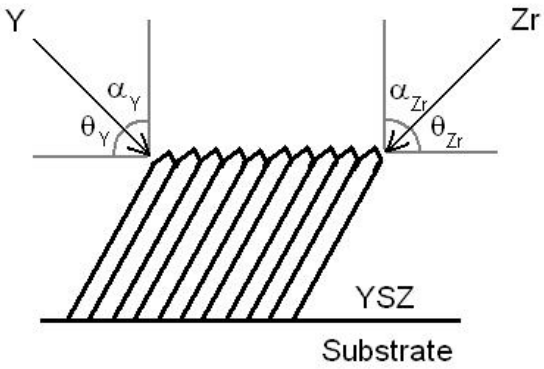

Figure 6.6: Schematic drawing of the incoming material arriving on the YSZ sample. The incident angle used in equation 6.2 is indicated by α.

The incident angle (α) corresponds to the angle measured from the incoming material to the normal and can be obtained via SIMTRA [240]. Therefore, simulations for Y and Zr were performed in order to determine the incident angle (α). The histograms of the simulated incident angle for Y for samples (A) 240 mm, (B) 160 mm, (C) 120 mm and (D) 90 mm and Zr at 90 mm are shown in Figure 6.7. The values in the x axis of the histogram are given in acos and vary from -1 to 1, i.e. from -90 to 90°. The angles corresponding to the maximum of the distribution is given in the caption of the figure.

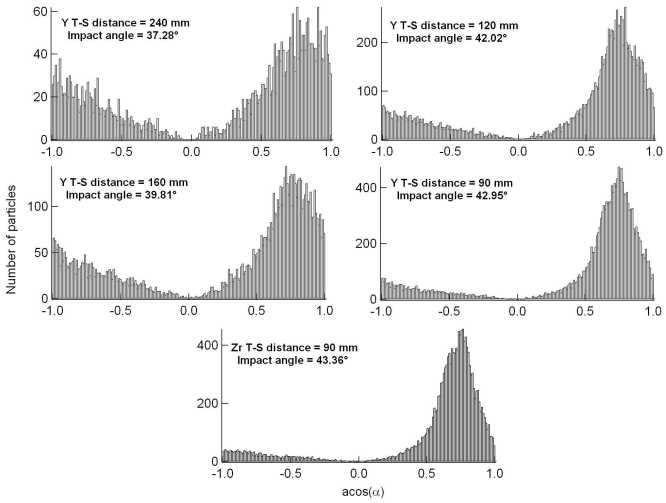

Figure 6.7: The incident angle distributions obtained for Y for samples (A) 240 mm, (B) 160 mm, (C) 120 mm , (D) 90 mm and Zr at 90 mm.

The angular distribution of Zr indicates that the incident angle lies on approximately 0.727, which corresponds to an angle of 43.36°. Note that the histogram indicates that the particles come mainly from the positive side (0 to 1), i.e. the particles arrive on the substrate with a defined orientation (from 0 to 90°). The Y distribution shows smaller impact angles when the Y T-S distance varies to larger values. This is associated with the Y T-S distance. At smaller Y T-S distance the free path is reduced and as a consequence the emitted atoms arrive on the substrate with almost no deviation. This can be seen by the negative part of the distribution where the contribution of the atoms arriving from another orientation is almost null (see Y T-S distance 90 and 120 mm). When the Y T-S distance increases, the mean free path also increases and the atoms arriving from the target have a broader distribution on the sample surface, which favored smaller impact angles. In addition, it is also possible to observe that the contribution of the atoms coming from another orientation also increases with the increase of Y T-S distance; however, the main contribution still comes from the positive side of the histogram.

Substituting the average α angles (Y and Zr) for samples 240 mm, 160 mm, 120 mm and 90 mm on equation 6.2 we obtain the following ratios 2.92, 3.10, 3.28 and 3.36. These results are in agreement with the ratios obtained in Figure 6.4 within the error of the STEM measurement.

- The second finding is that the composition measured by EDX-SEM is equivalent to the difference in composition measured by EDX-STEM. This allows us to rewrite equation 6.1 as,

$$\frac{\partial C}{\partial x} = \frac{C_1 - C_2}{\kappa_{//}} = \frac{C_{mac}}{\kappa_{//}} \frac{2(R-1)}{R+1} \tag{6.3}$$

with C_{mac} (macroscopic) the average composition of the sample, and R is the ratio between the high and low content of Y. As the latter ratio is independent of the T-S distance, equation 6.3 indicates that the compositional gradient can be retrieved from measurements at the macroscopic level, facilitating the analysis since no TEM sample preparation is needed. As R equals approximately C_1/C_2=3/1, (C_1-C_2) (at nano-scale) equals to C_{mac} showing the equivalence between both values. Therefore, a 1:1 relationship is expected between the compositional gradient at nano-scale (ADF-STEM and STEM-EDX measurements) and at the macroscopic level (SEM-EDX). This is confirmed in Figure 6.8.

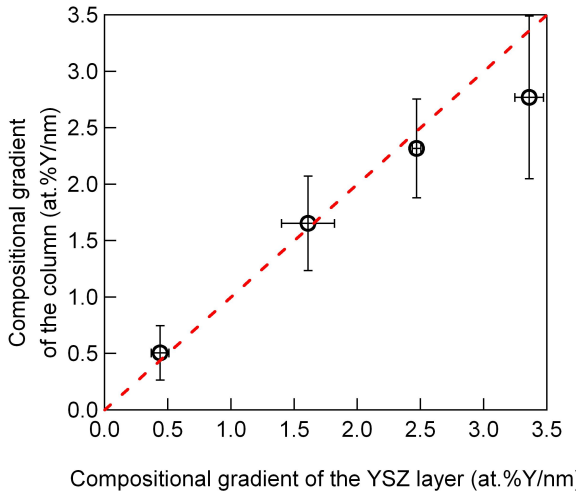

Figure 6.8: Compositional gradient of a single column (STEM-EDX) vs. the local compositional gradient of the layer (SEM-EDX). The dashed line shows the 1:1 relationship.

- Finally the third finding is related to stress in the column. We start by considering a pure ZrO_2 lattice. The introduction of Y_2O_3 deforms the resultant lattice because of the higher ionic radius of the Y, as seen in Part V (5.5), Chapter 5. Supposing that Y accumulates in the left hand

side of the lattice and the Zr remains in the right hand side, we can easily suggest that the left hand side will have a tensile stress while the stress on the right hand side will be compressive. This average in composition (and also in lattice parameter) is identified by the compositional profile in Figure 6.4a and in the color map of Figure 6.2 where two regions with different contents of Y are distinguished. However, the considered lattice parameter corresponds to the lattice obtained for a certain macroscopic composition. This macroscopic composition, as explained in one of the findings above, is the average between C_1 and C_2. As a consequence the average lattice is the contribution of the lattice in C_1 and C_2. As a result the average stress on the column is null due to the average between a compressive and a tensile stress. Therefore, the lattice parameter as seen in Figure 5.14, Chapter 5 follows a linear trend as suggested by Vegard's law.

6.2 Prediction of the grain tilt based on a stress model

In order to understand the effect of the grain tilt based on the film characteristics a model is proposed. This model is based on the work of Timoshenko [258] for the prediction of the bending of a bimetallic thermostat. In the latter, two different metal strips are connected to each other as indicated in Figure 6.9. As the two metals have different thermal expansions, heating will result in the bending of the structure as a whole, as illustrated in Figure 6.9b.

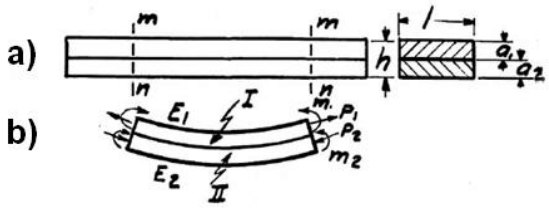

Figure 6.9: Schematic drawing of the effect of the two metal strips of the work of Timoshenko submitted to a variation of temperature [258]. a) The variables defining the metal strips; b) the curvature generated by the effect of the temperature variation.

Due to thermal expansion, the metal strip will have a curvature with a certain radius (ρ). This radius ρ in the work of Timoshenko is given by:

$$\frac{1}{\rho} = \frac{6(\alpha_1 - \alpha_2)(t_f - t_0)(1+m)^2}{w\left(3(1+m)^2 + (1+mn)\left(m^2 + \frac{1}{mn}\right)\right)} \tag{6.4}$$

with, α_i being the thermal coefficient of metal 1 and 2, (t_f-t_0) the variation of temperature, w the total width of the bimetal strips, m the ratio of the strip thicknesses, and n the ratio between the elastic moduli of both metals. Note that the product (α_1-α_2)(t_f-t_0) corresponds to the relative difference in length (L_1-L_2)/L between both strips.

An analogy exists between the metal strips of Timoshenko and our YSZ films. A schematic drawing of the YSZ columnar growth is shown in Figure 6.10. The Y source is located at the left hand side, while the Zr source is located on the right hand side, meaning that the increase of Y content leads to a tilt of the column towards the Zr side, as indicated in Figure 6.10a. In this drawing the compositional profile of each column (determined via STEM-EDX) can be identified. In addition, a straight line through the columns is shown. The latter corresponds to the macroscopic composition (determined via SEM-EDX). In the center of each column, there is a marked region which equals to the grain size value. L_2 defines the region of smaller expansion while L_1 defines the region of larger expansion of the lattice. This expansion is due to the insertion of Y_2O_3. The variable h corresponds to the total thickness of the film.

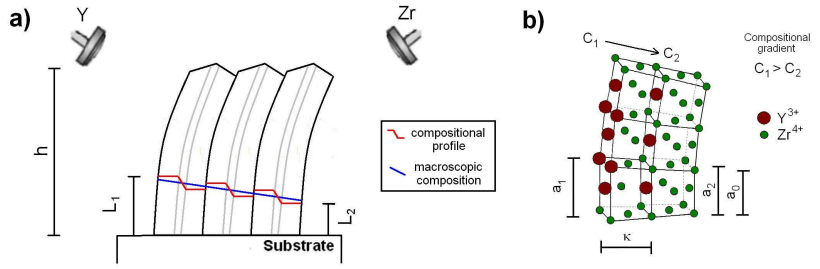

Figure 6.10: a) Schematic drawing of the columnar growth on the substrate. The Y and Zr target are positioned on the left and right hand side, respectively. The compositional profile and the macroscopic composition are indicate in the image. L_1 and L_2 represent the different expansions and h defines the total thickness of the film. The gray region in the column defines the variation of the compositional gradient within a grain size distance. b) Visualization of a schematic grain deformed by the addition of Y. The compositional gradient, lattice parameter and the grain size width are indicated in the figure.

As stated before, the product (α_1-α_2)(t_f-t_0) in the model of Timoshenko (equation 6.4) corresponds to a relative length difference between the two metal stripes over the initial length (L_1-L_2)/L. In our case, this product is the difference in lattice parameter between both sides of the column over the lattice parameter

(a) of a pure ZrO_2. Figure 6.10b shows the schematic drawing of the lattice deformation with the insertion of Y. The lattice parameter of YSZ was determined by XRD [259] as seen in section 5.1.3, Chapter 5. Moreover, it was shown to follow Vegard's law [7], i.e. it has a linear dependence with the composition. Hence, the relative length difference in the case of YSZ can be written as follows:

$$\frac{L_1 - L_2}{L} = \frac{a(C_1) - a(C_2)}{a} = \frac{\Delta C(r_Y - r_{Zr})}{a} \tag{6.5}$$

with a(C_1)-a(C_2) being the difference between the two lattice parameters of the column, which can also be given by the difference in composition (content of Y) multiplied by the difference of ionic radius of the two metals (0.72 and 0.9 Å for Zr and Y, respectively). This difference is the slope of the lattice parameter vs. composition as shown in Figure 5.14, Chapter 5.

We can expect that the elastic modulus of YSZ does not strongly depend on its composition, and therefore n in equation 6.4 can be set equal to 1. In the model of Timoshenko the radius is proportional to the total width of the metal strips w. However, based on the SEM images shown in Figure 5.30 of Chapter 5 and Figure 6.1 of this chapter, the columns become wider as the film thickness increases but no change in the tilt is noticed. This remarkable result can be explained as follows. The main difference with Timoshenko's model is that the columns are built from several individual grains. From the STEM-EDX and ADF-STEM measurements we observe that only the grains at the center of the column show a compositional gradient, and behave as the metal strips, i.e. two parts with a different length intimately attached to each other. Therefore, w in equation 6.4 has to be replaced by the grain size ($\kappa_{//}$) and not by the column width. Based on this reasoning we can assume that also m in equation 6.4 equals 1. Assuming for the case of YSZ that both m and n equal 1, equation 6.4 reduces to:

$$\frac{1}{\rho} = \frac{3\Delta C(r_Y - r_{Zr})}{2\kappa_{//} a} \tag{6.6}$$

As $\Delta C/\kappa_{//}$ equals the compositional gradient $\partial C/\partial x$, the inverse of the curvature is proportional to the compositional gradient. By approximating the bent column by a straight line, the measured tilt (β) can be calculated as,

$$\beta = \frac{1}{2} arcsin\left[\frac{3h(r_Y - r_{Zr})}{2a}\frac{\partial C}{\partial x}\right] \tag{6.7}$$

where h is the thickness of the film (see Figure 6.10a). This equation agrees with the equation proposed in a previous paper of our research group [253], even though a different reasoning was followed. In the work of Saraiva [260], the change in compositional gradient modifies the size of the metal cation from one

side to the other of the grain. As a consequence, there is an angle α defined by the difference between the angle formed by the cations and oxygen layers. In addition this tilt increases with the increase of the grain size for each d-spacing in the *hkl* plane. The total tilt gives the grain tilt (β). Both arguments are based on geometric arguments and therefore it is not surprising that both models agree. However, the current model has the advantage that the film characteristics can be taken into consideration.

Using the information of the obtained compositional gradient in combination with equation 6.7, the tilt angle was calculated. The calculation is performed for both the macroscopic compositional gradient (obtained via SEM-EDX) and the gradient measured at the nanometer scale (within a column, obtained via STEM-EDX). Both results, compared to the grain tilt are shown in Figure 6.11. Despite the simplicity of the model, the prediction agrees well with the experiment. As a result, the grain tilt can be predicted on YSZ thin films on a macroscopic scale and these results can be used to determine the tilt on nanometer scale.

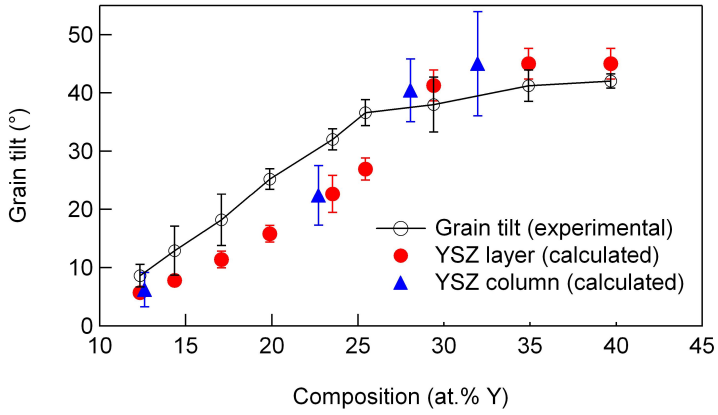

Figure 6.11: The experimental grain tilt plot at low pressure (from Figure 5.49) together with the calculated tilt based on the measured macroscopic compositional gradient (SEM-EDX, closed round markers), and the calculated tilt based on the measured compositional gradient at nanometer scale (STEM-EDX, closed triangle markers).

Since it was shown that the composition at macroscopic level is equivalent to the composition at nano-scale, we further investigate the use of the model to the other deposition conditions, namely current and high pressure.

First, we consider the model to the experiments with different discharge currents. The incident angle at different Y currents is the same as the one shown in sample A (240 mm) of Figure 6.7 because the deposition conditions are the same. This means that the ratio between compositions of the composition profile remains

3:1 and the macroscopic composition is equivalent to the average in composition of the profile at nano-scale. The grain size for each macroscopic value is defined using the exponential fit defined in section 5.1.3, Chapter 5. Figure 6.12 displays the grain tilt as predicted by the model using the experimental data in equation 6.7. The grain tilt is obtained from Figure 5.49. Note that the differences encountered in the variation of composition in relation to the experiments at low pressure are compensated by the difference in grain size obtained in section 5.1.3, Chapter 5, and as consequence the prediction fits nicely with the experimental grain tilt.

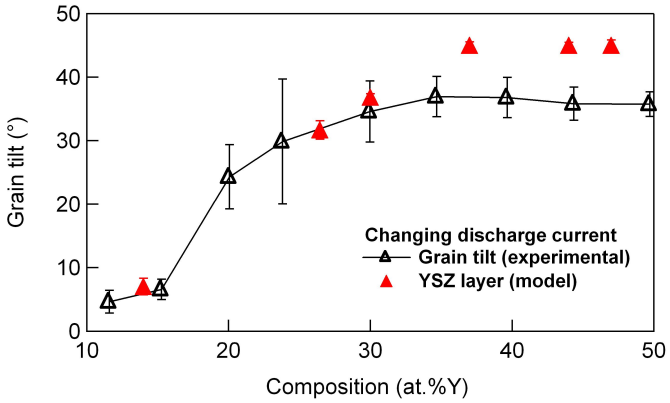

Figure 6.12: The experimental grain tilt in comparison with the calculated tilt based on the measured macroscopic compositional gradient for the experiments with different discharge currents.

The incident angle at high pressure is illustrated in Figure 6.13 for Y T-S distances of 240 mm, 160 mm, 120 mm, 90 mm and Zr T-S distance of 90 mm. The values of the impact angle are smaller than the ones found at low pressure. Note that the distribution of the incident angle is also wider when compared to the results of Figure 6.7. Due to the increase of pressure, the adparticles arrive with different orientations and directions resulting from the increase of scattering. This can be clearly observed for higher Y T-S distances, where the distance also contributes for the increase of scattering. Note that the amount of atoms arriving from a positive side (0 to 90°) is practically the same as the atoms coming from the negative side (0 to -90°). Therefore, it is expected that the compositional gradient in a single column is affected in a different way than the behavior explained above at low pressure. Based on the histograms presented in Figure 6.7, it is possible to conclude that the compositional gradient is smaller than the one seen at low pressure due to the contribution of the atoms coming from the negative side. Unfortunately, the use of STEM is limited because the sample preparation requires

long periods of time as well as the availability of the machine (up to several months) and therefore a nano-scale analysis at high pressure was not possible due to time constrictions.

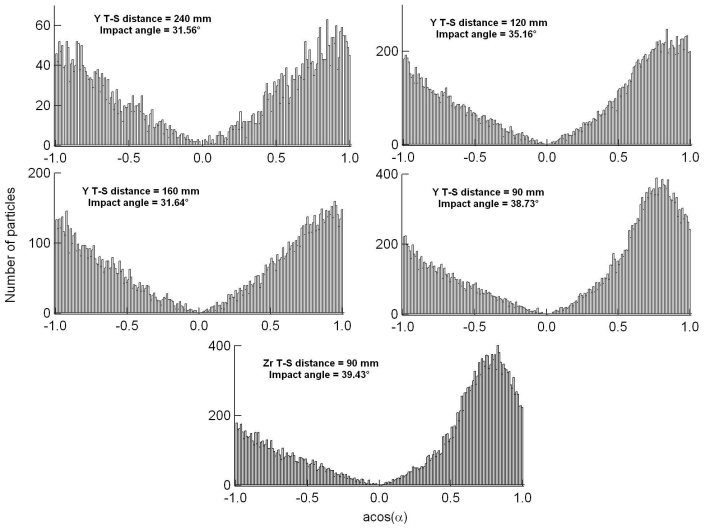

Figure 6.13: The incident angle distributions obtained for Y and Zr for three different Y T-S distances (240 mm, 160 mm and 80 mm) at high pressure.

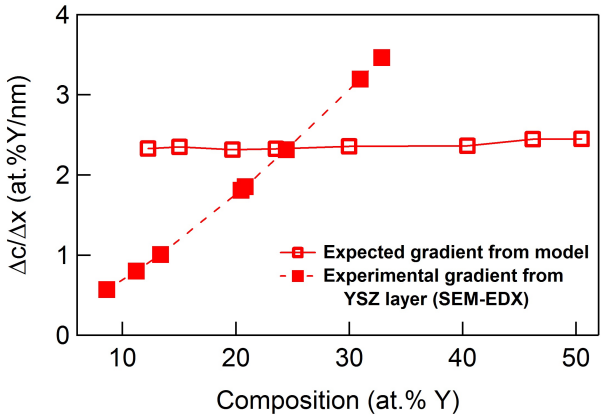

Figure 6.14: The expected compositional gradient at high pressure using the model (equation 6.7) and the compositional gradient of the layer (SEM-EDX).

Instead we represent in Figure 6.14 the expected compositional gradient at high pressure using the model (open markers) and the experimental compositional gradient based on the experimental results of the layer via SEM-EDX (closed markers). The behavior of the experimental gradient is similar to the one reported at low pressure, i. e. the compositional gradient increases with the increase of Y content. However, the expected gradient calculated using the model (equation 6.7) suggests that the gradient does not vary, being constant at approximately 2.3 at.%Y/nm. Above 25 at.% Y, a higher compositional gradient would lead to a grain tilt of 45°, thus the difference seen in Figure 6.14 does not affect the expected grain tilt.

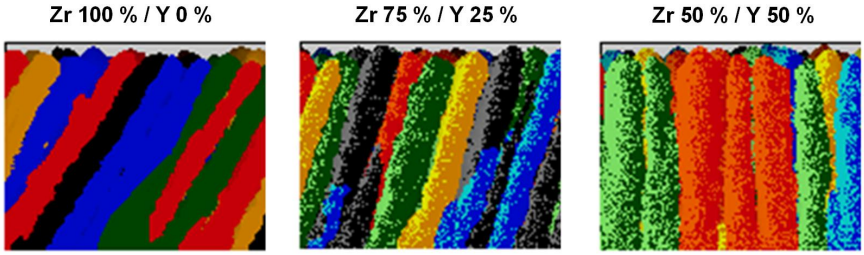

Figure 6.15: Simulation of the ballistic deposition on the YSZ system with Y content varying from 0 to 50 at.%.

The difference up to 25 at.% Y can be attributed to the competition between the ballistic deposition and the effect of the stress model. This can be observed by the results of the impact angle seen in Figure 6.13. At high Y T-S distance (low content of Y), the total compositional gradient is reduced due to the contribution of the atoms coming from different directions. A reduced compositional gradient cannot explain the constant value of compositional gradient seen in Figure 6.14 (open markers). A possible solution for this effect considers the ballistic deposition since at high pressure the directional mobility is reduced. In a ballistic deposition, particles follow a trajectory until they stick to a surface, being randomly placed on the growing film [261]. These particles act as shadowing centers and, due to shadowing effect all the tallest islands will receive more impinging atoms as compared to the shorter ones, growing into columns. The simulation image for a ballistic deposition using Simul3D[1] is given in Figure 6.15 for 0, 25 and 50 %Y, which corresponds to the composition under investigation. Based on the simulations up to 25 % Y, it is noticeable that the columns grow with a certain inclination determined by the closest target, which defines the inclination seen

[1]Simuld3D: software developed by A. Besnard from Laboratoire Bourguignon des Matériaux et Procédés.

in the SEM images (Figure 5.31, Chapter 5) and pole figures at high pressure (Figure 5.40, Chapter 5). When the fractions of Y and Zr are equal the columns are shown to grow straight. However, at this point, the insertion of Y^{3+} in the lattice creates a deformation of the lattice as explained by the stress model. This can also be observed by the histogram of Y T-S distance = 120 mm, where the contribution of the positive side is larger than the negative one, meaning that there is a higher compositional gradient increasing the grain tilt. Therefore, we conclude that above 25 at.% Y, it is the stress model that takes over the columnar growth maintaining the total inclination of the columns.

6.3 Full YSZ sample analyses at low pressure

The dual magnetron configuration induces anisotropy in the material flux towards the substrate, leading to a compositional gradient over the full sample. If we consider the relative composition in different positions of the full YSZ sample we can identify the grain as well as the columnar tilt along the sample. These tilts have a different angle in comparison to other positions on the YSZ layer.

In this section it will be shown that the model is also applicable to predict the tilt on a full YSZ sample taking into account the relative compositional gradient along the YSZ layer. In this section, we discuss the results of the samples deposited at 0.5 Pa with different Y T-S distances.

6.3.1 Prediction of the grain tilt on a full YSZ layer

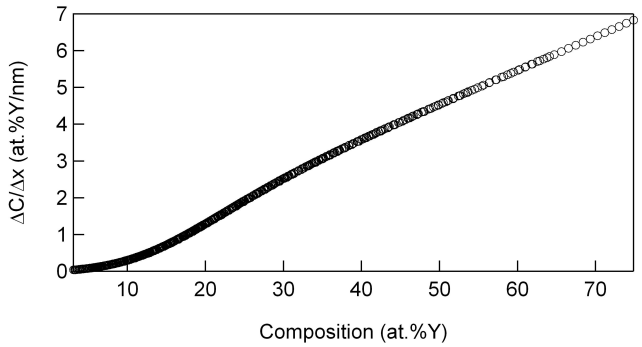

Figure 6.16: The compositional gradient of YSZ layer deposited on a glass substrate at different Y T-S distances. When R = 3, there is no influence of the Y T-S distance and the compositional gradient can be obtained by the ratio between average macroscopic composition and grain size

In this approach we consider the total composition variation of the deposited YSZ film on a glass substrate. As expected and already discussed in the Chapter 5, the content of Y increases with the decrease of the T-S distance.

The compositional gradient of the full YSZ layer was obtained considering the ratio (R) equal to 3. In this way, there is no influence of the Y T-S distance on the R and from equation 6.3 the compositional gradient is defined by the macroscopic composition divided by its respective grain size. The compositional gradient as a function of the substrate position was obtained at each 1 mm distance for every Y T-S distance. The representation of the compositional gradient vs. composition is given in Figure 6.16.

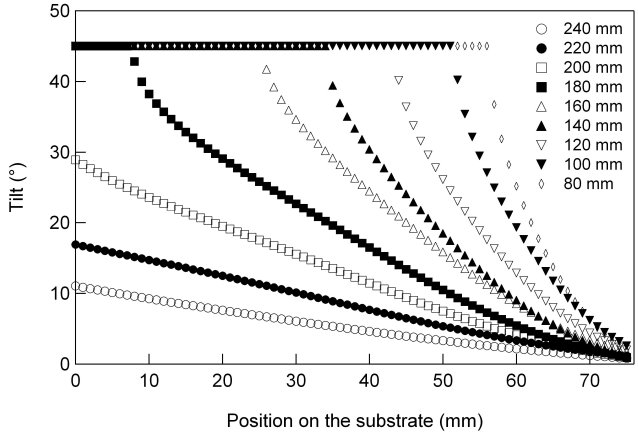

Figure 6.17: Tilt distribution along the substrate for different Y T-S distance. Note that a maximum tilt of 45° is reached. This maximum is dependent on the compositional gradient and that is why it starts at different positions values on the substrate.

The compositional gradient of Figure 6.16 and the thickness (h) can be substituted in equation 6.7. The film thickness varies as a function of the substrate position, as demonstrated in Figure 5.2a, Chapter 5. Using equation 6.7 we obtain the plots shown in Figure 6.17, where the tilt distribution along the substrate is illustrated for different Y T-S distances. The composition distribution varies not only as a function of the T-S distance but also as a function of the position on the substrate. Therefore, it is expected that the tilt along the sample changes. At lower Y T-S distances the tilt reaches its maximum, explaining the constant trend at 45°. As this maximum is dependent on the compositional gradient, it is reached at different positions on the substrate, depending on the Y T-S distance.

It is also possible to combine the grain tilt results obtained via XRD ($\theta/2\theta$), at different points of the sample, with the tilt predicted by the model. Figure 6.18 shows the measured and the calculated grain tilt along the full YSZ sample as a

function of the composition. The measured grain tilt is based on experimental results as already presented in Figure 5.49, Chapter 5. The calculated angle is the average grain tilt obtained using the model (blue triangle markers). This average is calculated by taking a fixed composition value at different Y T-S distances (set 2 of samples). Note that the angles obtained with the model fits nicely with the experimental results, indicating once more the accurateness of this model to predict the grain tilt not only in the center of the sample (as already shown in previous section) but also along a full YSZ sample.

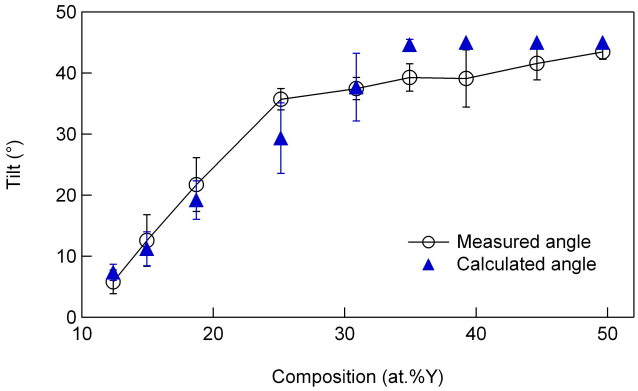

Figure 6.18: Fit between measured and calculate angle. The measured angle is obtained from the azimuthal angle of different Y T-S distances at different substrate positions and it is indicated by the circular open markers. The triangle markers represent the calculated angle based on the experimental compositional gradient and thickness.

6.3.2 Analyses of the columnar tilt on a full YSZ layer

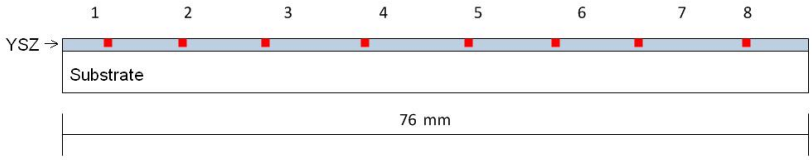

Figure 6.19: Lateral view of an YSZ layer deposited on a glass substrate. The square markers on the YSZ layer indicate the position on the substrate where the SEM cross section images were obtained.

A similar approach was followed for the columnar angle of the YSZ thin films. In this way, the columnar tilt at low pressure can be estimated from the plot columnar tilt vs. composition displayed in Figure 5.33, Chapter 5. A mapping of the columnar tilt along the substrate is obtained by considering the SEM cross section images of some samples with a fixed Y T-S distance. The cross section images were obtained in eight different positions along the YSZ sample as indicated in Figure 6.19. The positions on the substrate are indicated in Table 6.1.

Point	**1**	**2**	**3**	**4**	**5**	**6**	**7**	**8**
Substrate (mm)	5	10	20	30	42	52	60	70

Table 6.1: Schematic points as illustrated in Figure 6.19 and their equivalent substrate positions in mm.

Three different Y T-S distances (80, 120 and 200 mm) were chosen to demonstrate the change in columnar angle along the sample. Figure 6.20 shows the SEM cross section images of these eight points, followed by the plot of the expected columnar tilt (triangular markers), the measured columnar tilt based on SEM images (square markers) and the content of Y (circular markers). The position of Y (left) and Zr (right) targets are indicated above the SEM images of points 1 and 8, respectively.

The expected columnar tilt is obtained simply by taking the position on the substrate and its respective content of Y (see Figure 5.4, Chapter 5). With the right values of Y content it is possible to estimate the expected columnar tilt from Figure 5.33, Chapter 5. As seen in section 5.3.2.1, Chapter 5, it is expected that the columnar angle reaches a constant value around 30° for contents of Y superior to 24 at.%. As the columnar angle is obtained from Figure 5.33, we are limited to contents up to 40 at.% Y and an extrapolation cannot be made. The cross section images indicate that the columnar angle increases up to 40 at.% Y, being equivalent to the expected angle. However, very close to the Y source there is a decrease of the columnar angle, which occurs in points 1 to 3 in Figure 6.20a, point 1 and 2 in Figure 6.20b and point 1 in Figure 6.20c. This effect can be associated to the rotation of the lattice which affects the 3D growth, as already discussed in section 5.5.1.1, Chapter 5. In this way, the bent structure cannot be visualized in a 2D cut. This can be proved by analyzing the lateral view at the shortest distance between Y source and sample substrate. Figure 6.21 illustrates the lateral view of points between 1 and 2 for samples deposited with a Y T-S distance of (a) 80 mm, (b) 120 mm and (c) 200 mm. Note that all the images have a tilt columnar structure, which increases at shorter distances. As a conclusion, the proximity of the Y source to the sample substrate affects the columnar tilt, deviating the expected values to a lower columnar tilt.

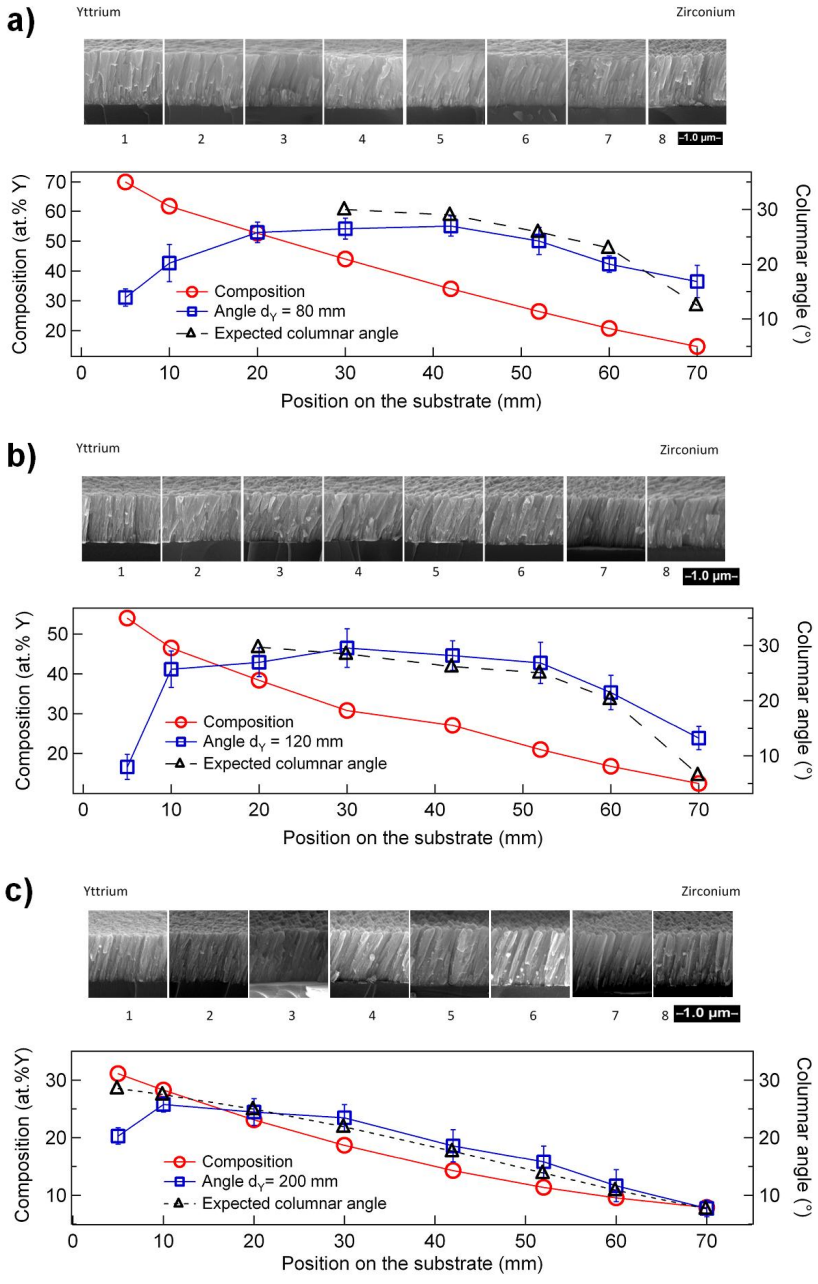

Figure 6.20: Cross section images of the eight points along the sample and plot of the composition and the columnar angle vs. position substrate, a) 80 mm; b) 120 mm and c) 200 mm. The dashed lines represent the expected columnar angle as a function of the position on the substrate while the blue line shows the measured columnar angle based on the cross section images.

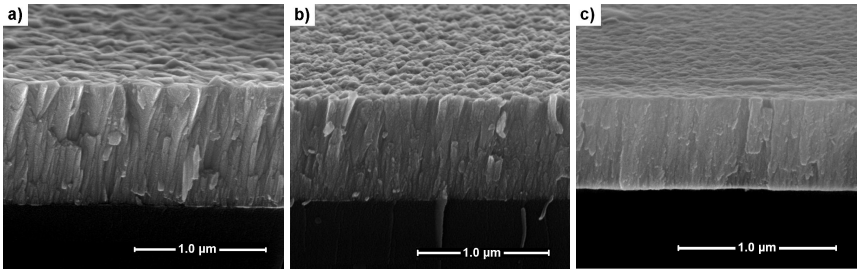

Figure 6.21: Lateral view of point 1 for samples deposited with a Y T-S distance of: a) 80 mm; b) 120 mm and c) 200 mm.

6.4 Summary and conclusions

Using ADF-STEM and STEM-EDX mapping in selected YSZ samples yielded a quantification of the compositional gradient as well as the coordinates of these values along the columnar structure. A compositional profile was identified from the STEM-EDX mapping. The average in composition on this profile matches with the composition on macroscopic level obtained via SEM-EDX. Hence, a 1:1 relation between both compositional gradients was observed.

Additionally, a new model based on a known theory used for bi-metal thermostats was developed to explain the grain tilt based on the YSZ characteristics. This model agrees well with the measured grain tilt. Furthermore, this model allows combining both nanometer and macroscopic scale compositional gradients. As a result, the grain tilt can be predicted at low pressure on YSZ thin films on a macroscopic scale and these results can be used to determine the tilt on nanometer scale. The model was also used for other deposition conditions. The experimental data at different discharge currents agree with the model. At high pressure, on the other hand, it was found that a combination between a ballistic deposition and the stress model explains the constant value of the grain tilt.

In the second part of this chapter, we extended the use of the model to a full YSZ sample. Using the obtained compositional gradient and the thickness of the film, which varies with the position on the substrate, we determined the expected grain tilt as a function of the Y T-S distance and position on the substrate. Finally, a good match between measured tilt and calculated tilt was found, indicating once more the validity of this model. The columnar tilt along the full YSZ layers agrees well with the estimated columnar tilt. However, the proximity of the substrate to the Y source at lower Y T-S distances affects the final columnar tilt. This effect is related to the rotation of the lattice. Therefore, a 2D cross section image cannot

visualize this tilt and consequently the column closer to the Y source seems to have a lower inclination.

In conclusion, using the experimental results in combination with a modified stress model it is possible to calculate the grain tilt of the YSZ system. Results indicate a good agreement between both measured and calculated results over the whole range of YSZ samples. Moreover, the understanding of the YSZ growth through the use of a model allows us to manipulate the characteristics as well as its crystallography and texture to a desired film.

In the next chapter we utilize this understanding to modify the structure of the film. Furthermore, the effect of the microstructure on the optical properties will be discussed.

7

Microstructural tuning and its influence on the optical properties

Based on the data given in former chapters, it is possible to modify the film in order to obtain a desired microstructure by changing the rotation angle of the substrate as well as deposition conditions. We start this chapter by showing how zig-zag columns can be produced using magnetron sputtering. Then, a view on the crystallographic properties of those films is given. Moreover, the optical properties of these films will be studied in order to determine any influence of the zig-zag structure on the refractive index and band gap energy. Using the transmittance spectra we also discuss the determination of the film thickness and film porosity, correlating them to the results previously reported in this thesis.

7.1 Development of zig-zag structures

Nanostructured wires and films are essential for many clean tech technologies due to their optical and electrical properties, such as solar energy utilization and methods for assuring clean air and water [41]. There are several techniques used to fabricate them, for example, using nanolithography [262], solution-based approaches [263, 264], template-based methods [263] and vapor-based methods [264, 265]. However, these techniques present some drawbacks which inhibit to manipulate diameters, orientations and positions of the grown nanostructures. Currently, glancing angle deposition based on a PVD method has been extensively

used [107–109, 266–270] to fabricate nanostructured films. The columnar structures are produced through the shadowing effect during film growth while the substrate rotation controls the shape of the columns. By changing the angle of incidence, the columns can be sculptured into C, S or zig-zag shapes [107, 109, 271]. In this chapter we propose an alternative method using the dual magnetron sputtering based exclusively on the crystallographic manipulation of the YSZ system. In Chapter 5, Part III (5.3) and IV (5.4), we have demonstrated that a columnar tilt can be induced by taking into consideration the difference in ionic radius between yttrium and zirconium. In this way, this feature can be used to develop zig-zag structures.

Experimentally, the only difference between the setup described in Chapter 4 and the setup used for the zig-zag structures is the substrate holder, which in this case rotates. The rotation can be performed in two different ways: manually, changing the angle in discrete values (e.g. at 45°, 180°), or using an external motor set beneath the chamber with rotation speed up to 0.5 turn per second. The schematic drawing of Figure 7.1 illustrates the rotatable substrate.

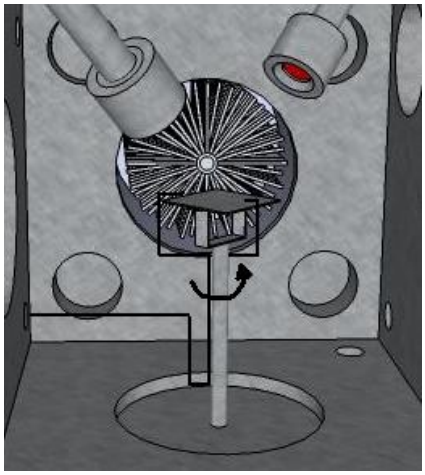

Figure 7.1: Schematic drawing of the experimental setup indicating how the rotation takes place at the substrate holder.

The formation of the zig-zag structure is based on the principle that the columnar growth in zone T in the YSZ system follows the source with the smallest ionic radius, i.e. the Zr target. By controlling the deposition conditions as seen in Chapters 5 and 6, it is possible to induce a different tilt to the film growth. Figure 7.2 shows the schematic drawing of the zig-zag formation when the substrate rotates 180°.

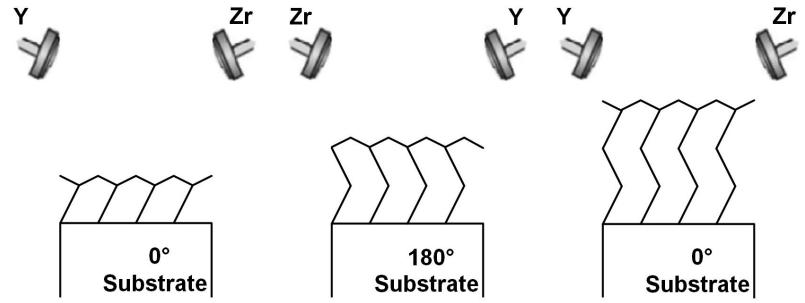

Figure 7.2: Schematic drawing of the zig-zag formation. The columns follow the source with the smallest ionic radius, i.e. the zirconium target.

The cross section of a sample deposited as indicated in the schematic drawing of Figure 7.2 is given in Figure 7.3. This figure shows a film deposited during 20 min with four rotations of 5 min. The T-S distance and current are 240 mm, 0.2 A and 90 mm, 0.5 A for Y and Zr, respectively. This image ensures that the columnar growth can be controlled by the deposition conditions. It is also noticeable that the columns grow in zone T. The first 5 min which include nucleation of the film present a smaller thickness when compared to the other 5 min deposited layers. The thickness of the last 3 layers is approximately the same. The blocks observed on the columns are related to the Au ultrathin coating necessary to eliminate the electrostatic charge during the SEM mapping. This ultrathin layer is deposited by low-vacuum sputter coating as described in section 4.6.5, Chapter 4. This effect can be visualized when the Au is sputtered with currents higher than 5 mA.

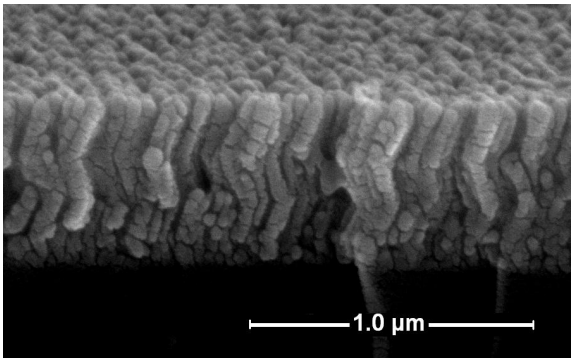

Figure 7.3: Example of a zig-zag structure formation. Film deposited with a Y T-S distance of 240 mm and Y current of 0.2 A during 20 min with four rotations of 5 min.

7.2 Crystallographic properties on YSZ thin films with rotating substrate

The zig-zag growth in YSZ thin films can be controlled based on the results of this thesis. This control reflects on the final microstructure and as a consequence on the film texture. This section discusses the crystallography of such films and how the substrate rotation can influence the film growth.

Section	**Rotation** [°]	**T-S$_{dist}$** [mm]	**d$_t$** [min]	**p** [Pa]	**Pole figure**	**SEM CS**	**T, n, E$_g$**
7.2.1	45	240	20=4x5	0.5	x	x	–
7.2.1	45	240	25=5+2x10	0.5	x	x	–
7.2.1	45	240	45=5+2x20	0.5	x	x	–
7.2.2	135	240	25=5+2x10	0.5	x	x	–
7.2.2	135	80	25=5+2x10	0.5	x	x	–
7.2.3	180	80	25=5+2x10	0.5	x	x	–
7.2.3	180	80	30=10+4x5	0.95	x	x	–
7.2.4/ 7.3	180	140	20=10+10x1	0.5	–	x	x
7.2.4/ 7.3	180	140	18=10+4x2	0.5	–	x	x
7.2.4/ 7.3	180	140	30=10+4x5	0.5	–	x	x
7.2.4/ 7.3	auto	220	11	0.5	x	x	x
7.3	180	80	20=4x5	0.95	–	–	x
7.3	180	160	20=4x5	0.95	–	–	x
7.3	180	240	20=4x5	0.95	–	–	x
7.3	180	80	20=4x5	0.5	–	–	x
7.3	180	160	20=4x5	0.5	–	–	x
7.3	180	240	20=4x5	0.5	–	–	x
7.3	YSZ	single	crystal				T
7.3	0	80	20	0.5	–	–	x
7.3	0	160	20	0.5	–	–	x
7.3	0	240	20	0.5	–	–	x

Table 7.1: Overview of the samples used in Chapter 7. The deposition conditions listed are: rotation of the substrate, Y T-S distance (T-S$_{dist}$), deposition time (d$_t$) and pressure (p). The "×" marks the analyses performed for these samples, namely, pole figures, SEM cross section images, transmittance (T), refractive index (n) and band gap (E$_g$).

The term *rotation* in this chapter is defined as follows: the sample is deposited at an initial substrate position. After an interval of time, the substrate rotates with

a certain angle. Then, the sample returns to its initial position being deposited at the same interval of time. This process continues until a certain deposition time is reached, switching from rotation 0° to a defined rotation and back. Rotations of 45°, 135° and 180° were performed while depositing YSZ films.

Currents of Y and Zr and Zr T-S distance are constant and equal to 0.2 A, 0.5 A and 90 mm, respectively. The Y T-S distance is variable in order to obtain a different compositional gradient and consequently, a different grain tilt. These samples are studied using set 1 of samples (position on the center of the sample). The rotations and deposition conditions used in this work are listed in Table 7.1.

7.2.1 Rotating the substrate at 45°

First, we consider a sample deposited at low pressure with a Y T-S distance of 240 mm. From the results of Chapters 5 and 6 we know that this film will have a composition of 12 at.% Y and a grain tilt of 8°. Figure 7.4 represents the crystallographic projection in CaRIne crystallography [251] of this film rotated at 45°. The first line indicates the crystallographic projection of the lattice at 0°, at 45° and the combination of both. The second and third lines indicate how the lattice should be oriented at 0°, 45° and how the resultant would be identified in pole figures. The colored balls represent the [111] and [200] directions.

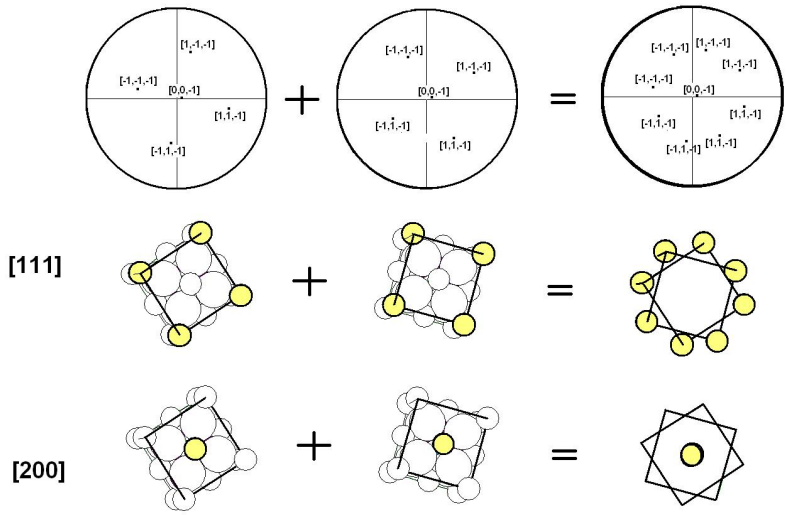

Figure 7.4: The first line indicates the crystallographic projection at 0°, 45° and a combination of both rotations. The second and third line indicates how the lattice should be oriented at 0°, 45° and when overlapped. The colored balls represent the [111] and [200] directions.

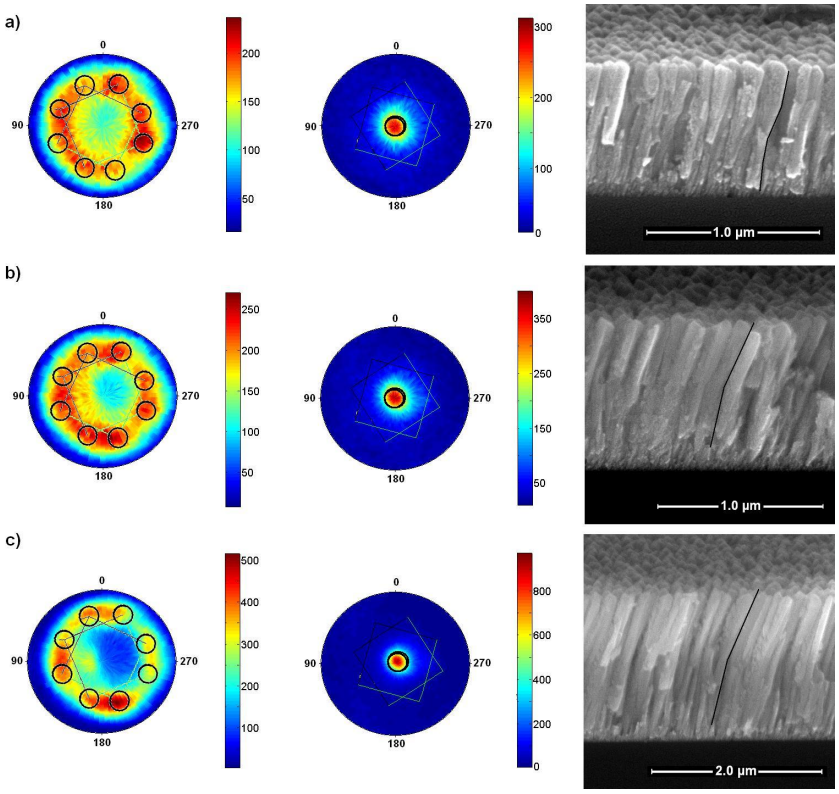

Figure 7.5: (111) and (100) pole figures illustrating the lattice position and SEM cross section images showing the columnar growth. Samples were deposited with a rotation of 45° during: a) 20 min (4×5 min); b) 25 min (5 min +2×10 min) and c) 45 min (5 min +2×20 min).

The representation of the texture and microstructure of three different films deposited at different deposition times are shown in Figure 7.5. Figure 7.5a illustrates a film deposited at 20 min with four rotations of 5 min each. Note that the (111) pole figure indicates a combination of several [111] peaks. Due to the lack of accuracy when changing the rotation manually, no evident distinction can be done. However, if the final [111] projection from Figure 7.4 is placed on the (111) pole, it is possible to identify the 8 resultant [111] peaks, suggesting that the superposition of the peaks occurs due to their broadness. The projection of the [200] direction is clear from the (100) pole figure. The SEM cross section image shows the columnar structure growing in zone T. Note that for every 250 nm there is a small change on the columnar tilt (approximately 8°). This is related to the 45° rotation which consequently changes the position of the Y and Zr sources in relation to the substrate. Since the growth follows the smallest ionic

radius, the column changes its orientation in order to continue following the Zr source. Samples in Figure 7.5b and c have an initial deposition time of 5 min before depositing the following YSZ layers during longer times. In this way, the subsequent layer can then be analyzed without the effect of the columnar overgrowth. Figure 7.5b has a rotation time of 10 min (5+2x10 min) while Figure 7.5c rotates each 20 min (5+2x20 min). From both figures, the change in the columnar orientation is clear at 500 nm and 1 μm, respectively as well as the contribution of the 8° tilt in the columns. In addition, it is noticeable that the direction of the tilt remains on the right side of the image, since at 45° the Zr source remains on the right hand side of the sample holder.

7.2.2 Rotating the substrate at 135°

Further playing with the crystallography of the thin films, we change the rotation to 135°. This rotation was chosen in order to visualize not only the eight peaks on the (111) pole but also the two peaks on the (100) pole. As the Y T-S distance of this sample is 240 mm, we can consider the crystallographic projection displayed in Figure 7.4. For this sample we keep the initial 5 min for the overgrowth before rotating. Figure 7.6 shows the pole figure and SEM cross section of a sample deposited during 25 min (5+2x10). Note that in this figure we can identify eight peaks in the (111) pole but only one peak in the (100) pole. In the latter, a small deviation on the (100) pole can be seen, indicating that the formation of two peaks has begun. This is due to the low content of Y at Y T-S distance of 240 mm. The content of Y is 12 at.% Y and consequently, the grain tilt is not large enough to be visualized in the (100) pole figure. The SEM cross section image shows the columnar structure growing in zone T. As the rotation is of 135°, there is a clear distinction of the direction of the columns from left to right.

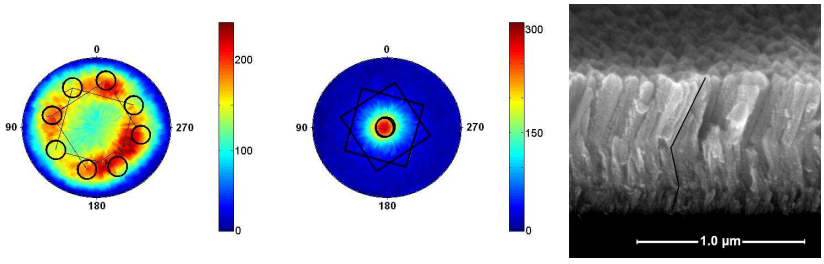

Figure 7.6: Pole figure and SEM cross section of a 135° rotation deposited during 25 min. Note that eight peaks can be identified in the (111) pole. However, there is only one peak on the (100) pole suggesting that the angle of the tilt is not large enough to make a distinction of two peaks on the (100) pole.

In order to make the distinction in the (100) pole, we decrease the Y T-S distance down to 80 mm keeping the same deposition time. At this distance we know from former chapters that the amount of Y will be higher (39 at.% Y). Hence, the grain tilt is larger (approximately 40°, see Figure 5.49). Figure 7.7 shows the crystallographic projection under those conditions. From this image it is expected to have five [111] peaks in the (111) pole, instead of 8 peaks, because of the overlap of some of these peaks due to their proximity. Moreover, it is also expected to see two poles in the (100) pole.

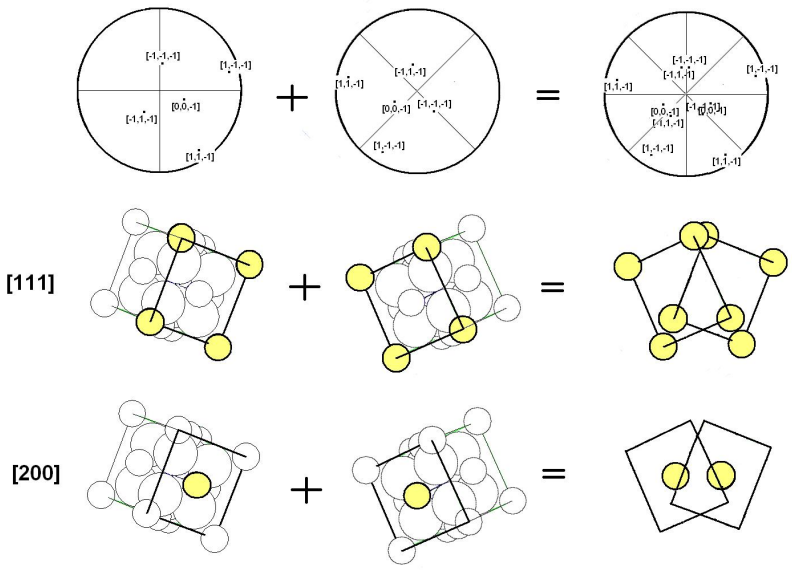

Figure 7.7: Crystallographic projection of a 135° rotation with a Y T-S distance of 80 mm. Five [111] peaks are expected on the (111) pole due to overlapping and two [200] peaks on the (100) pole.

Figure 7.8 shows the pole figures and the SEM cross section for the sample described above. Note the overlap of the [111] direction on the (111) pole. On the other hand, the (100) pole shows the contribution of two [200] peaks. As the content of Y is higher for this sample, the columnar tilt presents an arc shape rather than a straight line. This is in agreement with Part III (5.3), Chapter 5, where at high content of Y a bend column is formed. Note that the columnar tilt has a smaller angle when compared to the grain tilt angle as described in section 5.5.1, Chapter 5.

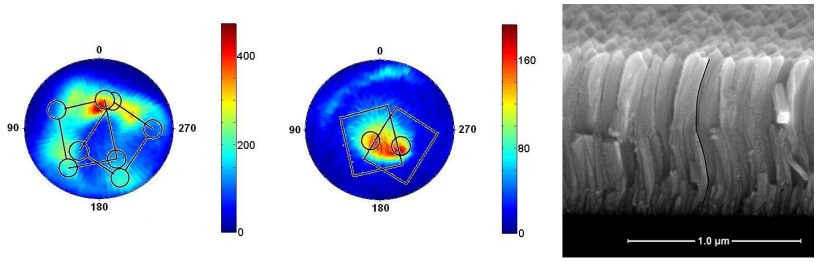

Figure 7.8: Pole figures and SEM cross section of a 135° rotation with Y T-S distance of 80 mm deposited during 25 min. Five peaks are formed in the (111) pole, where three of them reflect an overlap of two different [111] peaks. In the (100) pole two peaks can be identified. The correspondent cross section image shows the bend of the columns at higher content of Y.

7.2.3 Rotating the substrate at 180°

Figure 7.9 shows the pole figure of an YSZ sample with 180° rotation deposited during 25 min (5 min +2x10 min). The poles show the overlapping peaks on the (111) pole and the two [200] peaks on the (100) pole. The SEM cross image shows the columnar orientation when the substrate is rotated at 180°. It is evident that the columnar slope is different than the one described above. Although the content of Y is the same as the composition of the sample above (135°, 39 at.% Y, Y T-S distance = 80 mm), the grain tilt is less inclined. This can be explained by the 3D growth described in Part V (5.5), Chapter 5. The 2D image cannot verify the possible rotation of the lattice and as a result the SEM image shows a less inclined tilt. This means that 135° rotation shows this contribution better than when the substrate is rotated at 180°.

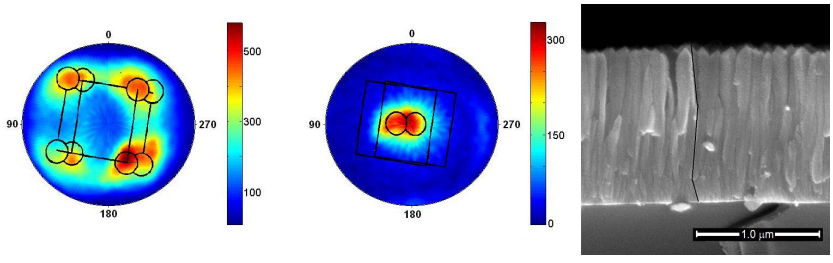

Figure 7.9: Pole figures and SEM cross section of a 180° rotation with Y T-S distance of 80 mm deposited during 25 min. On the (111) pole it is observed the four overlapped [111] peaks and on the (100) pole it is possible to identify two [200] peaks. The correspondent cross section image has a smaller columnar tilt explained by the rotation effect.

Another example of the rotation of the substrate was also performed at high pressure (0.95 Pa). This film has a different deposition time, being deposited during 30 min (10+4x5 min). As can be seen in Appendix A, the pressure influences the biaxial alignment of YSZ thin films. The crystallography of these samples should be similar to the one described above, except for the fact of the worsening of the biaxial alignment.

Figure 7.10 shows the pole figure and SEM cross section images of this YSZ sample. There is no clear peak on the (111) pole, but two overlapped peaks can be identified on the (100) pole. The SEM image confirms that the columnar structure grows in zone T.

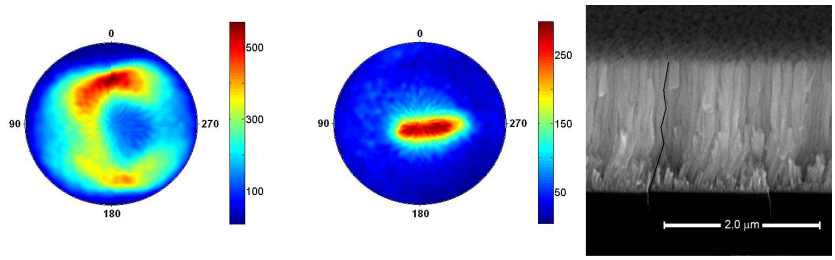

Figure 7.10: Pole figure and SEM cross section of a 180° rotation with Y T-S distance of 80 mm deposited during 30 min at 0.95 Pa. No clear peak can be identified on (111) pole. However, we can identify two overlapped [200] peaks on the (100) pole. The cross section image shows that the columns still grow in zone T.

From the figures above it is clear that the columnar growth and its tilt can be controlled by the deposition conditions. Even more, as the composition of Y is already known, and consequently its grain and columnar tilt, the crystallographic projection can be predicted. In this way, it is proven that the microstructure and texture of the YSZ system can be easily controlled by knowing one of the film parameters.

7.2.4 Multiple rotations

Using the feature described above we can deposit nice zig-zag structures by changing the rotation of the substrate in different intervals. Some examples of these structures are shown in Figure 7.11, with rotations every 1, 2 or 5 min. The deposition time of these samples are 20, 18 and 30 min, respectively and the samples are rotated at 180°. The Y T-S distance of these samples is 140 mm. In this way, the grain tilt of 38° is sufficient to be observed in the cross section and at the same time the columns possess a straight tilt rather than bent ones. The correspondent composition is 24 at.% Y. More details about the deposition conditions can be found in Table 7.1.

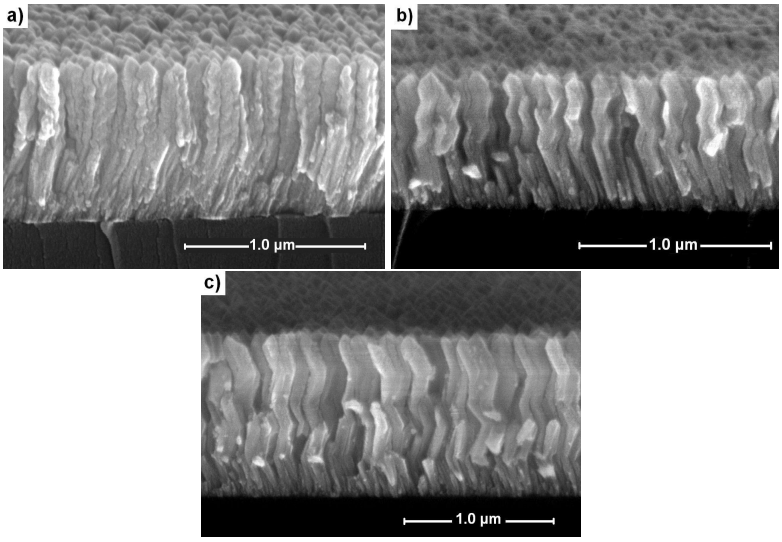

Figure 7.11: SEM cross section images of samples with multiple rotations. a) 20 min (10+10×1 min); b) 18 min (10+4×2 min) and c) 30 min (10+4×5 min).

The film with auto rotation used a motor to keep the rotation of the substrate constant. As an example, Figure 7.12 shows the pole figures and the SEM cross section of a sample deposited during 11 min. The Y T-S distance of this sample is 220 mm. Due to the constant rotation, the (111) pole has a random orientation resulting in a full ring. The (100) pole shows only one [200] peak. The SEM cross section image shows the formation of straight columns. This occurs due to the constant rotation which avoids a columnar tilt to a fixed direction, i.e. the Zr source has no fixed point when the substrate keeps on rotating.

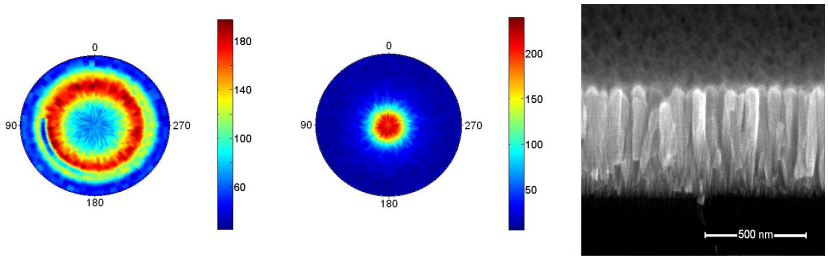

Figure 7.12: Random orientation of the [111] direction represented by a full ring on the (111) pole due to a constant rotation of the substrate. The (100) pole indicates the [200] out-of-plane preferred orientation. The SEM cross section image shows a straight columnar structure.

As described in Chapter 1, one of the interesting properties of YSZ thin films is related to the optical properties of these films. In the examples above we discussed the crystallographic and microstructural characteristics of these films. The change of microstructure can lead to different optical properties. Therefore, using these samples we focus on the optical properties and their relation to the crystallographic properties of the YSZ system.

7.3 Optical properties on the YSZ thin films

Some authors have described the use of YSZ as transparent ceramics, being used for example in optical electronics, optical coatings, high reflectivity mirrors and high temperature windows [41, 47, 272, 273]. In order to be suitable for those applications, these materials should possess high refractive index and a broad region of low absorption [35]. A large band gap is also necessary to support high electrical fields and temperatures [40]. Some values related to those parameters were already given in Chapter 1.

The change in microstructure can affect the optical characteristics of thin films. Therefore, a correlation between crystallography, microstructure and optical properties is done by analyzing the results of the refractive index and the band gap of some YSZ samples. In order to measure the optical properties, we use a normal incidence transmission for the determination of the refractive index (n), which is commonly used in literature [36, 274–276]. The optical constants such as refractive index and band gap were calculated from the transmittance spectra using the envelope method developed by Swanepoel [208]. In addition, the thickness is also obtained from the transmittance spectra and compared with the profilometer results.

In order to evaluate the optical properties as a function of the Y T-S distance, pressure and rotation of the substrate, some samples were selected at 0.5 Pa and 0.95 Pa. The conditions of these samples are listed in Table 7.1. Figure 7.13 illustrates the transmission spectra in the wavelength range of 250 to 1100 nm for samples deposited at (a) low pressure (0.5 Pa), (b) high pressure (0.95 Pa), (c) with multiple rotations (0.5 Pa) and (d) with no rotation of the substrate (0.5 Pa). The Y T-S distances of samples (a), (b) and (d) are 80, 160 and 240 mm, respectively. Samples with multiple rotations were rotated at 180° and deposited at Y T-S distance of 140 mm, except the sample with auto rotation which was deposited at 220 mm. Their microstructures were already discussed in section 7.2.4. The samples with no rotation of the substrate are the same samples deposited at low pressure in Chapter 5. All samples were deposited on glass substrate. The transmission spectrum of an YSZ single crystal sample was also added. This single crystal is a commercial crystal from CrysTec Kristalltechnologie with dimensions of 10 mm x 10 mm x 0.5 mm and a composition of 9.5 mol% Y_2O_3.

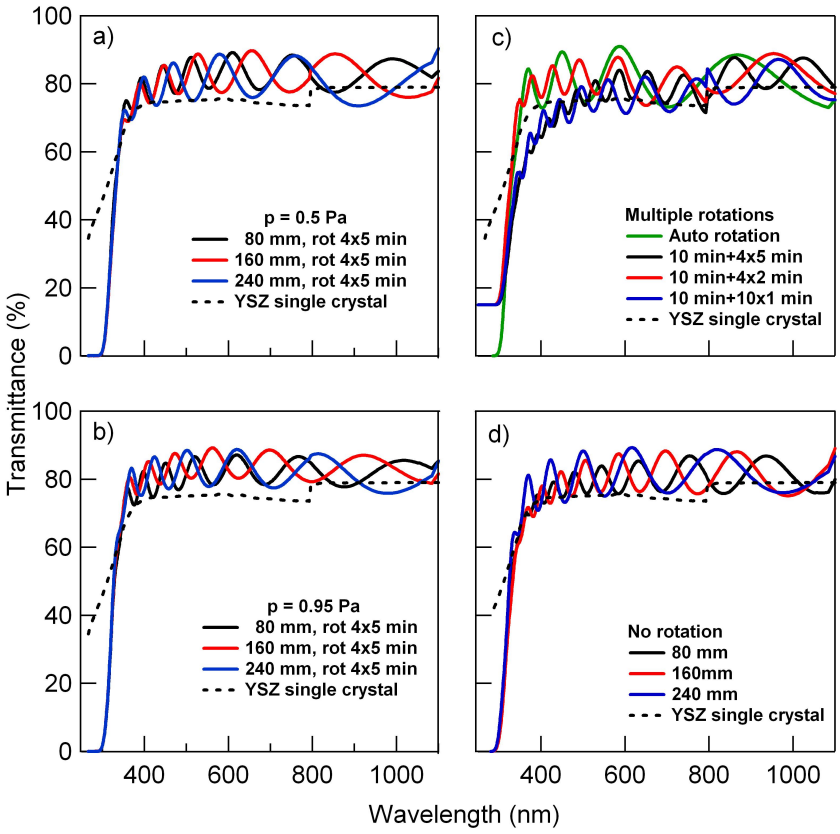

Figure 7.13: Transmittance spectra of samples with different Y T-S distances deposited at a) low pressure of 0.5 Pa; b) high pressure of 0.95 Pa; c) multiple rotations at 0.5 Pa and d) no substrate rotation at 0.5 Pa.

Starting from the transmission spectra of YSZ single crystal we observe that no fringes can be detected. This is due to the fact that there is no layer with a specific thickness but only a single crystal. The transmittance of this single crystal is approximately 75 % in the whole range of visible light. There is a step in the transmission spectrum at 800 nm which is attributed to the change of spectrophotometer detector. In the region of near infrared, a small increase of the transmittance at 80 % is seen. Below 400 nm (UV light) there is a decrease of the transmittance down to approximately 40 %.

Figure 7.13a shows the transmission spectra of three different Y T-S distances at low pressure. These films present a high degree of transparency down to a wavelength of 350 nm. Below this wavelength, there is a sharp absorption

edge until the transmittance is null. By analyzing the fringes it can be deduced that the thickness of the films is rather uniform because the amplitudes remain practically constant. This is expected since the film rotation keeps the thickness of the film uniform. Moreover, the amplitude between the maximum and minimum values of the fringe is smaller for lower Y T-S distance. Quantitatively, a smaller amplitude indicates a decrease on the refractive index. Despite of changing the Y T-S distance, the results of Figure 7.13a indicate that Y T-S distance has no influence on the transmittance, being for all samples in the range of 83 %. The film transmittance percentage is calculated as [208]:

$$T_i = \frac{2T_M T_m}{(T_M + T_m)} \tag{7.1}$$

where T_M and T_m are the transmission of the adjacent maxima and minima, respectively.

All samples present transmittance higher than the transmittance of the single crystal, since the single crystal is much thicker. Although the Y T-S distance is different for rotations of 4x5 min, no significant difference can be noticed at high pressure (Figure 7.13b) and the transmittance is in the range of 82 %. The absorption edge appears at the same wavelength as the ones observed in Figure 7.13a. The amplitudes at higher pressure are slightly smaller than at low pressure, which agrees with the literature [36].

The transmittance spectra of films grown with multiple rotations are displayed in Figure 7.13c. Two different transmittances behaviors can be observed. The transmittances of the sample with auto rotation and the sample 10+4x2 min are very similar (approximately 82 %) and also comparable with samples displayed in (a) and (b). On the other hand samples deposited with a rotation of 10+4x5 and 10+10x1 min show a slightly smaller transmittance: 79 % and 77 %, respectively. The first sample (4x5) has its transmittance reduced due to the increase of thickness. The second sample (10x1) has the same thickness as the other ones. However, its microstructure presents several zig-zags (see Figure 7.11a). This microstructure seems to affect the transmittance of light, being more affected in the visible light region rather than in the near infrared region. Taking the microstructure in consideration, one might consider that the auto rotation sample would also have its transmittance affected. But, by observing the microstructure of Figure 7.12 we realize that the zig-zag is so small (if exists) that the columns are practically straight and therefore the light is not scattered as in 10+10x1 sample. Another observation is that a small difference between the shoulders of these samples is noticed as can be seen in Figure 7.13c between wavelengths in the range of 350-400 nm. Literature [36] suggests that the broader shoulder is related to the visual appearance of the sample from a transparent to an opaque layer.

Finally, Figure 7.13d illustrates the results of samples with no rotations. The

difference in amplitudes from the near infrared region to the visible light region indicates that those films are not uniform in thickness. This is true because as no rotation is performed, the samples present a difference in thickness along the film as seen in Part I (5.1), Chapter 5. The transmittance is in average 81 %.

Sample	Pressure [Pa]	Profilometry [nm]	Transmittance spectra [nm]
80 mm, rot 4x5 min	0.5	840	834
160 mm, rot 4x5 min	0.5	730	747
240 mm, rot 4x5 min	0.5	650	671
80 mm, rot 4x5 min	0.95	890	877
160 mm, rot 4x5 min	0.95	800	773
240 mm, rot 4x5 min	0.95	680	653
Auto rotation	0.5	475	506
10 min +4x5 min	0.5	1249	1154
10 min +4x2 min	0.5	729	670
10 min +10x1 min	0.5	908	869
No rotation, 80 mm	0.5	1108	1104
No rotation, 160 mm	0.5	1168	1135
No rotation, 240 mm	0.5	746	723

Table 7.2: Comparison between thicknesses obtained via profilometry and transmittance spectra.

Using the interference fringes in the transmittance spectra, it is possible to calculate the thickness. The equation that allows obtaining the thickness considers two adjacent maxima (or minima) in the near infrared region and it was already described in section 4.6.1, Chapter 4. The thickness obtained via profilometry and the optical thickness are compared in Table 7.2. Note that the maximum error between the samples thickness obtained via both methods is of approximately 6 %, indicating the accuracy of both methods to determine the thickness of the film.

Based on the maxima and minima of the interference fringes we also calculate the refractive index (n) using Swanepoel method [208]. The refractive index is related to the phase velocity at which light travels inside the considered medium (YSZ film). The equations used in the interval of visible light are given by:

$$n = \left(N + \left(N^2 - s^2 \right)^{\frac{1}{2}} \right)^{\frac{1}{2}} \tag{7.2}$$

and

$$N = \frac{2s(T_M - T_m)}{(T_M T_m)} + \frac{s^2 + 1}{2} \tag{7.3}$$

where T_M and T_m are the transmission of the adjacent maxima and minima, respectively. And the parameter (s) is defined as:

$$T_s = \frac{2s}{s^2 + 1} \tag{7.4}$$

and T_s is the respective transmission related to the s value. The refractive index of the samples reported above is illustrated in Figure 7.14. The n index reported in literature varies in the range of 1.88 to 2.25 at wavelength of 550 nm, changing as a function of the Y content (from 50 to 0 mol% of Y_2O_3) [11, 35, 128]. From the results shown in Figure 7.14 we observe the behavior of the n index as a function of the wavelength, being practically constant in the visible light and increasing abruptly near the UV region.

At low pressure, Figure 7.14a the n index increases with the increase of Y T-S distance. It is known from literature that the refractive index decreases with the increase of Y content [11, 35, 36, 41, 135]. Knowing that the compositions are 33.7 ± 0.4 %, 19.5 ± 0.5 % and 12.2 ± 0.8 at.% Y for 80, 160 and 240 mm, respectively, it is possible to associate the variation of the refractive index with the composition of the film. The variation of the n index can also be related to the porosity of the films. In this way, there is more shadowing at higher columnar tilt (Y T-S distance 80 mm). This results in an increase of the porosity and consequently a lower refractive index. In the UV region, the n index increases significantly but the values are equivalent independently of the T-S distance due to the same value of absorption edge.

The first comparison made for Figure 7.14a and b suggests that pressure decreases the refractive index in the visible light as also reported by Heiroth et al. [36], where this difference was related to the evolution of the film porosity. This reduction could be already expected since the amplitude of the fringes in Figure 7.13a and b is smaller at high pressure. The compositions at high pressure for samples deposited at 80, 160 and 240 mm are 31 ± 1.07 %, 16.3 ± 1.7 %, 7.9 ± 1.83 at.% Y, in agreement with the compositions reported in Part I (5.1), Chapter 5 at the center of the sample substrate. As the contents of Y in those samples are different, there is also an influence of the Y content on the refractive index, as seen at low pressure. In addition, the microstructure cannot influence the n value at high pressure, because the columnar tilt is independent on the amount of Y in the film and there is no variation of the microstructure.

The films with multiple rotations (Figure 7.14c) have a similar behavior than samples of Figure 7.14a and b. From this figure it is evident that the auto rotation increases the refractive index. The first observation on the difference between n indexes can be related to the content of Y. The auto rotation sample has a smaller content of Y (9.58 at.% Y) than the other three samples (16 at.% Y). An alternative is to associate the difference in n index with the porosity of these films, as described for Figure 7.14a. In samples with auto rotation the porosity is strongly

reduced due to the constant rotation of the substrate. The porosity reflects on the microstructure. Thus, the resultant microstructure of the auto rotation samples delays the propagation of light, increasing the n index. For larger intervals of rotation the opposite effect is seen, i.e. the increase of rotation decreases the n index. This can be associated to the thickness of the film. If the film is thicker, light takes longer time to propagate and therefore its n value is higher. In sample 10+4x5 min a small decrease of the n index is observed at approximately 400 nm. This is resultant of the error on the envelope method used on the transmittance spectrum.

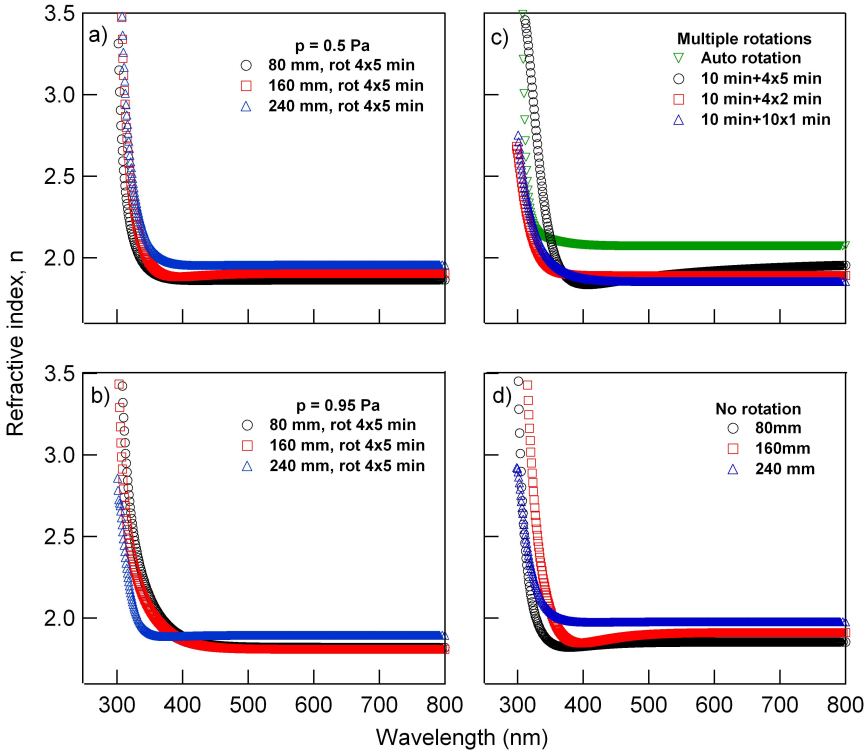

Figure 7.14: Refractive index of samples with different Y T-S distances deposited at a) 0.5 Pa; b) 0.95 Pa; c) multiple rotations at 0.5 Pa and d) no substrate rotation at 0.5 Pa.

Figure 7.14d indicates a difference of the n index with the change of Y T-S distance, agreeing with the other plots, where the n increases with the decrease of Y content or with the decrease of porosity. Comparing figures (a) and (d) there is a small difference in n index (2 %) which indicates the small contribution of the rotation to the YSZ film. The rotation induces a small increase of the n index,

indicating that the light passes slower in the film structure due to the light scattering on the zig-zag columns.

Using the values of the refractive index in the visible light it is possible to obtain the film porosity. The porosity is inversely related to the refractive index, i.e. a higher value of n gives a less porous film and vice versa. In order to analyze the values of porosity and compare it with the simulated results obtained in section 5.2.4, Chapter 5, we can estimate the porosity by using the analytical expression of Yoldas [277] given as:

$$P = 1 - \frac{n^2(\lambda) - 1}{n^2_{YSZ}(\lambda) - 1} \tag{7.5}$$

where n_{YSZ} is the refractive index of the bulk YSZ at a certain wavelength and n is the refractive index obtained for our films at the same wavelength. Based on literature, the refractive index of a bulk 9.5YSZ single crystal (17.4 at.% Y) at 550 nm is 2.15 [36, 278]. Unfortunately, we do not count with bulk YSZ of different compositions and the reference has a fixed value of Y_2O_3 of 9.5 mol%. Table 7.3 lists the porosity obtained using equation 7.5 for the samples shown in Figure 7.14. In addition to these results, the simulated results of porosity seen in section 5.2.4, Chapter 5 of samples represented in Figure 7.14d are added.

From the results displayed in Table 7.3, the following conclusions can be obtained:

- The porosity increases with the increase of pressure: this effect is associated with the momentum transfer and the scattered atoms arriving on the substrate. As seen in Mahieu et al. [243] the total momentum flux decreases with the increase of pressure, which results on a decrease of the film density. Moreover, the effect of scattering at low pressure results in a better alignment and as a consequence the packing is better than at high pressure. The increase of porosity with the decrease of Y T-S distance can be understood by the increase of the momentum transfer per sputtered atom as seen in section 5.2.4, Chapter 5.

- Multiple rotations: The auto rotation is the sample that presents the lowest porosity (9.13 %) which can be explained by the growth of homogeneous films with practically straight columns due to the constant rotation. The porosity obtained when rotating with different times and intervals are more difficult to be compared since based on these samples we cannot distinguish the contribution of the degree of rotation and the deposition time. However, it is noticeable that the level of porosity is high (approximately 30 %), indicating that the rotation performed does not decrease the porosity values.

Sample		Porosity [%]	Simulated porosity [%]
Low pressure	80 mm	31.71	–
Low pressure	160 mm	27.77	–
Low pressure	240 mm	22.21	–
High pressure	80 mm	35.93	–
High pressure	160 mm	37.07	–
High pressure	240 mm	28.73	–
Multiple rotations	Auto rotation	9.13	–
Multiple rotations	10 + 4x5 min	29.77	–
Multiple rotations	10 + 4x2 min	28.92	–
Multiple rotations	10 + 10x1 min	32.79	–
No rotation	80 mm	33.13	28.8
No rotation	160 mm	27.95	28.2
No rotation	240 mm	19.93	6.3

Table 7.3: Porosity calculated from the refractive index at 550 nm. The simulated values of porosity for samples with no rotation from section 5.2.4, Chapter 5, are added for comparison.

- No rotation: The porosity obtained for the samples with no rotation are equivalent (within the error) to the samples with 4x5 rotations deposited at low pressure. This indicates that a possible improvement in film density is difficult to be evaluated. Based on the results of the samples with no rotation and the porosity calculated via simulated/experimental results (section 5.2.4) we can compare the trends of both results. In general, it is observed that the level of porosity increases with the decrease of the Y T-S distance, which can be explained by the increase of momentum transfer per sputtered atom as well as the increase of shadowing when Y T-S is shorter. In addition, it is noticed that the simulated values of porosity at 80 and 160 mm are similar to the calculated ones. The difference between the values of porosity is related to the error of the measurement in combination with the error of the simulations. The error is more evident at 240 mm, where the simulated thickness presents the largest misfit between measured and simulated thickness (see Figure 5.27, Chapter 5). In addition, we should recall that the bulk used has a Y content of 17.4 at.%Y. If a bulk YSZ of smaller composition would be used to compare with samples deposited at 240 mm, the n_{YSZ} would be higher and as a consequence the calculated porosity would be smaller, decreasing the difference in value. As conclusion, it is possible to have an idea of the porosity values based exclusively on the simulation results.

Another optical characteristic obtained from the transmittance spectra is the band gap (E_g). As mentioned above, the refractive index indicates how fast the light passes through the film. Analogously, the electrical field, passing through the film before conduction, is limited by the band gap. The values encountered in literature for the band gap are in the range of 5.2 to 6 eV [36–39]. From literature it is known that YSZ presents a direct band gap [36–39, 279], i.e. there is a direct transition between valence and conduction band. Knowing that, it is possible to obtained the band gap from the following equation:

$$(\alpha h\nu)^2 = A(h\nu - E_g) \tag{7.6}$$

where (α) is the absorption coefficient, (hν) is the photon energy, A is a constant and E_g is the band gap value. The intercept at the energy axis at $(\alpha h\nu)^2 = 0$ gives the optical band gap.

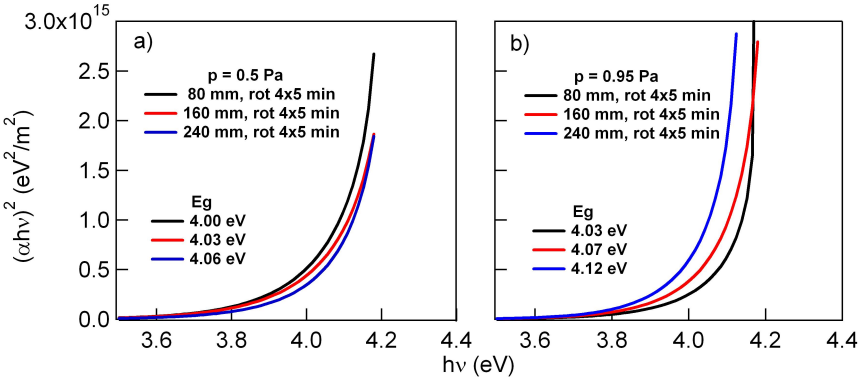

Figure 7.15: Band gap of samples with different Y T-S distances deposited on glass at a) 0.5 Pa and b) 0.95 Pa.

Figure 7.15 shows the $(\alpha h\nu)^2$ plot for samples at low and high pressure. From this plot it is observed that the band gap varies from 4.07 to 4.2 eV. This low E_g value has been reported elsewhere [279]. However, low E_g values (< 5 eV), can be analyzed in two ways: the first is related to the energy of an interband transition [36, 47, 279] while the second it is attributed to the absorption edge of the glass substrate.

The first is characteristic of a shift in the absorption spectra explained by the formation of color centers. These centers create states levels under the conduction band as reported in [47, 279]. Therefore, YSZ films with color centers are

intrinsically produced by exposing it to ionizing radiation or by adding charge carriers, for example, reducing it in hydrogen atmosphere. However, no color centers were induced in our films.

The second suggests that the glass substrate limits the absorption edge of the YSZ film because of the absorption of the glass in the UV region. The absorption edge of silicate glasses varies from 4 to 4.2 eV [280], explaining the values in Figure 7.15. Therefore, the band gap of YSZ films cannot be obtained due to the absorption edge of the substrate. A possible solution to determine the band gap in films with high band gap is to use another kind of substrate, such as sapphire or quartz. Sapphire for example has an absorption edge at wavelengths lower than 200 nm [281]. Figure 7.16 shows the obtained band gaps of the same samples as shown in Figures 7.13 and 7.14 deposited on sapphire substrate. Note that the values indicate a higher band gap than previously presented in Figure 7.15.

Comparing the $(\alpha h\nu)^2$ vs. $(h\nu)$ of both pressures, (a) and (b), we observe that the $(\alpha h\nu)^2$ and the band gap values at high pressure are in general lower than at low pressure. This is a consequence of the light scattering mainly in the grain boundaries [36]. Since it is known that at high pressure the grain size is smaller than at low pressure, this assumption of light scattering in the film seems reasonable.

Another analogy can be done as a function of the microstructure [36, 282]. Comparing Figure (a) and (d) it is noticeable a significant increase of the E_g value when the zig-zag formation is present. If the samples with no rotation are compared with each other, it is observed that the differences in E_g are too small to provoke a relevant difference in the band gap.

Finally, we compare the results obtained for multiple rotations (see Figure 7.16c). No difference in the band gap values at 4x5, 4x2 and 10x1 rotations can be seen. Instead the values are as low as encountered for no rotation. However, a high band gap of 5.63 eV was found for the auto rotation sample. Similar value was published in literature [282]. In fact, Kosacki et al. demonstrated that higher values of band gap (5.86 eV) are achieved when the grain size decrease to few nm. This occurs due to a quantum confinament which enhances several optical characteristics such as emission efficiency, gain in absorption, change in refractive index due to the confinement of electrons and holes in small volumes.

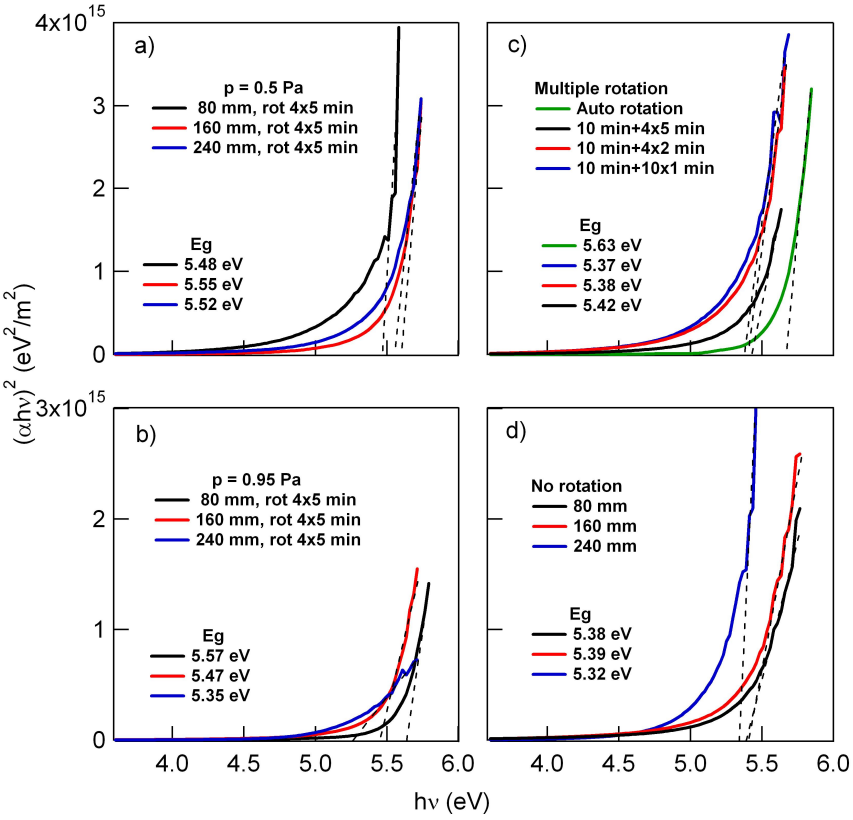

Figure 7.16: Band gap of samples with different Y T-S distances deposited on sapphire at a) 0.5 Pa and b) 0.95 Pa; c) multiple rotations at Y T-S distance of 80 mm, 0.5 Pa and d) no substrate rotation at 0.5 Pa.

Based on the results obtained above we realize that not only microstructure but also other conditions also affect the optical properties of the YSZ thin films, such as thickness, Y content, pressure and porosity level, being mutually dependent of each other.

A summary of all optical properties obtained in this chapter is listed in Table 7.4.

Sample	T-S distance [mm]	Pressure [Pa]	Transmission [%]	Optical thickness [nm]	Refractive index [nm]	Band gap	Porosity [%]
4x5 min	80	0.5	83	834	1.864	5.48	31.71
4x5 min	160	0.5	83	747	1.903	5.55	27.77
4x5 min	240	0.5	83	671	1.954	5.52	22.21
4x5 min	80	0.95	82	877	1.820	5.57	35.93
4x5 min	160	0.95	82	773	1.809	5.47	37.07
4x5 min	240	0.95	82	653	1.893	5.35	28.73
Auto rotation	220	0.5	82	506	2.070	5.63	9.13
10+4x5 min	140	0.5	79	1154	1.904	5.42	29.77
10+4x2 min	140	0.5	82	670	1.891	5.38	28.92
10+10x1 min	140	0.5	77	869	1.853	5.37	32.79
No rotation	80	0.5	81	1104	1.852	5.38	33.13
No rotation	160	0.5	81	1135	1.907	5.39	27.95
No rotation	240	0.5	81	723	1.975	5.32	19.93

Table 7.4: Summary of the optical properties obtained in this chapter.

7.4 Summary and conclusions

Based on the grain and columnar tilt previously discussed in this thesis, we observed that it is possible to control the growth of the YSZ film to a desired microstructure or a specific characteristic. The tilt was shown to follow the source with the smallest ionic radius (Zr source). Using this effect, zig-zag films were produced. In the first part of this chapter, some examples of substrate rotation were shown. In addition, the microstructure and texture of these films were discussed. Knowing the characteristics of the film, the inclination of the zig-zag column was easily controlled and tuned.

The optical properties were analyzed based on the film microstructure. The effect of the microstructure on the transmittance, the refractive index and the band gap are difficult to be determined because other factors also contribute to the variation on the optical properties, such as thickness, Y content, pressure and porosity. However, using auto rotation on the film growth, we obtained films with high refractive index (2.2) in the visible light and high band gap (5.63 eV). A comparison between the obtained thickness and porosity of the experimental and simulated values was presented and indicated equivalence between values.

We finish this thesis with a chapter about recommendations for future work, where an introduction on the ionic conductivity of thin films is given. In addition we describe how the measurement can be obtained, the drawbacks and limitations faced as well as some preliminary results on the YSZ system.

8

Recommendations for future work

8.1 Ionic conductivity of YSZ thin films: a preliminary test

The addition of Y_2O_3 up to 60 at.%Y was shown to completely stabilize the ZrO_2 in the cubic phase. Due to this addition, oxygen vacancies are introduced in the ZrO_2 lattice. Since the ionic conductivity is correlated with the amount of oxygen vacancies in the lattice, this addition results in an improved ionic conductivity. Therefore, cubic YSZ is a suitable material to be used as an electrolyte for solid oxide fuel cells (SOFC) applications [9, 10, 67, 85]. Although SOFC are successfully applied at high temperatures, lowering the operational temperature is one of the main goals in current research. One possible solution is to reduce the thickness of the electrolyte, thus, minimizing ohmic losses, lowering SOFC cost and improving its performance. However, this reduction induces an alteration in the characteristics and structure of the electrolyte [85]. The change in microstructure has turned out to be positive for the improvement of the ionic conductivity. Some authors have used YSZ nanostructured films as electrolyte using atomic layer deposition [88, 90, 91] in order to obtain films in the range of ten of nanometers. An alternative is the use of pulsed laser deposition to obtain layers varying from 20 up to 90 nm [28, 29]. Instead of decreasing the thickness to improve the ionic conductivity, we suggest a microstructural control using magnetron sputtering to produce nanostructured YSZ thin films.

The initial impedance spectroscopy measurements were done in collaboration

with the Institute for Chemical Technologies and Analytics (TUWien)[1]. This group is specialized in determining the ionic conductivity of very thin layers of YSZ. The sample sent to be measured is the same auto rotation sample used in Chapter 7. Impedance was measured using an impedance spectrometer (Novocontrol Alpha) from 1 Hz to 1 MHz at temperatures between 250 °C to 500 °C. The deposition conditions of this sample are listed in Table 8.1.

Sample	**B**
Pressure (Pa)	0.5
Flow O_2 (sccm)	2
Deposition time (min)	20
Thickness (μm)	0.795 ± 0.01
Composition (at.% Y)	9.58 ± 0.38
Rotation	Auto (0.5 rot/s)
Substrate	Si

Table 8.1: Deposition conditions of the YSZ sample prepared for impedance spectroscopy measurements.

Unfortunately, the measurement of impedance is not trivial, since several external factors should be taken into consideration. In this work two features were taken into consideration when impedance spectroscopy was performed.

- The first is related to the configuration of the sample. Based on the work of Navickas [29] a simultaneous in-plane and across-plane measurement can be done using silica layer (approximately 2 nm) between YSZ film and substrate. The schematic representation of the sample configuration is illustrated in Figure 8.1.

  The impedance of the silica layer is frequency dependent. At high frequencies it has very low impedances values. As a consequence, the current can flow across-plane into the conducting silicon substrate. At low frequencies the silica layer becomes insulating and the current is forced to flow in-plane, i.e. along the YSZ layer. This configuration allows the simultaneous in-plane and across-plane conductivity measurement due to the oxide layer present on the silicon wafer. The results of the across-plane measurements represent the conductivity of the grain bulk while the in-plane conductivity is affected by grain boundaries.

[1]We kindly thank Msc. E. Navickas for the impedance spectroscopy measurement.

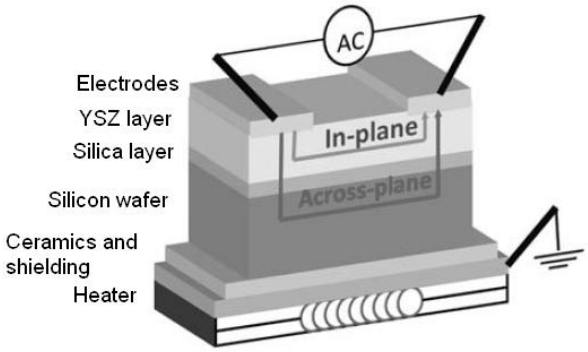

Figure 8.1: Schematic drawing of the sample configuration for impedance spectroscopy measurement [29].

- The second feature is related to the electrodes. The position and the type of the electrodes influence the total resistance. Two different types of electrodes were proposed in the work of Navickas [29, 283]: a circular microelectrode with different diameters (across-plane measurements) and stripe microelectrode with different distances (in-plane measurements). An illustration of the electrodes on the YSZ sample is displayed in Figure 8.2.

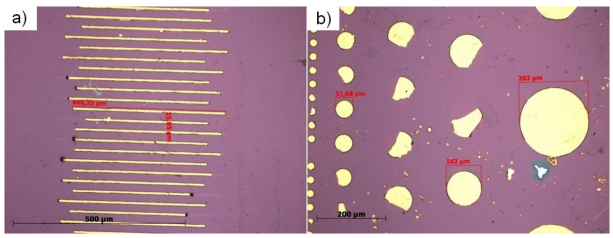

Figure 8.2: Microelectrodes of gold with a) stripe electrodes for in-plane measurements and b) a circular shape for the across-plane measurements.

The effect of both electrodes in the total impedance is given in the Nyquist plot of Figure 8.3. The temperature was set to 350 °C. Figure 8.3a shows the in-plane impedance (real and imaginary) as a function of the distance of the stripes. From this figure it is noticeable that the impedance increases with the increase of the distance between electrodes. The low frequency region in the Nyquist plot corresponds to the high values of the resistance (real part of the impedance, Z'). Complementary, the high frequency is located in the region of low Z'. Figure 8.3b indicates the impedance obtained

in across-plane measurements. Note that the variation of the resistance is located in the region of high frequency. In this case, the impedance decreases with the increase of the electrode diameter.

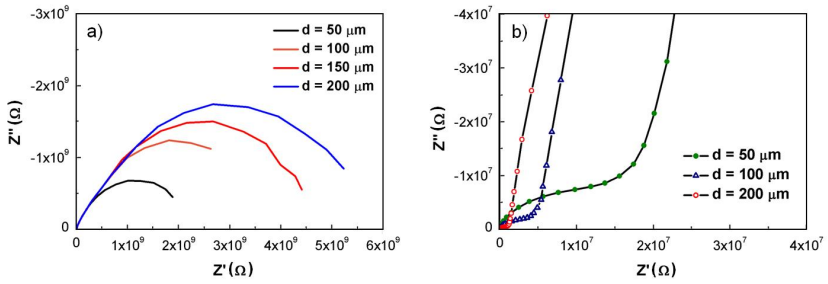

Figure 8.3: Nyquist plot of impedance as a function of the a) distance between the stripes electrodes and b) diameter of the microelectrodes.

Table 8.2 lists the total resistances obtained for both types of electrodes. Note that the in-plane resistance is higher than across-plane due to its geometrical configuration (see Figure 8.1).

	Electrode	**d [μm]**	**R [Ω]**
In-plane	Stripes	50	2.3×10^9
In-plane	Stripes	100	4.0×10^9
In-plane	Stripes	150	4.9×10^9
In-plane	Stripes	200	6.1×10^9
Across-plane	Circular	50	16.2×10^6
Across-plane	Circular	100	4.5×10^6
Across-plane	Circular	200	1.1×10^6

Table 8.2: Total resistances obtained for in-plane (stripes electrodes) and across-plane measurements (circular electrodes).

Since in-plane measurements can determine the impedance for in- and across-plane based on the frequency dependency of the silica layer, a 50 μm stripe electrode was used to determine the effect of temperature on the conductivity of the YSZ film. The temperature was varied in steps of 50 °C from 250 °C to 500 °C. The Arrhenius plot of our YSZ thin film and an YSZ polycrystalline are displayed in Figure 8.4. In addition the in-plane and across-plane conductivities from in-plane measurements are also added to the plot. The bulk YSZ polycrystalline

is a reference in order to compare results. These values are estimated based on the electrodes dimensions [29] and are given by:

$$\sigma_{across-plane} = \frac{2t_{YSZ}}{R_{YSZ\perp} ls} \tag{8.1}$$

$$\sigma_{in-plane} = \frac{d}{R_{YSZ||} t_{YSZ} l} \tag{8.2}$$

where t_{YSZ} is the thickness of the YSZ multiplied by two in equation 8.1 because the current passes the layer twice in the across-plane configuration. R_{YSZ} corresponds to the resistance at high frequency and l and s are the length and the width of the electrodes. The R_{YSZ} is the resistance at low frequency and d is the distance between electrodes. Analyzing Figure 8.4 we can conclude that the measured in-plane and across-plane from in-plane measurements are equivalent and any of these configurations can be used to determine the impedance of the studied films. The calculated activation energy for the polycrystalline YSZ and the film are 1.05 eV and 0.83 eV, respectively. According to literature [284], this difference reflects the effect of the grain boundary in the film. In addition, the fact that the conductivity of our samples (1.37×10^{-6} S/cm) is comparable to the conductivity of a bulk YSZ (1.67×10^{-5} S/cm) indicates that the conductivity of our films is meaningful.

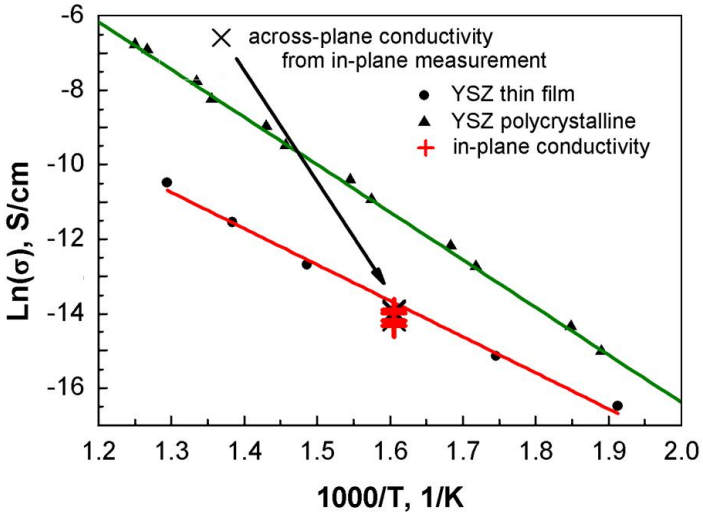

Figure 8.4: Arrhenius plot comparing the effect of the YSZ polycrystalline and our YSZ thin film. The in-plane and cross-plane conductivity are also added to the plot.

Unfortunately, due to time restrictions, no further investigations could be performed. However, we believe that more results with different films microstructures would allow us to understand the relations between microstructure and ionic conductivity. One might think that a limitation of our films is the porosity between columns, since the porosity values shown in previous chapter are approximately 30 %. A straight solution to the porosity is the use of HiPIMS, which allows the deposition of thin films with high densities [154]. However, by varying the rotation of the substrate samples a porosity of 9.3 % was obtained, meaning that the porosity can also be reduced when deposited via DC magnetron sputtering. The use of DC magnetron sputtering allows us to understanding the effects occurring in the YSZ system and to relate it with different film properties, including the ionic conductivity on thin films. Therefore, based on the results presented above, we encourage further research on the ionic properties of YSZ deposited by DCMS and to study the relations between conductivity and the film microstructure and texture.

8.2 Recommendations related to this thesis

Some answers remained unsolved during this thesis. Therefore, thinking about them, a list was added for future work and perspectives.

Although Chapter 5 explains in great extension the influence of several parameters on the YSZ system, more analysis can be performed in order to determine accurately when the rotates starts. In addition, it would be interesting to study the evolution of the 3D growth in the columns. In this way, not only how the rotates occurs would be solved but also how it is correlated to the material flux would be revealed. A possible change on the magnetron angle would allow us to understand this correlation.

The model was nicely developed in Chapter 6. However, the nano-scale analysis at high pressure was not completely acquired and only an assumption was done. The use of STEM-EDX could also be extended and an alternatively would be to identify the grains and the grain boundaries via bright-field images. In this way, it would be possible to certify that the compositional gradient is defined by a crystal size.

The optical properties results indicate that even though the measurements are easy to perform, the analysis of these results are complex because the parameters are interconnected. A proposal to this work is to perform measurements keeping a certain parameter invariable and determining the effect of the others on the optical properties.

Finally, knowing that it is possible to manipulate the characteristics of YSZ films, it would be interesting to study several properties in order to optimize the current YSZ film.

9
Summary

In this doctoral work, four goals can be distinguished. The first involves the creation of a library of the yttria-stabilized zirconia (YSZ) system, where the YSZ characteristics can easily be tuned based on the deposition conditions. The second consists on the understanding of the YSZ microstructure and texture behavior. The third part allows predicting the crystallographic aspects of the YSZ system. Finally, with the information of the first three goals it is possible to understand and control the YSZ growth which permits the manipulation of YSZ properties.

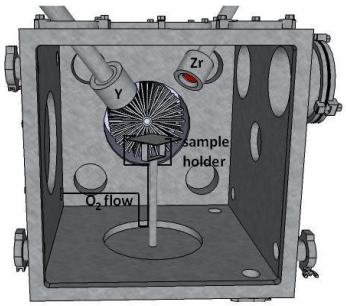

Figure 9.1: Schematic drawing of the experimental setup.

YSZ films were deposited using DC dual reactive magnetron sputtering. The targets were positioned with an inclination of 45° in relation to the substrate (see Figure 9.1). This geometry allows the growth of biaxial alignment films, i.e. the films have an out-of-plane as well as an in-plane orientation.

In this work, the influence of the current, the yttrium target-substrate (Y T-S) distance, the pressure and the deposition time was investigated. Each of these conditions affects the characteristics of the film (thickness, composition, grain size

and lattice parameter). The effect on the YSZ characteristics was studied in detail. The thickness and the composition are both defined by the amount of material arriving on the substrate. The reduction of the Y T-S distance increases thickness and content of Y. Pressure, on the other hand, inhibits the increase of thickness due to the increase of scattering, i.e. the particles will arrive with different orientations and directions.

The content of Y, on the other hand, is less influenced by pressure. On the contrary, current strongly affects not only the final thickness of the film but also the final content of Y, which was explained by the increase of deposition rate. The thickening of the film could also be achieved by increasing the deposition time. The composition along the film was compared to simulation results based on a Monte Carlo code. We demonstrated that the use of a cosine angular distribution gives an error of 20 %. By tuning the angular distribution, the fit between experimental and simulated data (see Figure 9.2) presented an average percentage error of 9 %. The thickness was also calculated based on simulation results. In addition, the porosity was obtained by calculating the ratio between measured and simulated thickness. The range of porosity varied up to 38 %.

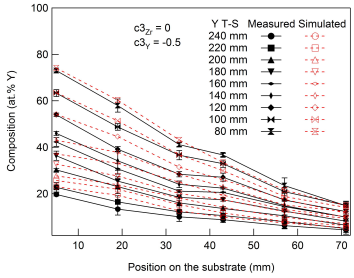

Figure 9.2: Comparison between measured and simulated composition.

The grain size and the lattice parameter vary as a function of the deposition conditions. Moreover, this variation is strongly dependent on the composition. The grain size indicated an exponential decay slope which varies as a function of the pressure. Smaller grain sizes were found at high pressure, due to the Y acting as barrier inhibiting the growth of the crystallites.

The lattice parameter is also dependent on the content of Y, following a linear trend for a large range of Y content varying from 10 up to 60 at.% Y (see Figure 9.3). This trend follows the linear trend suggested in Vegards' law.

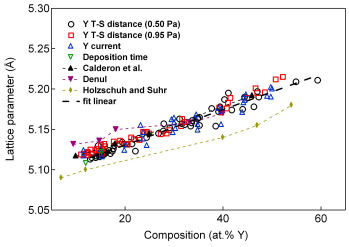

Figure 9.3: Linear trend between lattice parameter and content of Y.

The linear trend between lattice parameter and composition indicates the absence of stress in the lattice when the content of Y increases.

Although the insertion of Y would induce compressive stress, the results suggest that another mechanism takes place to relieve the stress. Based on nano scale analyses, we suggest that the linear behavior of the lattice is an average of a tensile and a compressive region, where the tensile stress occurs in the region rich on Y and the compressive in the region rich of Zr.

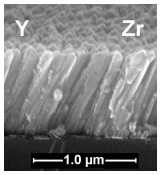

Figure 9.4: SEM image of a film deposited at 0.5 Pa and Y T-$S_{distance}$ = 200 mm.

The microstructure analyses of the YSZ system indicated that the films have a columnar structure. Based on scanning electron microscopy (SEM) images, our samples were identified to grow in zone T with well defined facetted V-shape columns (see Figure 9.4). The [200] direction was identified to be the out-of-plane preferred orientation. In addition, a columnar tilt was observed when the content of Y increases due to the change of Y T-S distance or current. High pressure seems to hinder the effect of the Y content in the structure, which was observed by the constant columnar tilt. Interestingly, the tilt of the columns follows the target with the smallest ionic radius, i.e. Zr target.

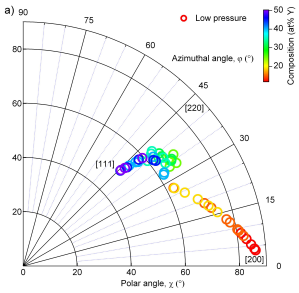

Figure 9.5: Example of a XRD/polar plot at low pressure.

The grain tilt shows a similar behavior. At low pressure, there is a tilt of the [200] preferred orientation when Y content increases. Above 35 at.% Y not only a tilt is noticed but also a rotation of the lattice. However, the rotation was not identified when current was changed. From both results, it is concluded that the rotation has no energetic background but it is related to a combination between T-S distance and Y content. Pressure shows no influence on the variation of the grain tilt. Instead a tilt between 35-40° was found. In addition, when the Y content is too high, the biaxial alignment is lost and the film becomes uniaxial aligned. The deposition time has no effect on the texture of the films.

In this work, we compared two methods to determine quantitatively the grain tilt: pole figure/polar plot and XRD/polar plot. The first takes the χ and φ values of the [200] direction on the pole figure as input for the polar plot. The azimuthal angle on this plot gives the grain tilt angle. The second approach (XRD/polar

plot) takes the fractions of the three highest intensity peaks (*hkl* directions) of the XRD diffraction and creates a resultant vector. This vector can be placed in the triangle formed by these directions in a polar plot (see Figure 9.5). Therefore, we have to be careful with this kind of plots because it can be interpreted in two ways: as a representation of the diffraction lines, showing the influence of the diffraction peaks in the XRD results, or as the result of the tilting of the crystals. Using the second interpretation, the azimuthal angle corresponds to the grain tilt. The disadvantage of this pole figure/polar plot in relation to X-ray diffraction (XRD) is the time involved to obtain a pole figure. Normally, it takes up to 2 hours to obtain the (111) and (100) pole in contrast to the 30 min needed to perform a full $\theta/2\theta$ scan. From only one $\theta/2\theta$ scan both [111] and [200] information are obtained. Moreover, the accuracy in χ and φ angles is far from ideal since our film alignment strongly depends on the deposition conditions. As a result, the error is caused by the uncertainty on the χ and φ values of the [200] direction.

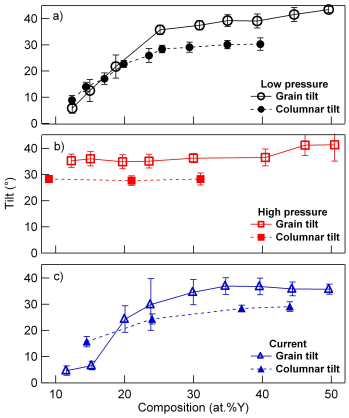

Figure 9.6: Columnar and grain tilt for different deposition conditions.

The columnar and grain tilt were shown to have a similar behavior. At low pressure (see Figure 9.6a), both are equal and increase linearly until approximately 24 at.% Y. This can be understood by the grains being formed as blocks on the top of each other. Each block is deformed when Y^{3+} is inserted in the ZrO_2 lattice. As a result, the lattice of one side differs from the other. Thus, the resultant column has a tilt as a function of the composition, which affects the lattice parameter and the grain size. Above 24 at.% Y, a discrepancy was found. This difference is related to the rotation of the lattice which was demonstrated to be approximately 12°. Due to the rotation, the 3D growth of the films cannot be observed in a 2D cross section. Similar behavior was found when the experiments were performed at different discharge currents (see Figure 9.6c). At high pressure (see Figure 9.6b), on the other hand, a constant value of tilt was found in the whole range of composition. However, grain and columnar tilt also differed in approximately 12°.

A model to predict the grain tilt was developed based on a known bi-metal strips stress model. This model takes into consideration the compositional gradient and the thickness of the films as well as the

characteristics of the materials (ionic radius, lattice parameter). The compositional gradient is obtained from a macroscopic and a nano scale approach. A compositional profile is observed in the STEM-EDX mapping of a single column where two regions are distinct: a region of high and low Y content. The difference on this compositional profile was shown to be the same as the macroscopic composition, since a 1:1 relation between both compositional gradients was found. Hence, the compositional gradient at macroscopic level is sufficient to predict the behavior at nano scale (see Figure 9.7). Comparing both results to the model revealed that despite of its simplicity the model provides a good agreement between measured and calculated results over the whole area of the YSZ samples. The model was also applied to the results with different current and high pressure. The model fits well for the change of current, agreeing with the results shown at low pressure. High pressure, on the other hand, was demonstrated to be influenced by two effects. At low content of Y, the tilt is generated by ballistic deposition and the closest target defines the tilt of the column. Above 25 at.% Y, the stress model takes over and the inclination of the column is given by the addition of Y. As a result the tilt remains constant along the compositional range.

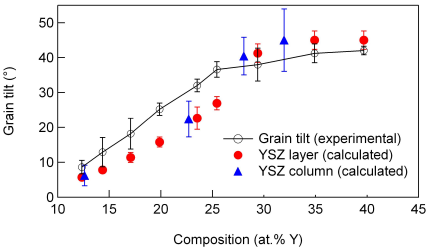

Figure 9.7: Prediction of the grain tilt based on macroscopic and nano scale in comparison with experimental results.

At this point the film characteristics, texture and microstructure are understood. This allows manipulating the film growth and thus the film properties. Using the columnar tilt, it is possible to play with the film growth in order to produce zig-zag structures (see Figure 9.8). This kind of microstructure affects the properties of thin films. The optical properties were studied in order to identify the effect of the microstructure on the light transmission. Due to other factors, such as thickness, content of Y, pressure and porosity, it is difficult to obtain a straight relation between microstructure and optical properties. However, it was shown that by tuning the film characteristic we can produce films with high refractive index, band gap or even diminish the porosity of the film.

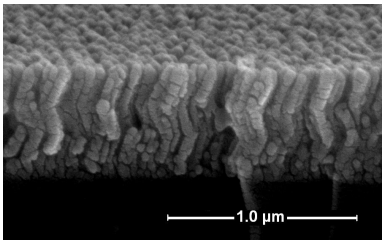

Figure 9.8: Zig-zag structure.

To finalize this thesis, ionic conductivity measurements were performed. Preliminary results on the ionic conductivity indicate that the conductivity of our films is meaningful when compared to the conductivity of a bulk YSZ. This is very positive, considering the difficulty in determining the impedance of thin films. The measurement of impedance is not trivial, since several external factors should be taken into account. A main difficulty of this technique is the contact between electrodes, which can take some time before being optimized. Therefore, as future work we suggest an investigation of the influence of the microstructure and texture on the ionic conduction of YSZ thin films.

A

Biaxial alignment influenced by pressure

Based on the experimental results shown in Part IV (5.4), Chapter 5, and the information given in Chapter 4, it was shown that our films have the interesting feature of biaxial alignment. In this appendix, we focus on the influence of the pressure and the deposition time to discuss the improvement and the worsening of this phenomenon.

A.1 Biaxial alignment influenced by pressure

The dimensions of the sputtering chamber and the amount of Ar flow needed to keep the discharge voltage on, makes it difficult to decrease the pressure to values lower than 0.25 Pa. A way to overcome this matter is to use a local Ar inlet on the surface of the magnetron. In this way, pressures as low as 0.09 Pa can be achieved. Using this concept, we use a single compound target (Lesker) containing 45 at.% of Y and 55 at.% of Zr in order to study the effect of the pressure on the alignment of YSZ thin films. In this setup there is also a local O_2 flow on the surface of the substrate, in order to obtain fully oxidized samples. The film thickness was kept in the same range as the experiments reported in Part I (5.1), Chapter 5. Therefore, the current was increased to 0.7 A. The T-S distance is fixed at 130 mm, the deposition time at 30 min and the flow of O_2 at 2 sccm. Those conditions are comparable with the ones used in the work of Mahieu [195]

at higher chamber pressures (0.2 to 0.8 Pa). In this work, we limit the pressure variation from 0.25 Pa down to 0.09 Pa.

The decrease of pressure was described to improve the alignment in Chapter 3. This was also shown in the work of Mahieu [195] from pressures decreasing from 0.8 to 0.3 Pa. The in-plane alignment is affected by the angular spread on the incoming material flux, which varies with the variation of pressure. During the transport through the gas, the sputtered particles collide with the gas acquiring different directions. When the material reaches the substrate, it will have a different angular spread. This effect becomes stronger at higher pressures where the sputtered particles have higher probability to collide and scatter. Due to the increase in scattering, the atoms arrive with different orientations, directions and energies. A proof of this effect was seen in Part IV (5.4), Chapter 5, at high pressure and high content of Y where the biaxial alignment is lost and the film becomes uniaxial aligned. This argument contradicts the results obtained at 0.2 Pa in the work of Mahieu, where the in-plane alignment worsens. By changing the pressure to lower values, we expect to show that the decrease of pressure improves the in-plane alignment. At low pressures, the sputtered particles are more likely to arrive with a certain direction and therefore, the alignment increases. Figure A.1 shows the pole figures at 0.25 Pa and 0.14 Pa. A possible improvement of the biaxial alignment cannot be clearly observed from these pole figures.

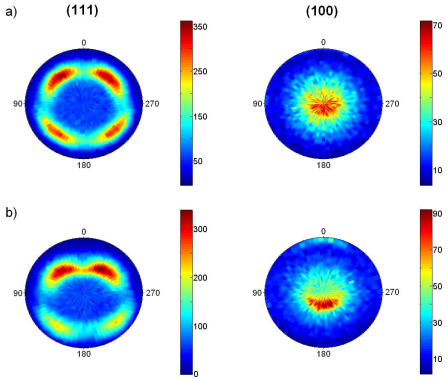

Figure A.1: Pole figures indicating the (111) and (100) pole at: a) 0.25 Pa and b) 0.14 Pa.

Another way to determine the improvement of the alignment is to obtain the full width at half maximum (FWHM). The FWHM was determined from 0.25 Pa to 0.09 Pa and these results were compared with the results of Mahieu [195]. Figure A.2 illustrates this comparison. Note that the FWHM decreases with the decrease of pressure, going in contrast to the results of Mahieu at 0.2 Pa but agreeing with the expected improvement of the alignment.

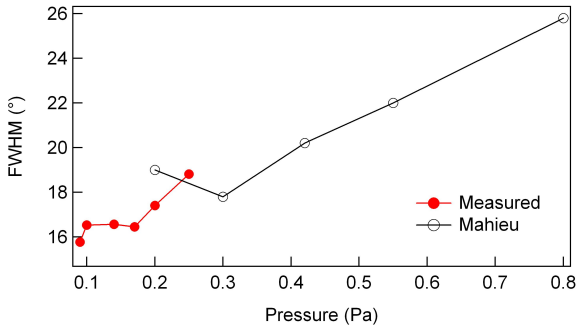

Figure A.2: FWHM as a function of pressure. Comparison of the results from Mahieu [195] at high pressure and measured results at lower pressures using a local Ar inlet on the target surface to obtain pressures down to 0.09 Pa.

A.2 Biaxial alignment influenced by thickness

The thickness has a direct effect on the biaxial alignment which can be seen in the pole figures of Figure A.3.

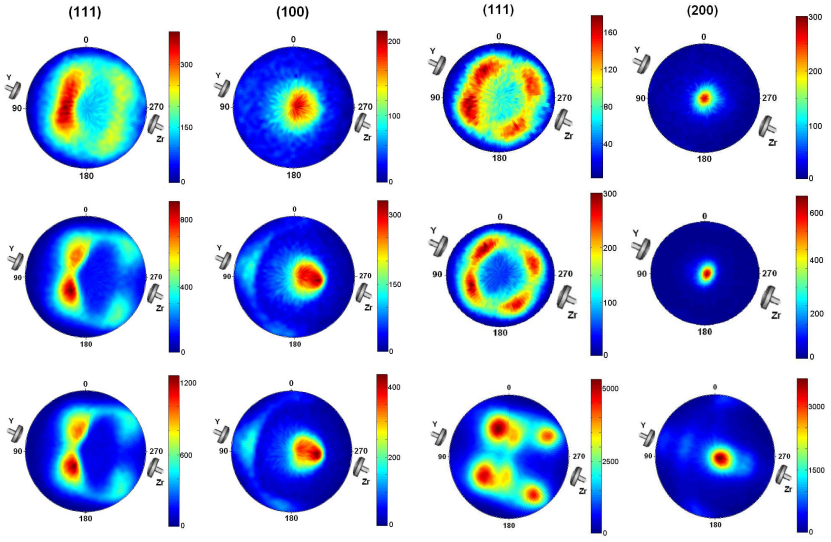

Figure A.3: The first column shows the pole figures at a) 10 min (0.5 μm), b) 18 min (1 μm) and c) 26 min (1.4 μm) deposited with a Y T-S distance of 80 mm (21.7 at.%Y). The pole figures of the second columns represent depositions performed at d) 20 min (0.6 μm), e) 40 min (1.4 μm) and f) 80 min (2.8 μm) with a Y T-S distance of 240 mm (9 at.%Y).

Two different comparisons were done in order to compare the influence of composition and time: 1^{st} taking into consideration shorter deposition times, i.e. depositions at 10, 18 and 26 min (Figures A.3a to c); and the 2^{nd} comparing longer deposition times, 20, 40 and 80 min (Figures A.3d to f). The 1^{st} and 2^{nd} column correspond to films deposited at a Y T-S distance of 80 mm illustrated by the (111) and (100) pole, while the 3^{rd} and 4^{th} columns illustrate the films deposited with a Y T-S distance of 240 mm. The compositions are 21.7 and 9 at.% Y, respectively. At 10 min (Figure A.3a), the biaxial alignment is poor. There is a main [200] out-of-plane preferred orientation but, the four [111] peaks are difficult to be identified. As soon as the deposition time increases to 18 min (Figure A.3b), a distinction of these fours peaks can be made and the width of the [200] peak is smaller. At 26 min (Figure A.3c) we observed that those peaks are better defined. In Figures d, e and f, there is a clear improvement of the alignment which can be detected not only by the change in width of the peaks but also by the peaks intensities indicated in the color bars. As thickness affects directly the alignment of these films independently of the composition of the film, we consider that the composition has no effect on the alignment. Some examples in literature of the improvement of the alignment as a function of the thickness can be found for MgO, TiN and Cr systems in [195, 218].

Figure A.4 displays the FWHM of YSZ films with 0.6 μm, 1.4 μm, 2 μm, 2.8 μm, 3 μm, 3.6 μm and 5.4 μm thickness in order to observe this improvement. The FWHM decreases with the increase of thickness, tending to a constant value when thickness is superior to 2.8 μm. In the work of Mahieu [134] is explained that this improve is due to the overgrowth mechanism. This means that the grains with different orientations cease to grow and the [200] grains, which are the geometric fastest growing direction, dominate the growth and consequently the final alignment of the film [118].

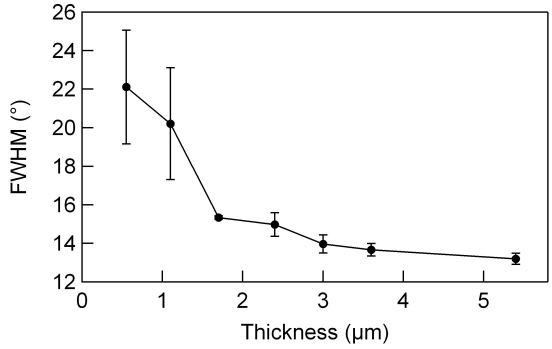

Figure A.4: FWHM as a function of thickness. The FWHM decreases with the increase of thickness (deposition time), improving the film alignment.

B

Calculating grain size and microstrain

In Section 5.1.3, Part 5.1, Chapter 5, it was discussed that the grain size can be calculated using Debye-Scherrer equation without taking into consideration any contribution of microstrains in the film. In this Appendix, the grain size and the microstrain are calculated using a Voigt function in the XRD pattern of the film, as suggested in [230, 285].

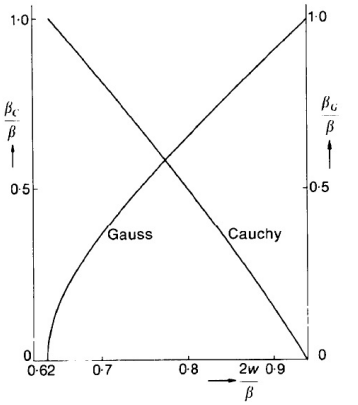

Figure B.1: Ratios of the integral breadths of the Cauchy (β_C) and Gaussian (β_G) components to the total integral breadth (β) as a function of the ratio between the FWHM (2w) and the total integral breadth (β). Figure obtained from [230].

From the fit of the Voigt function, we obtained the integral breadth and the FWHM of the peaks. Then, the ratios of the integral breadth of the Cauchy (β_C) and Gaussian (β_G) components to the total integral breadth (β) are calculated. The constitutent Cauchy and Gaussian components are obtained from Figure B.1 [230].

The Cauchy component allow us to calculate the values of the grain size while the Gaussian component allow us to calculate the microstrain using the equations below:

$$\kappa = \frac{K\lambda}{\beta_C \cos\theta} \tag{B.1}$$

$$\epsilon = \frac{\beta_G}{4\tan\theta} \tag{B.2}$$

Figure B.2 displays the calculated grain size with and without the contribution of the microstrain and the values of microstrains as a function of the position on the substrate for samples with different discharge currents.

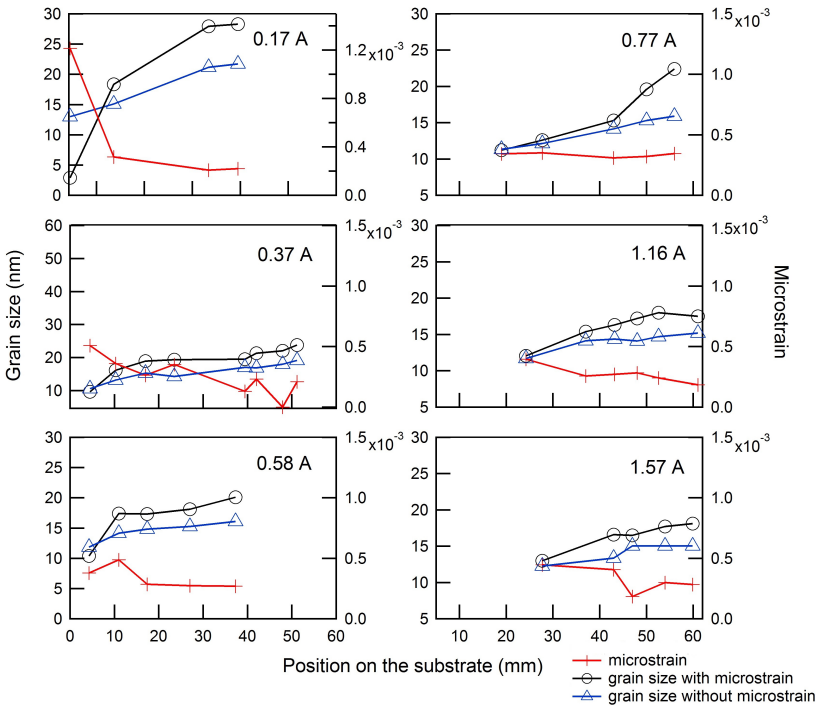

Figure B.2: Comparison between the calculated grain size with and without the microstrain contribution. The circle and the triangle markers represent the grain size with and without the contribution of the microstrain, respectively. The values of the microstrain are illustrated by the '+' marker.

From this figure, it is observed that the difference between both grain sizes is not large. The values of microstrains are also small. It is noticeable that the microstrain increases with the decrease of the position on the substrate (closer to Y target). It is known that this approximation to the position of the Y target leads to higher content of Y and consequently smaller grain sizes. From literature [285] it is expected that smaller crystallites will have higher values of microstrain, agreeing with the obtained results. Based on these results, the error on the analysis performed in Part 5.1 is not significant when comparing to the results of the grain size with the contribution of the microstrain.

C

Microstructure and texture of thick films

In Chapter 5, the change on the characteristics of YSZ thin films were discussed as a function of some deposition conditions. The effect of the deposition time was not longer discussed in Parts II to V (5.2 to 5.5) because it only affects the final thickness of the film and therefore no variation is expected on the other characteristics of the YSZ system such as, texture and microstructure.

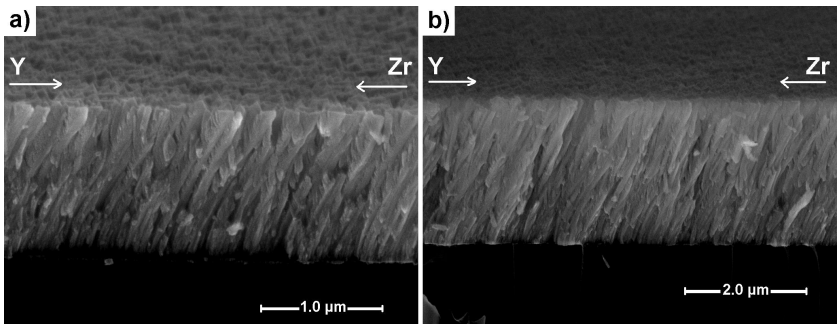

Figure C.1: SEM images for different deposition times, samples deposited during: a) 40 min (1.4 µm and 8 at.% Y) and b) 80 min (2.8 µm and 8 at.% Y). The change in thickness does not affect the final microstructure.

In this appendix we focus on the microstructure and texture of thicker films showing that these characteristics are invariable. From the images shown in Figure C.1 we observe that the variation of thickness from 1.4 μm to 2.8 μm has indeed no effect on the microstructure. The measured columnar angle are the same, being 30.7 ± 2.2° and 29.6 ± 1.9° for sample deposited at 40 and 80 min, respectively. In addition, both films grow in zone T.

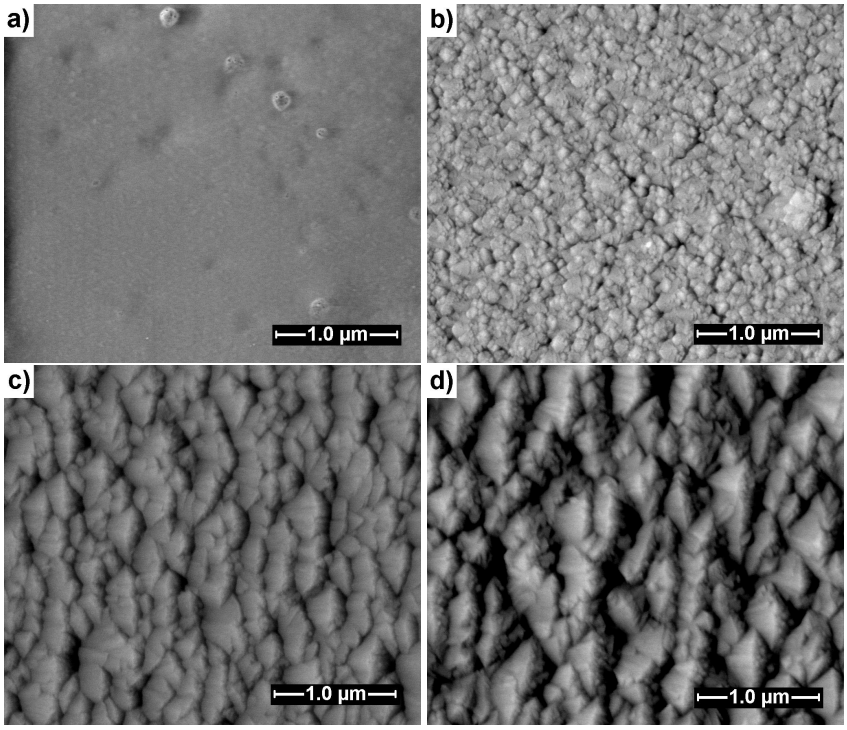

Figure C.2: Surface images of: a) glass substrate and of YSZ films deposited during: b) 40 min (1.4 μm); c) 100 min (3 μm) and d) 150 min (5.4 μm).

As we know that the growth in zone T is the same, we can observe how the thickness affects the final shape of the film surface. Figure C.2 illustrates the surface view of (a) the glass substrate and of YSZ films deposited at (b) 40 min (1.4 μm), (c) 100 min (3 μm) and (d) 150 min (5.4 μm). These images clearly show the thickening of the pyramidal surface structure of the film deposited on a flat glass surface. Note that the grains are faceted and nicely aligned.

And finally, the texture is represented in Figure C.3 by the XRD $\theta/2\theta$ spectra deposited during 20, 40, 60 and 80 min. From this image the [200] is shown to be the preferred orientation independently of the deposition time. This behavior is

evident since the deposition conditions remain the same and therefore no possible zone transition should be identified. Moreover, based on these results, it is possible to conclude that the grain tilt remain constant. However, the intensity peak is different which can be correlated with the improvement of the alignment previously reported in Appendix A.

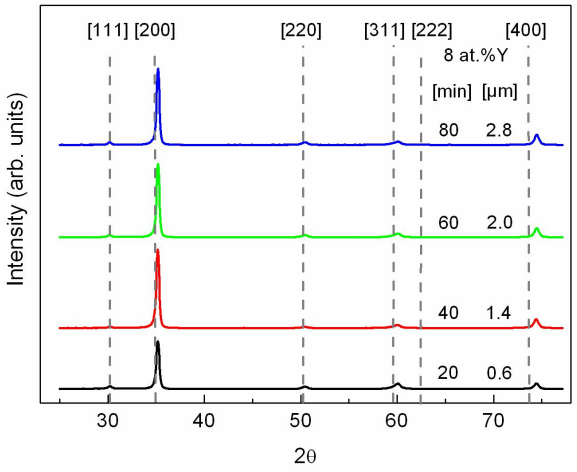

Figure C.3: XRD θ/2θ spectra for different deposition time (20, 40, 60 and 80 min) and thickness (0.6 µm, 1.4 µm, 2.0 µm and 2.8 µm) deposited at low pressure.

D

Publication list and Conference Contributions

D.1 Publications in peer reviewed international journals

D.1.1 Contributions to Scientific Journals:

1. J. S. Lamas, W. P. Leroy, Y-G. Lu, J. Verbeeck, G. Van Tendeloo, D. Depla. *Using the macroscopic scale to predict the nano-scale behavior of YSZ thin films*. Surface and Coatings Technology, 2013, DOI: 10.1016/j.surfcoat.2013.10.034.

2. J. S. Lamas, W. P. Leroy, D. Depla. *Influence of the target-substrate distance on the growth of YSZ thin films*. Surface and Coatings Technology, 241: 2629, 2014.

3. J. S. Lamas, W. P. Leroy, D. Depla. *The fictional transition of the preferential orientation of yttria-stabilized zirconia thin films*. Thin Solid Films, 525: 6-12, 2012.

4. J. S. Lamas, W. P. Leroy, D. Depla. *Influence of target-substrate distance and composition on the preferential orientation of yttria-stabilized zirconia thin films*. Thin Solid Films, 520(14): 478254, 2012.

D.1.2 Publication in journals without a reader committee:

1. J.S. Lamas, W. P. Leroy, D. Depla. *Influence of the target-substrate distance on the growth of YSZ thin films*. SVC 56^{th} Annual Technical Conference Proceedings, 2013.

2. D. Depla, M. Saraiva, J. Lamas. *Dual magnetron sputtering of mixed oxide layers*. Belvac, October, 2011.

D.2 Contributions to Scientific Meetings:

1. J. S. Lamas, W. P. Leroy, D. Depla, Yttria-Stabilized Zirconia thin films as oxygen ion conductor for solid oxide fuel cells, 19^{th} International Vacuum Congress IVC-19, Paris, 9-13^{th} September, 2013, oral presentation.

2. J. S. Lamas, W. P. Leroy, Y-G. Lu, J. Verbeeck, G. Van Tendeloo, D. Depla. *Influence of the Crystallographic Properties on the Ionic Conductivity of YSZ Thin Films*. Society of Vacuum Coaters SVC TechCon 2013, Providence, RI, 20-25^{th} April, 2013, oral presentation.

3. J. S. Lamas, W. P. Leroy, D. Depla. *Nanostructured thin fims for solid oxide fuel cells: crystallographic properties*. Seventh Belgian Crystallography Symposium BCS-7, Brussels, 10^{th} October, 2012, poster presentation.

4. J. S. Lamas, W. P. Leroy, D. Depla. *Nanostructured thin films of yttria-stabilized zirconia*. PSE2012, Garmisch-Partenkirchen, 10-14^{th} September, 2012, oral presentation.

5. J. S. Lamas, W. P. Leroy, D. Depla. *Nanostructured thin films for solid oxide fuel cells: crystallographic properties*. Belgian Physical Society BPS Meeting 2012, Brussels, 30^{th} May, 2012, poster presentation.

6. D. Depla, M. Saraiva and J. Lamas. *Magnetron sputter deposition of biaxial aligned thin films*. EMA2012, Orlando, 18-20^{th} January, 2012, oral presentation (invited).

7. D. Depla, M. Saraiva and J. Lamas. *Dual magnetron sputtering of mixed oxide thin films*. ISPP20122, Kyoto, 6-8^{th} July, 2011, oral presentation (invited).

8. J. S. Lamas, W. P. Leroy, D. Depla. *Influence of target-substrate distance and composition on the preferential orientation of thin films*. 18^{th} International Colloquium on Plasma Processes CIP 2011, Nantes, 4-8^{th} July, 2011, oral presentation.

9. J. S. Lamas, W. P. Leroy, D. Depla. *Influence of target-substrate distance and composition on the preferential orientation of thin films*. Belgian Physical Society BPS Meeting 2011, Namur, 25^{th} May, 2011, poster presentation.

10. J. S. Lamas, W. P. Leroy, D. Depla. *A two-dimensional view on the preferential orientation of Yttria-Stabilized zirconia thin films*. EMRS-2011 Spring Meeting, Nice, 9-13^{th} May, 2011, poster presentation.

D.3 Participation in schools /short courses:

1. Sputter Deposition, Society of Vacuum Coaters Tutorial course, Providence, RI, $21^{st}22^{nd}$ April, 2013.

2. Nanobeams PhD School: Plasma module, University of Luxembourg & Centre de Recherche Public - Gabriel Lippmann, Belvaux, 19^{th}-21^{st} September, 2012.

3. Doctoral Day on Sputtering, UMons, Mons, 8^{th} October, 2010.

D.4 Awards:

1. SVC Student Sponsorship Program, Providence, RI, 20-25^{th} April, 2013.
   Work titled: *Influence of the Crystallographic Properties on the Ionic Conductivity of YSZ Thin Films*.

2. Best Poster presentation at EMRS-2011 Spring Meeting, Nice, 9-13^{th} May, 2011.
   Work titled: *A two-dimensional view on the preferential orientation of Yttria-Stabilized zirconia thin films*.

D.5 Other contributions to Scientific Journals:

1. C. A. Baldan, J. S. Lamas, A. A. Bernardes, C. Y. Shigue, E. Ruppert. *Fault Current Limiter Using Transformer and Modular Device of YBCO Coated Conductor*. IEEE Transactions on Applied Superconductivity, 23(3): 5603804, 2013.

2. C. A. Baldan, J. S. Lamas, A. A. Bernardes, C. Y. Shigue, E. Ruppert. *Prototype Fault Current Limiter Using Transformer and a Modular Device of YBCO Coated Conductor*. Journal of Superconductivity and Novel Magnetism, 26(4): 12411245, 2013.

3. C. A. Baldan, J. S. Lamas, C. Y. Shigue, E. Ruppert, Test of a Modular Fault Current Limiter for 220 V Line Using YBCO Coated Conductor Tapes With Shunt Protection, IEEE Transactions on Applied Superconductivity, 21(3): 1242-1245, 2011.

4. J. S. Lamas, C. A.Baldan, C. Y. Shigue, A. Silhanek, V. Moshchalkov. *Electrical and Magnetic Characterization of BSCCO and YBCO HTS Tapes for Fault Current Limiter Application*. IEEE Transactions on Applied Superconductivity, 21(3): 3398-3402, 2011.

References

[1] M. Chen, B. Hallstedt, and L. J. Gauckler. *Thermodynamic modeling of the ZrO_2-$YO_{1.5}$ system*. Solid State Ionics, 170(3-4):255–274, 2004.

[2] G. A. Samara. *Low-Temperature Dielectric-properties of candidate substrates for high-temperature superconductors - $LAALO_3$ and ZrO_2-9.5 mol-percent-Y_2O_3*. Journal of Applied Physics, 68(8):4214–4219, 1990.

[3] O. Ruff and F. Ebert. *Contributions to the ceramics of highly refractory materials: Ii. System zirconia-lime*. Z. Anorg. Allg. Chem, 180(19), 1929.

[4] R. F. Geller and P. J. Yavorsky. *Effects of some oxide additions on the thermal length changes of zirconia*. Journal of Research os the National Bureau of Standards, 35:87, 1945.

[5] F. F. Lange. *Transformation toughening .3. Experimental-observations in the ZrO_2-Y_2O_3 system*. Journal of Materials Science, 17(1):240–246, 1982.

[6] F. Duwez, F. H. Brown, and F. Odell. *The Zirconia-Yttria System*. Journal of the Electrochemical Society, 98(9):356–362, 1951.

[7] A. R. Denton and N. W. Ashcroft. *Vegard Law*. Physical Review A, 43(6):3161–3164, 1991.

[8] T. Duangmanee, S. Wannakitti, R. Suwanwarangkul, and D. Charojrochkul. *Electrical Property of Thick Film Electrolyte for Solid Oxide Fuel Cell*. Journal of Metals, Materials and Minerals, 18(2):7–11, 2008.

[9] J. W. Fergus. *Electrolytes for solid oxide fuel cells*. Journal of Power Sources, 162(1):30–40, 2006.

[10] J. Will, A. Mitterdorfer, C. Kleinlogel, D. Perednis, and L. J. Gauckler. *Fabrication of thin electrolytes for second-generation solid oxide fuel cells*. Solid State Ionics, 131(1-2):79–96, 2000.

[11] P. T. Gao, L. J. Meng, M. P. dos Santos, V. Teixeira, and M. Andritschky. *Study of ZrO_2-Y_2O_3 films prepared by rf magnetron reactive sputtering*. Thin Solid Films, 377:32–36, 2000.

[12] C. Lopez-Gandara, F. M. Ramos, and A. Cirera. *YSZ-Based Oxygen Sensors and the Use of Nanomaterials: A Review from Classical Models to Current Trends*. Journal of Sensors, page 258489, 2009.

[13] J. M. Costantini, F. Guillet, S. Lambert, D. Grebille, F. Beuneu, and C. Trautmann. *X-ray diffraction study of the damage induced in yttria-stabilized zirconia by swift heavy ion irradiations*. Journal of Applied Physics, 104(7):8, 2008.

[14] R.S. Lima and B.R. Marple. *Nanostructured YSZ thermal barrier coatings engineered to counteract sintering effects*. Materials Science and Engineering: A, 485(1-2):182, 2008.

[15] N. P. Padture, M. Gell, and E. H. Jordan. *Thermal Barrier Coatings for Gas-Turbine Engine Applications*. Science, 296(5566):280, 2002.

[16] *Fuel Cells - Electrolyte*. http://www.doitpoms.ac.uk/tlplib/fuel-cells/sofc_electrolyte.php, 2004.

[17] H. Tomaszewski. *Toughening effects in Al_2O_3-ZrO_2 system*. Ceramics International, 14(2):117–125, 1988.

[18] C.S. Montross. *Relationships of tetragonal precipitate statistics with bulk properties in magnesia-partially stabilized zirconia*. Journal of the European Ceramic Society, 11(5):471–480, 1993.

[19] D. G. Jensen. *Enhanced toughness of a partially stabilised zirconia at elevated temperatures*. Journal of the European Ceramic Society, 16(8):825–831, 1996.

[20] S. Maschio, A. Bachiorrini, E. Lucchini, and S. Brckner. *Synthesis and sintering of chemically derived BaO-ZrO_2 solid solutions*. Journal of the European Ceramic Society, 24(8):2241–2246, 2004.

[21] R. Küngas, J.M. Vohs, and R. J. Gorte. *Effect of the Ionic Conductivity of the Electrolyte in Composite SOFC Cathodes*. Journal of The Electrochemical Society, 158(6):B743–B748, 2011.

[22] W. Vangool. *Structural aspects of anomalously fast ionic conductivity in solids*. Journal of Solid State Chemistry, 7(1):55–58, 1973.

[23] B. V. R. Chowdari and S. K. Akhter. *Ionic transport studies of lithium phosphoarsenate glassy system*. Solid State Ionics, 28:747–751, 1988.

[24] M. T. Lanagan, J. K. Yamamoto, A. Bhalla, and S. G. Sankar. *The dielectric properties of yttria-stabilized zirconia*. Materials Letters, 7(12):437–440, 1989.

[25] N.Q. Minh and T. Takahashi. *Science and Technology of Ceramic Fuel Cells*. Elsevier, New York, 1995.

[26] B. Kumar, C. Chen, C. Varanasi, and J.P. Fellner. *Electrical properties of heterogeneously doped yttria stabilized zirconia*. Journal of Power Sources, 140(1):12–20, 2005.

[27] Y. W. Zhang, S. Jin, Y. Yang, G. B. Li, S. J. Tian, J. T. Jia, C. S. Liao, and C. H. Yan. *Electrical conductivity enhancement in nanocrystalline $(RE_2O_3)(0.08)(ZrO_2)(0.92)$ (RE=Sc, Y) thin films*. Applied Physics Letters, 77(21):3409–3411, 2000.

[28] M. Gerstl, E. Navickas, G. Friedbacher, F. Kubel, M. Ahrens, and J. Fleig. *The separation of grain and grain boundary impedance in thin yttria stabilized zirconia (YSZ) layers*. Solid State Ionics, 185(1):32–41, 2011.

[29] E. Navickas, M. Gerstl, F. Kubel, and J. Fleig. *Simultaneous Measurement of the In- and Across-Plane Ionic Conductivity of YSZ Thin Films*. Journal of the Electrochemical Society, 159(4):B411–B416, 2012.

[30] S. J. Ha, B. C. Shin, M. W. Cho, K. J. Lee, and W. S. Cho. *High speed end-milling characteristics of pre-sintered Al_2O_3/Y-TZP ceramic composites for dental applications*. Journal of the Ceramic Society of Japan, 118(1383):1053–1056, 2010.

[31] D. R. R. Lazar, M. C. Bottino, M. Ozcan, L. F. Valandro, R. Amaral, V. Ussui, and A. H. A. Bressiani. *Y-TZP ceramic processing from coprecipitated powders: A comparative study with three commercial dental ceramics*. Dental Materials, 24(12):1676–1685, 2008.

[32] J. Vleugels, Z. X. Yuan, and O. Van Der Biest. *Mechanical properties of Y_2O_3/Al_2O_3-coated Y-TZP ceramics*. Journal of the European Ceramic Society, 22(6):873–881, 2002.

[33] Y. Zhang, A. Pajares, and B. R. Lawn. *Fatigue and damage tolerance of Y-TZP ceramics in layered biomechanical systems*. Journal of Biomedical Materials Research Part B-Applied Biomaterials, 71B(1):166–171, 2004.

[34] C. Piconi and G. Maccauro. *Zirconia as a ceramic biomaterial*. Biomaterials, 20:1–25, 1999.

[35] Q.-L. Xiao, C. Xu, S.-Y. Shao, J.-D. Shao, and Z.-X. Fan. *Y_2O_3 stabilized ZrO_2 thin films deposited by electron-beam evaporation: Optical properties, structure and residual stresses*. Vacuum, 83(2):366–371, 2008.

[36] S. Heiroth, R. Ghisleni, T. Lippert, J. Michler, and A. Wokaun. *Optical and mechanical properties of amorphous and crystalline yttria-stabilized zirconia thin films prepared by pulsed laser deposition*. Acta Materialia, 59:2330–2340, 2011.

[37] N. Nicoloso, A. Lobert, and B. Leibold. *Optical absorption studies of tetragonal and cubic thin-film yttria-stabilized zirconia*. Sensors and Actuators B: Chemical, 8(3):253–256, 1992.

[38] S. Ostanin, A. J. Craven, D. W. McComb, D. Vlachos, A. Alavi, M. W. Finnis, and A. T. Paxton. *Effect of relaxation on the oxygen K-edge electron energy-loss near-edge structure in yttria-stabilized zirconia*. Physical Review B, 62(22):14728–14735, 2000.

[39] S. K. Pandey, O. P. Thakur, R. Raman, A. Goyal, and A. Gupta. *Structural and optical properties of YSZ thin films grown by PLD technique*. Applied Surface Science, 257(15):6833–6836, 2011.

[40] B.K. Ridley. *Large-Bandgap Semiconductors*. Journal of Physics, 23:577–582, 1999.

[41] R. C. Buchanan and S. Pope. *Optical and electrical properties of yttria stabilized zirconia (YSZ) crystals*. Journal of the Electrochemical Society, 130(4):962–966, 1983.

[42] G. Garcia, J. Casado, J. Llibre, J. Cifre, A. Figueras, S. Gal, and J. Bassas. *Structural Properties of Yttria-Stabilized Zirconia Films Grown on SIlicon (001) using MOCVD*. Chemical Vapor Deposition, 3(2):91, 1997.

[43] J.Y. Dai, H.C. Ong, and R.P.H. Chang. *Structural properties of YSZ thin films grown by pulsed laser deposition*. Journal of Materials Research, 14(4):1329, 1999.

[44] J.-W. Lee, T. E. Schlesinger, A. K. Stamper, M. Migliuolo, D. W. Greve, and E. Laughlin. *Characterization of yttria-stabilized zirconium oxide buffer layers for high-temperature superconductor thin films*. Journal of Applied Physics, 64(11):6502–6504, 1988.

[45] H. Hayashi, T. Saitou, N. Maruyama, H. Inaba, K. Kawamura, and M. Mori. *Thermal expansion coefficient of yttria stabilized zirconia for various yttria contents*. Solid State Ionics, 176(5-6):613–619, 2005.

[46] A. Rauf, Q. Yu, L. Jin, and C. Zhou. *Microstructure and thermal properties of nanostructured lanthana-doped yttria-stabilized zirconia thermal barrier coatings by air plasma spraying*. Scripta Materialia, 66(2):109–112, 2012.

[47] J. E. Alaniz, F. G. Perez-Gutierrez, G. Aguilar, and J. E. Garay. *Optical properties of transparent nanocrystalline yttria stabilized zirconia*. Optical Materials, 32(1):62–68, 2009.

[48] F. Mauvy, P. Lenormand, C. Lalanne, F. Ansart, J. M. Bassat, and J. C. Grenier. *Electrochemical characterization of YSZ thick films deposited by dip-coating process*. Journal of Power Sources, 171(2):783–788, 2007.

[49] Y. Matsuoka and E. Ban. *Properties of sprayed YSZ buffer layers on alumina substrates for YBCO thick films*. Journal of Alloys and Compounds, 268(1-2):226–232, 1998.

[50] H. Holzschuh and H. Suhr. *Textured (100) Yttria-stabilized zirconia thin-films deposited by plasma-enhanced chemical vapor-deposition*. Applied Physics Letters, 59(4):470–472, 1991.

[51] P. Briois and A. Billard. *A comparison of electrical properties of sputter-deposited electrolyte coatings dedicated to intermediate temperature solid oxide fuel cells*. Surface & Coatings Technology, 201(3-4):1328–1334, 2006.

[52] P. Amezaga-Madrid, W. Antunez-Flores, J. Gonzalez-Hernandez, J. Saenz-Hernandez, K. Campos-Venegas, O. Solis-Canto, C. Ornelas-Gutierrez, O. Vega-Becerra, R. Martinez-Sanchez, and M. Miki-Yoshida. *Microstructural properties of multi-nano-layered YSZ thin films*. Journal of Alloys and Compounds, 495(2):629–633, 2010.

[53] G. Sakthinathan, R. Saravanan, and C. Uthirapathy. *Thermal characteristics of yttria stabilized zirconia nanolubricants*. Thermal science, 16(2):481–487, 2012.

[54] K. Vernieuwe, P. Lommens, J.C. Martins, F. Van Den Broeck, I. Van Driessche, and K. De Buysser. *Aqueous ZrO_2 and YSZ Colloidal Systems through Microwave Assisted Hydrothermal Synthesis*. Materials, 6:4082–4095, 2013.

[55] D. K. Fork, S. M. Garrison, M. Hawley, and T. H. Geballe. *Effects of homoepitaxial surfaces and interface compounds on the inplane epitaxy of YBCO films on yttria-stabilized zirconia*. Journal of Materials Research, 7(7):1641–1651, 1992.

[56] N. Savvides, A. Thorley, S. Gnanarajan, J. Hermann, A. Katsaros, and A. Molodyk. *YBCO Coated Tapes Fabricated by IBAD and Magnetron Sputtering Techniques*. Physica C, 341-348:2491–2492, 2000.

[57] D. D. Hass. *Directed Vapor Deposition of Thermal Barrier Coatings*. PhD thesis, University of Virginia, 2000.

[58] M. Karadge, X. Zhao, M. Preuss, and P. Xiao. *Microtexture of the thermally grown alumina in commercial thermal barrier coatings*. Scripta Materialia, 54:639–644, 2006.

[59] H. Zhao, F. Yu, T.D Bennett, and H. N. G. Wadley. *Morphology and thermal conductivity of yttria-stabilized zirconia coatings*. Acta Materialia, 54:5195–5207, 2006.

[60] W.R Chen, R. Archer, X. Huang, and B.R. Marple. *TGO Growth and crack propagation in a thermal barrier coating*. Journal of Thermal Spray Technology, 17(5-6):858, 2008.

[61] K. D. Harris, D. Vick, E. J. Gonzalez, T. Smy, K. Robbie, and M. J. Brett. *Porous thin lms for thermal barrier coatings*. Surface & Coatings Technology, 138:185–191, 2001.

[62] D. D. Hass, P. A. Parrish, and H. N. G. Wadley. *Electron beam directed vapor deposition of thermal barrier coatings*. Journal of Vacuum Science & Technology A: Vacuum, Surfaces, and Films, 16(6):3396, 1998.

[63] T. Kimura and T. Goto. *Ir-YSZ nano-composite electrodes for oxygen sensors*. Surface and Coatings Technology, 198(1-3):36–39, 2005.

[64] C.M.S. Rodrigues, J.A. Labrincha, and F. M. B. Marques. *Postmortem characterization of one yttria stabilized zirconia (YSZ)-based oxygen sensor*. Solid State Ionics, 136-137:671–675, 2000.

[65] R. Ramamoorthy, P.K. Dutta, and S.A. Akbar. *Oxygen sensors: Materials, methods, designs and applications*. Journal of Materials Science, 38:4271–4282, 2003.

[66] C.C Liu. *Electrochemical Sensors*. CRC Press LLC, Boca Raton, 2000.

[67] N.Q. Minh. *Solid oxide fuel cell technology: features and applications*. Solid State Ionics, 174(1-4):271–277, 2004.

[68] P. Singh. *Solid Oxide Fuel Cells: Technology Status*. International Journal of Applied Ceramic Technology, 1(1):5, 2004.

[69] M.A.J. Cropper, S. Geiger, and D.M. Jollie. *Fuel cells: a survey of current developments*. Journal of Power Sources, 131:57, 2004.

[70] M. C. Williams. *Status and Promise of Fuel Cell Technology*. Fuel Cells, 1(2):87, 2001.

[71] A. Weyl and D. Janke. *High-temperature ionic conduction in multicomponent solid oxide solutions based on zirconia*. Journal of the American Ceramic Society, 80(4):861–873, 1997.

[72] C. Brahim, A. Ringuedé, E. Gourba, M. Cassir, A. Billard, and P. Briois. *Electrical properties of thin bilayered YSZ/GDC SOFC electrolyte elaborated by sputtering*. Journal of Power Sources, 156(1):45–49, 2006.

[73] N. El Habra, M. Bolzan, C. De Zorzi, M. Favaro, M. Casarin, C. Sada, and G. Rossetto. *Stabilized Zirconia Based Materials for Solid Oxide Fuel Cells (SOFC) obtained by MOCVD and Aerosol-CVD*. The electrochemical society, 25(8):805, 2009.

[74] K. C. Lau, H. Turner, and B.I. Dunlap. *Kinetic Monte Carlo simulation of the Yttria Stabilized Zirconia (YSZ) fuel cell cathode*. Solid State Ionics, 179:1912, 2008.

[75] B. Hobein, F. Tietz, D. Stover, M. Cekada, and P. Panjan. *DC sputtering of yttria-stabilised zirconia films for solid oxide fuel cell applications*. Journal of the European Ceramic Society, 21(10-11):1843–1846, 2001.

[76] T. Mori, Y. Wang, J. Drennan, G. Auchterlonie, J.G. Li, and T. Ikegami. *Influence of particle morphology on nanostructural feature and conducting property in Sm-doped CeO_2 sintered body*. Solid State Ionics, 175:641–649, 2004.

[77] S. Gnanarajan and N. Savvides. *Evolution of texture of CeO_2 thin film buffer layers prepared by ion-assisted deposition*. Thin Solid Films, 350(1-2):124–129, 1999.

[78] W. Zhao, S. An, and L. Ma. *Processing and characterization of Bi_2O_3 and Sm_2O_3 Codoped CeO_2 electrolyte for intermediate-temperature solid oxide fuel cell*. Journal of the American Ceramic Society, 94(5):1496–1502, 2011.

[79] T. Klemens, J. Nielsen, P. Blennow, Å.H. Persson, T. Stegk, B.H. Christensen, and S. Snderby. *High performance metal-supported solid oxide fuel cells with Gd-doped ceria barrier layers*. Journal of Power Sources, 196:9459, 2011.

[80] S.P.S. Badwal, F.T. Ciacchi, and D. Milosevic. *Scandia - zirconia electrolytes for intermediate temperature solid oxide fuel cell operation*. Solid State Ionics, 136-137:91, 2000.

[81] J.T.S. Irvine, T. Politova, N. Zakowsky, A. Kruth, S. Tao, R. Travis, and O. Attia. *Scandia-Zirconia Electrolytes and Electrodes for SOFCS*. NATO Science Series, 202:35, 2005.

[82] R. Devanathan, S. Thevuthasan, and J. D. Gale. *Defect interactions and ionic transport in scandia stabilized zirconia*. Phys Chem Chem Phys, 11(26):5506–5511, 2009.

[83] N. Jiang, E.D. Wachsman, and S.H. Jung. *A higher conductivity Bi_2O_3-based electrolyte*. Solid State Ionics, 150:347–353, 2002.

[84] A. V. Shlyakhtina and L. G. Shcherbakova. *New solid electrolytes of the pyrochlore family*. Russian Journal of Electrochemistry, 48(1):1–25, 2012. Russ J Electrochem.

[85] P. K. Srivastava, T. Quach, Y. Y. Duan, R. Donelson, S. P. Jiang, F. T. Ciacchi, and S. P. S. Badwal. *Electrode supported solid oxide fuel cells: Electrolyte films prepared by DC magnetron sputtering*. Solid State Ionics, 99(3-4):311–319, 1997.

[86] H. A. Hamedani. *Investigation of deposition parameters in ultrasonic spray pyrolysis for fabrication of solid oxide fuel cell cathode*. PhD thesis, Georgia Institute of Technology, 2008.

[87] P. M. M. B. Tavares. *Filmes finos supercondutores do sistema Bi-Sr-Ca-Cu-O obtidos por deposição química de vapores organometálicos assistida por aerossol*. PhD thesis, Universidade de Trás-Os-Montes e Alto Douro, 2001.

[88] S. Joon Hyung, C. Cheng-Chieh, H. Hong, and F. B. Prinz. *Atomic layer deposition of yttria-stabilized zirconia for solid oxide fuel cells*. Chemistry of Materials, 19(15):3850–3854, 2007.

[89] Y. Jee, I. Chang, J.-W. Son, J.-H. Lee, S. Kang, and S. W. Cha. *Fabrication of Thin Solid Oxide Film Fuel Cells*. Journal of the Korean Ceramic Society, 47(1):82–85, 2010.

[90] C. C. Chao, C. M. Hsu, Y. Cui, and F. B. Prinz. *Improved Solid Oxide Fuel Cell Performance with Nanostructured Electrolytes*. Acs Nano, 5(7):5692–5696, 2011.

[91] K. S. Son, K. Bae, J. W. Kim, J. S. Ha, and J. H. Shim. *Ion conduction in nanoscale yttria-stabilized zirconia fabricated by atomic layer deposition with various doping rates*. Journal of Vacuum Science & Technology A, 31(1), 2013. Son, Kyung Sik Bae, Kiho Kim, Jun Woo Ha, Jeong Suk Shim, Joon Hyung.

[92] E. B. Ramirez, A. Huanosta, J. P. Sebastian, L. Huerta, A. Ortiz, and J. C. Alonso. *Structure, composition and electrical properties of YSZ films deposited by ultrasonic spray pyrolysis*. Journal of Materials Science, 42(3):901–907, 2007.

[93] A. Zalga, B. Abakevicien, A. Zarkov, A. Beganskien, A. Kareiva, and S. Tamulevicius. *On the Properties of Yttria-Stabilized Zirconia Thin Films Prepared by Sol-Gel Method*. Materials Science, 17(2):191–196, 2011.

[94] I. Van Driessche, S. Hopkins, P. Lommens, X. Granados, D. Andreouli, B. Glowacki, I. M. Arabatzis, M. Arin, S. Ricart, I. Fasaki, E. Georgiopoulos, and R. Tomov. *Efficient and Environmentally Friendly Ink-Jet Printing of Ceramic Thin Films*. Nanoscience and Nanotechnology Letters, 5(4):466–474, 2013.

[95] G. Laukaitis and J. Dudonis. *Development of SOFC thin film electrolyte using electron beam evaporation technique from the cubic phase YSZ powder*. Materials Science, 11(1):9–1313, 2005.

[96] G. Laukaitis, J. Dudonis, and D. Milcius. *YSZ thin films deposited by e-beam technique*. Thin Solid Films, 515(2):678–682, 2006.

[97] M. Hartmanova, I. Thurzo, M. Jergel, J. Bartos, F. Kadlec, V. Zelezny, D. Tunega, F. Kundracik, S. Chromik, and M. Brunel. *Characterization of yttria-stabilized zirconia thin films deposited by electron beam evaporation on silicon substrates*. Journal of Materials Science, 33(4):969–975, 1998.

[98] G. Laukaitis, J. Dudonis, A. F. Orliukas, and D. Milcius. *Properties of YSZ thin films deposited by e-beam technique*. Solid State Ionics, 179(1-6):182–187, 2008.

[99] J. K. Hirvonen. *Ion beam assisted thin film deposition*. Materials Science Reports, 6(6):215–274, 1991.

[100] R. J. Gaboriaud, F. Pailloux, P. Guerin, and F. Paumier. *Yttrium sesquioxide, Y_2O_3, thin films deposited on Si by ion beam sputtering: microstructure and dielectric properties*. Thin Solid Films, 400(1-2):106–110, 2001.

[101] P. C. McIntyre, K. G. Ressler, N. Sonnenberg, and M. J. Cima. *Transmission electron microscopy investigation of biaxial alignment development in YSZ films fabricated using ion beam assisted deposition*. Journal of Vacuum Science & Technology a-Vacuum Surfaces and Films, 14(1):210–215, 1996.

[102] A. Knierim, R. Auer, J. Geerk, Y. Li, G. Linker, O. Meyer, J. Reiner, P. Schweiss, and R. Smithey. *Influence of the process parameters on the growth of YSZ-layers prepared by ion beam assisted deposition (IBAD)*. Nuclear Instruments & Methods in Physics Research Section B-Beam Interactions with Materials and Atoms, 127:832–836, 1997.

[103] Y. J. Mao, B. Y. Jiang, C. X. Ren, F. Zhang, X. H. Liu, and S. C. Zou. *Control of the YSZ biaxial alignment on polycrystalline Ni - Cr substrates by ion beam selective resputtering*. Thin Solid Films, 312(1-2):27–31, 1998.

[104] V. Betz, B. Holzapfel, and L. Schultz. *In situ reflection high energy electron bombardment analysis of biaxially oriented yttria-stabilized zirconia thin film growth on amorphous substrates*. Thin Solid Films, 301(1-2):28–34, 1997.

[105] J. Denul, G. De Winter, and R. De Gryse. *Ion assisted deposition of biaxially aligned YSZ layers on metal tape*. Physica C-Superconductivity and Its Applications, 351(1):45–48, 2001.

[106] J. H. Suh, S. H. Oh, H. S. Kim, S.-Y. Choi, and C.-G. Park. *Effects of neutralizers on the crystal orientation of YSZ films grown by using ion beam sputtering*. Vacuum, 74(3-4):423–430, 2004.

[107] K. Robbie and M. J. Brett. *Sculptured thin films and glancing angle deposition: Growth mechanics and applications*. Journal of Vacuum Science & Technology A: Vacuum, Surfaces, and Films, 15(3):1460, 1997.

[108] K. Robbie, J.C. Sit, and M.J. Brett. *Advanced techniques for glancing angle deposition*. Journal of Vacuum Science & Technology B: Microelectronics and Nanometer Structures, 16(3):1115, 1998.

[109] Y. Zhao, D. Ye, G.-C. Wang, and T.-M. Lu. *Designing nanostructures by glancing angle deposition*. Proceedings of the SPIE - The International Society for Optical Engineering, 5219(1):59–7373, 2003.

[110] K. G. Ressler, N. Sonnenberg, and M. J. Cima. *The development of biaxial alignment in yttria-stabilized zirconia films fabricated by ion beam assisted deposition*. Journal of Electronic Materials, 25(1):35, 1996.

[111] K. G. Ressler, N. Sonnenberg, and M. J. Cima. *Mechanism of biaxial alignment of oxide thin films during ion-beam-assisted deposition*. Journal of the American Ceramic Society, 80(10):2637–2648, 1997.

[112] Y. J. Mao, C. X. Ren, J. Yuan, F. Zhang, X. H. Liu, and S. C. Zou. *Study on the growth of biaxially aligned yttria-stabilized zirconia films during ion beam assisted deposition*. Journal of Vacuum Science & Technology a-Vacuum Surfaces and Films, 15(5):2687–2692, 1997.

[113] H. C. Mu, C. X. Ren, B. Y. Jiang, X. Z. Ding, Y. H. Yu, X. Wang, X. H. Liu, G. E. Zhou, and Y. B. Jia. *Growth of biaxially textured yttria-stabilized zirconia thin films on Si(111) substrate by ion beam assisted deposition*. Chinese Physics Letters, 17(3):221–223, 2000.

[114] Z. Wang, B. J. Yan, F. Feng, H. Chen, K. Shi, and Z. Han. *A competition between (001) and (011) alignments in yttria stabilized zirconia thin films fabricated by ion beam assisted deposition*. Physica C-Superconductivity and Its Applications, 470(15-16):622–625, 2010.

[115] M. Kidszun, R. Huhne, B. Holzapfel, and L. Schultz. *Ion-beam-assisted deposition of textured NbN thin lms*. Superconductor Science and Technology, 23:025010, 2010.

[116] *Ion-beam assisted deposition*. http://www.ifw-dresden.de/index.php?id=459&L=0, 2013.

[117] X. M. Xiong, Y. L. Zhou, Z. H. Chen, H. B. Lu, A. J. Zhu, D. F. Cui, H. S. Wang, and G. Z. Yang. *Room temperature deposition of yttria-stabilized zirconia buffer layer on metallic substrates by laser ablation*. Chinese Science Bulletin, 42(16):1345–1350, 1997.

[118] P. Li, J. Carroll, and J. Mazumder. *Room temperature growth of biaxially aligned yttria-stabilized zirconia films on glass substrates by pulsed-laser deposition*. Journal of Physics D-Applied Physics, 36(13):1605–1608, 2003.

[119] D. Hong, L. Liu, X. Song, and Y. Li. *Influence of O_2 Pressure on the Structure and Surface Morphology of YSZ Layer for YBCO Coated Conductor Deposited by PLD on Ni-W Tape*. Journal Supercond Nov Magn, 24:17071713, 2011.

[120] S. Heiroth, T. Lippert, A. Wokaun, M. Do uml beli, J. L. M. Rupp, B. Scherrer, and L. J. Gauckler. *Yttria-stabilized zirconia thin films by pulsed laser deposition: Microstructural and compositional control*. Journal of the European Ceramic Society, pages 489–95, 2010.

[121] A. Cavallaro, M. Burriel, J. Roqueta, A. Apostolidis, A. Bernardi, A. Tarancon, R. Srinivasan, S. N. Cook, H. L. Fraser, J. A. Kilner, D. W. McComb, and J. Santiso. *Electronic nature of the enhanced conductivity in YSZ-STO multilayers deposited by PLD*. Solid State Ionics, 181(13-14):592–601, 2010.

[122] J. H. Joo and G. M. Choi. *Electrical conductivity of YSZ film grown by pulsed laser deposition*. Solid State Ionics, 177(11-12):1053–1057, 2006.

[123] H. U. Krebs, M. Weisheit, J. Faupel, E. Suske, T. Scharf, C. Fuhse, M. Stormer, K. Sturm, M. Seibt, H. Kijewski, D. Nelke, E. Panchenko, and M. Buback. *Pulsed laser deposition (PLD) - A versatile thin film technique*, volume 43 of *Advances in Solid State Physics*. Springer-Verlag Berlin, Berlin, 2003.

[124] R. Schwarz. *Pulsed Laser Deposition (PLD) - Abstract*. http://groups.ist.utl.pt/rschwarz/rschwarzgroup_files/PLD_files/PLD.htm, 2013.

[125] E. S. Thiele, L. S. Wang, T. O. Mason, and S. A. Barnett. *Deposition and properties of Ytrria-stabilized Zirconia thin-films using reactive direct-current magnetron sputtering*. Journal of Vacuum Science & Technology a-Vacuum Surfaces and Films, 9(6):3054–3060, 1991.

[126] R. Wendt, K. Ellmer, and K. Wiesemann. *Thermal power at a substrate during ZnO:Al thin film deposition in a planar magnetron sputtering system*. Journal of Applied Physics, 82(5):2115–2122, 1997.

[127] W. C. Tsai and T. Y. Tseng. *Characterization of yttria-stabilized zirconia thin films grown by planar magnetron sputtering*. Thin Solid Films, 306(1):86–91, 1997.

[128] M. Boulouz, A. Boulouz, A. Giani, and A. Boyer. *Influence of substrate temperature and target composition on the properties of yttria-stabilized zirconia thin films grown by rf reactive magnetron sputtering*. Thin Solid Films, 323(1-2):85–92, 1998.

[129] K. Koski, J. Holsa, and P. Juliet. *Properties of aluminium oxide thin films deposited by reactive magnetron sputtering*. Thin Solid Films, 339(1-2):240–248, 1999.

[130] D. Y. Kaufman, P.M. DeLuca, T. Tsai, and S. A. Barnett. *High-rate deposition of biaxially textured yttria-stabilized zirconia by dual magnetron oblique sputtering*. Journal of Vacuum Science & Technology A, 17(5):2826, 1999.

[131] I. Safi. *Recent aspects concerning DC reactive magnetron sputtering of thin films: A review*. Surface & Coatings Technology, 127(2-3):203–219, 2000.

[132] M. Massi, H.S. Maciel, C. Otani, R.D. Mansano, and P. Verdonck. *Electrical and structural characterization of DLC films deposited by magnetron sputtering*. Journal of Materials Science: Materials in Electronics, 12:343, 2001.

[133] S. Venkataraj, O. Kappertz, H. Weis, R. Drese, R. Jayavel, and M. Wuttig. *Structural and optical properties of thin zirconium oxide films prepared by reactive direct current magnetron sputtering*. Journal of Applied Physics, 92(7):3599–3607, 2002.

[134] S. Mahieu, G. Buyle, P. Ghekiere, S. Heirwegh, R. De Gryse, and D. Depla. *Mechanism of biaxial alignment in thin films, deposited by magnetron sputtering*. Thin Solid Films, 515(2):416–420, 2006.

[135] P. Briois, F. Lapostolle, V. Demange, E. Djurado, and A. Billard. *Structural investigations of YSZ coatings prepared by DC magnetron sputtering*. Surface & Coatings Technology, 201(12):6012–6018, 2007.

[136] D. Pamu, K. Sudheendran, M. G. Krishna, and K. C. J. Raju. *Crystallographic texture, morphology, optical, and microwave dielectric properties of dc magnetron sputtered nanostructured zirconia thin films*. Journal of Vacuum Science & Technology A, 26(2):185–192, 2008.

[137] M. Saraiva, H. Chen, W. P. Leroy, S. Mahieu, N. Jehanathan, O. Lebedev, V. Georgieva, R. Persoons, and D. Depla. *Influence of Al Content on the Properties of MgO Grown by Reactive Magnetron Sputtering*. Plasma Processes and Polymers, 6:S751–S754, 2009.

[138] D. Depla, S. Mahieu, and J. E. Greene. *Sputter deposition processes*. Elsevier, 3^{rd} edition, 2009.

[139] P. Coddet, M.C. Pera, and A. Billard. *Reactive co-sputter deposition of YSZ coatings using plasma emission monitoring*. Surface & Coatings Technology, 205:3987, 2011.

[140] *Thin Films, Inc.* http://www.thinfilmsinc.com/, 2010.

[141] *Soleras Advanced Coatings*. http://www.soleras.com/, 2012.

[142] *AGC Glass Europe*. http://www.agc-glass.eu/, 2012.

[143] *Hüttinger Elektronik*. http://www.huettinger.com/en.html, 2013.

[144] *Advanced Energy, Inc.* http://www.advanced-energy.com/, 2013.

[145] *OC Oerlikon Balzers AG*. http://www.oerlikon.com/balzers/en/, 2013.

[146] *Nova Fabrica High Vacuum and Thin Film Components*. http://www.novafabrica.biz/, 2013.

[147] *Ara-Authentic GmbH*. http://www.ara-coatings.de/, 2013.

[148] *Von Ardenne*. http://www.vonardenne.biz/VON_ARDENNE.html, 2013.

[149] *Umicore Thin Film Products*. http://www.thinfilmproducts.umicore.com/Home/, 2013.

[150] E. Chen. *Thin Film Deposition*, 2004.

[151] J. A. Thornton and A.S. Penfield. *Thin Film Processes*. Academic Press, NY, 1975.

[152] P. D. Davidse. *Theory and practice of RF sputtering*. Vacuum, 17(3):139–145, 1967.

[153] A.P. Ehiasarian. *High-power impulse magnetron sputtering and its applications*. Pure Appl. Chem., 82(6):1247–1258, 2010.

[154] K. Sarakinos, J. Alami, and S. Konstantinidis. *High power pulsed magnetron sputtering: A review on scientific and engineering state of the art*. Surface and Coatings Technology, 204(11):1661–1684, 2010.

[155] U. Helmersson, M. Lattemann, J. Bohlmark, A. P. Ehiasarian, and J. T. Gudmundsson. *Ionized physical vapor deposition (IPVD): A review of technology and applications*. Thin Solid Films, 513(1-2):1–24, 2006.

[156] A. F. Jankowski and J. P. Hayes. *Reactive sputter deposition of yttria-stabilized zirconia*. Surface & Coatings Technology, 76(1-3):126–131, 1995.

[157] S. Mahieu, P. Ghekiere, D. Depla, R. De Gryse, O. I. Lebedev, and G. Van Tendeloo. *Mechanism of in-plane alignment in magnetron sputtered biaxially aligned yttria-stabilized zirconia*. Journal of Crystal Growth, 290(1):272–279, 2006.

[158] P. Sigmund. *Theory of Sputtering. I. Sputtering Yield of Amorphous and Polycrystalline Targets*. Physical Review, 184(2):383–416, 1969.

[159] H. Lüth. *Solid Surfaces, Interfaces and Thin Film*. Springer-Verlag Berlin Heidelberg New York, 4^{th} edition, 2001.

[160] D. Depla, S. Mahieu, and R. De Gryse. *Magnetron sputter deposition: Linking discharge voltage with target properties*. Thin Solid Films, 517(9):2825–2839, 2009.

[161] M. P. Seah. *An accurate semi-empirical equation for sputtering yields, II: for neon, argon and xenon ions*. Nuclear Instruments and Methods in Physics Research Section B: Beam Interactions with Materials and Atoms, 229(3/4):348–358, 2005.

[162] M. P. Seah and T. S. Nunney. *Sputtering yields of compounds using argon ions*. Journal of Physics D-Applied Physics, 43(25):13, 2010.

[163] M.W. Thompson. *II. The energy spectrum of ejected atoms during the high energy sputtering of gold*. Philosophical Magazine, 18(152):377–414, 1968.

[164] M. W. Thompson. *Atomic collision cascades in solids*. Vacuum, 66(2):99–114, 2002.

[165] P. Ghekiere. *Structure Evolution of Biaxially Aligned Thin Films Deposited by Sputtering*. PhD thesis, University of Ghent, 2007.

[166] Y. Yamamura, Y. Mizuno, and H. Kimura. *Angular distributions of sputtered atoms for low-energy heavy ions, medium ions and light ions*. Nuclear Instruments & Methods in Physics Research B, 13:393, 1986.

[167] Y. Yamamura and K. Muraoka. *Over-cosine angular distribution of sputtered atoms at normal incidence*. Nuclear Instruments & Methods in Physics Research B, 42:175, 1989.

[168] D. Depla and S. Mahieu. *Reactive Sputter Deposition*. Springer, Belgium, 2008.

[169] J. F. Ziegler, M. D. Ziegler, and J. P. Biersack. *The Stopping and Range of Ions in Matter*, 2008.

[170] M. J. Goeckner, J. A. Goree, and T. E. Sheridan. *Monte Carlo simulation of ions in a magnetron plasma*. IEEE Transactions on Plasma Science, 19(2):301–308, 1991.

[171] G. M. Turner. *Monte Carlo calculations of gas rarefaction in a magnetron sputtering discharge*. Journal of Vacuum Science & Technology A, 13(4):2161, 1995.

[172] S. Mahieu, G. Buyle, P. Ghekiere, S. Heirwegh, R. De Gryse, and D. Depla. *Monte Carlo simulation of the transport of atoms in DC magnetron sputtering*. Nuclear Instruments & Methods in Physics Research Section B-Beam Interactions with Materials and Atoms, 243(2):313–319, 2006.

[173] K. Van Aeken, S. Mahieu, and D. Depla. *The metal flux from a rotating cylindrical magnetron: a Monte Carlo simulation*. Journal of Physics D: Applied Physics, 41:205307, 2008.

[174] V. S. Smentkowski. *Trends in sputtering*. Progress in Surface Science, 64(1-2):1–58, 2000.

[175] Inc. AJA International. *Sputtering - What is Sputtering?* http://www.ajaint.com/whatis.htm, 2001.

[176] P. J. Kelly and R. D. Arnell. *Magnetron sputtering: a review of recent developments and applications*. Vacuum, 56(3):159–172, 2000.

[177] R.K. Waits. *Planar magnetron sputtering*. Journal of Vacuum Science & Technology, 15(2):179–187, 1978.

[178] W. D. Westwood. *Sputter Deposition*. Education Committee, AVS, 2003.

[179] *TORUS Production Magnetron Sputter Sources*. www.lesker.com, 2013.

[180] A. Anders. *Discharge physics of high power impulse magnetron sputtering*. Surface and Coatings Technology, 205, Supplement 2(0):S1–S9, 2011.

[181] W. Window and N. Savvides. *Charged particle fluxes from planar magnetron sputtering sources*. Journal of Vacuum Science & Technology A (Vacuum, Surfaces, and Films), 4(2):196–202202, 1986.

[182] A. G. Dirks and H. J. Leamy. *Columnar microstructure in vapor-deposited thin films*. Thin Solid Films, 47(3):219–233, 1977.

[183] D. Depla, G. Buyle, J. Haemers, and R. De Gryse. *Discharge voltage measurements during magnetron sputtering*. Surface & Coatings Technology, 200(14-15):4329, 2006.

[184] L.C. Wu and J. E. Greene. *Mechanisms of the reactive- and chemical-sputter deposition of TiO_2 from Ti and TIC targets in mixed $Ar+O_2$ discharges*. Journal of Applied Physics, 50(7):4966–4971, 1979.

[185] S. Berg, H. O. Blom, T. Larsson, and C. Nender. *Modeling of reactive sputtering of compound materials*. Journal of Vacuum Science & Technology a-Vacuum Surfaces and Films, 5(2):202–207, 1987.

[186] D. Depla and R. De Gryse. *Target poisoning during reactive magnetron sputtering: Part I: the influence of ion implantation*. Surface & Coatings Technology, 183(2-3):184–189, 2004.

[187] J. A. Venables. *Introduction to Surface and Thin Film Processes*. Cambridge University Press, 2000.

[188] M. Batzill and U. Diebold. *The surface and materials science of tin oxide*. Progress in Surface Science, 79:108, 2005.

[189] A. Zangwill. *Physics at surface*. Cambridge University Press, 4^{th} edition, 1988.

[190] K. Lautern. *Molecular beam epitaxy (MBE)*. www.physik.uni-kl.de, 2012.

[191] J. A. Venables, G. D. T. Spiller, and M. Hanbcken. *Nucleation and growth of thin films*. Reports on Progress in Physics, 47:399 – 459, 1984.

[192] T. Young. *An Essay on the Cohesion of Fluids*. Philosophical Transactions of the Royal Society of London, page 95, 1805.

[193] C. Ratsch and J.A. Venables. *Nucleation theory and the early stages of thin film growth*. Journal of Vacuum Science & Technology A, 21(5):S96–S109, 2003.

[194] R. Q. Hwang, C. Günther, J. Schröder, S. Günther, E. Kopatzki, and R. J. Behm. *Nucleation and Growth of Thin Metal-Films on Clean and Modified Metal Substrates Studied by Scanning Tunneling Microscopy*. Journal of Vacuum Science & Technology a-Vacuum Surfaces and Films, 10:1970–1980, 1992.

[195] S. Mahieu. *Biaxial alignment in sputter deposited thin films*. PhD thesis, University of Ghent, 2006.

[196] C. V. Thompson and R. Carel. *Texture development in polycrystalline thin-films*. Materials Science and Engineering B-Solid State Materials for Advanced Technology, 32(3):211–219, 1995.

[197] R. D. Vengrenovitch. *On The Ostwald Ripening Theory*. Acta Metallurgica, 30(6):1079 – 1086, 1982.

[198] R. Tsybukh. *A comparative study of platinum nanodeposits on HOPG (0001), MnO(100) and MnO_x/MnO(100) surfaces by STM and AFM after heat treatment in UHV, O_2 , CO and H_2*. PhD thesis, Leiden University, 2010.

[199] C. R. Stoldt, C. J. Jenks, P. A. Thiel, A. M. Cadilhe, and J. W. Evans. *Smoluchowski ripening of Ag islands on Ag(100)*. Journal of Chemical Physics, 111(11):5157–5166, 1999.

[200] B. A. Movchan and Demchish.Av. *Study of structure and properties of thick vacuum condensates of nickel, titanium, tungsten, aluminium oxide and zirconium dioxide*. Physics of Metals and Metallography-Ussr, 28(4):83, 1969.

[201] J. A. Thornton. *Influence of apparatus geometry and deposition conditions on structure and topography of thick sputtered coatings*. Journal of Vacuum Science & Technology, 11(4):666–670, 1974.

[202] J. A. Thornton. *The microstructure of sputterdeposited coatings*. Journal of Vacuum Science & Technology A, 4:3059–3065, 1986.

[203] R. Messier, A. P. Giri, and R. A. Roy. *Revised structure zone model for thin film physical structure*. Journal of Vacuum Science & Technology A, 2:500 – 503, 1984.

[204] P. B. Barna and M. Adamik. *Fundamental structure forming phenomena of polycrystalline films and the structure zone models*. Thin Solid Films, 317:27–33, 1998.

[205] I. Petrov, P. B. Barna, L. Hultman, and J. E. Greene. *Microstructural evolution during film growth*. Journal of Vacuum Science & Technology A, 21(5):S117–S128, 2003.

[206] W. D. Sproul, D. J. Christie, and D. C. Carter. *Control of reactive sputtering processes*. Thin Solid Films, 491(1/2):1–17, 2005.

[207] V. V. Poroshin, D. Yu Bogomolov, and A. G. Kostyuk. *Automated measuring system based on high-precision Talystep profilometer for monitoring surface-roughness standards*. Russian Engineering Research, 30(6):642–644, 2010.

[208] R. Swanepoel. *Determination of the thickness and optical-constants of amorphous-silicon*. Journal of Physics E-Scientific Instruments, 16(12):1214–1222, 1983.

[209] M. Stahl, T. Trottenberg, and H. Kersten. *A calorimetric probe for plasma diagnostics*. Review of Scientific Instruments, 81(2):023504, 2010.

[210] S. D. Ekpe and S. K. Dew. *Investigation of thermal flux to the substrate during sputter deposition of aluminum*. Journal of Vacuum Science & Technology A, 20(6):1877, 2002.

[211] X. M. Xiong, Y. L. Zhou, H. B. Lu, Z. H. Chen, and G. Z. Yang. *Preparation of Y-Ba-Cu-O films on polycrystalline metal substrates with biaxially aligned yttria-stabilized zirconia buffer layers deposited by ion beam assisted pulsed laser deposition*. Physica C-Superconductivity and Its Applications, 298(3-4):178–184, 1998.

[212] L. D. Doucette, M. Pereira da Cunha, and R.J. Lad. *Precise orientation of single crystals by a simple x-ray diffraction rocking curve method*. Review of Scientific Instruments, 76(3):036106, 2005.

[213] D. C. Kundaliya, S.B. Ogalea, S. Dhara, K.F. McDonaldb, E. Knoeselb, T. Osedachb, S.E. Loflandb, S.R. Shindea, and T. Venkatesana. *Large second-harmonic kerr rotation in $GaFeO_3$ thin films on YSZ buffered silicon*. Journal of Magnetism and Magnetic Materials, 299:2, 2006.

[214] B. K. Tanner, S. J. Miles, G. G. Peterson, and R. N. Sacks. *Measurement of aluminum concentration in GaAlAs epitaxial layers by double-axis X-ray-diffraction*. Materials Letters, 7(5-6):239–241, 1988.

[215] F. C. Gandarilla, F. C. Cereijo, L. F. Cobas, and J. P. Gómez. *Textura cristalográfica*. Revista Mexicana de Fsica, 44(3):222–230, 1998.

[216] C. Detavernier and C. Lavoie. *Texture in thin films*. Icotom 14: Textures of Materials, Pts 1and 2, 495-497:1333–1342, 2005.

[217] *Materials Research Laboratory at UCSB*. http://www.mrl.ucsb.edu/centralfacilities/x-ray/basics, 2003.

[218] P. Ghekiere, S. Mahieu, R. De Gryse, and D. Depla. *Structure evolution of the biaxial alignment in sputter-deposited MgO and Cr*. Thin Solid Films, 515(2):485–488, 2006.

[219] P. Ghekiere, S. Mahieu, G. De Winter, R. De Gryse, and D. Depla. *Influence of the deposition parameters on the biaxial alignment of MgO grown by unbalanced magnetron sputtering*. Journal of Crystal Growth, 271(3-4):462–468, 2004.

[220] L. Peng, J. Carroll, and J. Mazumder. *Room temperature growth of biaxially aligned yttria-stabilized zirconia films on glass substrates by pulsed-laser deposition*. Journal of Physics D (Applied Physics), 36(13):1605–1608, 2003.

[221] K. Wada, N. Yamaguchi, and H. Matsubara. *Crystallographic texture evolution in ZrO_2-Y_2O_3 layers produced by electron beam physical vapor deposition*. Surface & Coatings Technology, 184(1):55–62, 2004.

[222] S. Mahieu, P. Ghekiere, G. De Winter, S. Heirwegh, D. Depla, R. De Gryse, O. I. Lebedev, and G. Van Tendeloo. *Mechanism of preferential orientation in sputter deposited titanium nitride and yttria-stabilized zirconia layers*. Journal of Crystal Growth, 279(1-2):100–109, 2005.

[223] J. A. Thornton. *Magnetron Sputtering - Basic Physics and Application to Cylindrical Magnetrons*. Journal of Vacuum Science & Technology, 15(2):171, 1978.

[224] G. Buyle, W. De Bosscher, D. Depla, K. Eufinger, J. Haemers, and R. De Gryse. *Recapture of secondary electrons by the target in a DC planar magnetron discharge*. Vacuum, 70(1):29, 2003.

[225] P. Scherrer. *Bestimmung der Grsse und der Inneren Struktur von Kolloidteilchen Mittels Rntgenstrahlen*. Nachrichten von der Gesellschaft der Wissenschaften, 2:98–100, 1918.

[226] A. L. Patterson. *The Scherrer Formula for X-Ray Particle Size Determination*. Physical Review, 56:978, 1939.

[227] K. Y. Chan and B. S. Teo. *Effect of Ar pressure on grain size of magnetron sputter-deposited Cu thin films*. Iet Science Measurement & Technology, 1(2):87–90, 2007.

[228] V. B. Glushkova, L. V. Sazonova, and F. Hanic. *Lattice parameters of cubic solid solutions in the systems uR_2O_3-(1-u)MO_2*. Ceramurgia International/Ceramurgia International, 4(4):176–8, 1978.

[229] R.. J. Heritage, P. Porteous, and B. J. Sheppard. *Determining the composition of InP-GaP Alloys using Vergard's law*. Journal of Materials Science, 5(8):709–710, 1970.

[230] Th. H. de Keijser, J. I. Langford, E. J. Mittemeijer, and A. B. P. Vogels. *Use of the Voigt function in a single-line method for the analysis of X-ray diffraction line broadening*. Journal of Applied Crystallography, 15(3):308–314, 1982.

[231] J. Denul. *Sputterdepositie van ZrO_2: Y_2O_3 bufferlagen en $YBa_2Cu_3O_{7-x}$ toplagen : invloed van de depositieparameters op de groei en de eigenschappen*. PhD thesis, University of Ghent, 1998.

[232] M. O. Zacate, L. Minervini, D. J. Bradfield, R. W. Grimes, and K. E. Sickafus. *Defect cluster formation in M_2O_3-doped cubic ZrO_2*. Solid State Ionics, 128(1-4):243–254, 2000.

[233] J. M. Calderon-Moreno and M. Yoshimura. *Characterization by Raman spectroscopy of solid solutions in the yttria-rich side of the zirconia-yttria system*. Solid State Ionics, 154:125–133, 2002.

[234] A. P. Bechepeche, O. Treu, E. Longo, C. O. Paiva-Santos, and J. A. Varela. *Experimental and theoretical aspects of the stabilization of zirconia*. Journal of Materials Science, 34(11):2751–2756, 1999.

[235] K. L. Barbalace. *Periodic Table of Elements*. http://environmentalchemistry.com/yogi/periodic/, 1995.

[236] F. Gencarelli, B. Vincent, J. Demeulemeester, A. Vantomme, A. Moussa, A. Franquet, A. Kumar, H. Bender, J. Meersschaut, W. Vandervorst, R. Loo, M. Caymax, K. Temst, and M. Heyns. *Crystalline Properties and Strain Relaxation Mechanism of CVD Grown GeSn*. Ecs Journal of Solid State Science and Technology, 2(4):P134–P137, 2013.

[237] M. Reason, X. Weng, W. Ye, D. Dettling, S. Hanson, G. Obeidi, and R. S. Goldman. *Stress evolution in GaAsN alloy films*. Journal of Applied Physics, 97(10), 2005.

[238] M.J. Ashwin, R.J.H Morris, D. Walker, P.A. Thomas, M.G. Dowsett, T.S. Jones, and Veal T.D. *Molecular-beam epitaxy and lattice parameter of GaN_xSb_{1-x}: deviation from Vegard's law for x >0.02*. Journal of Applied Physics, 46:264003, 2013.

[239] G.C.A.M. Janssen. *Stress and strain in polycrystalline thin films*. Thin Solid Films, 515:6654–6664, 2007.

[240] K. Van Aeken. *Simulation of Metal TRAnsport*, 2008.

[241] F. Boydens, W. P. Leroy, R. Persoons, and D. Depla. *The influence of target surface morphology on the deposition flux during direct-current magnetron sputtering*. Thin Solid Films, 531:32–41, 2013.

[242] Y. Yamamura, T. Takiguchi, and M. Ishida. *Energy and anulgar-distributions of sputtered atoms at normal incidence*. Radiation Effects and Defects in Solids, 118(3):237–261, 1991.

[243] S. Mahieu, W. P. Leroy, K. Van Aeken, M. Wolter, J. Colaux, S. Lucas, G. Abadias, P. Matthys, and D. Depla. *Sputter deposited transition metal nitrides as back electrode for CIGS solar cells*. Solar Energy, 85(3):538–544, 2011.

[244] N. Sonnenberg, A. S. Longo, M. J. Cima, B. P. Chang, K. G. Ressler, P. C. McIntyre, and Y. P. Liu. *Preparation of biaxially aligned cubic zirconia films on pyrex glass substrates using ion-beam-assisted deposition*. Journal of Applied Physics, 74(2):1027–1034, 1993.

[245] S. Sonderby, A. J. Nielsen, B. H. Christensen, K. P. Almtoft, J. Lu, J. Jensen, L. P. Nielsen, and P. Eklund. *Reactive magnetron sputtering of uniform yttria-stabilized zirconia coatings in an industrial setup*. Surface & Coatings Technology, 206(19-20):4126–4131, 2012.

[246] Baron Roberts. *Meazure version 2.0*, 2001-2004.

[247] S. D. Ekpe and S. K. Dew. *Theoretical and experimental determination of the energy flux-during magnetron sputter deposition onto an unbiased substrate*. Journal of Vacuum Science & Technology A, 21(2):476, 2003.

[248] S. D. Ekpe and S. K. Dew. *Measurement of energy flux at the substrate in a magnetron sputter system using an integrated sensor*. Journal of Vacuum Science & Technology A, 22(4):1420, 2004.

[249] T.P. Drüsedau, T. Bock, T.M. John, F. Klabunde, and W. Eckstein. *Energy transfer into the growing film during sputter deposition: An investigation by calorimetric measurements and Monte Carlo simulations*. Journal of Vacuum Science & Technology A, 17(5):2896, 1999.

[250] S. Mahieu and D. Depla. *Reactive sputter deposition of TiN layers: modelling the growth by characterization of particle fluxes towards the substrate*. Journal of Physics D-Applied Physics, 42(5):16, 2009.

[251] C. Boudias and D. Monceau. *The Crystallographic Software for Research and Teaching*, 1989-2005.

[252] J. S. Lamas, W. P. Leroy, and D. Depla. *The fictional transition of the preferential orientation of yttria-stabilized zirconia thin films*. Thin Solid Films, 525:6–12, 2012.

[253] M. Saraiva and D. Depla. *Texture and microstructure in co-sputtered Mg-M-O (M=Mg, Al, Cr, Ti, Zr, and Y) films*. Journal of Applied Physics, 111:104903, 2012.

[254] R. Becker and S. Panchanadeeswaran. *Crystal rotations represented as Rodrigues vectors*. Textures and Microstructures, 10(3):167–194, 1989.

[255] G. Radnóczi, M.-A Hasan, and J.-E Sundgren. *Defects in amorphous and solid phase epitaxial silicon*. Thin Solid Films, 240(1-2):39, 1994.

[256] G. H. Vineyard. *Grazing-Incidence diffraction and the distorted-wave approximation for the study of surfaces*. Physical Review B, 26(8):4146–4159, 1982.

[257] M. Ohring. *Materials Science of Thin Films: Deposition and Structure*. Academic Press, New Jersey, second edition, 2002.

[258] S. Timoshenko. *Analysis of bi-metal thermostats*. Journal of the Optical Society of America, 11(3):233–255, 1925.

[259] J. S. Lamas, W. P. Leroy, and D. Depla. *Influence of target-substrate distance and composition on the preferential orientation of yttria-stabilized zirconia thin films*. Thin Solid Films, 520(14):4782, 2012.

[260] M. Saraiva. *Sputter deposition of MgO Thin Films: The effect of Cation Substitution*. PhD thesis, Ghent University, 2012.

[261] P. Meakin, P. Ramanlal, L. M. Sander, and R. C. Ball. *Ballistic deposition on surfaces*. Physical Review A, 34(6):5091–5103, 1986.

[262] Y.-W. Su, C.-S. Wu, C.-C. Chen, and C.-D. Chen. *Fabrication of two-dimensional arrays of CdSe pillars using e-beam lithography and electrochemical deposition*. Advanced Materials, 15(1):49–51, 2003.

[263] M. Vorozhtsova, J. Drbohlavova, and J. Hubalek. *Chemical Microsensors with Ordered Nanostructures*. Minin, Prof. Igor, 2011.

[264] R.S. Wagner and W.C. Ellis. *Vapor-liquid-solid mechanism of single crystal growth*. Applied Physics Letters, 4(5):89–90, 1964.

[265] Y. Wu and P. Yang. *Direct observation of vapor-liquid-solid nanowire growth*. Journal of American Society, 123:3165–3166, 2001.

[266] L. S. Yu, J. M. E. Harper, J. J. Cuomo, and D. A. Smith. *Alignment of thin films by glancing angle ion bombardment during deposition*. Applied Physics Letters, 47(9):932–933, 1985.

[267] B. Dick, M.J. Brett, and T. Smy. *Investigation of substrate rotation at glancing incidence on thin-film morphology*. Journal of Vacuum Science & Technology B: Microelectronics and Nanometer Structures, 21(6):2569, 2003.

[268] J. Lintymer, J. Gavoille, N. Martin, and J. Takadoum. *Glancing angle deposition to modify microstructure and properties of sputter deposited chromium thin films*. Surface & Coatings Technology, 174:316–323, 2003.

[269] J. Lintymer, N. Martin, J. M. Chappe, and J. Takadoum. *Glancing angle deposition to control microstructure and roughness of chromium thin films*. Wear, 264(5-6):444–449, 2008.

[270] L. Gonzalez-Garcia, J. Parra-Barranco, J. R. Sanchez-Valencia, A. Barranco, A. Borras, A. R. Gonzalez-Elipe, M. C. Garcia-Gutierrez, J. J. Hernandez, D. R. Rueda, and T. A. Ezquerra. *Correlation lengths, porosity and water adsorption in TiO_2 thin films prepared by glancing angle deposition*. Nanotechnology, 23(20):10, 2012.

[271] P. Solar, A. Choukourov, J. Hanus, E. Pavlova, D. Slavinska, and H. Biederman. *Nanocomposite structured thin films by magnetron sputtering at glancing angle deposition*. In International Plasma Chemistry Society, Bochum, Germany, 2009.

[272] P. Amezaga-Madrid, W. Antunez-Flores, I. Monarrez-Garcia, J. Gonzalez-Hernandez, R. Martinez-Sanchez, and M. Miki-Yoshida. *Synthesis, structural characterization and optical properties of multilayered Yttria-stabilized ZrO_2 thin films obtained by aerosol assisted chemical vapour deposition*. Thin Solid Films, 516(23):8282–8288, 2008.

[273] A. L. Larsson and G. A. Niklasson. *Optical properties of electrochromic all-solid-state devices*. Solar Energy Materials and Solar Cells, 84(1-4):351–360, 2004.

[274] P. O. Nilsson. *Determination of optical constants from intensity measurements at normal incidence*. Applied Optics, 7(3):435–442, 1968.

[275] T. C. Paulick. *Inversion of normal-incidence (R,T) measurements to obtain n + ik for thin films*. Applied Optics, 25(4):562–564, 1986.

[276] D. Poelman and P. F. Smet. *Methods for the determination of the optical constants of thin films from single transmission measurements: a critical review*. Journal of Physics D-Applied Physics, 36(15):1850–1857, 2003.

[277] B. E. Yoldas. *Investigations of porous oxides as an anti-reflective coating for glass surfaces*. Applied Optics, 19(9):1425–1429, 1980.

[278] Crystec Kristalltechnologie. *Y:ZrO_2-YSZ*. www.crystec.de, 2013.

[279] V. R. PaiVerneker, A. N. Petelin, F. J. Crowne, and D. C. Nagle. *Color-center-induced band-gap shift in yttria-stabilized zirconia*. Physical Review B, 40(12):8555–8557, 1989.

[280] A. A. Higazy, A. Hussein, and M. A. Awaida. *A study of the optical absorption edge in silicate glasses containing TiO_2 oxide*. Journal of Materials Science, 24(6):2203–2208, 1989.

[281] J. S. Co. Tydex. *Synthetic Sapphire*. http://www.tydexoptics.com/pdf/Sapphire.pdf, 1994-2013.

[282] I. Kosacki, V. Petrovsky, and H. U. Anderson. *Band gap energy in nanocrystalline ZrO_2:16%Y thin films*. Applied Physics Letters, 74(3):341–343, 1999.

[283] E. Navickas, M. Gerstl, G. Friedbacher, F. Kubel, and J. Fleig. *Measurement of the across-plane conductivity of YSZ thin films on silicon*. Solid State Ionics, 211:58–64, 2012.

[284] P. Mondal, A. Klein, W. Jaegermann, and H. Hahn. *Enhanced specific grain boundary conductivity in nanocrystalline Y_2O_3-stabilized zirconia*. Solid State Ionics, 118(3-4):331–339, 1999.

[285] A. R. Bushroa, R. G. Rahbari, H. H. Masjuki, and M. R. Muhamad. *Approximation of crystallite size and microstrain via XRD line broadening analysis in TiSiN thin films*. Vacuum, 86:1107–1112, 2012.